ASME
SETTING THE STANDARD

Transactions of the ASME, Journal of Fluids Engineering
(ISSN 0098-2202) is published monthly by
The American Society of Mechanical Engineers,
Three Park Avenue, New York, NY 10016.
Periodicals postage paid at New York, NY
and additional mailing offices.
POSTMASTER: Send address changes to Transactions of the
ASME, Journal of Fluids Engineering, c/o THE AMERICAN
SOCIETY OF MECHANICAL ENGINEERS,
22 Law Drive, Box 2300, Fairfield, NJ 07007-2300.
CHANGES OF ADDRESS must be received at Society
headquarters seven weeks before they are to be effective.
Please send old label and new address.

Journal of Fluids Engineering

Published Monthly by ASME

VOLUME 131 • NUMBER 7 • JULY 2009

RESEARCH PAPERS

Flows in Complex Systems

Fundamental Issues and Canonical Flows

Multiphase Flows

Techniques and Procedures

(Contents continued on inside back cover)

This journal is printed on acid-free paper, which exceeds the ANSI Z39.48-1992 specification for permanence of paper and library materials. ♾™
♻ 85% recycled content, including 10% post-consumer fibers.

(**Contents continued**)

Journal of Fluids Engineering **Volume 131, Number 7** **JULY 2009**

TECHNICAL BRIEFS

The ASME Journal of Fluids Engineering is abstracted and indexed in the following:

Applied Science & Technology Index, Chemical Abstracts, Chemical Engineering and Biotechnology Abstracts (Electronic equivalent of Process and Chemical Engineering), Civil Engineering Abstracts, Computer & Information Systems Abstracts, Corrosion Abstracts, Current Contents, Ei EncompassLit, Electronics & Communications Abstracts, Engineered Materials Abstracts, Engineering Index, Environmental Engineering Abstracts, Environmental Science and Pollution Management, Excerpta Medica, Fluidex, Index to Scientific Reviews, INSPEC, International Building Services Abstracts, Mechanical & Transportation Engineering Abstracts, Mechanical Engineering Abstracts, METADEX (The electronic equivalent of Metals Abstracts and Alloys Index), Petroleum Abstracts, Process and Chemical Engineering, Referativnyi Zhurnal, Science Citation Index, SciSearch (The electronic equivalent of Science Citation Index), Shock and Vibration Digest, Solid State and Superconductivity Abstracts, Theoretical Chemical Engineering

Numerical Simulation of Flow Past Multiple Porous Cylinders

M. H. Al-Hajeri
Faculty of Technical Studies,
PAAET,
Roudha, Kuwait 73460

A. Aroussi
Director of Studies
School of Engineering,
Leicester University,
Leicester, LE1 7RH, UK

A. Witry
Automotive R&D Center,
Windsor, ON, N9B 3P4 Canada

The present study numerically investigates two-dimensional laminar flow past three circular porous cylinders arranged in an in-line array. Six approaches to face velocity (V_i/V_f) ratios are used and particle trajectories are computed for a range of velocities and particle diameters. Furthermore, the flow past a solid cylinder, which had similar geometry characteristics to the porous cylinders used in this study, is compared with the flow around multiple porous cylinders. For the same range of Reynolds number (312–520), the flow behavior around the solid cylinder differs from the flow around the porous cylinders. The flow characteristics around solid cylinders are determined by the Reynolds number, whereas the flow characteristics around the porous cylinders are detrained by the V_i/V_f ratio. Stagnation areas are found behind each porous cylinder, and the size of these areas increases as the V_i/V_f velocity ratio increases. Furthermore, for the particle ranges used in power plants (<50 μm), the particles were uniformly distributed around the surface of the porous cylinders. [DOI: 10.1115/1.3153363]

1 Introduction

The flow over a bank of porous cylinders is a subject of interest in many engineering applications such as filtration in power plants and incinerators. It is beneficial to study the behavior of flow past solid cylinders before studying the flow past porous cylinders in order to understand clearly the differences and limitations. Zukauskas [1] provided readers with a rich review of experimental investigations of fluid flow over tube banks. The first numerical investigation of the flow in tube banks was reported by Launder and Massey [2]. Comprehensive studies were carried out by Farhanieh [3] using computational methods. His studies show that the expected trend of increased pressure drops accompanying any increases in heat transfer coefficients. Furthermore, Wilson and Bassiouny [4] reviewed and studied the laminar and turbulent flow past a single cylinder and across an in-line and staggered tube bank.

Verma and Bhatt [5] and Kirsh [6] analytically studied the flow past a porous circular cylinder at a small Reynolds number. Numerical analysis of vortex shedding behind a porous square cylinder was conducted by Jue [7]. He found that for flow past a lower permeability cylinder, the vortex occurs earlier and the shedding period is longer. Analytical studies for flow between fixed porous cylinders are conducted by Djordjevic [8] and von Welfersdorf [9], and between rotating cylinders by Min and Lueptow [10] and Chang [11].

The porous cylinder presents exactly the candle filter that is used in various applications such as cogeneration power plants for cleaning the gas before entering the gas turbine to protect the turbine blade from damaging. It is also used in incinerators to separate the air from the solid particles. A candle filter element generally consists of a long slender hollow tube closed at one end. Kerr and Probert [12] carried out an experimental investigation in candle filters. At the Aachen University [13], an array of six candle filter elements was mounted downstream of a combustor. Furthermore, an array of 130 candle filter elements was investigated at Grimethorpe [14]. The ceramic candle filters were tested at various operating conditions to investigate the flow conditions in the candle filter vicinity. Alhajeri et al. [15] studied the flow around a single candle filter using the particle image velocimetry (PIV) experimental technique. In addition, they used computational fluid dynamics (CFD) to investigate the flow past a candle filter, using constant filtration velocity as a boundary condition replacing the porous boundary.

The geometry of multiple filters looks similar to that of a tube bank. However, there are major differences between the two cases: The tubes are solid and modeled as wall cells but the porous cylinders are modeled as porous live cells. In the case of the porous cylinders, there is suction through the filter so no boundary layer forms around the filters as is the case in the flow past solid cylinders. Oscillating vortex street is found behind the tube for a Reynolds numbers greater than 100. However, from the study that will be discussed in this paper, for the flow around multiple porous cylinders, the vortex shedding appeared only with a high Reynolds number. In general, the flow around multiple porous cylinders is entirely different from the flow past multiple porous cylinders with approach/filtration (V_i/V_f) velocity ratios that are used in the filtration process.

2 Mathematical Formulation

The aim of this investigation is to understand the effects on the flow past a porous circular cylinder that result from the permeability of the porous material and the slip of the fluid particles at the outer surface of the porous material. The flow field is divided into two regions, i.e., the free fluid region (outside the cylinders) and the flow through the porous media. In the free fluid region, the equations that govern the steady-state flow of a two-dimensional incompressible fluid are the differential expressions for mass and momentum conservation. These are given by

$$\frac{\partial u}{\partial x} + \frac{\partial v}{\partial y} = 0 \tag{1}$$

$$u\frac{\partial u}{\partial x} + v\frac{\partial u}{\partial y} = -\frac{1}{\rho}\frac{\partial p}{\partial x} + \nu\left(\frac{\partial^2 u}{\partial x^2} + \frac{\partial^2 u}{\partial y^2}\right) \tag{2}$$

$$u\frac{\partial v}{\partial x} + v\frac{\partial v}{\partial y} = -\frac{1}{\rho}\frac{\partial p}{\partial y} + \nu\left(\frac{\partial^2 v}{\partial x^2} + \frac{\partial^2 v}{\partial y^2}\right) \tag{3}$$

where ρ, p, and ν are the dimensional density, pressure, and kinematic viscosity, respectively. Also, u and v are the velocity components in x- and y-directions.

The flow is governed by Darcy's law in the second region, where the fluid flows through porous material (inside the circular cylinder).

Contributed by the Fluids Engineering Division of ASME for publication in the JOURNAL OF FLUIDS ENGINEERING. Manuscript received June 20, 2007; final manuscript received April 15, 2009; published online June 19, 2009. Assoc. Editor: Ian Eames.

$$u = \frac{K_p}{\mu} \nabla P \tag{4}$$

where K_p, p, and μ are the permeability of the medium, pressure, and the dynamics viscosity, respectively.

For flow past a solid cylinder, the renormalization group (RNG) k-ε is used due to its capability for low Reynolds numbers [16]. The RNG k-ε theory, developed in the 1980s, is based on the work done by Orszag and co-workers [17,18], and was derived using a rigorous statistical technique called the RNG theory. In the RNG model, the local turbulent kinetic energy k and local energy dissipation rate ε are used to eliminate the length scale l from the dynamics and the Reynolds averaged Navier–Stokes (RANS) equation of motion [19].

In the RNG formulation the turbulent viscosity μ_t is evaluated by $\mu_{\text{eff}} - \mu_l$, where μ_l is the laminar viscosity. The effective viscosity μ_{eff} is computed by

$$\mu_{\text{eff}} = \mu_l \left(1 + \sqrt{\frac{C_\mu}{v_l}} \frac{k}{\sqrt{\varepsilon}}\right)^2 \tag{5}$$

where $C_\mu = 0.0845$. The kinetic energy of the turbulence k and its dissipation rate ε are governed by separate transport equations. Unlike the standard k-ε formulation, the RNG-based k-ε turbulence model contains very few empirically adjustable parameters. In the RNG-based k-ε model, the k and ε transport equations are

$$\frac{\partial}{\partial x_i}(\rho U_i k) = \frac{\partial}{\partial x_i}\left(\alpha \rho \mu_t \frac{\partial k}{\partial x_i}\right) + P_k - \rho\varepsilon \tag{6}$$

$$\frac{\partial}{\partial x_i}(\rho_g U_i \varepsilon) = \frac{\partial}{\partial x_i}\left(\alpha \rho \mu_t \frac{\partial \varepsilon}{\partial x_i}\right) + \frac{\varepsilon}{k}(C_{1\varepsilon} P_k - C_{2\varepsilon}\rho\varepsilon) - \rho R \tag{7}$$

where α is an inverse Prandtl number, which may be obtained from the following equation [18]:

$$\left|\frac{\alpha - 1.3929}{\alpha_0 - 1.3929}\right|^{0.6321} \left|\frac{\alpha + 2.3929}{\alpha_0 + 2.3929}\right|^{0.3679} = \frac{\mu_l}{\mu_{\text{eff}}} \tag{8}$$

where $\alpha_0 = 1$. The turbulence production P_k is evaluated by

$$P_k = \rho \mu_t \left(\frac{\partial U_i}{\partial x_j} + \frac{\partial U_j}{\partial x_i}\right)\left(\frac{\partial U_i}{\partial x_j}\right) \tag{9}$$

The rate of strain term R in the ε-equation is expressed as

$$R = \frac{C_\mu \eta^3 (1 - \eta/\eta_0)}{1 + \beta \eta^3} \frac{\varepsilon^2}{k} \tag{10}$$

$$\eta = \frac{k}{\varepsilon}(2S_{ij}^2)^{1/2} \tag{11}$$

$$S_{ij} = \frac{1}{2}\left(\frac{\partial U_i}{\partial x_j} + \frac{\partial U_j}{\partial x_i}\right) \tag{12}$$

where $\beta = 0.015$ and $\eta_o = 4.38$. According to the RNG theory, the constants in the turbulent transport equations take the value of $C_{1\varepsilon} = 1.42$ and $C_{2\varepsilon} = 1.68$, respectively.

In summary, the RNG k-ε model provides improved accuracy in applications with separated flows, flows with high streamline curvature and high strain rate, low Reynolds number flow (the case in this paper), transitional flow, wake flows, and vortex shedding systems. In complex flows, such as high-swirling flows, velocities and turbulent intensities vary considerably in each direction. Thus, the RNG k-ε model is not adequate for these cases [20].

3 The Geometry and Grid

The physical model of the two-dimensional horizontal plane for flow around three porous cylinders is shown in Fig. 1. The three porous cylinders are arranged in in-line (or square) array. The

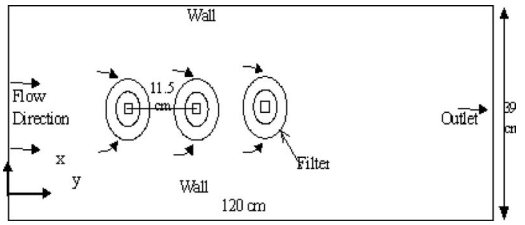

Fig. 1 The physical geometry of the multiple filter model

domain extends sufficiently far downstream to about ten times of the porous cylinder diameter ($10d$) or 68.5 cm from the center of the third porous cylinder. The outlet is far beyond any recirculation zones that may be created by the porous cylinder. This is also to minimize the effects of the outflow boundary conditions on the flow characteristics in the vicinity of the third porous cylinder. The inflow boundary is located at a distance of four porous cylinder diameters in front of the first porous cylinder.

The viscous pressure drop along the porous cylinder cavity is negligible compared with the viscous pressure drop through the wall [20]. Therefore, a two-dimensional computational model will be considered.

The duct length is 120 cm and the width is 39 cm. The porous cylinders are placed in the middle of the width distance. Thus, the porous cylinder centers are 19.5 cm from the wall. This is wide enough to encompass the range of vortex shedding if this occurred in the range of Reynolds numbers used in this study. Ireland et al. [21] and Li et al. [22] found that for turbulent flow when the ratio of the domain width to the cylinder diameter is greater than 5, the duct wall boundary effect can be neglected. The porous cylinders have an outer diameter of 6.5 cm and an inner diameter of 3 cm. The distance between each of the two porous cylinders centers is 11.5 cm.

The unstructured mesh was created in FLUENT's mesh generator GAMBIT. The distribution of grids in the duct is constant; however, the grids are condensed around and inside the porous cylinders to ensure accurate simulation for the fluid inside the high gradient zone. In the present study FLUENT is used to model the problem. The unstructured grid is shown in Fig. 2.

4 Boundary Conditions

The domain is a two-dimensional plane and has four boundaries, as shown in Fig. 1. The inflow boundary or the main inlet is set as a constant x-component and zero y-component of the velocity. In this study, six approach velocities or inlet velocities V_i, as

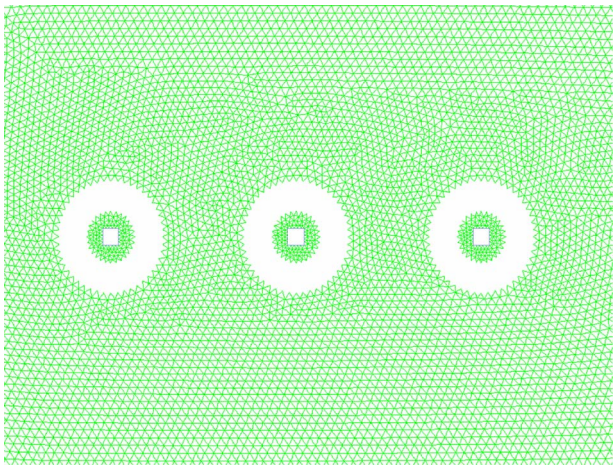

Fig. 2 Middle part of the unstructured mesh without the filter mesh

Table 1 Summary of boundary conditions and physical parameters

Face velocity V_f	4 cm/s
Approach velocity V_i	7.2 cm/s, 8 cm/s, 8.8 cm/s, 10 cm/s, 12 cm/s, and 20 cm/s
V_i/V_f	1.8, 2, 2.2, 2.5, 3, and 5
Fluid	Air
Viscosity	1.8×10^{-5} kg/ms
Density	1.2 kg/m^3
No. of cells	32,286
Turbulence model	Laminar

used in the Grimethorpe investigation [14] (7.2 cm/s, 8 cm/s, 8.8 cm/s, 10 cm/s, 12 cm/s, and 20 cm/s), are used to create six V_i/V_f velocity ratios (1.8, 2, 2.2, 2.5, 3, and 5). The V_i/V_f velocity ratio is based on one porous cylinder. This means that the approach velocity is divided over the face velocity for one porous cylinder. The face velocity is the filtration velocity or the velocity at the outer face of the filter at the outflow boundary; the velocities are left free so that the default boundary condition of zero stress in normal and tangential directions is obtained. The upper and bottom boundaries are also set. A no-slip velocity boundary condition is applied on the wall, that is, both the x- and y-components of the velocity are constrained to be zero.

To make the fluid flow through the three porous cylinders, where the greatest pressure drop in the model occurs in the porous cylinder thickness, sinks inside the porous cylinders should be modeled. Therefore, an inlet in the shape of a rectangular cylinder is placed inside each porous cylinder. These inlets are set to reverse flow so they will act as outlets. The reason for this is to maintain several face filtration velocities. Here, the face filtration velocity V_f is assumed to be 4 cm/s. Table 1 lists the boundary conditions and physical parameters for the model.

As shown in Fig. 3, live cells surround the porous medium region in the domain. Here, the porous cells are not allowed to come into contact with the exterior geometrical domain due to code constraints. Hence, a region of live cells is placed at the low-pressure side of the porous cylinder. To maintain a constant face velocity at the surface of the porous cylinder, mass balance between the porous cylinder outer surface and inlet 2 is applied using Eq. (13). The permeability of the porous cylinder is assumed to be 1.6×10^{-10} m^2/m, and this is equivalent to the permeability used in the comprehensive experimental investigation done by Grimethorpe [14].

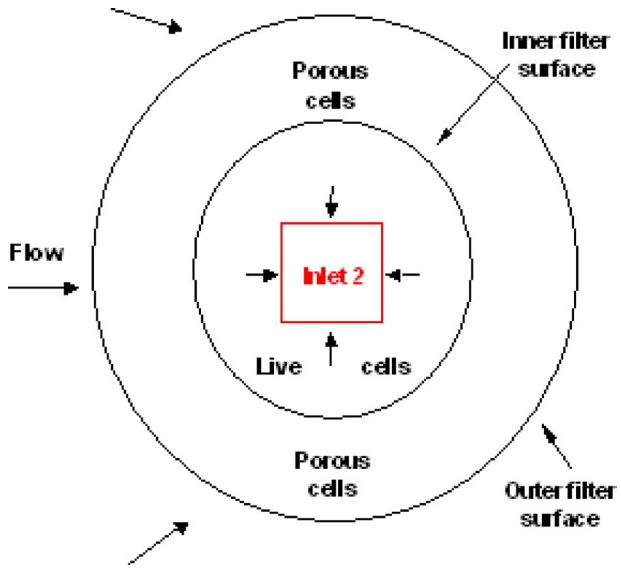

Fig. 3 The filter and the second inlet (or inlet 2)

$$V_2 = \frac{\pi R_o V_f}{L_{p2}} \tag{13}$$

5 Discussion of the Results

In the case of the flow in a tube bank, three flow regimes are distinguished by their Reynolds number: a laminar flow regime at $\mathrm{Re}<100$, a mixed flow regime at $10^2<\mathrm{Re}<2\times10^5$, and a turbulent flow regime at $\mathrm{Re}>2\times10^5$ [4,2]. The classification of the flow in the tube bank cannot be applied to the flow around the multiple porous cylinders. This is due to the fact that the flow behaviors are different in both cases and the effects of the porous cylinder act as a boundary layer bleeding mechanism. In this study, the Reynolds numbers based on porous cylinder diameters range from 312 to 520. However, it cannot be assumed that the flow is in the mixing flow regime as it is in the case of the flow past tube bank. Therefore, the flow will be modeled as laminar in the case of flow past porous cylinders.

The face velocity of 4 cm/s and the V_i/V_f velocity ratio of 2.5 are used here. Figure 4(h) shows the location of the x- and y-velocity profiles. The velocities in the y-direction (v-velocity) are shown in Figs. 4(a)–4(c) for different x-axis locations. The profile at distance of 40 cm on the x-axes across the center of the porous cylinder is shown in Fig. 4(b). Near the porous cylinder the velocity component in the y-direction increases due to the suction through the porous cylinder. Because the area of inlet 2 is smaller than the porous cylinder surface, the velocity at inlet 2 should be set higher than the face velocity. Thus, the v-velocity is at its highest in one side and at its lowest in the other when the set velocity is negative.

The profile at a distance of 33.5 cm is located between the first and second porous cylinders. The v-velocity profile for this location shows that the flow is symmetrical between the first two porous cylinders. It also shows that the fluid near the horizontal centerlines of the duct flows toward the second porous cylinder in a horizontal streamline.

Figures 4(d)–4(g) show the profiles for the velocities in the x-direction for different locations on the x- and y-axes. In the profile at distances of 40 cm on the x-axes, the highest velocity is at the porous cylinder surface. This is due to the reduction in the area of the flow in the presence of the porous cylinders. At inlet 2, the velocity is at minimum because the flow is entering the inlet vertically in the y-direction (the dominant velocity at both sides of the inlet 2 is y-component velocity). In the last porous cylinder, the velocity is higher near the porous cylinder and at the top. This is due to the flow start shedding behind the last porous cylinder, and this is clear in the profile, which is behind at an x-distance equal to 58.5. The velocity starts to oscillate to one side but this is a very small shed, and it does not appear as it was found in the tube bank.

The stagnation region is clear in the profile when x is equal to 58.5 cm. The velocity falls to the lowest value or almost zero. In this region, the flow is separated behind the porous cylinder, creating a stagnation region. Figure 4(g) shows the velocity profile in the x-direction at $y=19.5$ cm. The velocity reaches the maximum and minimum velocities at inlet 2 (due to the reverse flow behind the porous cylinder). Also, the u-velocity behind the third porous cylinder is constant.

5.1 Particle Tracking. To characterize the behavior of particles of different diameters in the presence of various flow fields, a parameter of comparison was required. Thus, a useful comparison criterion, the radius of convergence (see Fig. 5(a)), was chosen. It is essential to estimate the optimum distance between the porous cylinders and the velocity range which can be used. The radius of convergence is defined as the farthest perpendicular dis-

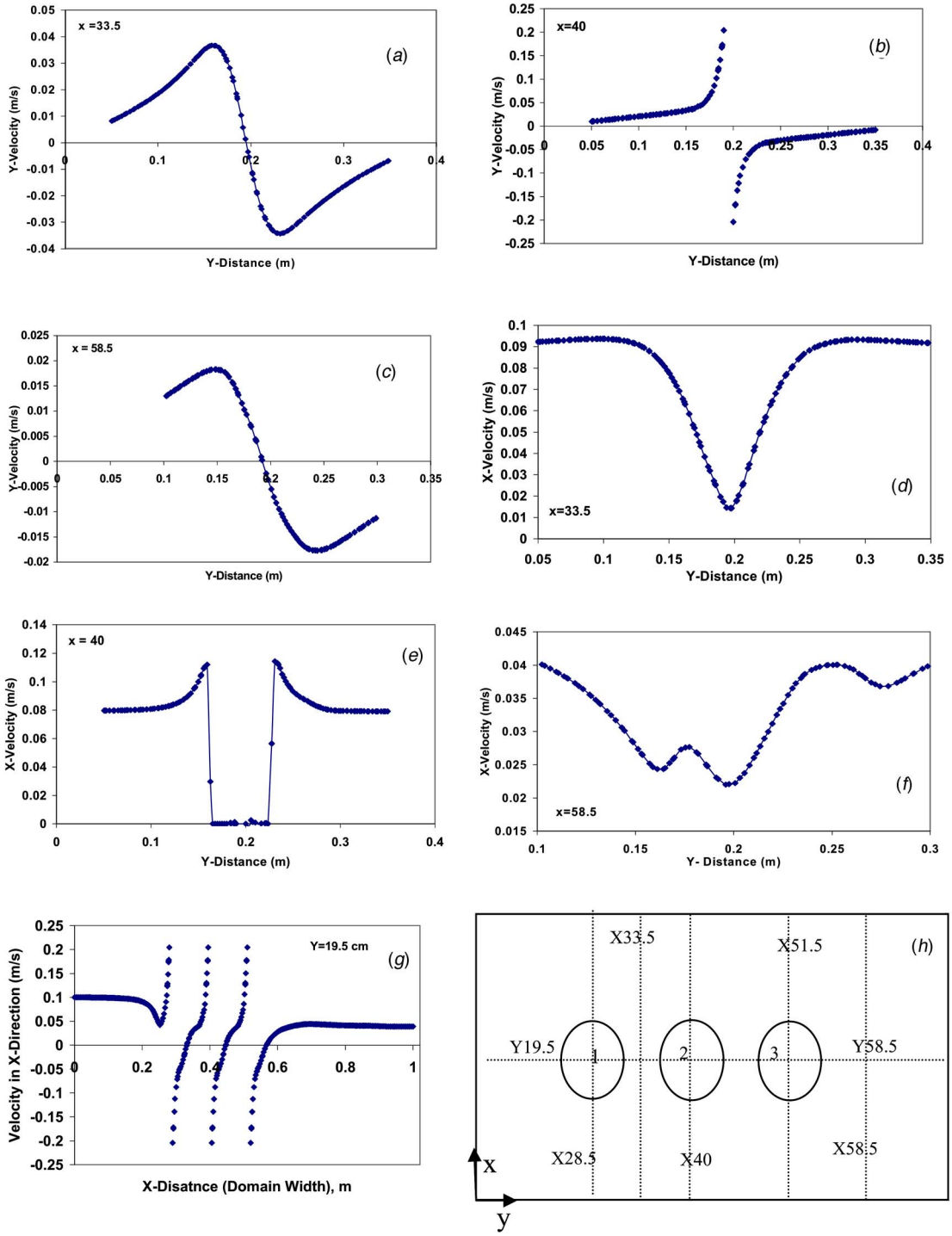

Fig. 4 Velocity in the *y*-direction at (*a*) *x*=33.5 cm, (*b*) *x*=40 cm, (*c*) *x*=58.5 cm, and (*g*) *y*=33.5 cm, and velocity in the *x*-direction at (*d*) *x*=33.5 cm, (*e*) *x*=40 cm, and (*f*) *x*=58.5 cm; (*h*) the location of the velocity profiles (filters location are from 16.25 cm to 22.75 cm in *y*-distance)

tance from the cylinder centerline, at the inlet plane, from which a particle would impinge on the porous cylinder, as shown in Fig. 5(*b*). The radius of convergence depends on the inlet velocity, the particle size, and the face velocity [23].

Spherically shaped particles, having diameters of 1 μm, 50 μm, 100 μm, and 200 μm, were injected with an assumed ash density of 600 kg/m^3. Although particle diameters between 1 μm and 50 μm are the main focus in power plant applications, the results show that no change in the trajectory occurred for particles in the range 1–50 μm in the cross flow investigation. However, the radius of convergence varies if the particle has a diameter of 100 μm or larger. However, a larger particle diameter is important for other applications such as incinerators.

Figures 5(*b*) and 5(*c*) show the particle tracking for a particle size of 1 μm. The V_i/V_f velocity ratio used in the first figure is 1.8, and the face velocity is 4 cm/s, while the second figure for the V_i/V_f velocity ratio is 5 and for two particle sizes 1 μm and 200 μm. The particle trajectory in Fig. 5(*b*) is only for the particles released from positions in the inlet, where they will enter one of the porous cylinders. Due to the mass balance between the

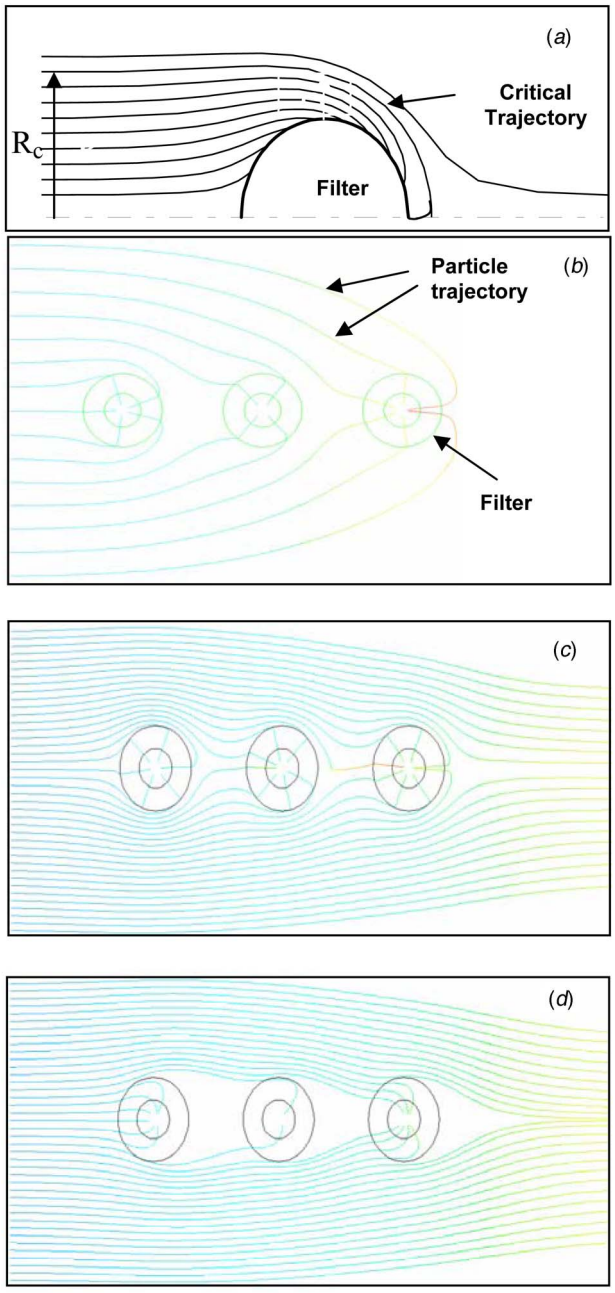

Fig. 5 (*a*) The radius of convergence. Particle tracking of (*b*) 1 μm and V_i/V_f of 1.8, (*c*) 1 μm and V_i/V_f of 5, and (*d*) 200 μm and V_i/V_f of 5.

main inlet on one side and the porous cylinders and outlet on the other, most of the fluid that has entered the duct is drawn by the porous cylinders in the low velocity case ratio. However, for the high velocity ratio, the inlet velocity is high while the face velocity is kept constant. Consequently, the inlet mass flow rate is higher than what the porous cylinder needs, and most of the fluid passes at the main stream toward the outlet. At high velocity ratio and large particle size, the deposition is not as uniform as in the small particle size case. This is due to the high inertia force.

Figure 6 shows the relationship between the radius of convergence (R_c) and the V_i/V_f velocity ratios for a face velocity of 4 cm/s. The graphs show that the V_i/V_f ratio is the main factor affecting the radius of convergence in the cross flow regime. Also, a similar trend appears for all the particles (1–200 μm). At a V_i/V_f ratio of 1.8, the radius of convergence (R_c) for particle size

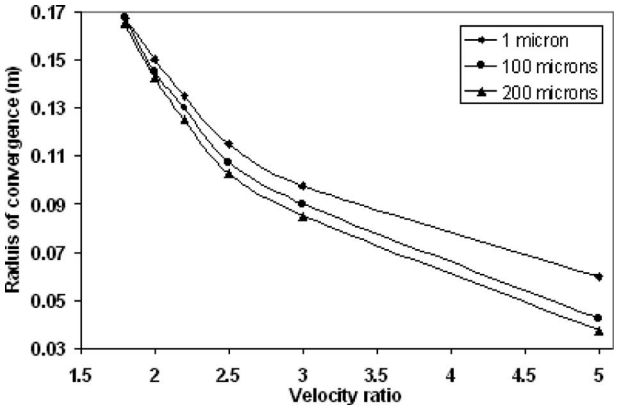

Fig. 6 The radius of convergence

of 1–100 μm is similar. This means that the particles follow the fluid streamline, and this is due to the low approach velocity. As the V_i/V_f velocity ratio increases, R_c diverges slightly in value. For the high V_i/V_f ratio of 5, the particles do not follow the streamline because of the high momentum, with which the particle is released in the case of a high approach velocity. The graph curves show that as the V_i/V_f ratio decreases, the radius of convergence increases. At low V_i/V_f ratio, R_c is 16.75 cm or 86% of the area of the inlet, while at the highest velocity ratio and with a particle diameter of 200 μm, R_c is only 3.75 cm or 19.2% of the inlet area. This mean 19% of the flow rate is drawn by the porous cylinders.

In reality, the velocity ratio is quite high for porous cylinders installed at the outer ring or near the inlet of the porous cylinders array such as ceramic candle filter vicinity. This is necessary so that the fluid reaches the porous cylinders in the middle of the porous cylinder array. Therefore, as the porous cylinder locations move to the middle, the V_i/V_f velocity ratio decreases. In addition, it is more likely that the porous cylinders at the other side of the square array and far from the inlet have lower V_i/V_f ratios. A full CFD model of such arrays like ceramic candle filter (which has 138 porous cylinders in the Grimethorpe design) is the next step and should be examined. Also, the inlet should not be at one side in the real model, and four to six inlets are essential for distributing equally the flow over the porous cylinder array. This could also reduce the vibration caused by high-pressure flow at one side.

5.2 Velocity Fields. The velocity ratio used here is found by dividing the inlet velocity over the face velocity for one porous cylinder. However, the inlet flow rate should be higher than the total mass flow rate for the three porous cylinders to allow the fluid to flow through to the outlet. At a V_i/V_f velocity ratio of 1.57, the inlet flow rate is equal to the flow rate for the three porous cylinders. Therefore, a V_i/V_f velocity ratio of 1.8 is the lowest ratio used in this investigation. As the number of porous cylinders increases, the inlet flow rate should be increased.

Velocity magnitude contours for three cases are shown in Figs. 7–9. These cases are of different V_i/V_f velocity ratios of 1.8, 2.5, and 5. At a V_i/V_f ratio of 1.8, the velocity in the area behind the last porous cylinder to the outlet is very low. This is due to the fact that most of the flows are drawn by the porous cylinders and only 12.7% of the flow bypasses to the outlet. As the V_i/V_f ratio is increased, the amount of fluid which flow in the area behind the porous cylinder to the outlet are increased to 21.5%, 37.2%, 47.6%, and 68.6% for V_i/V_f ratios of 2, 2.5, 3, and 5, respectively. The stagnation area size downstream of the first porous cylinder increases with increases in the V_i/V_f ratio. This is due to the fact that the approach velocity, and consequently the inertia force, is small enough to allow the flow to enter the porous cylinder.

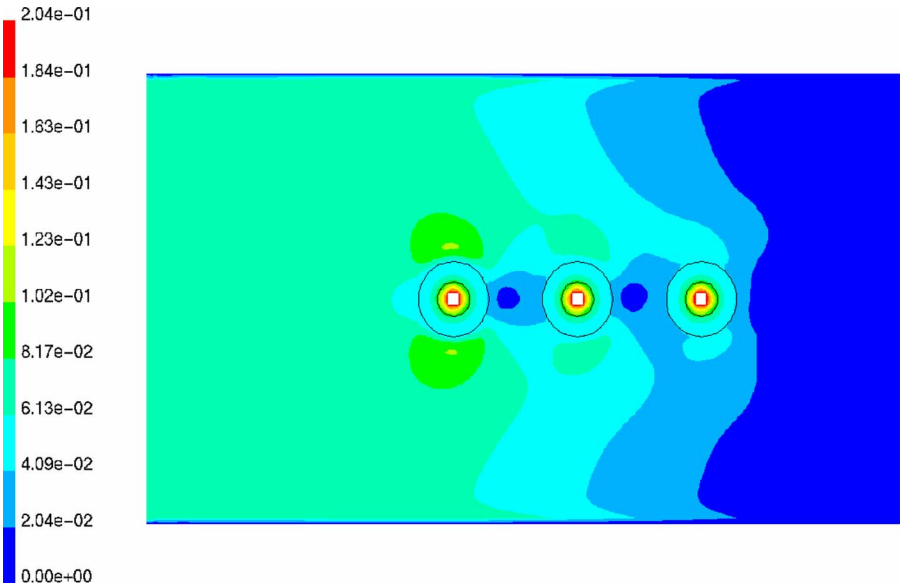

Fig. 7 Velocity magnitude contours (in m/s) for a V_i/V_f ratio of 1.8 and face velocity of 4 cm/s

The velocity at the upper and lower sides of the porous cylinder is increased, the highest velocity in this region is very close to the porous cylinder, and the maximum velocity is increased as the approach V_i/V_f ratio is increased. The flow in each side of the second and third porous cylinders demonstrates similar behavior to that of the first porous cylinder. However, the velocity at the second porous cylinder is lower than that at the first porous cylinder. At the third porous cylinder, the velocity is the lowest of the three. This is due to the reduction in the flow rate after each porous cylinder's suction.

The velocity is reduced between each of the two porous cylinders and behind the third porous cylinder. In a spot behind each porous cylinder where the flow is divided, some of the streamline curve toward the second porous cylinder and some are forced to turn toward the first porous cylinder due to the pressure drop through the porous cylinder, as shown in Figs. 10 and 11. This forms a stagnation region, which is located behind the porous cylinder, crossing the horizontal centerline. The stagnation region elongates horizontally as the V_i/V_f ratio increases. Furthermore, as the V_i/V_f ratio increases, the stagnation region moves toward the back of the porous cylinder. As the flow rate decreases due to the porous cylinder's suction, the size of the stagnation point behind the porous cylinders is increased. Thus, behind the third porous cylinder, the stagnation region is the greatest.

It can be seen from the velocity contours that the flow in the high V_i/V_f ratio case behaves like the flow in the tube bank. However, for the velocity ratio range that is used in this investigation, the flow between the porous cylinders is different than that in the tube bank case; however, the high V_i/V_f ratio is not suitable

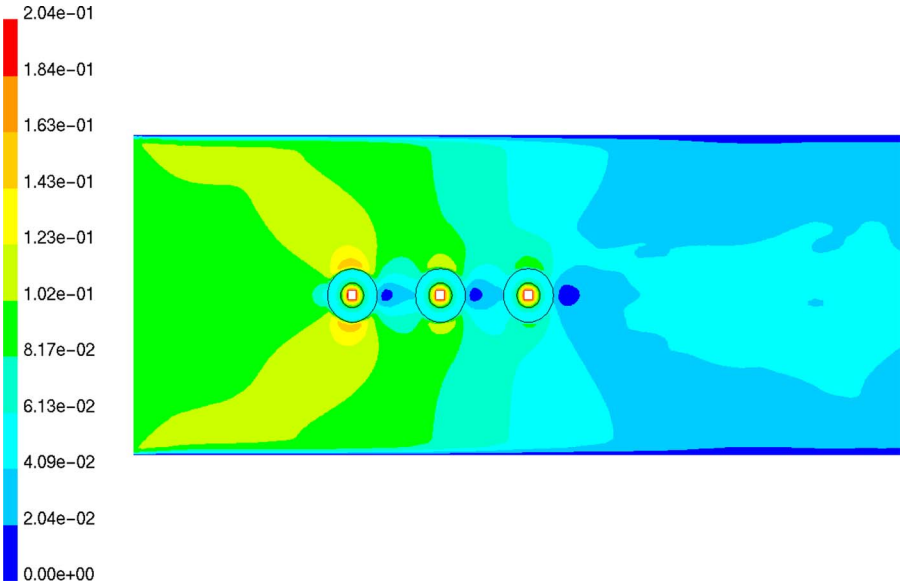

Fig. 8 Velocity magnitude contours (in m/s) for a V_i/V_f ratio of 2.5 and face velocity of 4 cm/s

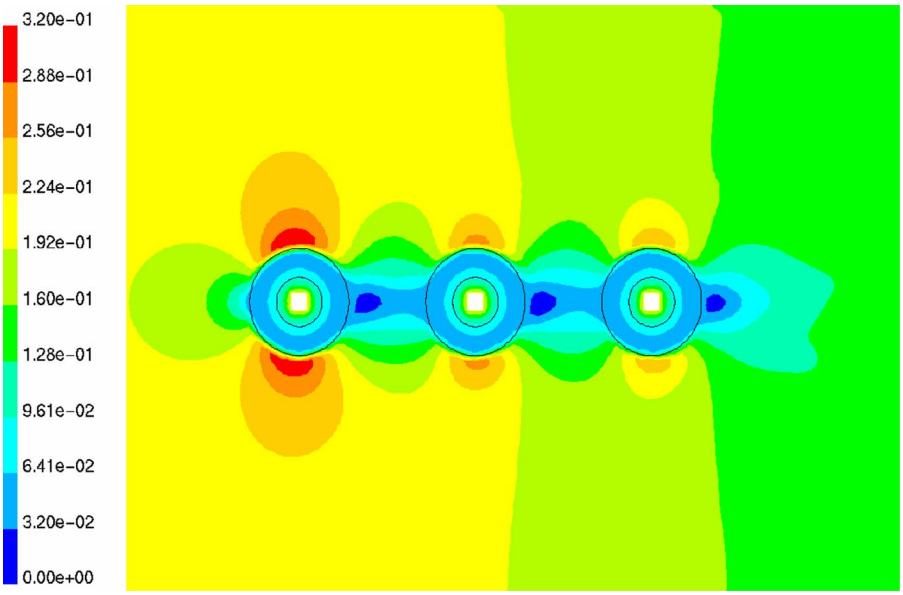

Fig. 9 Velocity magnitude contours (in m/s) for a V_i/V_f ratio of 5 and face velocity of 4 cm/s

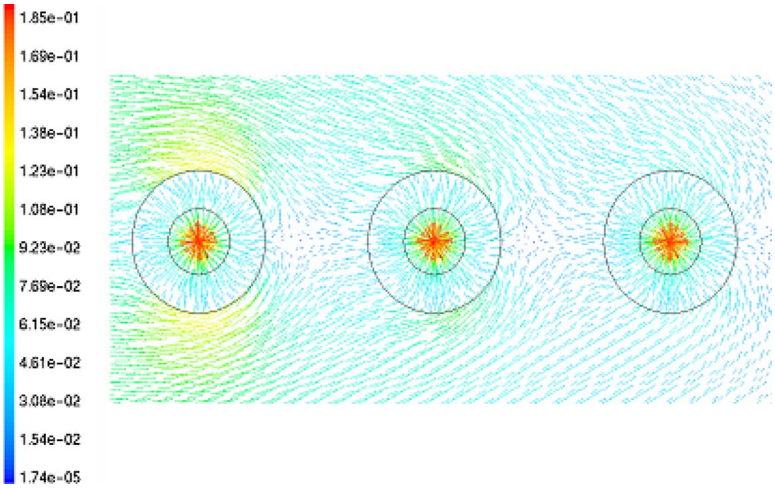

Fig. 10 Velocity vectors (in m/s) between the filters for a V_i/V_f ratio of 2 and face velocity of 4 cm/s

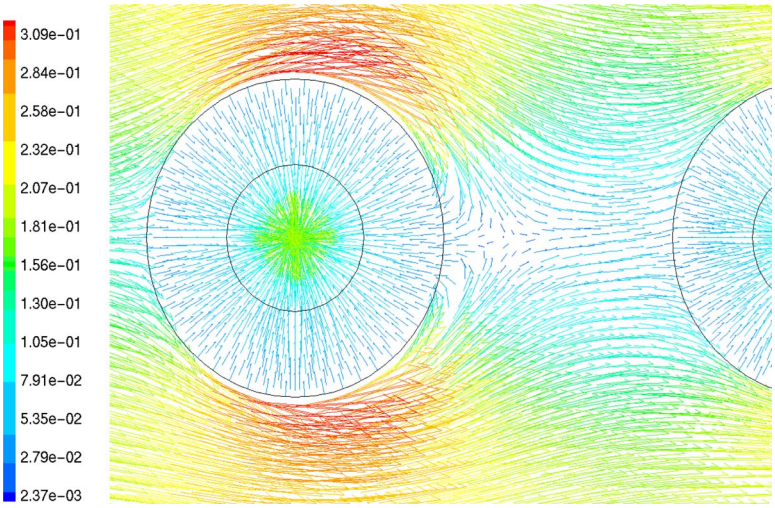

Fig. 11 Velocity vectors (in m/s) between the first and second filter for a V_i/V_f ratio of 5 (V_f=4 cm/s)

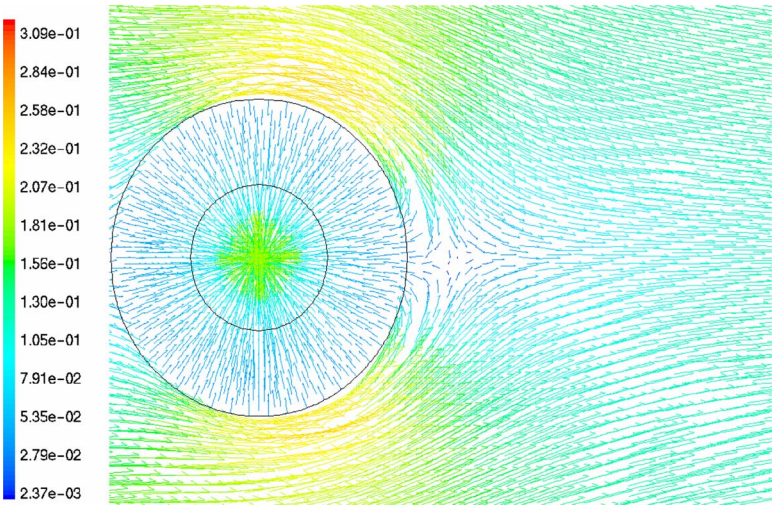

Fig. 12 Velocity vectors (in m/s) behind the last filter for a V_i/V_f ratio of 5 (V_f=4 cm/s)

to be used in the filtration case because the distribution of flow around the porous cylinder will not be uniform. This is due to the high inertia force making the fluid pass the porous cylinder instead of turning toward it.

The vector plots show that the flow does not separate from the porous cylinder as in the case of the flow past cylinder. The flow behaviors in the area between the first and second porous cylinders are similar to those in the area between the second and third porous cylinders. The stagnation region behind the third porous cylinder is greater than that between the porous cylinders and its location is farther downstream, as indicated in Figs. 12 and 13. The reason for this difference is the distance between the porous cylinders. As the distance is increased, the stagnation region moves farther downstream. The farthest distance that the stagnation region reaches to is behind the last porous cylinder. Between the porous cylinders and behind the stagnation point, the streamlines come together symmetrically before entering the second porous cylinder. Downstream of the porous cylinders, the streamlines also come together as at the front of the first porous cylinder. The maximum velocity is increased as the V_i/V_f velocity ratio is increased, as indicated in Fig. 14. The figure shows that as the V_i/V_f velocity ratio increase by 1, the maximum velocity/face velocity ratio is increased by 1.3.

Most of the pressure drop is through the porous media because the porous cylinder permeability is very low. This satisfies Darcy's law. Therefore, in the pressure contours, the porous region will not be considered to show the other area. Static pressure contours for a V_i/V_f ratio of 1.8 is indicated in Fig. 13. At the area where the velocity is low, the static pressure is high. The maximum static pressure is upstream of the porous cylinder, between the porous cylinders and the stagnation region. Furthermore, the static pressure is increased as it passes the porous cylinders. The pressure drop across the porous cylinders is higher at the last porous cylinder and lowest at the first. This is due to the high pressure drop outside the porous region in the high velocity region around the first porous cylinder.

Al-Hajeri and Aroussi [23] investigated the same geometry and parameters used in this study using PIV and CFD. They found that the CFD results matched closely the PIV experimental findings.

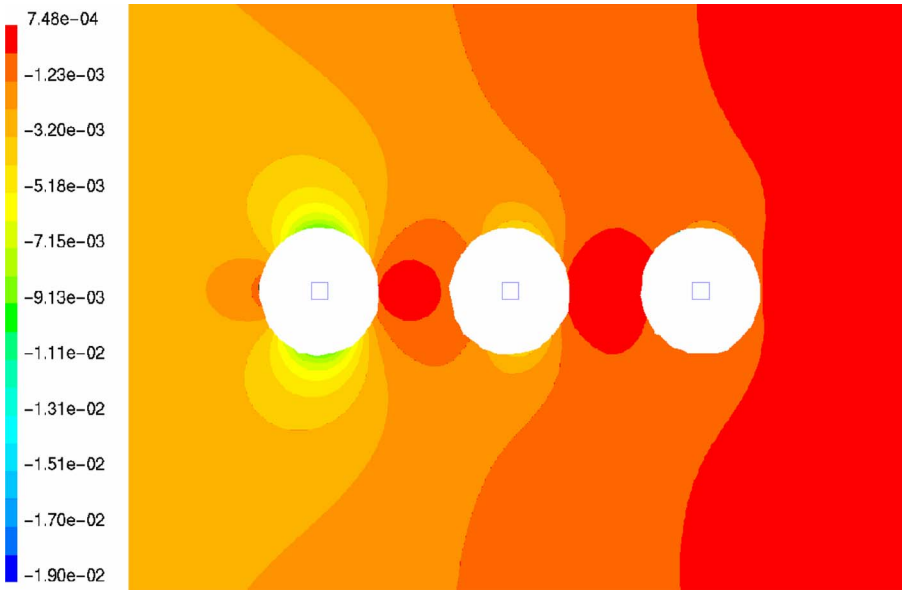

Fig. 13 Static pressure for a V_i/V_f ratio of 1.8 (V_f=4 cm/s)

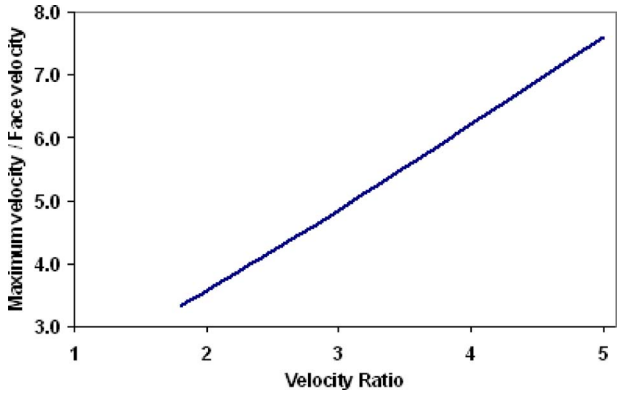

Fig. 14 The maximum velocity for different V_i/V_f ratios (V_f =4 cm/s)

This will lead to understand that the results found in this study are accurate and then validated.

6 Flow in a Bank of Solid Cylinders

The results of our numerical investigation of the flow around three solid cylinders mounted in a square array are presented here. The geometry and the physical parameters were similar to those used for the flow around multiple filters. The approach velocity in this model was 7.2 cm/s and the Reynolds number was 312. In geometry of this model, the inlet 2 cells change from inlet live cells to wall cells, so the filter will be replaced by cylinder. The mathematical model used here was the RNG k-ε turbulence model.

Flows at the front of the first cylinder are divided symmetrically, creating a low velocity region as indicated in Fig. 15(a). In addition, the boundary layer separates symmetrically from the two sides at 80 deg from the back of the cylinder, forming two eddies between the two cylinders, as shown in Fig. 15(b). Similar flow behavior exists between the second and third cylinders, as shown in Fig. 15(b). Behind the last cylinder, vortices are shed alternately from each side of the cylinder and persist for some distance downstream, forming a double row called the Karman vortex street. Figures 15(c) and 15(d) show clearly the Karman vortex street. At the last cylinder, the boundary layer also separates at 80 deg from the back horizontal centerline.

The stagnation region behind the cylinders moved toward the back of the cylinders. Also, the size of the stagnation region was greater than that in the case of the flow around the filter. Because there was no suction in the cylinder as there was in the case of the filter, the mainstream velocity was high, as indicated in Fig. 15(d). However, the high velocity was at the upper and lower sides of the three cylinders. This was not similar to the results obtained for the case of flow around multiple filters.

7 Conclusions

Flow past a bank of porous cylinders in cross flow was investigated numerically. Particle trajectories were obtained for a number of particle diameters and different V_i/V_f values.

The porous cylinder acted as a boundary layer bleeding mechanism. For a similar range of Reynolds numbers, the flow in a tube of solid cylinders differed from the flow past the porous cylinder, and the boundary layer separated on the cylinder surface, creating eddies and the Karman vortex street downstream of the cylinders. The flow in bank of the solid cylinders depended on the Reynolds numbers, while in the case of the porous cylinders, it depended on the V_i/V_f values.

High velocity occurred at the sides of the porous cylinders. However, at the first porous cylinder, the velocity was higher than it was at the last porous cylinder. This was due to the suction of the porous cylinders, which reduced the flow rate in the model.

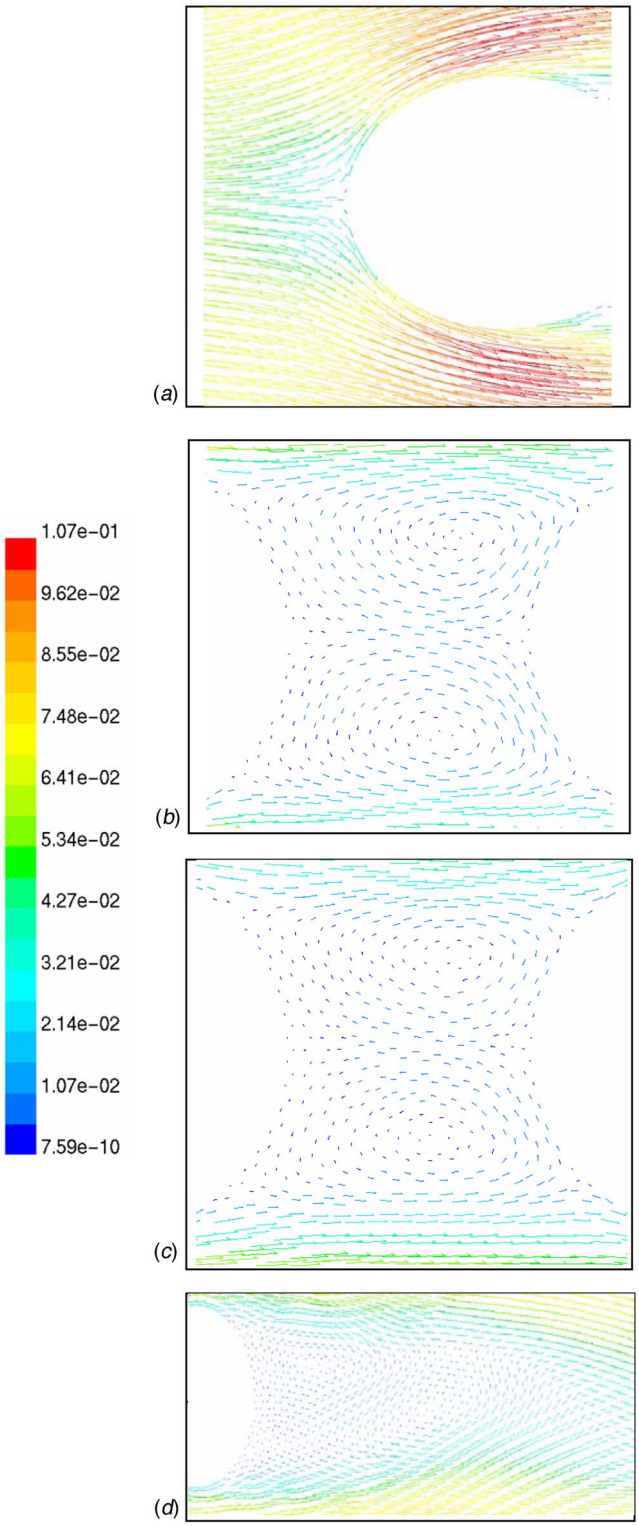

Fig. 15 Velocity vectors for solid cylinders for approach velocity of 7.2 cm/s (*a*) upstream of the first cylinder, (*b*) between the first and second cylinders, (*c*) between the second and third cylinders, and (*d*) downstream of the first cylinder

Stagnation areas were found behind each porous cylinder, and their sizes increased as the V_i/V_f values increased. The streamlines came together behind the porous cylinders, as they did in the front of the first porous cylinder.

Particles with diameters of 1 μm, 100 μm, and 200 μm were tracked through the domain for different V_i/V_f values. It was

found that the radius of convergence (R_c) yielded the deposition directly. The radius of convergence was uniquely defined by the particle sizes and the V_i/V_f value. For a V_i/V_f value of 1.8, the R_c was 86% of the inlet area, while at the V_i/V_f value of 5, R_c was approximately 17% of the inlet area. For the particle ranges that occurred in the power plant applications (<50 μm), the particles were uniformly distributed around the surface of the porous cylinder. However, the larger particles did not deposit at the rear part of the porous cylinder due to their high inertial force. At a low V_i/V_f value, the R_c for particle sizes of 1–100 μm was similar. This means that the particles follow the fluid streamline, and this was due to the low approach velocity.

In the flow in the bank of solid cylinders, for a Reynolds number of 312, a pair of eddies was created behind the first and second cylinders. Vortex shedding was also created behind the last cylinder. The maximum velocities occurred at the upper and lower side of the cylinders, and the velocities were identical for the three cylinders.

Nomenclature

C_μ = constant
k = kinetic energy (k-ε model in CFD)
K = permeability
L_2 = length of inlet 2
p = pressure
R_0 = filter radius
u = velocity components in x-direction
v = velocity components in y-direction
V_2 = velocity at inlet 2
V_f = filter face velocity
A = inverse Prandtl number
ε = dissipation rate
μ = viscosity
ν = kinematics viscosity
ρ = density
eff = effective
i,j = directional indices
l = laminar

References

[1] Zukauskas, A., 1972, "Heat Transfer From Tubes in Cross-Flow," Adv. Heat Transfer, **8**, pp. 93–160.
[2] Launder, B., and Massey, T., 1978, "The Numerical Prediction of Viscous Flow and Heat Transfer in Tube Bank," ASME J. Heat Transfer, **100**, pp. 565–571.
[3] Farhanieh, B., 1995, "Analysis of Three Dimensional Laminar Flow and Heat Transfer Characteristics in a Corrugated Duct With Varying Trapezoidal Cross Section," Heat Transfer Eng., **16**, pp. 375–384.
[4] Safwat Wilson, S., and Bassiouny, K., 2000, "Modeling of Heat Transfer for Flow Across Tube Banks," Chem. Eng. Process., **39**, pp. 1–14.
[5] Verma, P. D., and Bhatt, B. S., 1976, "Flow Past a Porous Circular Cylinder at Small Reynolds Number," Journal of Pure Science, **15**(3), pp. 908–914.
[6] Kirsh, V., 2006, "Stokes Flow Past Periodic Rows of Porous Cylinders," Theor. Found. Chem. Eng., **40**(5), pp. 465–471.
[7] Jue, T., 2004, "Numerical Analysis of Vortex Shedding Behind a Porous Square Cylinder," Int. J. Numer. Methods Heat Fluid Flow, **14**(5), pp. 649–663.
[8] Djordjevic, V. D., 2005, "Circular Couette Flow Between Porous Cylinders," J. Mech. Eng. Sci., **219**, pp. 743–747.
[9] von Wolfersdorf, L., and Mönch, W., 2000, "Potential Flow Past Porous Circular Cylinder," ZAMM, **80**(7), pp. 457–471.
[10] Min, K., and Lueptow, R., 1994, "Hydrodynamic Stability of Viscous Flow Between Rotating Porous Cylinders With Radial Flow," Phys. Fluids, **6**(1), pp. 144–155.
[11] Chang, M., 2003, "Hydrodynamic Stability of Taylor–Dean Flow Between Rotating Porous Cylinders With Radial Flow," Phys. Fluids, **15**(5), pp. 1178–1187.
[12] Kerr, K., and Probert, D., 1985, "Pulsating Pressure Filter for Fluidized Bed Combustion Gas Clean Up," Appl. Energy, **20**(2), pp. 85–101.
[13] EPRI, 1992, "High-Temperature Gas Filtration. Vol 2: Operating Performance of a Pilot-Scale Filter," EPRI Report No. GS-6489.
[14] EPRI 1992, "Grimethorpe High-Pressure/High Temperature Gas Filter Experimental Program, Vol. 1: Design, Commissioning and Modification of a Large Hot-Gas Filter on the Grimethorpe PFBC," EPRI Report No. TR-100–499.
[15] Alhajeri, M., Aroussi, A., Simmons, K., and Pickering, S., 2006, "CFD and PIV Investigation of Flow Past Single Hot Gas Filter," Chem. Eng. Technol., **29**(3), pp. 348–354.
[16] Fluent Inc., 1998, FLUENT v5, Fluent User's Guide.
[17] Yakhot, V., and Orszag, S., 1986, "Renormalization Group Analysis of Turbulence," J. Sci. Comput., **1**, pp. 3–51.
[18] Orszag, S., Yakhot, V., Flannery, W., Boysan, F., Choudhury, D., Maruszewski, J., and Patel, B., 1993, "Renormalization Group Modelling and Turbulence Simulation," International Conference on Near-Wall Turbulent Flows, pp. 1031–1046.
[19] Kim, Y. J., and Kim, S. S., 1991, "Numerical Simulation of Particle Deposition Onto a Circular Cylinder in Nonisothermal Two-Phase Cross Flow," Third ASME/JSME Thermal Engineering Joint Conference, Reno, NV.
[20] Speziale, C., and Thangam, S., 1992, "Analysis of an RNG Based Turbulence Model for Separated Flows," Int. J. Energy Science, **30**, pp. 1379–1388.
[21] Ireland, P., Tustin, M., and Hudson, D., 1993, "Determination of the Temperature of a Hot Ceramic Candle Filter During Cool Gas Cleaning," Seventh Congress and Exposition on Gas Turbines in Cogeneration and Utility Industrial and Independent Power Generation, Vol. 8, pp. 45–53.
[22] Li, J., Chambarel, A., Donneaud, M., and Martin, R., 1991, "Numerical Study of Laminar Flow Past One and Two Circular Cylinders," Comput. Fluids, **19**, pp. 155–70.
[23] Al-Hajeri, M. H., and Aroussi, A., 2002, "Velocity Measurements in a Rigid Ceramic Filter in a Cross-Flow Arrangement," CFD Conference, Windsor, Canada.

Unsteady Flow Patterns for a Double Suction Centrifugal Pump

José González
e-mail: aviados@uniovi.es

Jesús Manuel Fernández Oro

Katia M. Argüelles Díaz

Eduardo Blanco

Área de Mecánica de Fluidos,
Universidad de Oviedo,
Campus de Viesques,
33271 Gijón (Asturias), Spain

The flow in a double suction centrifugal pump is presented in this paper. The static performance of the machine has been obtained in a proper test rig, and the results have been compared with equivalent numerical results from an Unsteady Reynolds Averaged Navier–Stokes Equations (URANS) calculation. In a second step, the numerical results have been exploited to get detailed information about the flow inside the turbomachine. The main goal of the study is, on one hand, the validation of the numerical procedure proposed and, on the other hand, the detailed flow-field analysis for the machine, which points out the possibilities and drawbacks of the pump design. For a double suction machine, the inlet flow is characterized by the existence of a particular geometry that tries to force a uniform flow, at least for the nominal flow rate. On the contrary, at off-design conditions the lack of uniformity produces an unsteady incidence that gives rise to strong hydraulic loading variations. Instantaneous and average pressure fields have been analyzed in this paper to study the evolution of such inlet flow unsteadiness throughout the impeller and the volute. The analysis of both static and dynamic effects on the pump shaft has been carried out from the numerical calculation of the radial forces. The results have shown that the performance of the double suction centrifugal pump is suitable for typical design conditions. The best operation point or nominal flow rate is found to be at $\varphi = 0.274$, which turns out to produce a specific speed $\omega_S = 1.25$, well in the range for centrifugal impellers. This operating point is also found to be the one with better efficiency and with better flow characteristics, regarding the axisymmetry of the flow pattern and the fluid forces obtained. However, some particular features produce also interesting results for off-design operating points. [DOI: 10.1115/1.3153367]

1 Introduction

The flow field inside a centrifugal impeller is very complex, with unsteady and three-dimensional effects, so many studies have been carried out in the last decades to address these features (see, for example, Refs. [1,2]). Besides, if the volute casing geometry has any peculiarity, such as a double suction at the inlet or a double volute tongue at the outlet, the flow structure becomes even more complex, and it is still far from being fully understood [2]. The basic knowledge to accomplish the study of the flow in a centrifugal impeller and the inherent geometrical difficulties provide a very restricted frame for any research.

When cavitation problems are likely to arise and large flow rates are required, a double suction centrifugal pump is a quite common solution [3]. They are the most suitable option in situations where the axial forces could establish a limitation for a conventional unit. As a drawback, the axial balance and the possibility of working at high flow rates increase the radial forces. Basically, there are three reasons why industry manufacturers build double suction pumps: to reduce the axial thrust exerted on the bearings (improving their useful life), to improve suction performance (reducing NPSHr) because the flow rate is split, and to reduce capital cost by keeping the pump casing and piping more compact.

For any hydraulic turbomachine, the flow is always three-dimensional and unsteady. In fact, the unsteadiness constitutes the most important source of vibration and hydraulic noise in this type of machines [4]. Therefore, any flow analysis should be done keeping both dynamic and 3D effects, because their combination gives rise to the real working flow patterns [2]. In the past, it was a common practice to start the design of any of those machines with a steady flow assumption. However, this assumption is only valid for operating points near the nominal one, so more complex and accurate data are needed for understanding the off-design performance. Nowadays, most of the pump designers consider the unsteady calculations as a standard tool.

Different numerical methods to solve the URANS equations for turbomachinery applications have been widely developed. These applications are just an example of the many situations where the numerical solution of the flow field has proven its worth [5]. The numerical simulation of a commercial pump is not easy due to the usual computational fluid dynamics (CFD) difficulties: turbulence modeling, flow separation, boundary layer effects, etc. [6]. For the present double suction centrifugal pump, there are also other problems, such as the extremely difficult geometry (especially at the inlet) and the complex fluid dynamic effects. Examples of a numerical solution applied to the dynamic effects on centrifugal pumps have been reported by different authors [7–10]), and some recent works have applied numerical methods to double suction geometries [3,11]. Analysis on radial forces or other advanced features for centrifugal pumps, such as the studies by Agostinelli et al. [12] or Aysheshim et al. [13], have not been yet published for a machine like the one considered in this paper, but probably will be the objective in the near future.

The experimental facilities and instrumentation to perform a detailed analysis of the flow dynamics inside any hydraulic machine have become more and more complex and expensive. So it is in this context where CFD techniques find direct application because almost any geometry can be analyzed and meaningful information can be obtained [6]. In this frame, the numerical research on hydraulic machinery, particularly in the field of the centrifugal pumps, has been increasingly used as a design tool [10].

In this paper, a numerical modeling of the flow field in a double suction centrifugal pump is carried out. The simulations have been conducted for different operating points, and the numerical model has been validated through comparisons with experimental performance curves. After this, flow patterns in the impeller, volute, and

Contributed by the Fluids Engineering Division of ASME for publication in the JOURNAL OF FLUIDS ENGINEERING. Manuscript received January 25, 2008; final manuscript received April 16, 2009; published online June 22, 2009. Assoc. Editor: Philippe Dupont. Paper presented at the Fourth ASME/JSME Joint Fluids Engineering Conference (FEDSM2003), Honolulu, HI, July 6–10, 2003.

Fig. 1 Experimental set-up for the pump measurements

suction regions have been obtained and carefully analyzed, so valuable conclusions about the flow structure are reported along the paper. In particular, the suction flow field is of special interest due to the induced distortion of the axial and tangential velocity fields. Pressure evolution is also considered at the pump inlet, where cavitation is likely to arise.

2 Machine Description and Experimental Tests

The machine consists of a six blade, double aspirating impeller (see Fig. 1) with an outer diameter of 0.46 m and an outlet blade angle of 32 deg. The pump has a single duct for the double suction inlet, with an inlet tongue, and a vaneless spiral volute casing at the exit (Fig. 2). The geometrical and operating parameters of the pump are shown in Table 1. The rotational speed was set to $\omega = 154.99$ rad/s, ± 1 rad/s.

Experiments were conducted in a hydraulic setup, where water was pumped from and returned to a 200 m^3 reservoir. Standard pressure manometers were used for the head measurements, and an electromagnetic Krohne flow-meter was installed in the setup to obtain the flow rate. The uncertainties were found to be less than $\pm 1.5\%$ for the head and efficiency, and less than $\pm 2.5\%$ for the flow rate (confidence level of 95%). All the uncertainties were calculated following the method proposed by Kline [14].

The relatively high specific speed and the double suction at the inlet are the most relevant features of the studied pump. Although there is an experimental limitation of the available data, a definition of the flow features can be obtained if the numerical model is considered. Another remarkable feature is the existence of an upstream or inlet tongue, clearly observed in Fig. 3. This upstream tongue, placed after the inlet pipe and before the impeller inlet, is intended for a uniform inlet. The coordinate system shown in

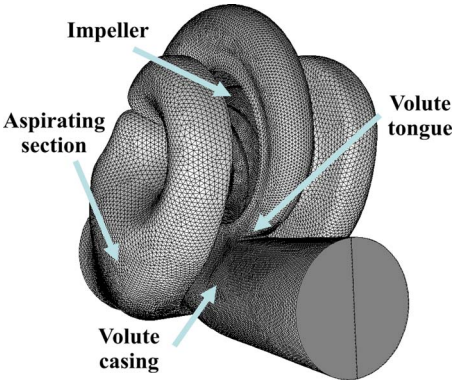

Fig. 2 Sketch of the pump unstructured mesh. (Inlet and outlet pipe far enough to impose boundary conditions.)

Table 1 Pump main dimensions and nominal characteristics

No. of blades	$z=6$
Impeller outlet diameter	$D_2=0.46$ m
Outlet blade angle	$\beta_2=32$ deg
Outlet impeller width	$B=0.045$ m
Rotational speed	$\omega=154.99$ rad/s
Nominal flow rate	$Q_N=0.694$ m^3/s
Head at nominal flow rate	$H_N=49.50$ m
Specific speed	$\omega_S=1.25$

Figs. 3 and 4 will be used in Secs. 3–6 of the paper. The symmetry plane ($Z=0$) sets the reference for different planes in which the increasing Z-axis is coincident with the rotating shaft (see Fig. 4). The X plane would be seen as a vertical line in this figure, while Y corresponds to the drawing plane. As can be observed in Fig. 4, values higher than $Z=0.15$ cut the pump giving information in a section placed further upstream of the rotor inlet and values lower than that produce a cut with relevant information in the inlet part. The geometry is quite complex, so further explanations should keep in mind the geometrical considerations explained in this paragraph.

3 Numerical Model

The 3D unsteady Navier–Stokes equations were solved using the FLUENT sotware. Due to symmetry considerations, only a half of the pump was modeled.

3.1 Geometry and Grid. The discretization of the geometry was done keeping the balance between calculation time (more details are included in Sec. 3.3) and the accuracy order of the simulation for the flow structure. Special care was observed in the region near the tongue by carrying a detailed study of flow vectors and the placement of the stagnation point. Unstructured mesh of tetrahedral cells was generated to define the inlet and outlet zones (more than 100,000 cells and around 150,000 cells, respectively) and the same kind of cells were used to define the impeller and volute (almost 250,000 cells and 235,000 cells, respectively). In the volute, a mesh refinement was introduced for the region near the tongue. Once the geometry was developed, the model was ready to be simulated. The final grid generated for the inlet section, the volute, and the impeller are shown in Fig. 3. The infor-

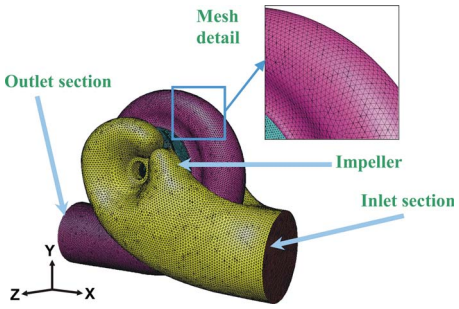

Fig. 3 Unstructured mesh considered for the numerical study (a detail is enlarged)

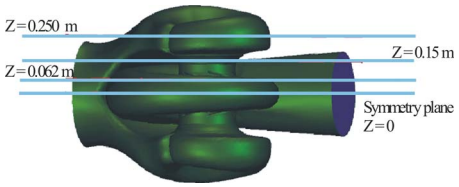

Fig. 4 Schematic of the pump defining the reference planes

mation between the static and rotating parts of the machine was transferred using a "sliding mesh" technique, defining four different flow interfaces (two groups to account for the impeller relative motion).

3.2 Mathematical Model. The 3D unsteady Navier–Stokes equations, including the source term for the centrifugal force in the impeller, were solved using the commercial code FLUENT. Turbulence closure was achieved with the standard k-ε model, and wall functions based on the logarithmic law were used to model the boundary layers. The SIMPLEC (Semi-Implicit Method for Pressure-Linked Equations–Consistent) algorithm was employed to resolve the pressure-velocity coupling, and second order spatial and temporal discretizations were established in the mathematical model.

3.3 Boundary Conditions. For a specific operating point, pressure boundary conditions were established at the inlet and at the outlet of the numerical domain. At the inlet, a total pressure equal to zero was set, while at the outlet, a pressure drop proportional to the kinetic energy was imposed. Therefore, the inlet/outlet boundary conditions were as similar as possible to the real working conditions in the pump. The no-slip condition was imposed in all the walls of the model: impeller blades, volute casing, inlet pipe, etc.

The operating point was changed by modifying the pressure drop at the outlet boundary, which is similar to a partial closure of a valve. In this manner, comparison between different operating points allows an easy detection of possible cavitation inception (same pressure level at the inlet), even though this is not the main goal of the present research.

3.4 Numerical Solution Control. The simulations were parallelized in a cluster with 20 Athlon-K7 nodes. For the unsteady calculations the time step was set to 2.703×10^{-4} s, in order to get an enough resolution for the dynamic analysis (the Courant number was kept below 3, which assures numerical stability and time accuracy). Mesh independency was studied only through local refinement near the tongue, and the preliminary tests with lower a number of cells indicated neither local nor global flow variations. Besides, in the numerical domain the averaged cell sizes are in the range considered as optimum for other pump geometries previously investigated by the authors [10,15].

The number of iterations was adjusted to reduce the residual for a given variable in all the cells below 10^{-5}. The numerical calculations started with a steady solution, considering the impeller without rotation at a fixed position. After the steady solution was found, the unsteady calculations were initialized from those results. Typically, ten impeller revolutions were needed to achieve convergence for the periodic solutions, which corresponds to about 350 h of CPU time.

The numerical uncertainty of the results was related to the change in some reference values when different mesh refinements were considered near the tongue, following the guidelines proposed by Freitas [16]. Such uncertainty was estimated to be about 1.5% and 0.5% for both steady and unsteady calculations, respectively. The variation in the global and local variables was considered under reasonable limits. For example, the effect on ψ gave a value of $\pm 0.8\%$ at nominal conditions for two different meshes.

4 Static Results and Discussion

Once the periodic state is reached for the unsteady calculations, two main possibilities are available: a full unsteady definition of the flow using any of the relative impeller positions or a blade-to-blade averaged flow analysis. In this section the second approach is considered in order to obtain the averaged flow description. Although some instantaneous information is lost, the information is accumulated for a detailed analysis. For that purpose, the numerical results were averaged over a blade passing period.

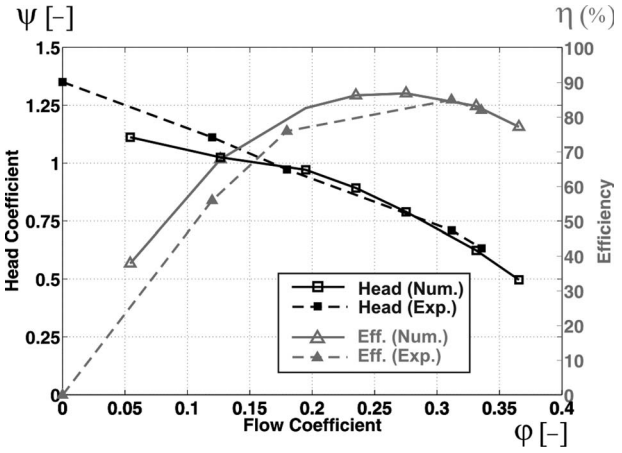

Fig. 5 Comparison of the performance curves (nondimensional variables)

Figure 5 shows both the numerical and experimental performance curve obtained for the double suction centrifugal pump. In that figure, the axes are the nondimensional flow rate and pressure rise according to

$$\varphi = \frac{Q}{\pi D_2 B U_2} \tag{1}$$

$$\psi = \frac{gH}{U_2^2/2} \tag{2}$$

where the subscript 2 refers to the pump outlet section. As can be observed, the expected trend using the Euler turbomachinery formula for centrifugal machines, with decreasing head for increasing flow rates, is found both numerical and experimentally. Considering the head curve, the agreement between both sets of figures is quite good, especially for flow rates higher than $\varphi = 0.17$. At lower flow rates, there are considerable differences due to the flow separation, which is not totally well captured by the numerical model, with an overestimation of the losses. However, this happens only for a narrow range of flow rates. The mentioned agreement is clear for the nominal flow rate, which corresponds to $\varphi = 0.274$. Globally speaking, the agreement found in the comparison between both curves has encouraged the research, thus leading to a performance of a detailed flow analysis, which is explained in Secs. 5 and 6.

For the efficiency, a quite similar conclusion can be drawn. Note that the efficiency comparison is estimated through direct consideration of both numerical and experimental torques. However, in the experimental results, the torque is measured in the shaft, while in the numerical scheme it is assumed that there are no mechanical losses. As a consequence, it is expected to observe higher discrepancies between numerical and experimental data due to the numerical simplification of the disk friction at the impeller hub and shroud (a more detailed explanation for such difference was analyzed in Ref. [15]). Although the impeller is a covered unit, there is a small gap between the outer part of the impeller and the volute, but this region has not been numerically modeled.

The relative outlet flow angle is plotted in Fig. 6. This angle, considered from the tangential direction, gives an idea of the blade loading and may result in a good indicator of the separation inception. Averaged values for a blade passing period are plotted for the different analyzed flow rates. Dashed lines with a cubic spline approximation are added to the figure. The initial position of the volute tongue is also plotted in the figure. As summarized in Table 1, the outlet blade angle is 32 deg. Notice that this angle is recovered for flow rates close to the nominal one, but differs quite

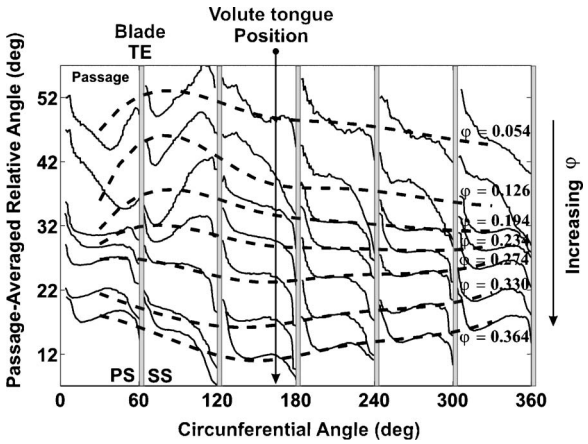

Fig. 6 Numerical prediction for the exit flow angle (seven studied flow rates)

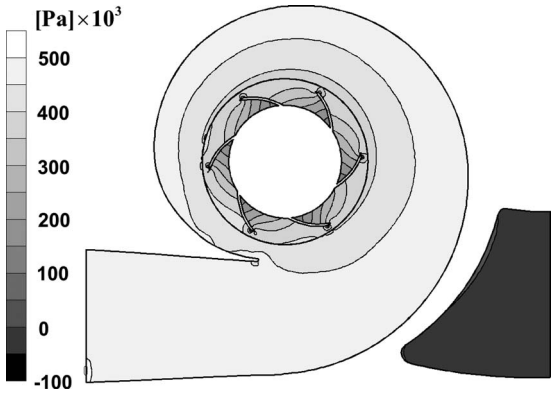

Fig. 7 Static pressure distribution in the $Z=0$ plane for the nominal flow rate ($\varphi=0.274$)

importantly for low and high flow rates. A closer look at the figure points out that the best flow rate in order to recover the blade angle corresponds to $\varphi=0.234$. Increasing the flow rate produces a decrease in the flow angle. The effect of the wakes can also be observed. For any blade, an angle decrease is found at the pressure side, while a sudden increase is observed at the suction side. Similar behavior is obtained for all the studied flow rates. In fact, the important differences for low flow rates between blade and flow angle depict a clear flow separation, which numerically is not fully well captured. Globally speaking, the effect of slip is clearly found for high flow rates. For lower flow rates, especially for the lowest one, there is an important difference between the blade and the flow angle. This effect is in agreement with the classic theory, and the loss of efficiency in these flow rates would come from the lower height of the velocity triangle. About the blade to blade distribution, an increase in the angle is found for the suction side of each blade, and a decrease is observed for the pressure side. In the suction side, the effect comes from the boundary layer separation. As far as this behavior is kept constant for all blade positions, independently of the volute position and the flow rate, it seems that the blade boundary layer has a predominant effect on the blade to blade angle distribution.

5 Unsteady Numerical Flow Analysis

To better explain the results obtained and to summarize the observed details, different sections of the machine are considered. To follow the explanations, Fig. 3 must be kept in mind, together with the consideration about the analyzed flow rates. As an initial approach, the absolute frame is considered and three different flow rates are selected for the representation: the nominal one ($\varphi=0.274$), a lower flow rate ($\varphi=0.126$), and a higher flow rate ($\varphi=0.364$).

In order to analyze the working conditions inside the pump, the phase-averaged unsteady fields were stored along a blade passing period, and the pressure and velocity fields for different positions of the impeller were obtained. In this way it is possible to represent an instantaneous snapshot of the flow field for every rotor phase. Figure 7 shows the static pressure in the symmetry plane for the nominal flow rate, where a quite axisymmetric pattern is obtained in the impeller. The pressure increases softly through the different flow passages, and no particular effect of the volute tongue is observed.

A transversal section of the pump is plotted in Fig. 8 (plane $X=0$ m) for the three flow rates. As expected, the pressure increases along the machine, and the possible cavitation is clearly limited to high flow rates and regions near the impeller inlet. Since the same inlet condition was imposed for all the flow rates, it would be possible to search locations and intensities of possible cavitation inception. As very closely related unsteady phenomena, an analysis of the inlet flow conditions is performed in the following paragraphs.

In order to observe the effect of the inlet tongue, Fig. 9 shows the averaged static pressure distribution at the plane $Z=0.25$ m, for the three flow rates. This inlet tongue should minimize the flow prerotation and produce uniform inlet conditions (at least for the nominal flow rate), acting as a flow conditioner. The flow in the pump evolves in a direction normal to the plane plotted in the figure and then around the central orifice. A good design of this inlet tongue would impose a uniform inlet condition, and this is the case for the nominal flow rate. For the other two flow rates, the pressure patterns look very similar, although for the higher flow rate important gradients are more evident as a consequence of the significant flow distortions introduced by the high velocities. From Fig. 9, it can be concluded that the inlet tongue is quite well designed for any of the operating flow rates.

Second, and closer to the impeller inlet, the plane $Z=0.15$ is considered. Figure 10 shows the swirling velocity in this section. Nondimensional values, obtained from the peripheral velocity, that is, V_θ/U_2, are plotted in this figure, together with the line of zero tangential velocity. A similar pattern for the three considered flows is found. Actually, two different effects with increasing strength in function of the flow rate are observed: a velocity increase in the rotation direction (clockwise turning) in the main inlet section and a smaller negative rotation (anticlockwise turning) placed in the interior diameter of the inlet section (placed at 180 deg from the volute tongue). As far as the inlet tongue imposes a quasi-uniform inlet velocity, this must be the combined effect of the pressure increase upstream of the impeller and at the inlet tongue section. Therefore, the effect of this inlet volute is

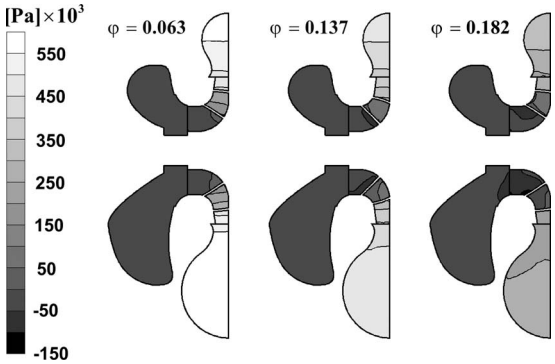

Fig. 8 Pressure field at the plane $X=0$ for three different flow rates: $\varphi=0.126$, $\varphi=0.274$, and $\varphi=0.364$

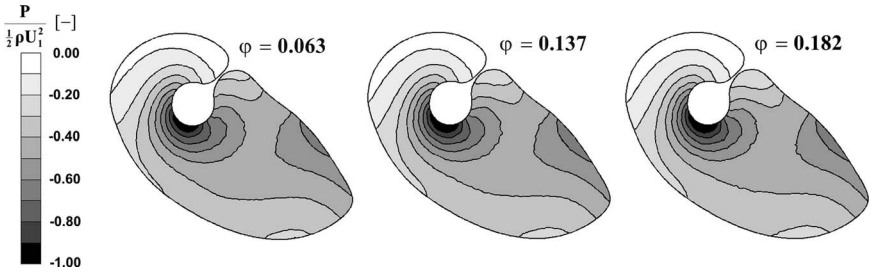

Fig. 9 Nondimensional static pressure distribution at the suction, in the inlet tongue (Z=0.25) and three flow rates (φ=0.126, φ=0.274, and φ=0.364)

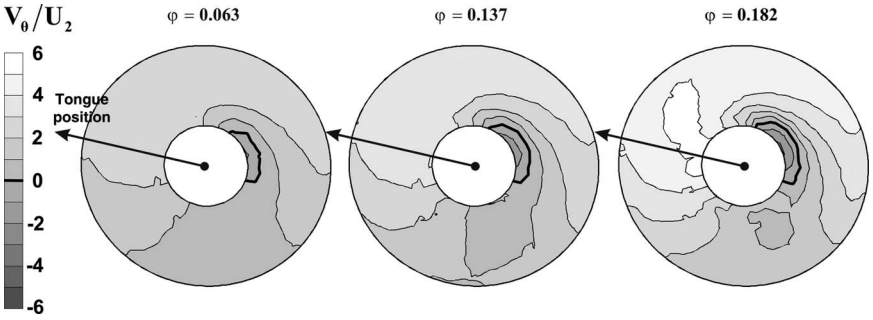

Fig. 10 Averaged tangential velocity field at the impeller inlet (Z=0.15) and three flow rates (φ=0.126, φ=0.274, and φ=0.364)

clearly manifested in all the tangential velocities for all flow rates, presenting an almost constant strength in the prerotation.

To better investigate previous effects, the averaged prerotation angle is plotted in Fig. 11 for six flow rates. As far as the results are averaged for a whole passage, no effect of the blades is expected. On the contrary, a relevant feature is observed in these results: for the lower flow rate (φ=0.126), and even though the averaging process should have smeared the blades contribution, a periodic pattern is found. This means that the inlet tongue modifies the interaction with the impeller blades, producing an important non-axisymmetric effect. As the flow rate increases, the prerotation angle is progressively improved showing more uniform characteristics. From this figure, it can be concluded that there is a position of resonance for the blades at lower flow rates (upper left graph). It could indicate an interaction between the flow imposed by the inlet tongue and the pressure patterns due to the impeller and volute tongue. This is quite a result because in Fig. 9 the flow seems to be quite similar for the analyzed flow rates, but in a downstream section, as the one analyzed in Fig. 11, the appearance of this position of resonance shows the strength of this feature and the spatial limit of such effect.

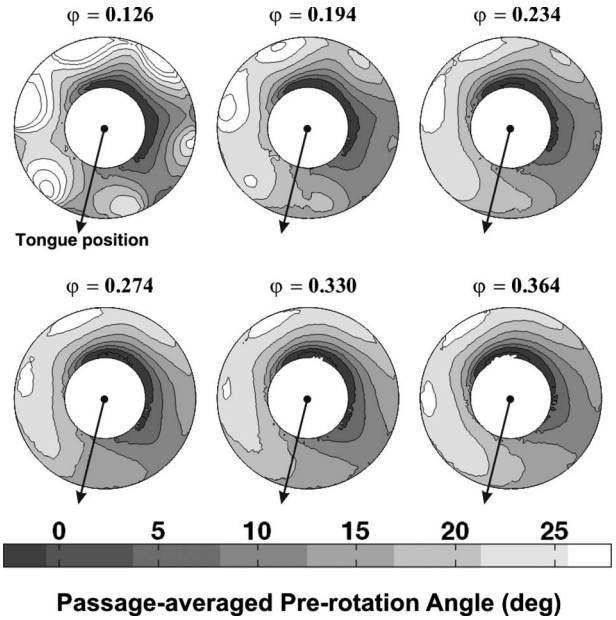

Fig. 11 Prerotation angle after the inlet tongue section, Z =0.062 for six of the analyzed flow rates

To conclude the analysis on the absolute frame of reference, the streamlines around the volute tongue are presented for three different flow rates in Fig. 12. For the nominal flow rate (φ =0.274) a good flow distribution around the volute tongue is obtained. In other words, the stagnation point is in the symmetry plane of the tongue. This aspect, together with the soft division of the flow, provides a working regime with minimum loss conditions. At this volute tongue, there is no separation, and the whole machine produces a maximum efficiency. For high flow rates (φ =0.364), although the flow is aligned with the plane of the plot (Z=0), a wide zone with a recirculation bubble is observed. This zone, placed downstream of the volute tongue, is a consequence of the low angle of the particles when leaving the impeller and the impact with the tongue. This impact is not as smooth as for the nominal flow condition and gives rise to the observed low energy zone. On the other hand, for low flow rates (φ=0.126) there is a clear 3D structure, and the flow leaves the symmetry plane with a quite complex pattern. Again, there is a separation zone, placed for this flow on the impeller side of the volute tongue. The flow, besides that separation trend, which is an effect of the so high angle when leaving the impeller, is pushed into the volute with a secondary rotation. As a result, the obtained flow pattern becomes much more complex. The 3D structure is due to the strong separation of the flow for the lower flow rates and the important unsteady effects occurring. There is even some backflow from the volute to the impeller, as can be observed. For the different flow rates analyzed, the movement of the stagnation point around the

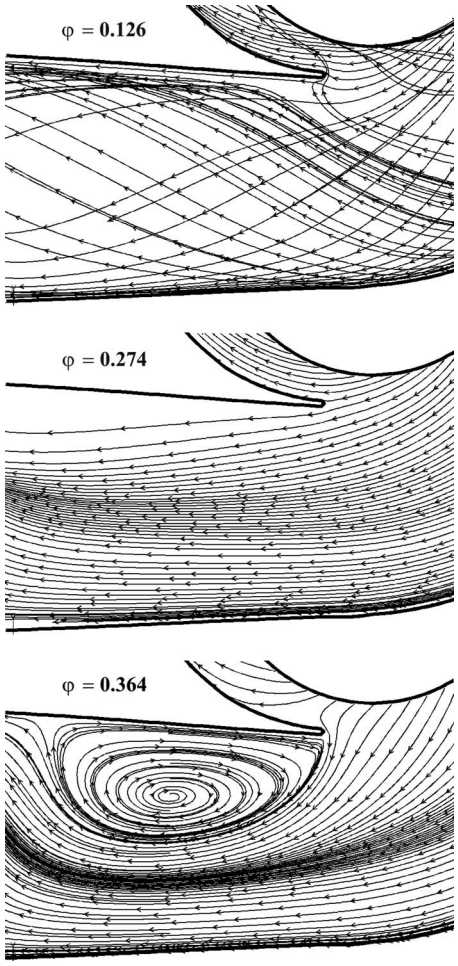

Fig. 12 Velocity field around the volute tongue for three flow rates (φ=0.126, φ=0.274, and φ=0.364)

tip of the volute tongue agrees with the expected results, when compared with published data for a single aspirating centrifugal pump [17].

The radial velocity in the relative frame of reference (flow rotating with the impeller) is shown in Fig. 13 for seven flow rates at the impeller outlet. The values are normalized using the mean radial velocity corresponding to the maximum flow rate and, therefore, they never exceed the unity. In this figure, the *X*-direction represents the angular position around the outlet section, while the *Y*-direction stands for half of the impeller width at the outlet (ranging from the center of the outlet width to the shroud). The plotted radial velocity is averaged for a blade passing period in the relative frame of reference in order to better understand the flow leaving the impeller and the tongue effect on the velocity patterns. The tongue effect is clearer at low flow rates, with a region of high velocities just after its position. For the nominal and higher flow rates, a more axisymmetric pattern is obtained, and the six wakes corresponding to the blades positions becomes clearer. Therefore, a quite uniform core-wake structure is recovered, pointing out that the volute tongue design is optimal for the nominal and higher flow rates.

Similarly to Fig. 13, Fig. 14 shows the averaged tangential velocity fields in the relative frame of reference for seven flow rates. The values are made nondimensional with the impeller tip speed at the outlet section, so the scale must be different for every flow rate. For the tangential velocity the core-wake structure is more extended and, therefore, the effect of the volute tongue is more limited in space. Again, only for the lowest flow rate a more disturbed flow is obtained. On the other hand, the velocity field would be the combination of both radial and tangential velocities, so the global effect of the volute tongue is to increase the flow distortion as the flow rate decreases.

6 Resulting Forces and Dynamic Effects

A different approach to the previously commented figures, can be oriented toward the effect of all the nonaxisymmetric effects on the impeller shaft. For such purpose, an integration of the pressure and velocity fields is possible with the available numerical data to obtain the resulting radial forces. As a first step, the equation considered and applied around the impeller outlet section is

$$F_R = \int PdA = \int_0^B \left(\int_0^{2\pi} 2\pi RP(\phi)d\phi \right) dZ \tag{3}$$

From the pressure fields as a function of the flow rate, a radial force is obtained, which considers only the pressure effect. Figure 15 shows the obtained results and the normalization value. As expected (for example, see Ref. [18]), higher forces are obtained for flow rates far from the nominal one. The classical quadrant change for a centrifugal machine as a function of the flow rate is also observed. Both conclusions do not differ with the expected trends for a typical centrifugal impeller. The calculated force is only due to the pressure distribution, and then the additional effect corresponding to the momentum exchange is not included in the calculation.

The existing data could also be analyzed using the static pressure obtained. In this sense, the data available is for any point in the domain, for the analyzed flow rates and for different instants, covering a blade passage. From such data, the classic formula for a fluctuating quantity could be applied to the static pressure, according to $P=\bar{P}+P'$.

As an example of the values obtained, Fig. 16 shows the evolution of P' in two diametrically opposed positions at the volute. A sketch of the selected points is also shown in the figure. These two points are chosen because the observed curves for any other point in the volute are always placed somewhere between the two curves shown. For points close to the volute tongue a "V-shaped" curve similar to the point at 0 deg is obtained. On the other hand, for points far from the volute tongue, flatter curves (similar to the 180 deg one) are found. In any case, and not only for the points shown, a minimum pressure fluctuation is found for the nominal flow rate.

Considering again the relative importance of the fluctuating pressure field at the blade passing frequency (also studied in Ref. [18] for a different geometry), a filtering of the total fluctuation for the static pressure is obtained. This construction, performed using a classical fast Fourier transformation (FFT) of the time domain signal, allows the effect of the pressure force to be filtered at the blade passing frequency. The result is an unsteady force that rotates around the impeller at a speed ω (i.e., one full rotation for each blade passing period), presented in Fig. 17. The *X* and *Y* axes show the forces on each respective direction, made nondimensional using the factor $\frac{1}{2}\rho U_2^2 \pi D_2 B$. The results show the classical ellipsoidal-shaped curves for all the studied flow rates. The main axes of the ellipses enlarges as the flow rate differs from the nominal one. The effect of the volute tongue is only implicit on the elliptical shape, changing the strength and inclination of the ellipses. On the other hand, the calculated force would be added, for any flow rate, to the average values (shown in Fig. 15) and would be the main cause of shaft fatigue. Due to minimum force amplitudes, it is expected that the nominal flow rate would ensure a maximum shaft effective life. Although this force is again only due to pressure effects, and the total force would be three or four times higher, the trends observed are somehow related to the total force, as recently reported by other authors [19].

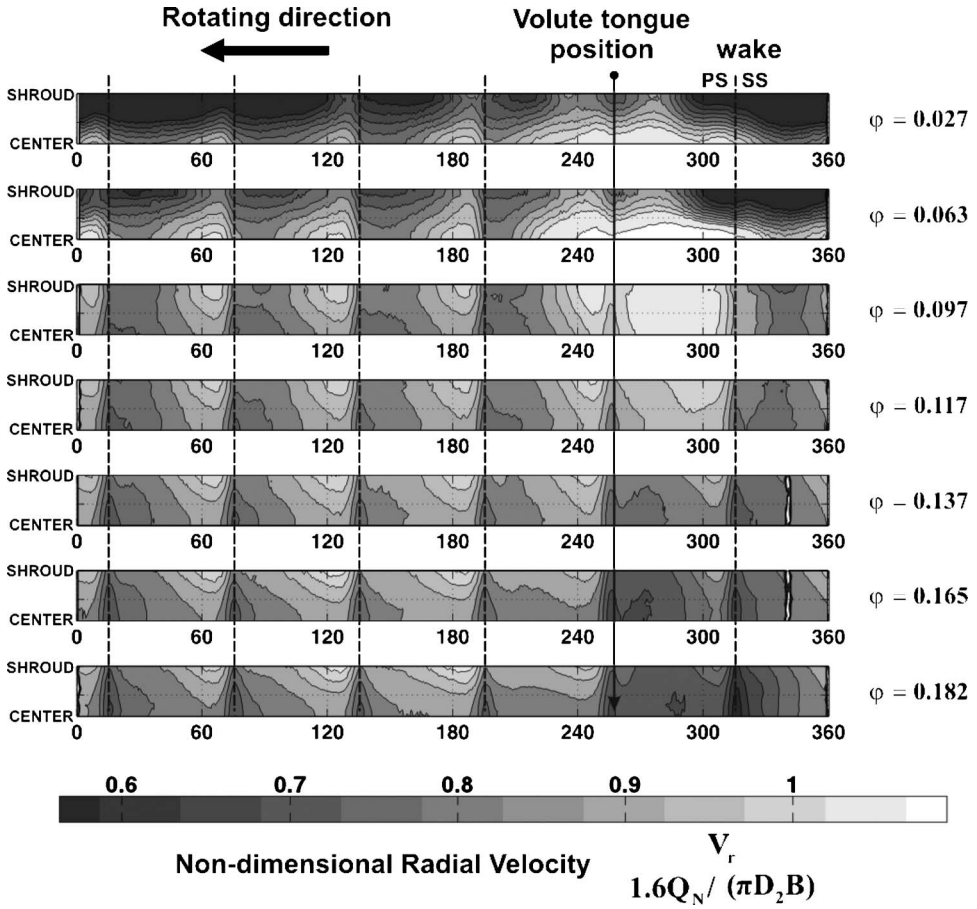

Fig. 13 Radial velocity at the impeller outlet averaged in the relative frame

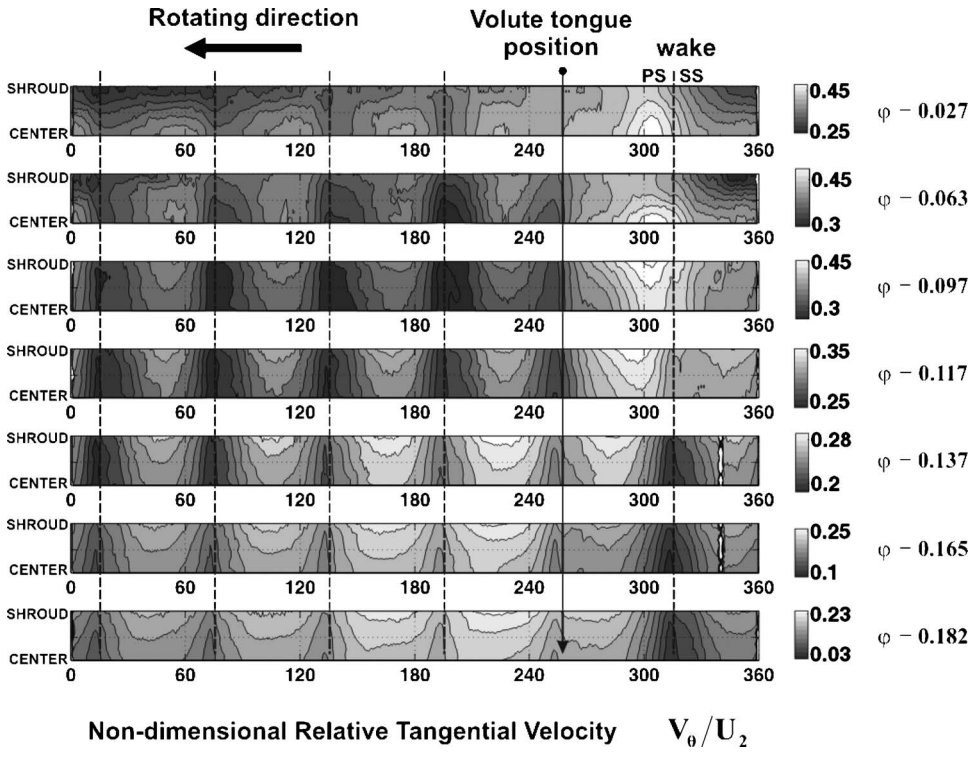

Fig. 14 Swirling or tangential velocity at the impeller outlet averaged in the relative frame

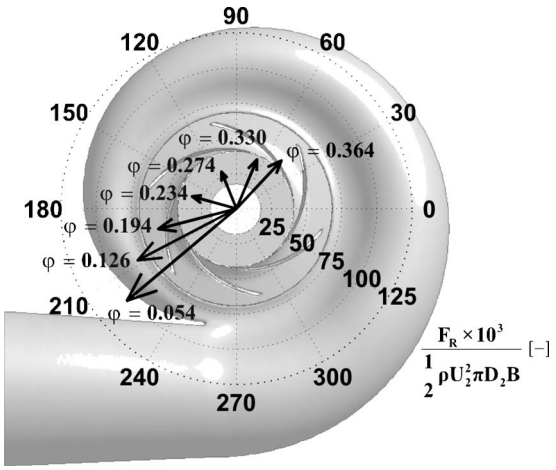

Fig. 15 Integrated pressure force on the impeller due to the flow (only pressure effect)

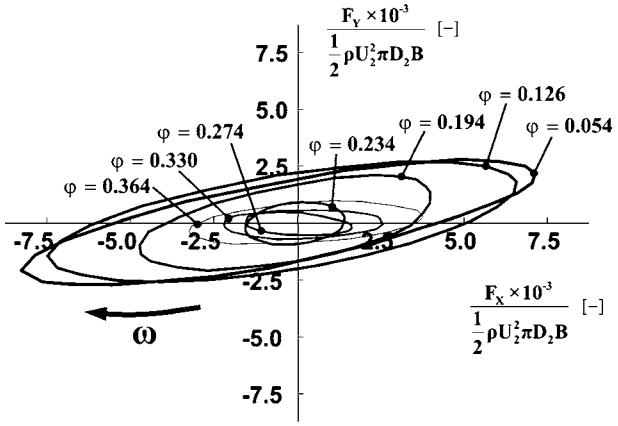

Fig. 17 Fluctuating pressure force at the blade passing frequency

7 Conclusions

A numerical analysis of the flow inside a double suction centrifugal pump has been carried out. The static performance curves obtained with the numerical model have been compared with experimental data, and a good agreement has been found for both design and off-design operating conditions, although separation has not been fully captured by the numerical model for low flow rates.

A lack of uniformity has been found in the proximity of the impeller inlet for flow rates far from the nominal one, indicating that the pump geometry produces a deviation from the axisymmetric flow distributions even for small differences respect to the design conditions. For low flow rates, a position of resonance has been found, which could point out an interaction between the inlet tongue and the impeller flow. The referred lack of uniformity might lead to important radial forces that could limit the use of this particular geometry. Besides, for high flow rates, some prerotation has been found.

Different features have been analyzed in the absolute frame of reference. The averaged flow solution has shown the design effectiveness for nominal flow rates, producing minimum losses and optimum flow angle distributions. However, for low flow rates it has been observed that the inlet tongue is not so well adapted. On the other hand, this is not a drawback because double suction centrifugal pumps are mainly designed for high flow rates, with typical efficiencies over 75%.

The numerical analysis in the relative frame of reference has shown an axisymmetric flow distribution for high flow rates, and a quite uniform core-wake pattern has been recovered. Besides, significant effects derived from the volute tongue have been found for low flow rates. The minimum values of the radial forces have been found for nominal or close to nominal flow rates, as can be observed not only from the averaged values but also from the blade passing frequency filtered values.

As a global conclusion, it can be said that the analyzed double suction centrifugal pump performs particularly well for the nominal and higher flow rates, constituting a quite important advantage for the design features expected.

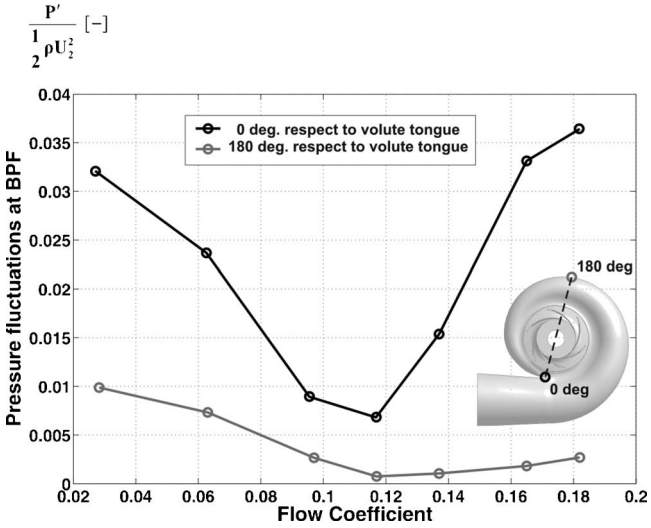

Fig. 16 Fluctuating pressure as a function of flow rate at two different volute positions, $Z=0$

Acknowledgment

The authors gratefully acknowledge the financial support from the "Ministerio de Ciencia e Innovación" (Spain), under Project Nos. DPI-2006-15034-C02-01 and TRA2007-62708.

Nomenclature

A = surface, (m^2)
B = height at the outlet section (m)
d = differential of any variable, in Eq. (3)
D_2 = impeller diameter at outlet (m)
F_X, F_Y = unsteady force on the impeller, X and Y components (N)
F_R = radial force on the impeller shaft (N)
H and H_N = pump head and pump head at the best efficiency point (nominal) (m)
k = turbulent kinetic energy (m^2/s^2)
P, $\bar{P}$, and P' = static pressure, average value and fluctuating value (Pa)
Q, Q_N = flow rate and flow rate at nominal point (m^3/s)
U_1, U_2 = peripheral velocity at impeller inlet and outlet, respectively (m/s)
V_θ = tangential velocity (m/s)
V_r = radial velocity (m/s)
X, Y, and Z = coordinate system, shown in Figs. 3 and 4
z = number of blades
β_2 = impeller blade angle (outlet section) (deg)
ε = turbulent dissipation (m^2/s^3)
φ = flow coefficient, see Eq. (1) for definition
ϕ = angular position around the impeller exit, see Eq. (3)

ρ = density of the fluid (water in this paper) (kg/m^3)

ω and ω_S = rotating speed and specific speed, respectively, where $\omega_S = \omega Q_N^{1/2}/(gH_N)^{3/4}$ (rad/s)

ψ = head coefficient according to Eq. (2)

η = machine efficiency

References

[1] Karassik, I. G., Krutzsch, W. C., Fraser, W. H., and Messina, J. P., 1985, *Pump Handbook*, 2nd ed., McGraw Hill, New York.

[2] Neumann, B., 1991, *The Interaction Between Geometry and Performance of a Centrifugal Pump*, MEP, London.

[3] Kyung, C., Pyun, P., Hyun, C., and Sang, L., 2002, "A Study of Flow Analysis for a Double Suction Centrifugal Pump," ASME Paper No. FEDSM2002-31180.

[4] Brennen, C. E., 1994, *Hydrodynamics of Pumps*, Oxford University Press, VT.

[5] Gunzburger, M. D., and Nicolaides, R. A., 1993, *Incompressible Computational Fluid Dynamics. Trends and Advances*, Cambridge University Press, Cambridge.

[6] Laskminarayana, B., 1996, *Fluid Dynamics and Heat Transfer of Turbomachinery*, Wiley, New York.

[7] Shi, F., and Tsukamoto, H., 2001, "Numerical Study of Pressure Fluctuations Caused by Impeller-Diffuser Interaction in a Diffuser Pump Stage," ASME J. Fluids Eng., **123**, pp. 466–474.

[8] Tsukamoto, H., Uno, M., Hamafuku, N., and Okamura, T., 1995, "Pressure Fluctuation Downstream of a Diffuser Pump Impeller," ASME FED, **216**, pp. 133–138, reprinted from Book No. G00966-1995.

[9] Croba, D., and Kueny, J. L., 1996, "Numerical Calculation of 2D, Unsteady Flow in Centrifugal Pumps: Impeller and Volute Interaction," Int. J. Numer. Methods Fluids, **22**, pp. 467–481.

[10] González, J., Fernández, J., Blanco, E., and Santolaria, C., 2002, "Numerical Simulation of the Dynamic Effects Due to Impeller-Volute Interaction in a Centrifugal Pump," ASME J. Fluids Eng., **124**, pp. 348–355.

[11] González, J., Santolaria, C., Castro, F., and Parra, M. T., 2003, "Numerical Model for the Unsteady Flow Behaviour Inside a Double Suction Pump," ASME FEDSM2003, Jul., Vol. 2B, pp. 1149–1155.

[12] Agostinelli, A., Nobles, D., and Mockridge, C., 1960, "An Experimental Investigation of Radial Thrust in Centrifugal Pumps," ASME J. Eng. Power, **82**, pp. 120–126.

[13] Aysheshim, W., and Stoffel, B., 2002, "Rotor-Stator-Interaction and Turbulence in a Centrifugal Pump Stage," IAHR, Proceedings of the XXI Symposium on Hydraulic Machinery and Systems.

[14] Kline, S. J., 1985, "The Purposes of Uncertainty Analysis," ASME J. Fluids Eng., **107**, pp. 153–160.

[15] González, J., 2000, "Modelización Numérica del Flujo no Estacionario en Bombas Centrífugas. Efectos Dinámicos de la Interacción entre Rodete y Voluta," Ph.D. thesis, Universidad de Oviedo, Spain, in Spanish.

[16] Freitas, C. J., 1993, "Journal of Fluids Engineering Editorial Policy Statement on the Control of Numerical Accuracy," ASME J. Fluids Eng., **115**, pp. 339–340.

[17] Miner, S. M., Flack, R. D., and Allaire, P. E., 1992, "Two Dimensional Flow Analysis of a Laboratory Centrifugal Pump," J. Turbomach., **114**, pp. 333–339.

[18] González, J., Santolaria, C., Parrondo, J. L., Fernández, J., and Blanco, E., 2003, "Unsteady Radial Forces on the Impeller of a Centrifugal Pump With Radial Gap Variation," ASME FEDSM2003, Jul., Vol. 2B, pp. 1173–1181.

[19] Barrio, R., Blanco, E., Parrondo, J., González, J., and Fernández, J., 2008, "The Effect of Impeller Cutback on the Fluid-Dynamic Pulsations and Load at the Blade-Passing Frequency in a Centrifugal Pump," ASME J. Fluids Eng., **130**, p. 111102.

Detailed CFD Analysis of the Steady Flow in a Wells Turbine Under Incipient and Deep Stall Conditions

M. Torresi
e-mail: m.torresi@poliba.it

S. M. Camporeale
e-mail: camporeale@poliba.it

Dipartimento di Ingegneria Meccanica e Gestionale,
Politecnico di Bari,
via Re David, 200,
70125 Bari, Italy

G. Pascazio[1]
Dipartimento di Ingegneria Meccanica e Gestionale,
Centro di Eccellenza in Meccanica Computazionale,
Politecnico di Bari,
via Re David, 200,
70125 Bari, Italy
e-mail: pascazio@poliba.it

This paper presents the results of the numerical simulations carried out to evaluate the performance of a high solidity Wells turbine designed for an oscillating water column wave energy conversion device. The Wells turbine has several favorable features (e.g., simplicity and high rotational speed) but is characterized by a relatively narrow operating range with high efficiency. The aim of this work is to investigate the flow-field through the turbine blades in order to offer a description of the complex flow mechanism that originates separation and, consequently, low efficiency at high flow-rates. Simulations have been performed by solving the Reynolds-averaged Navier–Stokes equations together with three turbulence models, namely, the Spalart–Allmaras, k-ω, and Reynolds-stress models. The capability of the three models to provide an accurate prediction of the complex flow through the Wells turbine has been assessed in two ways: the comparison of the computed results with the available experimental data and the analysis of the flow by means of the anisotropy invariant maps. Then, a detailed description of the flow at different flow-rates is provided, focusing on the interaction of the tip-leakage flow with the main stream and enlightening its role on the turbine performance.
[DOI: 10.1115/1.3155921]

1 Introduction

In the past two decades, within the research interest in renewable energy, efforts have been devoted to exploit the benefits of sea-wave energy by means of different kinds of devices [1]. Among these devices, the energy converters based on the idea of the Japanese wave energy pioneer, Yoshio Masuda [2], perform the conversion of the wave motion into an oscillating air-flow inside a column and for this reason are referred to as oscillating water column (OWC) systems. The energy of this oscillating air-flow can be effectively converted into a unidirectional rotational motion by the self-rectifying Wells turbine [3]. In order to improve the energy conversion process, the turbine should have good efficiency for a wide range of flow-rates [3–5]. To this purpose, analyses of the flow through the Wells turbine have been carried out by means of experimental [6–8] and analytical [9,10] methods. In the past years, thanks to the development achieved in computational fluid dynamic (CFD), the numerical simulation of three-dimensional turbulent flows became practicable and several numerical studies on the flow-field through turbines for OWC devices have been presented in the open literature [11–15]. In consideration of the low sea-wave frequencies, a quasisteady approach is often employed to analyze the turbine performance. In particular, three-dimensional simulations were carried out by Thakker et al. [11] in order to provide the performance of a Wells turbine with CA9 blade profile; Kim et al. [12] in order to study the blade sweep influence on the performance of a Wells turbine using either NACA0020 or CA9 blade profiles; Dhanasekaran and Govardhan [13] in order to investigate the characteristics of a Wells turbine with NACA0021 constant chord blades; and Thakker and Dhanasekaran [14] and Torresi et al. [15] to evaluate the tip clearance effects.

Recently, Boccotti [16] patented an innovative OWC plant, named resonant wave energy converter (model no. 3), REWEC3. This system is essentially a caisson breakwater embodying an OWC, which is connected to the sea through a small opening. Waves cannot enter this OWC and the oscillations of the water column are due to the wave pressure on the small opening [17]. The main feature of such a plant is that its natural frequency can be designed to be approximately equal to the wave motion frequency associated with the yearly maximum wave energy contribution [18]. In this situation, the system works in resonant conditions, with higher conversion efficiency with respect to conventional OWC plants [19]. A small prototype of a monoplane Wells turbine without guide vanes has been built in order to be matched with the REWEC3 located off the beach of Reggio Calabria. The prototype has been first tested in an open wind tunnel facility [20,21] and, recently, on the REWEC3 plant [22].

The aim of this work is to characterize the turbine performance and determine the main flow features at different working conditions, with particular care on the incipient and deep stall conditions. The analysis has been performed by means of three-dimensional numerical simulations using the commercial code FLUENT, which solves the steady incompressible Reynolds-averaged Navier–Stokes (RANS) equations, discretized by a finite volume approach. The use of properly designed fine meshes allowed us to adequately resolve the main flow features, including the tip-leakage flow. The main mesh characteristics (e.g., grid density, aspect ratio, first cell height at walls, and cell's stretching ratio) have been defined on the basis of previous works dealing with the numerical simulation of the flow through Wells turbines [15,20,23–25]. The simulations have been performed using three turbulence models: the one-equation model by Spalart and Allmaras [26], the two-equation k-ω shear stress transport (SST) model proposed by Menter [27] with low-Reynolds number correction [28], and the Reynolds-stress model of Launder [29,30]. The capability of these three models to provide accurate predictions has been verified by comparing the computed results with the available experimental data [20,21] and by analyzing the flow by

[1]Corresponding author.

Contributed by the Fluids Engineering Division of ASME for publication in the JOURNAL OF FLUIDS ENGINEERING. Manuscript received March 14, 2008; final manuscript received May 6, 2009; published online June 25, 2009. Assoc. Editor: Chunill Hah.

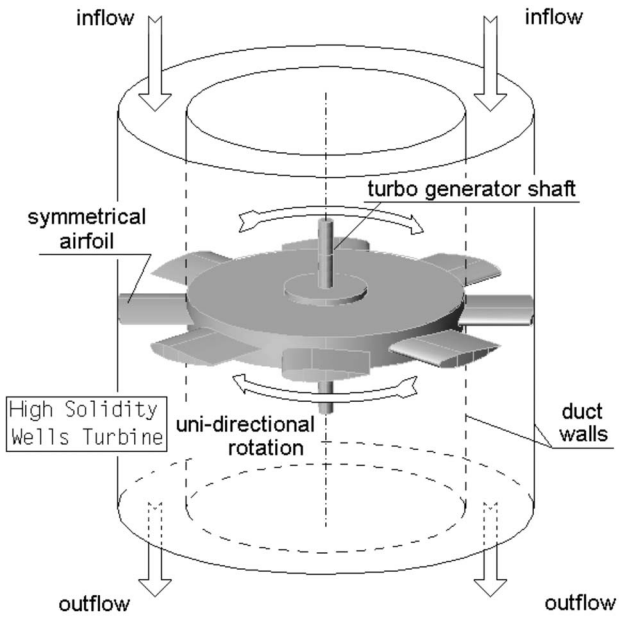

Fig. 1 High solidity Wells turbine

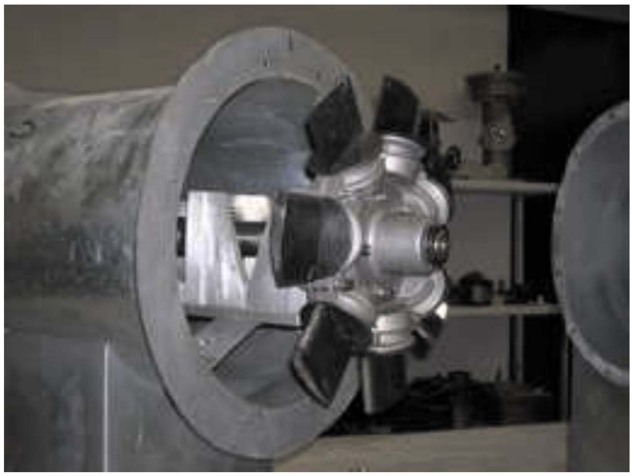

Fig. 3 Wells turbine prototype

means of the invariant theory of turbulence. The latter analysis was chosen in view of the complex flow structure. In particular, the presence of separation and stall conditions, along with streamline curvature, swirl, and rotation, which are known to induce strong anisotropy of the Reynolds-stress tensor, makes this flow simulation a very severe test for turbulence models based on the linear eddy viscosity concept, like those commonly employed in the simulations of a Wells turbine [11–15].

Finally, the paper provides a detailed description of the flow-field for different values of the flow coefficient, describing the interaction of the tip-leakage flow with the main stream and enlightening its role on the turbine performance.

2 The Wells Turbine

Sea-wave energy power plants experienced a renewed interest after the introduction of the Wells turbine [31]. In fact, in OWC wave energy converters, due to the wave motion, pressure fluctuations are generated inside a plenum, thus producing an oscillating air-flow, whose energy can be effectively converted into a unidirectional rotational motion by the self-rectifying Wells turbine. In its basic configuration, this is an axial-flow turbine, composed of a rotor with untwisted airfoil blades of symmetrical cross section, usually belonging to the NACA00XX series, radially set at 90 deg stagger angle; see Fig. 1.

The main feature of the Wells turbine is its capability of producing a time-averaged positive power from a cyclically reversing flow. A simplified scheme of the working principle is given in Fig. 2, which illustrates the forces acting on a cascade blade mounted on the turbine hub. Given the absolute velocity C and the tangential rotor velocity U, the relative flow velocity W is obtained. According to the two-dimensional cascade theory, the undisturbed flow velocity W_∞ is the average of the upstream (W_1) and downstream (W_2) relative velocities and forms an angle α with respect to the blade chord. The lift, L, and drag, D, forces (perpendicular and parallel to W_∞, respectively) can be resolved into the tangential, F_u, and axial, F_n, components, whose magnitudes vary during the cycle. However, the direction of F_u is predominantly independent of the axial-flow direction [4]. F_u will be negative whenever the drag becomes dominant, namely, either when the flow-rate approaches zero or when severe stall conditions occur. Another important feature of the Wells turbine is related to its high rotational speed, which allows one to directly match it to the electrical generator and enables energy to be stored by fly-wheel effect [32].

The Wells turbine prototype under investigation is shown in Fig. 3. The turbine is characterized by the following parameters: hub radius, $R_{hub}=101$ mm; tip radius, $R_{tip}=155$ mm; NACA0015 blade profile with constant chord length, $c=74$ mm; and number of blades, $N=7$. Therefore, the hub-to-tip ratio, $h=R_{hub}/R_{tip}$, and the solidity, $s=Nc/(2\pi R_{mid})$ with $R_{mid}=128$ mm, are equal to 0.65 and 0.64, respectively. The chosen hub-to-tip ratio and solidity turn out to be very close to the optimum values in terms of efficiency, according to a recent study [25] based on factorial design and carried out by means of an actuator disk theory [33], which accounts for three-dimensional effects. The hub is made up of aluminum and obtained from a commercial fan. The blades have been produced in composite material reinforced by carbon fiber with suited attachment in order to fix the blade with a stagger angle equal to 90 deg.

The turbine performance has been assessed in a test facility, as discussed in Refs. [20,21].

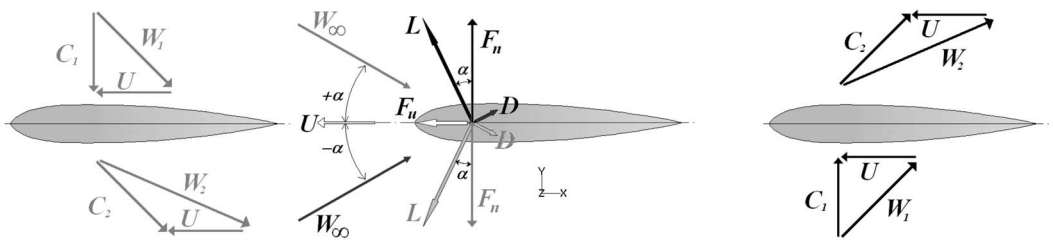

Fig. 2 Velocity diagrams and forces acting on a cascade blade, where (1) and (2) refer to the upstream and downstream conditions, respectively

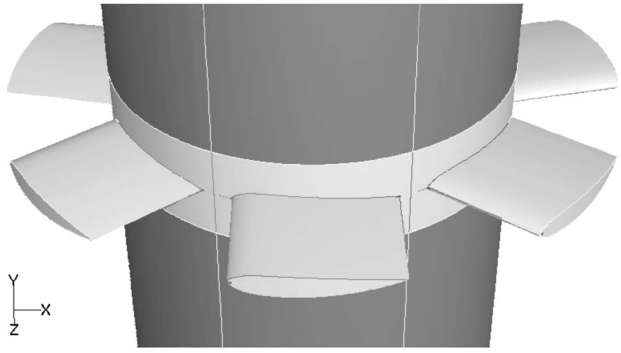

Fig. 4 Turbine model geometry

3 Numerical Model

The commercial code FLUENT is used to carry out the simulations. The steady incompressible three-dimensional RANS equations are discretized by means of a finite volume approach. The pressure-velocity coupling is achieved by means of the semi-implicit method for pressure-linked equations (SIMPLE) algorithm. The equations are solved in a noninertial reference frame rotating at the same angular speed of the turbine, the relative velocity being used as the dependent variable. The convective terms are discretized using a second-order-accurate upwind scheme, whereas pressure and viscous terms are discretized by means of a second-order-accurate centered scheme. An implicit segregated solver is employed. Concerning the turbulence effects, three different models available in the code have been used. Two models, namely, the one-equation model by Spalart and Allmaras [26] and the two-equation k-ω SST model proposed by Menter [27], rely on the Boussinesq approach to linearly relate the Reynolds stresses to the mean strain-rate tensor components by means of a computed turbulent viscosity. In particular, the k-ω SST model is used in its low-Reynolds number version [28] in order to properly predict the asymptotic behavior of the turbulent quantities when approaching a solid wall. In the third model, that is, the Launder Reynolds-stress model [29,30], the Boussinesq approach is avoided and each component of the turbulent stress tensor is computed by solving the corresponding transport equation. In this way, though with an increased computational effort due to the higher number of transport equations, the drawbacks of the isotropic eddy viscosity assumption are overcome, thus obtaining a model that, in principle, is closer to the physics of the turbulence phenomena and, therefore, more suitable for problems with marked anisotropy of the Reynolds-stress tensor, such as in the presence of streamline curvature, swirl, rotation, and rapid changes in strain rate.

3.1 Computational Domain. A simplified model of the turbine geometry has been used in the computations, considering only the flow in the annulus as shown in Fig. 4. In fact, the analysis performed by the authors in a previous study [21] indicates that, for the geometrical and flow configurations considered here, the presence of the hub-nose influences only marginally the turbine performance, and thus has not been taken into account in this paper. Moreover, the value of the tip gap has been taken equal to 2% of the chord length, approximately equal to that of the prototype. Taking into account the turbine symmetry, only one-seventh of the annulus has been computed, imposing periodic boundary conditions in the tangential direction. The computational domain has been limited in the axial direction to four chord lengths upstream and six chord lengths downstream of the blade.

Particular care has been devoted to the mesh generation. Relying on the experience acquired by the authors in the numerical simulation of the flow through Wells turbines [15,20,23–25], three grids have been generated (Grid A, Grid B, and Grid C), in order to carry out a grid-sensitivity study. For all the meshes, the computational domain has been discretized by means of a fully structured multiblock grid, even in the gap region, using a body-fitted C mesh close to the blade and an H-type mesh elsewhere, as detailed in Fig. 5, where the mesh on the blade-tip surface is provided. A global view of the meshes on the blade and hub surfaces is provided in Fig. 6 according to Grid A. The mesh generation of the three grids has been carried out by means of

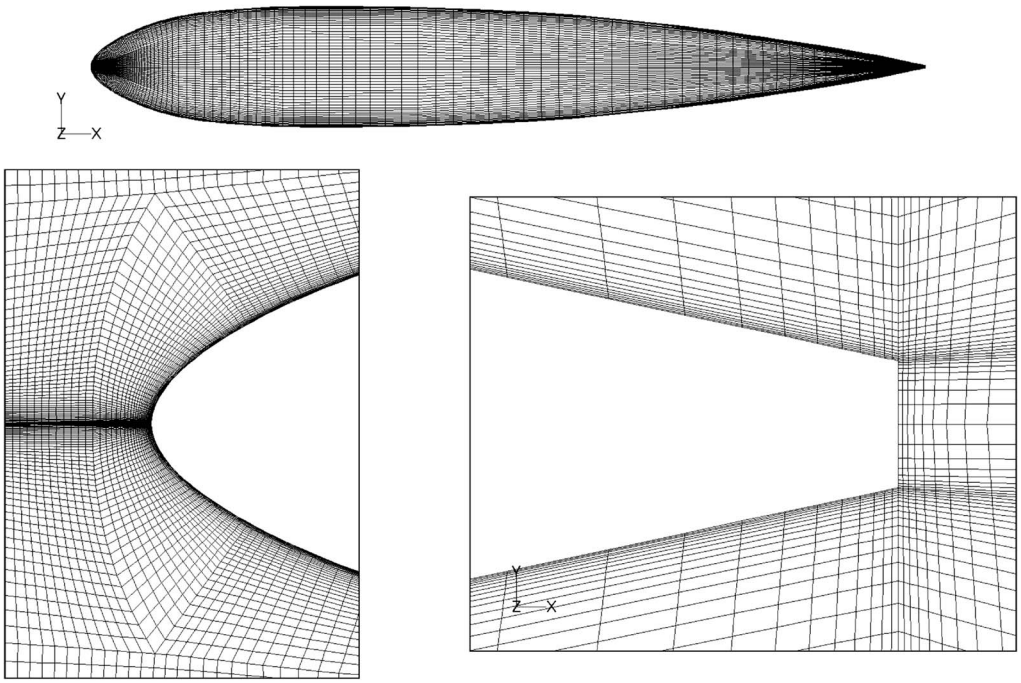

Fig. 5 Computational Grid A: discretization of the blade-tip surface and the leading- and trailing-edge regions

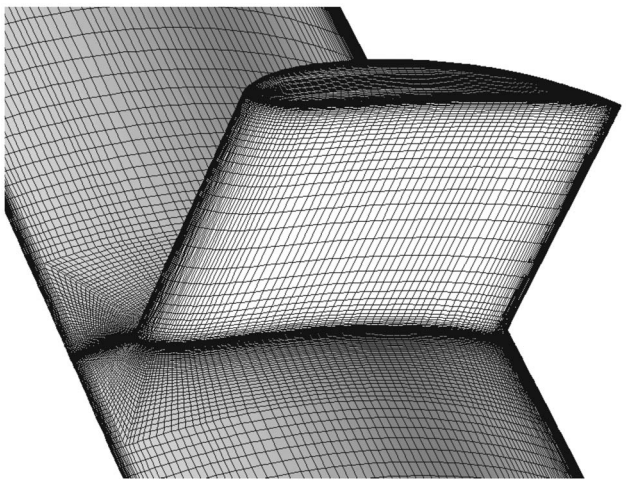

Fig. 6 Computational grid: discretization of the blade and hub surfaces

code GAMBIT, with the following parameters.

The following are observed for Grid A.

- Both sides of the blade profile have been discretized using 132 intervals.
- On the truncated trailing-edge, 16 equispaced cells have been used.
- The height of the first cell close to the blade profile is equal to $5\times10^{-5}c$.
- 48 intervals have been employed in the radial direction, the height of the first cell at the hub surface being equal to $4\times10^{-4}c$.
- Twelve nonuniformly spaced cells have been used in the radial gap zone, the height of the first cell at the blade tip and at the case being equal to $2\times10^{-3}c$ and $1.1\times10^{-3}c$, respectively.
- The overall number of cells is equal to about 2×10^{6}.

Grid B differs from Grid A due to the following features.

- 130 intervals, instead of 132, have been used in order to discretize both sides of the blade profile.
- On the truncated trailing-edge the same number of cells has been applied but they have been symmetrically clustered near the ends, where a cell size equal to $4\times10^{-5}c$ has been used.
- The first cell height at the blade profile has been reduced from $5\times10^{-5}c$ to $3\times10^{-5}c$.
- Along the blade span the cell distribution has been modified in order to have the 48 cells symmetrically distributed about the midspan and clustered near the ends, the height of the first cell at the hub surface being equal to $10^{-4}c$.
- In the radial gap zone the number of intervals has been raised to 20 (symmetrically distributed about the midpoint), the first cell at blade tip being equal to $10^{-4}c$.
- The overall number of cells is equal to about 2.4×10^{6}.

Grid C differs from Grid B due to the following features.

- Along the blade span the number of cells has been doubled to 96, also reducing the first cell height near the tip to $6\times10^{-5}c$.
- In the radial gap zone the number of intervals has been raised to 24, also reducing the first cell height near the tip to $6\times10^{-5}c$.
- The overall number of cells is equal to about 4.1×10^{6}.

With the aim of obtaining an accurate prediction of the flow in the boundary-layer region, all grids have been designed in order to obtain quasi-orthogonal cells along the blade surface and a reduced growing rate, as shown in Figs. 7 and 8. All meshes used to discretize the computational domain are fine enough to resolve the viscous sublayer (y^+ close to 1) at the blade and hub surfaces, so that the turbulence equations are solved up to the walls and no near-wall modeling is needed. Concerning the other surfaces (case and tip-blade) the y^+ values of the first cells at the wall range between 10 and 30 in the case of Grid A, whereas it is about equal to 1 in the cases of Grids B and C. The enhanced resolution of Grid C with respect to Grid B concerns mainly the refinement of the domain discretization in the radial direction.

As far as the boundary treatment is concerned, the following conditions have been used.

- No-slip boundary conditions are imposed at the blade surface, hub, rotor, and casing.
- Periodicity is imposed along the meridional surfaces delimiting the 1/7 domain in the tangential direction.
- A uniform velocity profile has been used at the inflow surface along with turbulent intensity, I, equal to 1% and turbulence length scale, L, equal to $1/100c$.
- Radial equilibrium has been imposed at the outflow surface of the annulus.

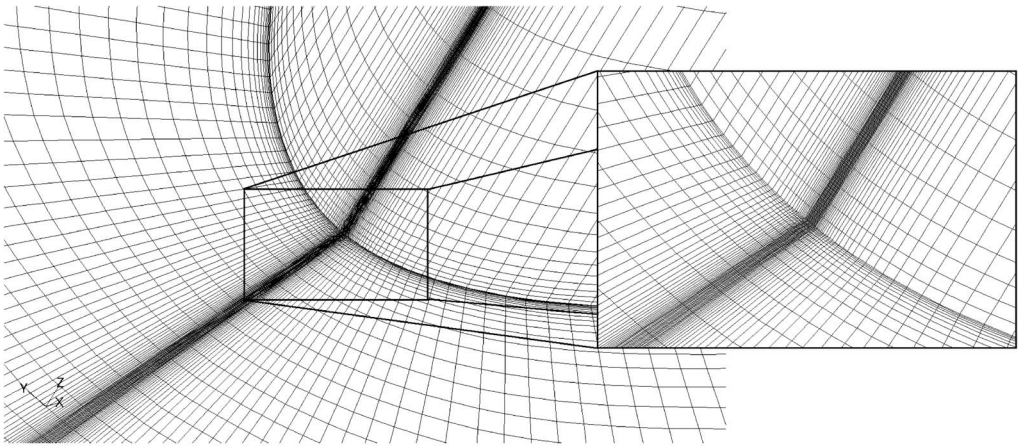

Fig. 7 Computational Grid A: partial view of the leading-edge

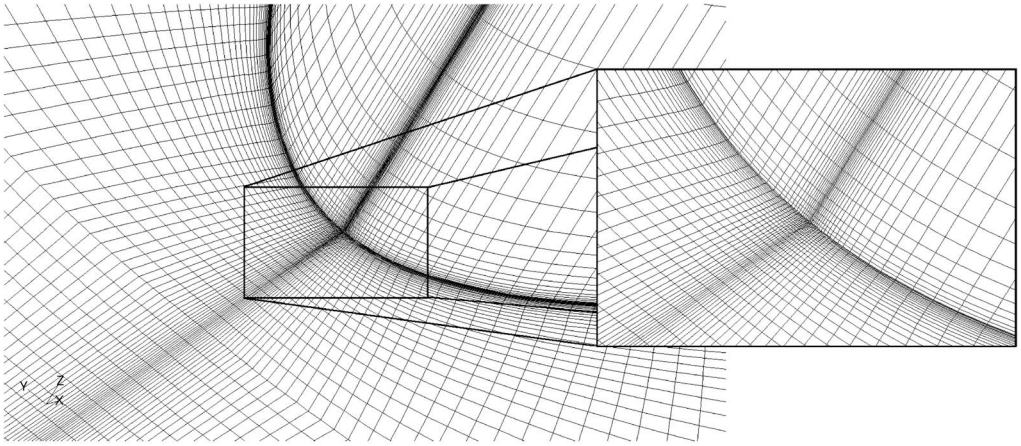

Fig. 8 Computational Grid B: partial view of the leading-edge

4 Results

4.1 Global Performance Analysis. During the experimental tests [20,21], the blower's rotational speed was kept constant while the rotational speed of the Wells turbine was changed from 2000 rpm up to 2700 rpm, in order to consider different steady flow configurations.

The turbine performance is described employing the following dimensionless parameters.

- For flow coefficient,

$$U^\star = \frac{V}{U_{\text{tip}}} \tag{1}$$

  where $V = Q/A_{\text{annulus}}$ indicates the bulk inlet velocity, Q being the volume flow-rate, and U_{tip} is the tip-blade velocity.
- For torque coefficient,

$$T^\star = \frac{T}{\rho\omega^2 R_{\text{tip}}^5} \tag{2}$$

  where T is the turbine's shaft torque, $\rho = 1.225\ \text{kg/m}^3$ is the air density, and ω is the turbine angular speed.
- For stagnation pressure drop coefficient,

$$\Delta P^\star = \frac{\Delta P^0}{\rho\omega^2 R_{\text{tip}}^2} \tag{3}$$

  where ΔP^0 is the stagnation pressure drop across the turbine, evaluated using the mass average values at the inlet and outlet sections of the computational domain, respectively; notice that such a variable, needed to compute the turbine efficiency, has been obtained only from the numerical simulations.
- For pressure drop coefficient,

$$\Delta P_s^\star = \frac{\Delta P}{\rho\omega^2 R_{\text{tip}}^2} \tag{4}$$

  where ΔP is the pressure drop across the turbine, evaluated using the mass average values at the inlet and outlet sections of the computational domain, respectively.
- For efficiency,

$$\eta = \frac{T\omega}{Q\Delta P^0} \tag{5}$$

In all computations the steady state solution has been obtained by requiring that the maximum L_1 norm of the residuals of the conservation and turbulent transport equations is lower than 10^{-4}. Using Grid B, such a condition has been reached using a number of iterations ranging from about 5000 to 10,000 for all the flow conditions and turbulence models; moreover, the computational cost per iteration required by the k-ω and Reynolds-stress models was about 20% and 60% higher than that required by the Spalart–Allmaras model.

As a first step, a grid-sensitivity analysis has been carried out. To this purpose, the global turbine performances obtained using the Spalart–Allmaras turbulence model on Grids A, B, and C for $U^\star$ equal to 0.218 and 0.238 have been computed and are shown in Tables 1 and 2. Due to the small differences between the results of all the grids, we can argue that Grid A is already sufficiently refined to capture the main performance parameters; the solutions obtained using Grid B can be considered more reliable than those obtained using Grid A, due to its favorable features in terms of y^+ values at all walls; and a more refined mesh, such as Grid C, with a spanwise doubling of the number of cells, turns out to be superfluous. Thus, in the following only the results obtained with Grid B will be shown.

The turbine performance has been first evaluated by comparing the experimental and computed torque and pressure drop coefficients versus the flow-rate coefficient. Figures 9–12 show the variations of the computed dimensionless parameters versus the flow-rate coefficient, obtained using the three turbulence models. In particular, three significant $U^\star$ values used in the following analyses are put in evidence.

It appears that the results of the present simulations with all the turbulence models are in reasonable agreement with the experimental data in terms of pressure drop; actually, the k-ω and Reynolds-stress models predict slightly lower values with respect to the results of the Spalart–Allmaras model and experimental data. This behavior of the turbulence models is confirmed by the

Table 1 Grid-sensitivity study for $U^\star = 0.218$

	$T^\star$	$\Delta P^\star$	$\Delta P_s^\star$	η
Grid A	0.1173	0.5166	0.5681	0.5068
Grid B	0.1156	0.5236	0.5676	0.4997
Grid C	0.1161	0.5263	0.5722	0.4979

Table 2 Grid-sensitivity study for $U^\star = 0.238$

	$T^\star$	$\Delta P^\star$	$\Delta P_s^\star$	η
Grid A	0.1404	0.5698	0.6309	0.5005
Grid B	0.1385	0.5826	0.6333	0.4918
Grid C	0.1384	0.6023	0.6389	0.4871

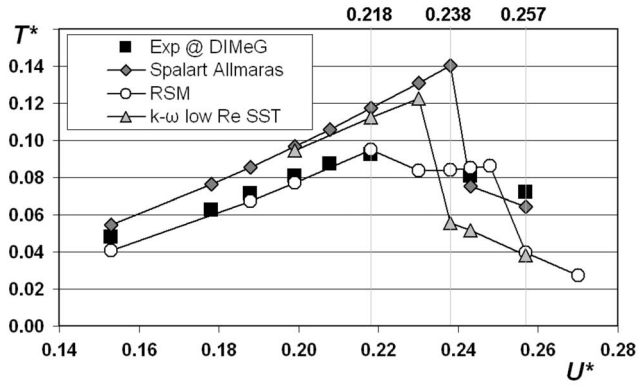

Fig. 9 Torque coefficient, $T^\star$

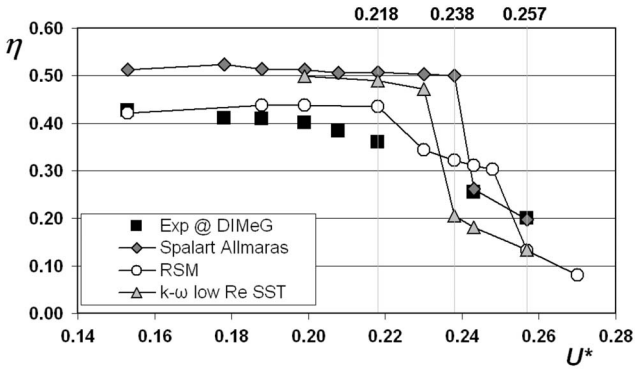

Fig. 12 Efficiency, η

distributions of the stagnation pressure drop coefficient, given in Fig. 11, which also shows that, due to the small amount of the kinetic energy in the measure sections, $\Delta P^\star \simeq \Delta P_s^\star$. Concerning the torque distribution, the stall condition is roughly predicted by the three models with non-negligible differences. The Reynolds-stress model appears to be able to better predict the torque distribution before the stall inception ($U^\star < 0.22$) and, more importantly, to capture the behavior at incipient stall condition ($0.22 < U^\star < 0.25$), with a local plateau before the deep stall conditions, occurring when $U^\star > 0.25$, where greater discrepancies with other turbulence models are observed. It can be noticed that the presence of a relatively flat behavior, with a barely appreciable local maximum in the torque coefficient distribution at incipient stall condition, is often observed in high solidity Wells turbines (e.g., the experimental results of Curran and Gato [34]). On the other hand, the results obtained using the Spalart–Allmaras model provide a higher (20–30%) torque value before stall inception, predict a delayed abrupt stall condition, and, finally, provide closer results with respect to the experimental data in the deep stall conditions. The performance predicted by the k-ω model are similar to those of the Spalart–Allmaras model for $U^\star < 0.22$, whereas, for higher values of $U^\star$, it predicts an early abrupt stall condition.

A further consideration is in order: The efficiency distribution, provided in Fig. 12, presents a slightly decreasing trend until stall inception and this value (between 0.4 and 0.5) indicate a low turbine efficiency. This could be due to the small dimensions of the prototype, and thus a small value of the Reynolds number (about 2×10^5), which implies a negative scale effect, in agreement with the prediction based on several experimental results [3] registering a reduction in maximum efficiency with the reduction in the Reynolds number.

In order to gain a better understanding of the turbine performance, it is worthwhile to investigate in which amount the different blade portions contribute to the overall torque and how these amounts change when varying $U^\star$. To this purpose, a torque parameter, γ, has been defined, indicating the torque contribution per unit radial blade length,

$$\gamma(R) = \int_0^{L(R)} t(R,\ell)\, d\ell$$

where $t(R,\ell)$ is the local blade-torque contribution per unit area, ℓ is the curvilinear coordinate measured along the blade surface (for a given R), and $L(R)$ is the profile length at R. It is worth noting that the main contributions to the blade torque are those given by the blade pressure and suction surfaces, whereas the contributions of the tip and rotating-hub surfaces are negligible. Moreover, the viscous stress contribution to the torque, which is taken into account in the present analysis, is always two to three orders of magnitude lower with respect to the pressure one.

The distributions of γ versus the blade-height fraction, $r^\star = (R - R_{\text{hub}})/(R_{\text{tip}} - R_{\text{hub}})$, obtained using the three turbulence models and for $U^\star$ equal to 0.218 (without stall), 0.238 (incipient stall), and 0.257 (deep stall) are given in Fig. 13. The Spalart–Allmaras turbulence model provides similar γ distributions for $U^\star$ equal to 0.218 and 0.238, the latter case presenting slightly higher values at all radial positions; the sharp performance decrease at $U^\star = 0.257$ is due to the stall condition observed from about the 30% of the blade span. On the other hand, the k-ω turbulence model predicts similar γ distribution for $U^\star$ equal to 0.238 and 0.257, justifying the abrupt early stall condition, the latter case presenting lower values at all radial positions. Finally, the results of the Reynolds-stress turbulence model show that for $U^\star$ equal to 0.218 and 0.238 the flow features remain unchanged only from hub to about 40% of the blade span, the latter case presenting lower γ values due to the missing relief-effect at the blade-tip region; also,

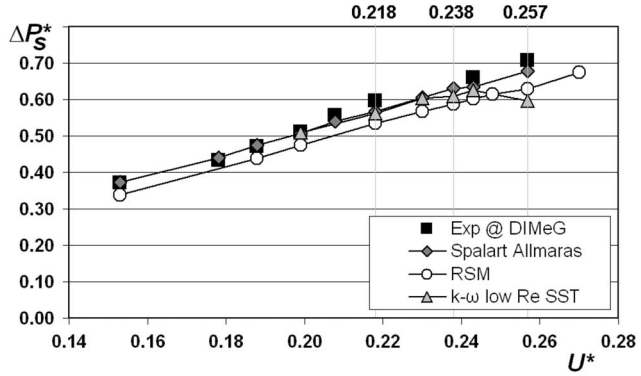

Fig. 10 Nondimensional pressure drop, $\Delta P_s^\star$

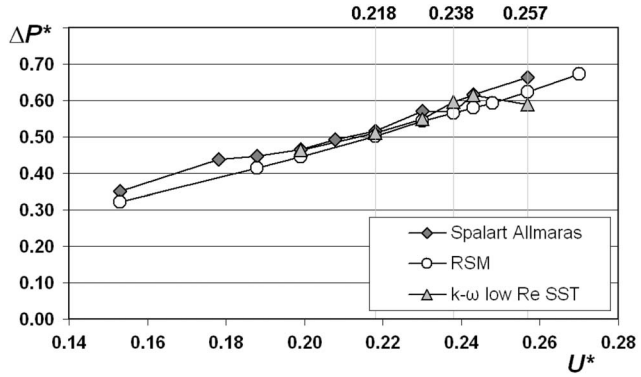

Fig. 11 Nondimensional stagnation pressure drop, $\Delta P^\star$

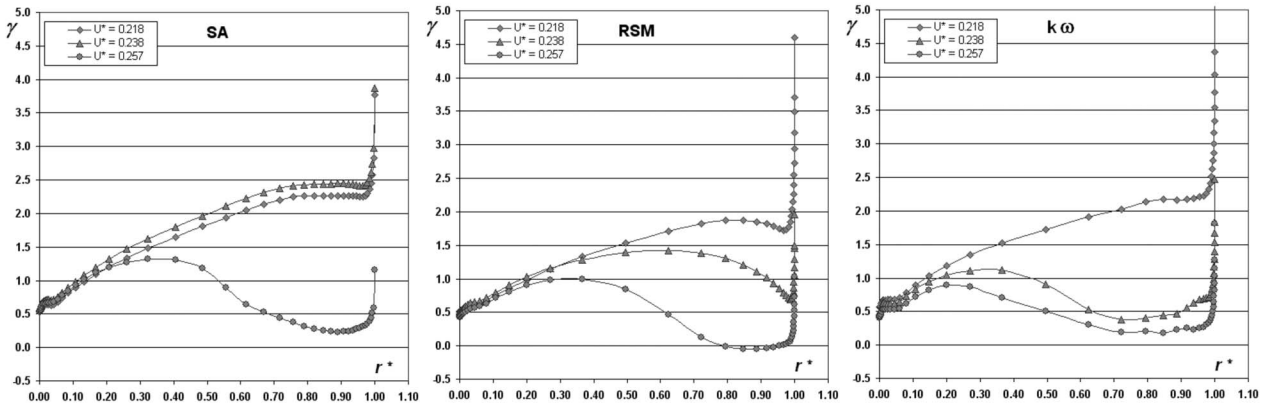

Fig. 13 Distribution of the torque parameter γ [N] versus the blade-height fraction, r^*

for $U^*=0.257$, the behavior from hub to about 25% of the blade span remains almost equal, but the differences appear more pronounced over the remaining blade portion, due to a large separation region from tip to midspan, with a non-negligible part with negative torque.

The above mentioned relief-effect is due to the beneficial effect that the tip-leakage flow has on the turbine performance, as it will be discussed in more detail in Sec. 4.3, caused by tip vortex capability to partially counterbalance the tendency of the flow to separate at the tip suction side.

Finally, Fig. 13 shows that for all the flow conditions and all the turbulence models the distributions of γ in a thin region close to the blade tip present a high positive gradient. The reason for such a finding could be traced back to the pressure behavior over the blade surface in the tip region, as shown for the Reynolds-stress model and $U^*=0.238$ in Fig. 14, where the gauge pressure, P_g, distributions along the blade at different radial positions from $r^*=0.9935$ to $r^*=0.9994$ are provided. It appears that pressure on the blade pressure side decreases very rapidly when approaching the blade-tip surface due to the tip-leakage flow acceleration, while the pressure on the suction side remains almost unchanged.

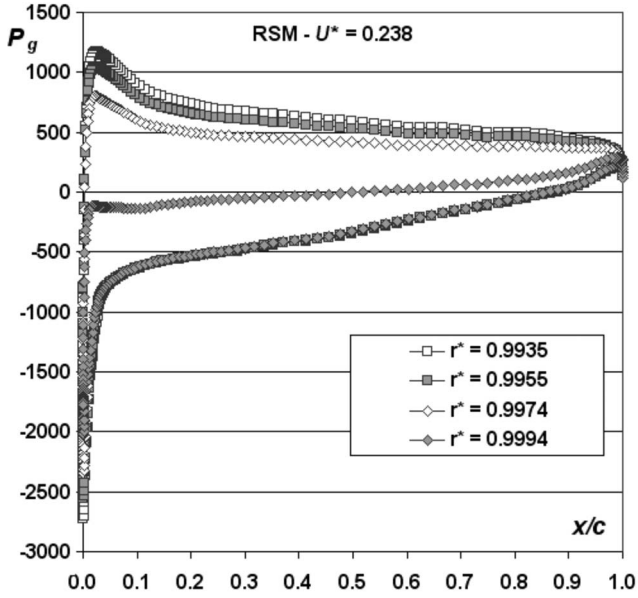

Fig. 14 Gauge pressure (N/m^2) distributions along the chord fraction at different r^* values obtained using the Reynolds-stress model for $U^*=0.238$

Consequently, the suction-side contribution to the torque is almost constant, whereas the pressure side one is markedly changed. Up to $r^*=0.9974$ the rear pressure-side contribution to the torque is positive but unable to counteract the negative front one, as will be more clearly shown in the following analysis considering the torque contribution per unit area versus the chord fraction. On the other hand, when the tip section is reached ($r^*=0.9994$), a stagnation region is no more visible and the flow decelerates over the whole pressure side in the tangential direction, so that its contribution to the torque is positive.

In order to complete the picture of the spatial distribution of the torque exerted by the fluid on the blade surface, the distribution of the torque per unit area, t (measured in N/m), has been analyzed along the blade profile at different radial positions: $R=0.11$ m (close to hub), $R=0.13$ m (close to midspan), and $R=0.15$ m (close to tip). Figures 15(*a*)–15(*c*) provide these distributions for three values of U^*, namely, 0.218, 0.238, and 0.257, and two turbulence models, namely, the Spalart–Allmaras and Reynolds-stress models. Moreover, for the same conditions of Figs. 15(*a*)–15(*c*), the sum t_s of the pressure- and suction-side terms of t is plotted in Figs. 15(*d*)–15(*f*) versus the chord fraction. Consistently with the radial distribution of Fig. 13, the following are observed: (a) The values of t are higher in magnitude in the leading-edge region, whereas lower and mainly positive values are obtained in the rear 60% portion of the blade; (b) in the hub region ($R=0.11$ m) the variations of t with U^* are negligible, so that the torque obtained in this region over both sides of the blade can be considered almost constant for the different flow conditions; (c) the variations of t with U^* increase along with R and mainly interest the suction side of the blade; again, the leading-edge region is characterized by more relevant t variations; (d) for $U^*=0.257$ and both turbulence models, at $R=0.13$ m the negative values of t_s in the leading-edge region indicate that the stall condition involves also the midspan region; indeed, it will be shown later that such a result can be traced back to the separation region, starting from the blade tip and extending to midspan; on the other hand, for the other U^* values, the differences between the results of the two models are small and comparable to those at $R=0.11$ m; (e) differently from the previous cases, at $R=0.15$ m only for $U^*=0.218$ and $U^*=0.257$ the two models show a similar behavior, whereas for $U^*=0.238$ the Spalart–Allmaras model still presents positive t_s values at the leading-edge, indicating a lack of separation, which, on the other hand, is correctly predicted by the Reynolds-stress model.

From the above analysis one can see that the flow through the Wells turbine is characterized by a high level of complexity, which becomes even greater in stall conditions. Therefore, it is not surprising that, using a RANS approach, the results provided by the three turbulence models are qualitatively similar but quantita-

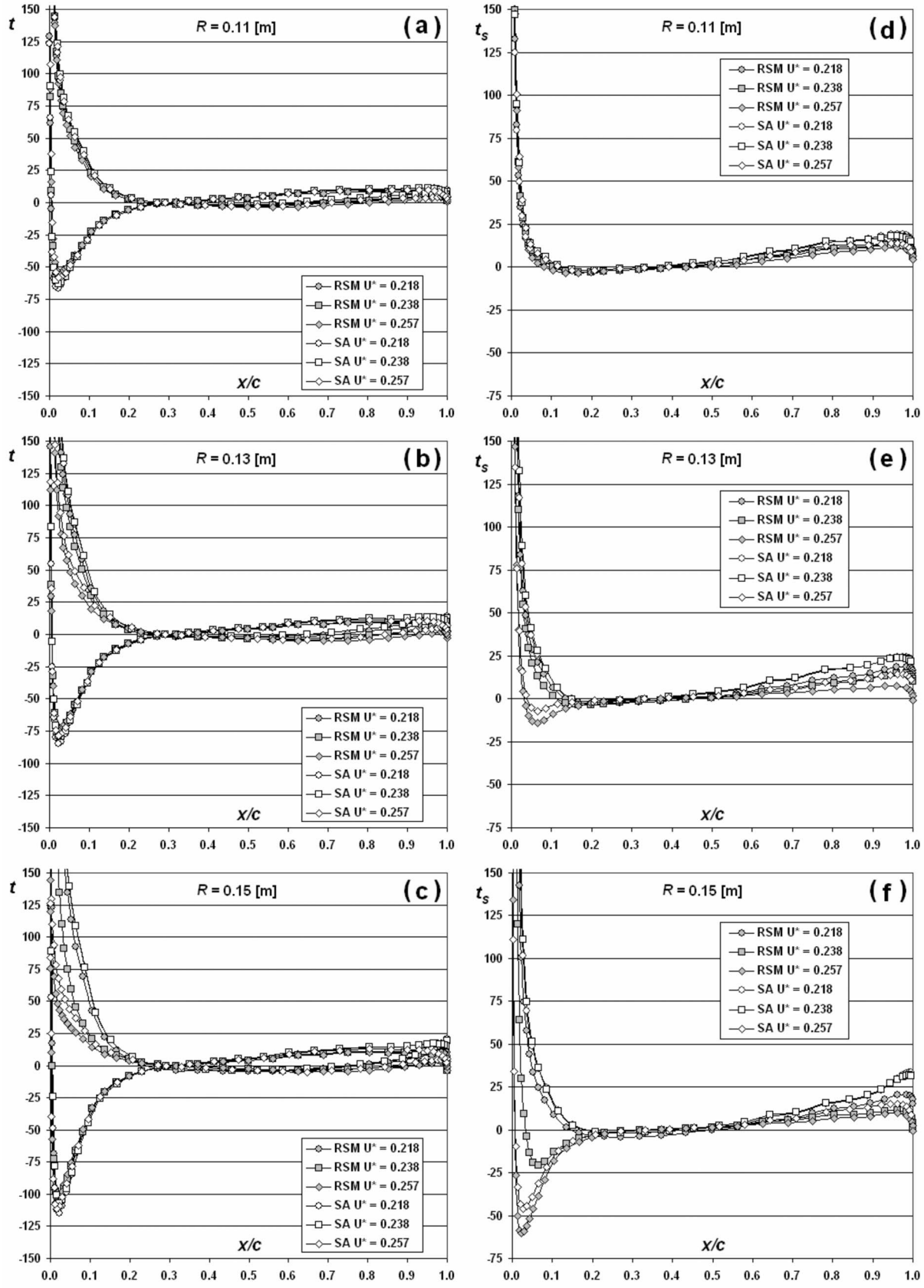

Fig. 15 Torque per unit area t (N/m) ((*a*)–(*c*)) and sum t_s (N/m) of the pressure- and suction-side terms of t versus the chord fraction ((*d*)–(*f*))

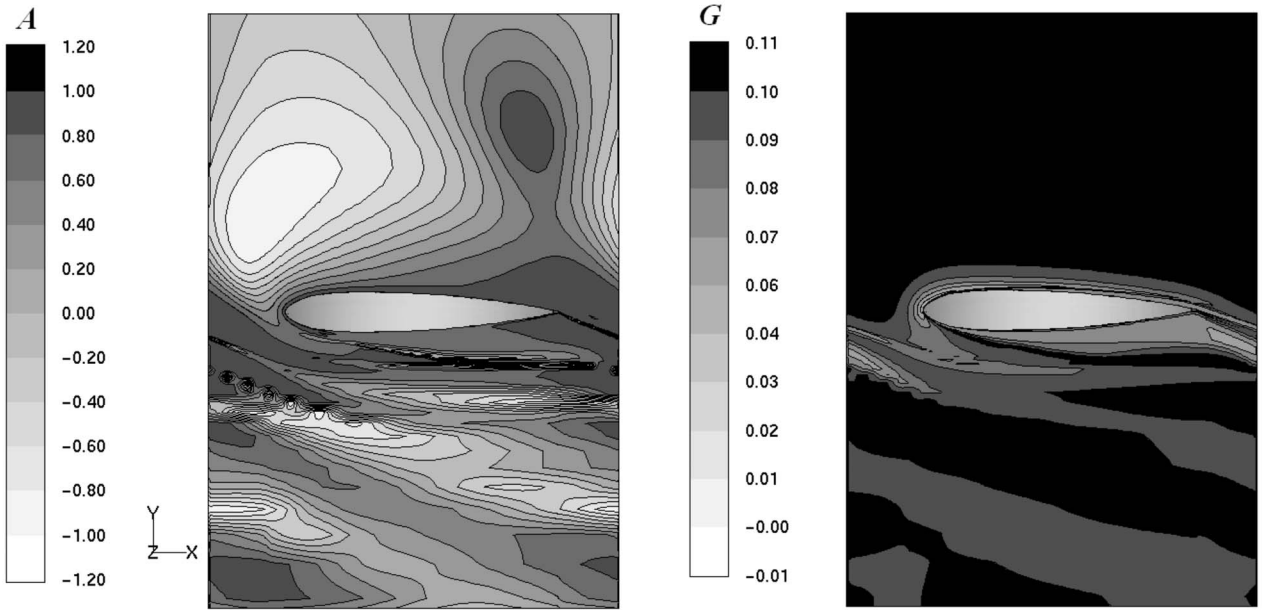

Fig. 16 Anisotropy invariant contours at midspan obtained using the Reynolds-stress model

tively quite different. The results of the Reynolds-stress model are closer to the experimental data, whereas, before separation takes place, the two eddy viscosity models provide results in good agreement with each other but different from those of the Reynolds-stress model. The main differences are found in the detection of the stall condition, namely, the separation condition, the separation-zone detection, and the corresponding flow-field.

4.2 Anisotropy Invariant Analysis. In order to set up an alternative comparative study among the results of the three turbulence models and recognize which of them could provide the most reliable solutions, we shall analyze the properties of the nondimensional anisotropy tensor

$$a_{ij} = \frac{\overline{u_i' u_j'}}{q^2} - \frac{1}{3}\delta_{ij} \tag{6}$$

where q^2 is the trace of the $\overline{u_i' u_j'}$ tensor, equal to twice the turbulence kinetic energy ($q^2 = 2k$), and δ_{ij} is the Kronecker delta function. In the case of linear eddy viscosity model, the anisotropy tensor clearly renders the nature of the Boussinesq assumption

$$a_{ij} = -\frac{\nu_T}{k} S_{ij} \tag{7}$$

where ν_T is the kinematic turbulent viscosity and S_{ij} is the mean strain-rate tensor

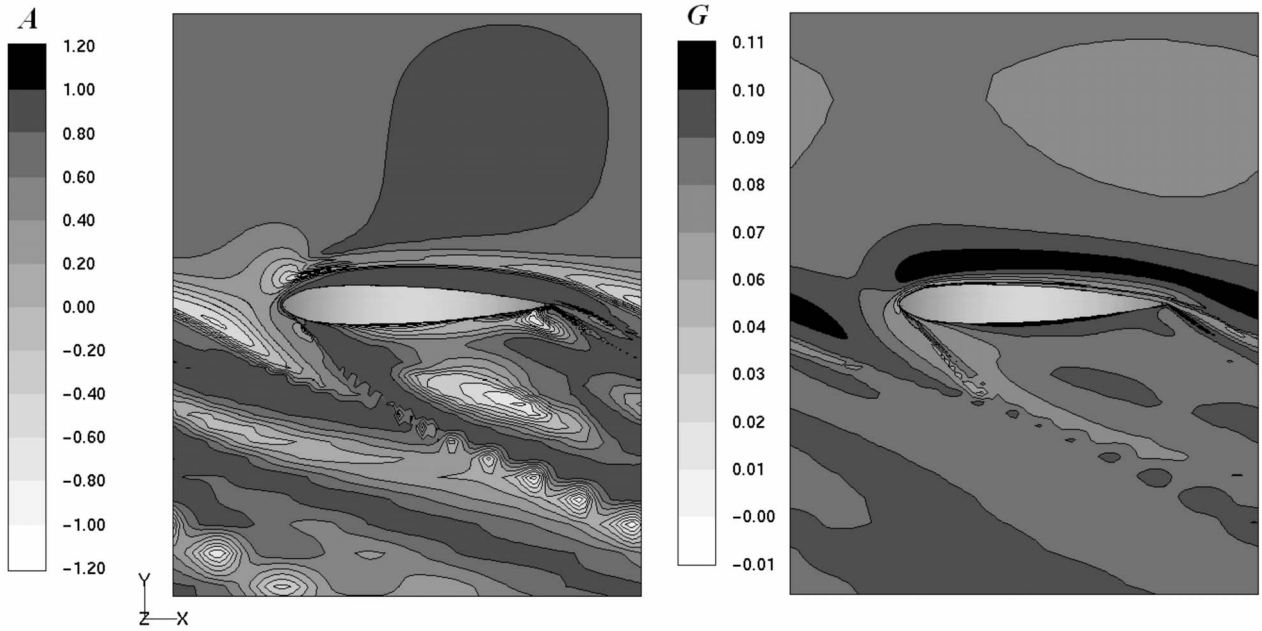

Fig. 17 Anisotropy invariant contours at R=0.15 m obtained using the Reynolds-stress model

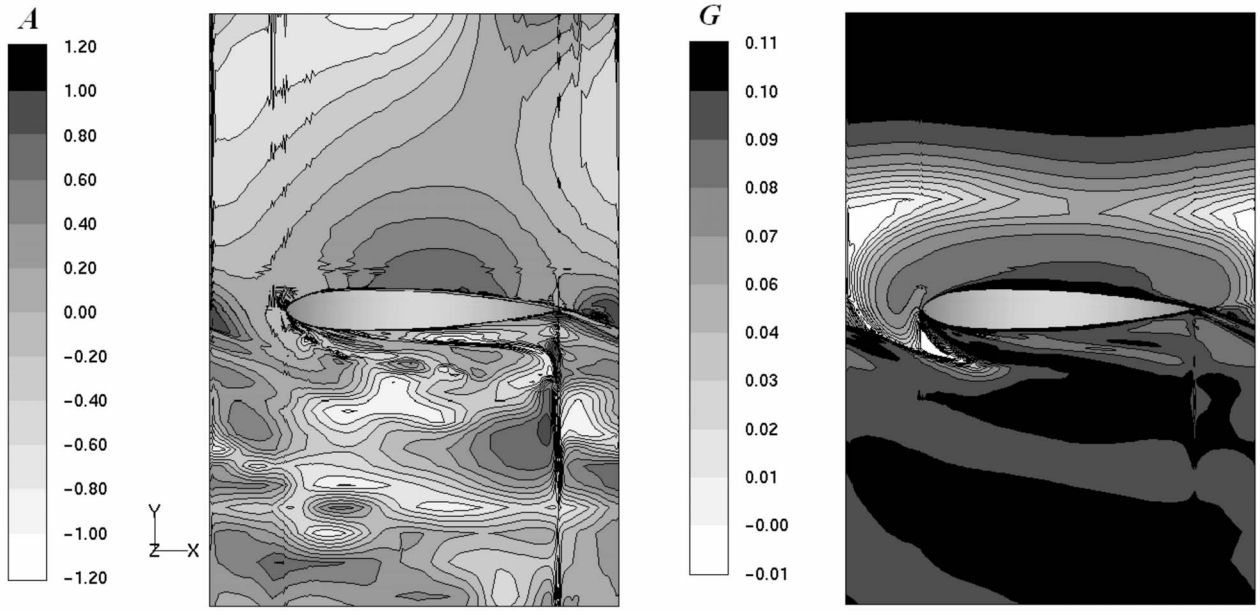

Fig. 18 Anisotropy invariant contours at midspan obtained using the *k-ω* model

$$S_{ij} = \frac{1}{2}\left(\frac{\partial U_i}{\partial x_j} + \frac{\partial U_j}{\partial x_i}\right) \tag{8}$$

Besides the trace, two other scalar invariants can be defined, which will be used to investigate the results of the simulations, according to the invariant theory of Lumley [35]. Since the anisotropy tensor is symmetric and has trace equal to zero, these two scalar invariants can be defined as follows:

$$\mathrm{II} = a_{ij}a_{ji}, \quad \mathrm{III} = a_{ij}a_{jk}a_{ki} \tag{9}$$

In the axisymmetric turbulence limit, these quantities have to satisfy the following relation:

$$\mathrm{II} = \tfrac{3}{2}\left(\tfrac{4}{3}|\mathrm{III}|\right)^{2/3} \tag{10}$$

Therefore, according to Escudié and Liné [36], an axisymmetric invariant can be defined as follows:

$$A = \frac{4/3\mathrm{III}}{(2/3\mathrm{II})^{3/2}} \tag{11}$$

so that for $A = \pm 1$ the axisymmetric limit is recovered, with a "rodlike" structure for $A = -1$ (the normal stresses are larger than the streamwise components) and a "disklike" structure for $A = 1$ (the streamwise stress is the largest one). On the other hand, when

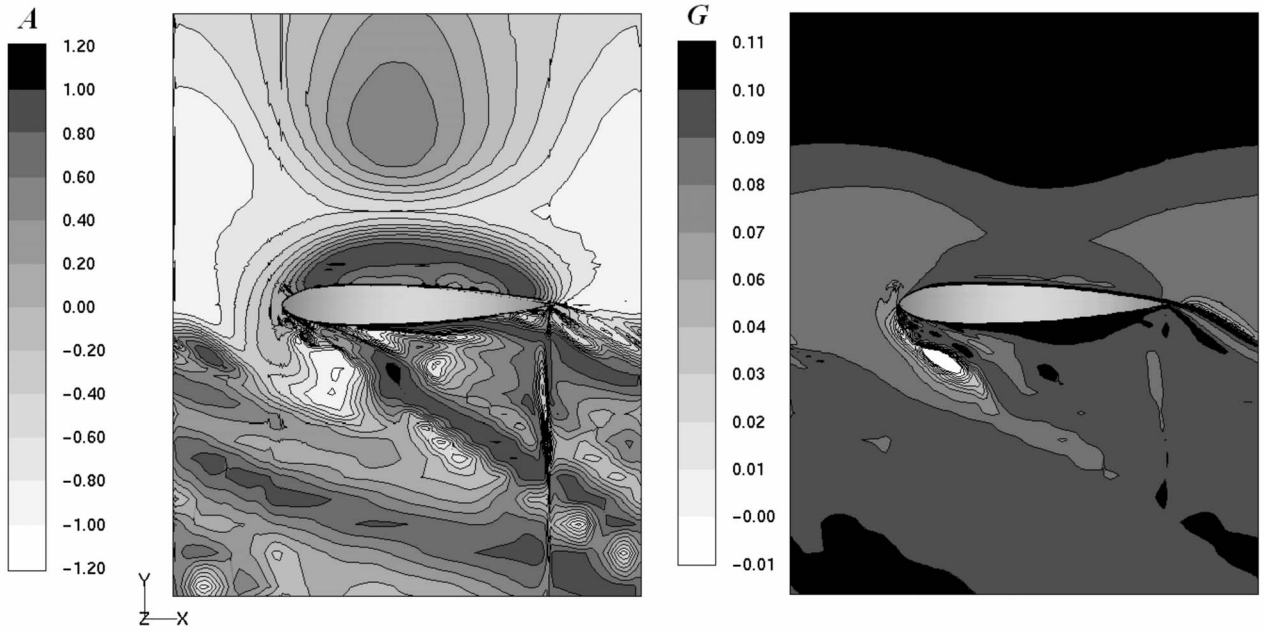

Fig. 19 Anisotropy invariant contours at *R*=0.15 m obtained using the *k-ω* model

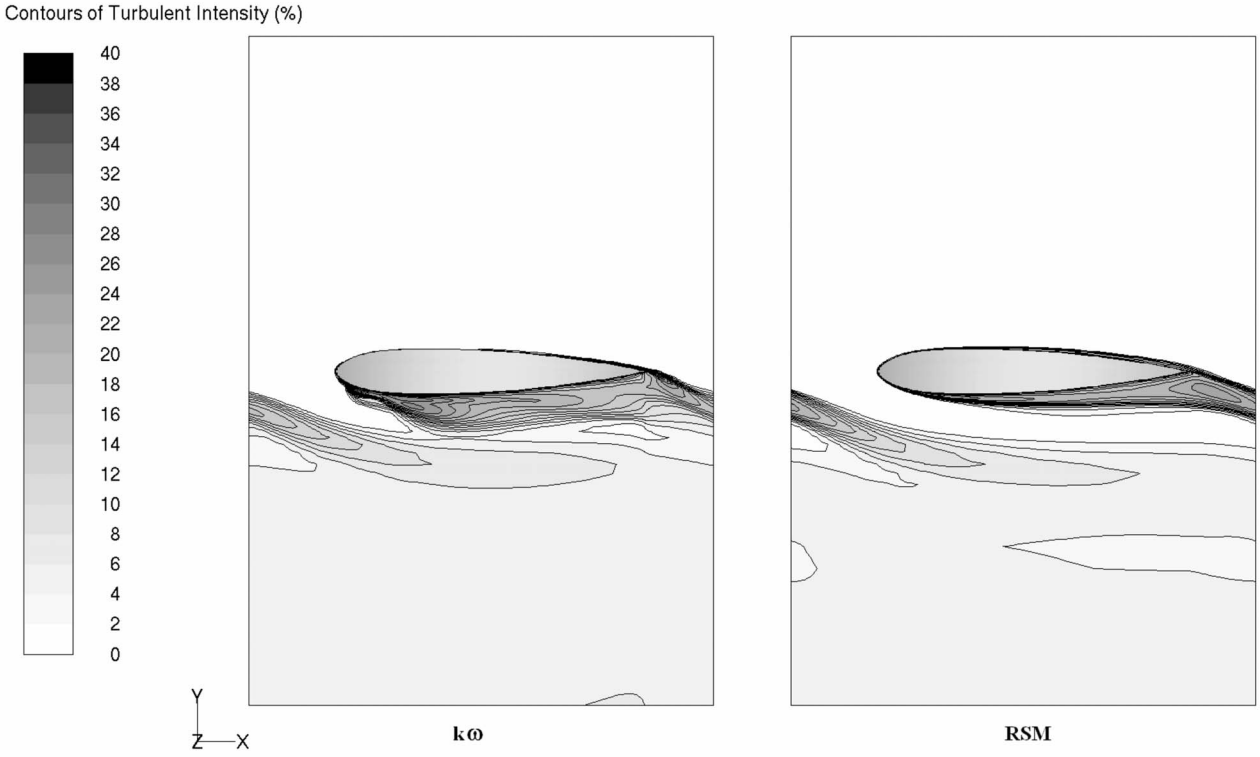

Fig. 20 Turbulent intensity contours at midspan obtained using the *k-ω* model (left) and the Reynolds-stress model (right)

the two-dimensional turbulence limit is reached, the two invariants have to satisfy the following relation:

$$\mathrm{II} = \tfrac{2}{9} + 2\mathrm{III} \tag{12}$$

so that, according to Ref. [36], a two-dimensional invariant can be defined as follows:

$$G = \tfrac{1}{2}(2\mathrm{III} - \mathrm{II}) + \tfrac{1}{9} \tag{13}$$

hence for $G=0$ the two-dimensional limit is recovered. Therefore, as suggested by Escudié and Liné [36], the turbulence anisotropy can be studied in terms of invariant maps in the (A,G) plane. In such a plane, apart from the above mentioned limits for axisymmetry and two-dimensionality, other special cases are three-dimensional isotropy, for $G=1/9$ and any value of A; two-dimensional isotropy, for $G=0$ and $A=-1$; and one-dimensional isotropy, for $G=0$ and $A=1$. The realizability conditions are

$$-1 \leq A \leq 1, \quad 0 \leq G \leq 1/9 \tag{14}$$

The anisotropy maps have been computed on two different blade-to-blade planes, namely, at midspan and at $R=0.15$ m (close to tip). The critical case $U^{\star}=0.238$ has been considered when the turbulence models show relevant differences in predicting the incipient stall condition starting from the tip. The results for the Reynolds-stress model are given in Figs. 16 and 17. For the sake of brevity, only one of the eddy viscosity models is considered, namely, the *k-ω* one, and the corresponding maps are given in Figs. 18 and 19.

The Reynolds-stress model substantially provides an isotropic Reynolds-stress tensor at midspan due to the turbulence state at the inlet section and to the sufficiently large distance from the hub and case walls. This is evident from the contours of G, Fig. 16, which give G values almost everywhere between 0.09 and 1/9, any consideration on the value of A being of no interest. The field is crossed by lower levels of G close to the blade boundary-layer and along the blade wakes.

Moving toward the blade, as anisotropy increases due to the presence of the blade walls, G tends to decrease while assuming the axisymmetric disklike structure $(A \rightarrow 1)$, according to the analysis of stagnation flows provided in Ref. [37]. The tendency toward the axisymmetric disklike structure is observed also in the cylindrical surface at $R=0.15$ m, close to the blade tip, Fig. 17, where the isotropy region $(G=1/9)$ almost disappeared due to the presence of the case wall, consistently, for example, with the results of fully developed channel flows [38]. In the separation region, starting at the leading-edge, a structure similar to that at the blade walls is encountered due to the presence of a shear flow.

This picture is substantially altered when analyzing the results of the *k-ω* turbulence model. In the midspan plane, Fig. 18, the isotropy region is limited too far upstream of the blade, followed by a region tending to the two-dimensional limit and presenting unrealizable values (negative G values), which are also detected in the leading-edge region. An unexpected isotropic region is also seen along the pressure side. In the plane at $R=0.15$ m, Fig. 19, the *k-ω* turbulence model presents an isotropic behavior upstream of the blade, with almost the same extent of that at midspan; unrealizable conditions are still observed, with $G<0$ and $A>1$. Wide regions with negative A values and $G<0.08$ indicate a two-dimensional axisymmetric structure, in contrast with the expected one-dimensional character due to the case wall proximity.

The different structures put in evidence by means of the anisotropy invariant maps have their counterparts in the turbulent properties. In particular, the turbulent intensity and the turbulent viscosity ratio obtained at midspan by the *k-ω* model are higher than those of the Reynolds stress in proximity of the leading-edge on the suction side (see Figs. 20 and 21), indicating flow separation. In fact, a deep stall condition is predicted at this $U^{\star}$ unlike the results of the Reynolds-stress model.

The above analysis confirms the difficulties of turbulence mod-

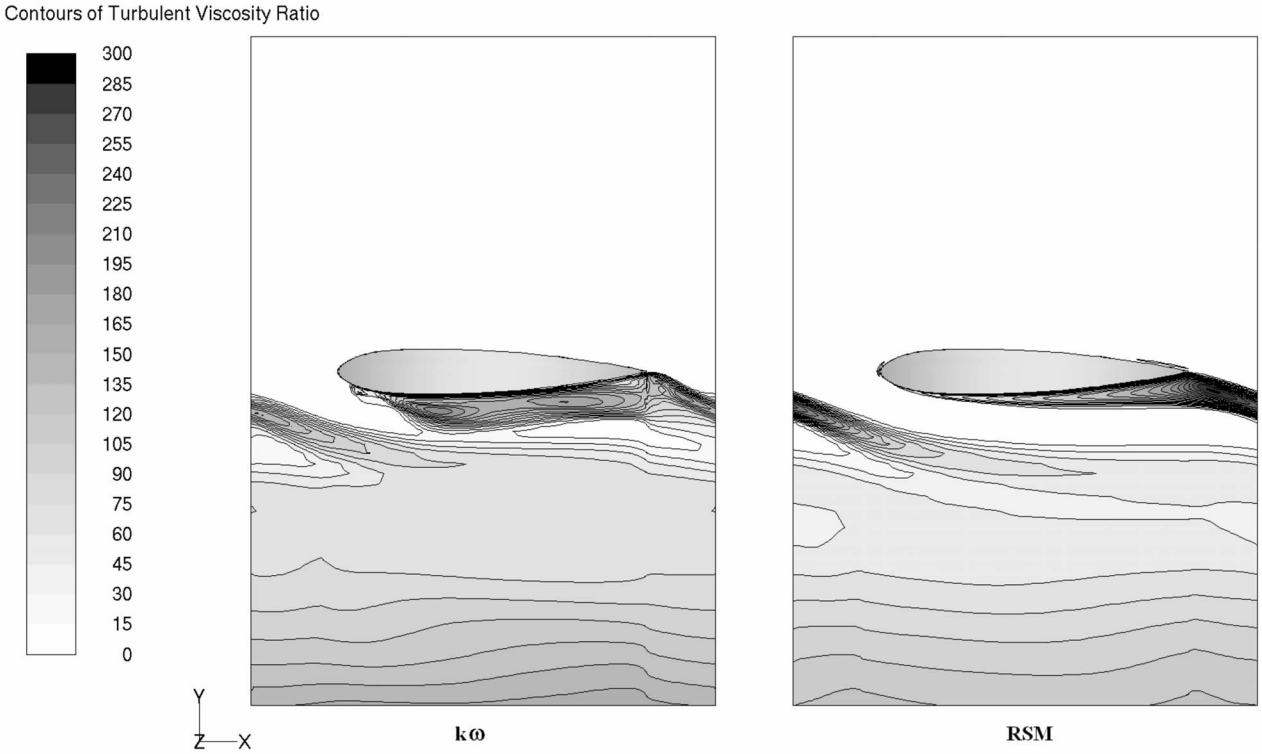

Fig. 21 Turbulent viscosity ratio contours at midspan obtained using the *k-ω* model (left) and the Reynolds-stress model (right)

els employing a linear eddy viscosity approach to provide a correct description of turbulence phenomena, particularly in complex flows, such as the one considered in this paper, involving streamline curvature, swirl, and rotational effects. The Reynolds-stress model, avoiding the turbulence isotropy hypothesis, partially overcomes the above drawbacks and thus turns out to be more reliable, also in view of the better agreement with the experimental data in terms of pressure drop and torque coefficients. According to such a conclusion, the detailed flow analysis provided in Sec. 4.3 has been carried out by means of the Reynolds-stress model, maintaining constant turbulence intensity and length scale values equal to 1% and $1/100c$, respectively. In view of the lack of experimental data for such quantities, a sensitivity analysis has been preliminarily carried out ($I=1-5\%$; $L/c=1/100-1/20$), which revealed negligible (less than 1%) variations in terms of global performance and, more importantly, of flow behavior.

4.3 Detailed Analysis of the Flow-Field. The flow structure can be explained in more detail by analyzing the flow-field through the turbine for different flow regimes, before and after the stall condition. In particular, the three flow conditions with $U^\star$ equal to 0.218, 0.238, and 0.257 have been considered. The analysis of the flow structure has been carried out considering its chordwise evolution by means of the vorticity component ω_x perpen-

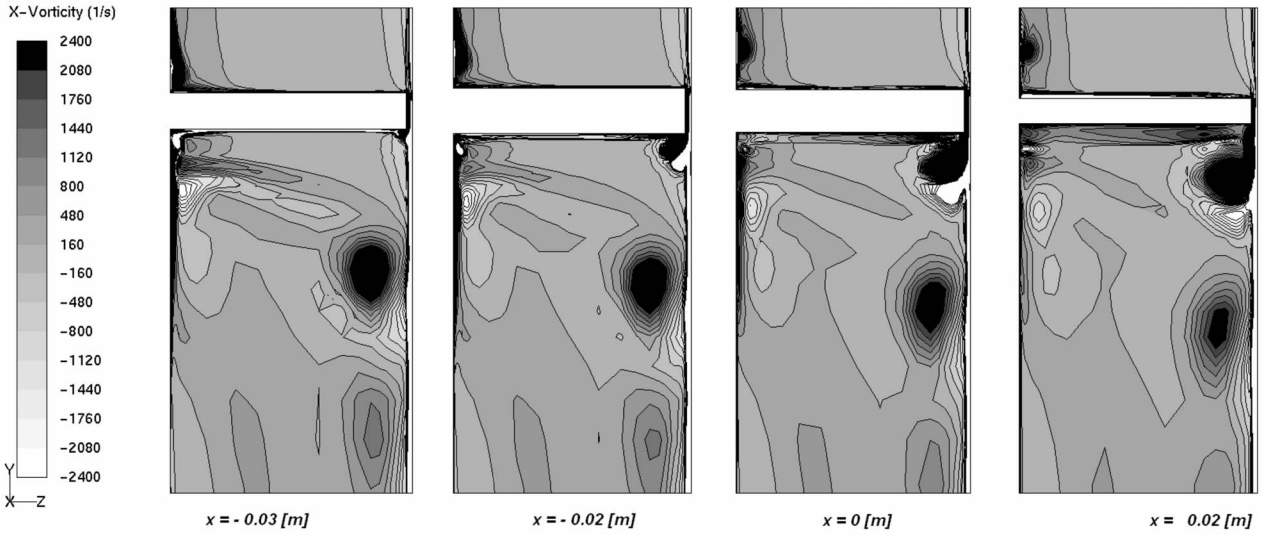

Fig. 22 ω_x contours for $U^\star=0.218$

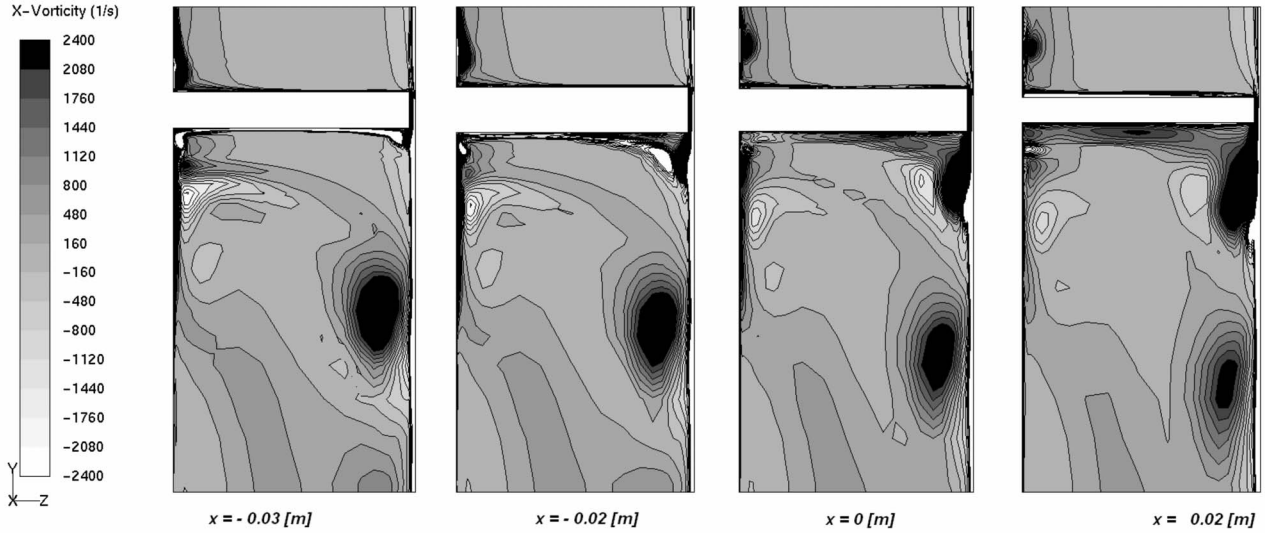

Fig. 23 ω_x **contours for** $U^*=0.238$

dicular to four planes: the midchord one ($x=0$) and three planes parallel to that and located at the following chord positions $x=-0.03$ m (close to the leading-edge, $x_{le}=-0.037$ m), $x=-0.02$ m, and $x=0.02$ m. The corresponding contours are shown in Figs. 22–24.

For $U^*=0.218$ the flow remains attached over almost the whole suction surface of the blade. A way to verify this is to consider the radial vorticity contours in blade-to-blade planes at different radial positions: If no separation occurs, the radial vorticity, coherently with an attached boundary layer growing streamwise, should be positive/negative along the blade suction/pressure side. For example, Fig. 25 provides these contours near the hub ($R=0.11$ m), at midspan, and near the tip ($R=0.15$ m): In all cases the flow is attached on both sides of the blade. The whole picture is shown in Fig. 26 where, for the three U^* values, the regions of negative radial vorticity along the blade suction side are given: For $U^*=0.218$ a marginal separation region is detected at the hub region in the trailing-edge blade portion.

Figure 22 also shows that the blade-tip region is interested by the presence of a tip-leakage flow, which starts already close to the leading-edge and grows moving toward the trailing-edge. This structure is characterized by two contrarotating vortices, the vortex with positive x-vorticity values originating from the tip-blade surface and that with negative values developing along the case surface, both bending toward the blade suction surface, the positive vortex being stronger than the negative one. Therefore, in such conditions, the tip-leakage flow has a beneficial effect (relief-effect) on the turbine performance, since the tip vortex partially counterbalances the tendency to separation at the tip suction side. Moreover, in the near-tip blade-to-blade plane, Fig. 25 shows how the radial vorticity is influenced by the relief-effect: Limiting the growth of negative radial vorticity region up to the wall, the tendency to separation is avoided.

In this condition, away from the hub and tip-blade sections, the ω_x vorticity close to the suction side presents negative values in all planes. This is clearly seen at $x=-0.03$ m and $x=-0.02$ m, but is also true in the remaining two sections, as shown in Fig. 27, where the regions of negative vorticity are thinner.

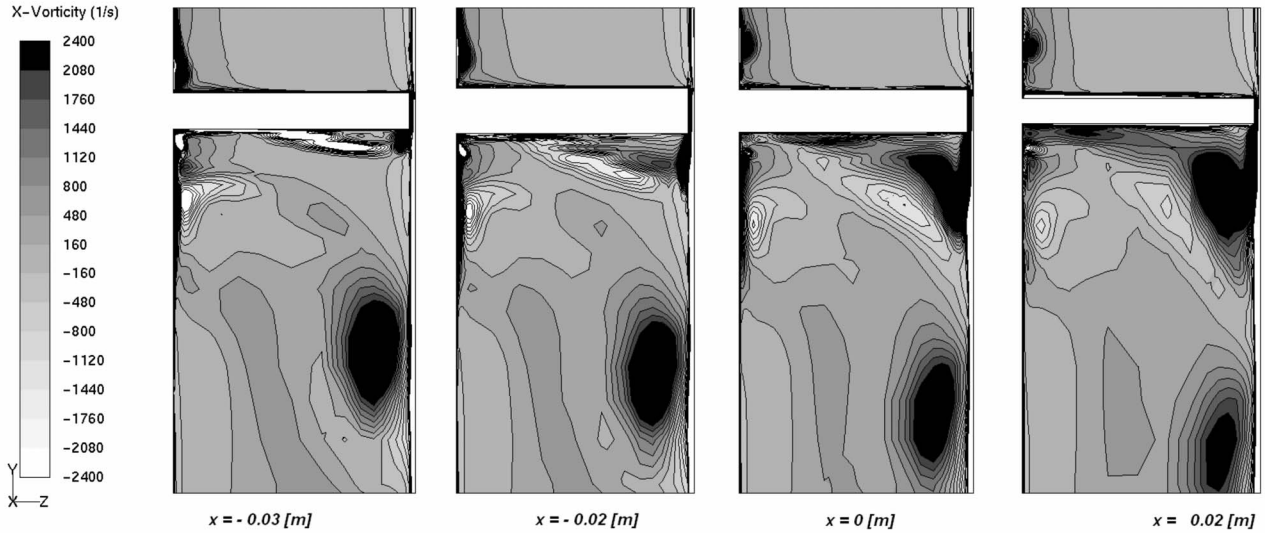

Fig. 24 ω_x **contours for** $U^*=0.257$

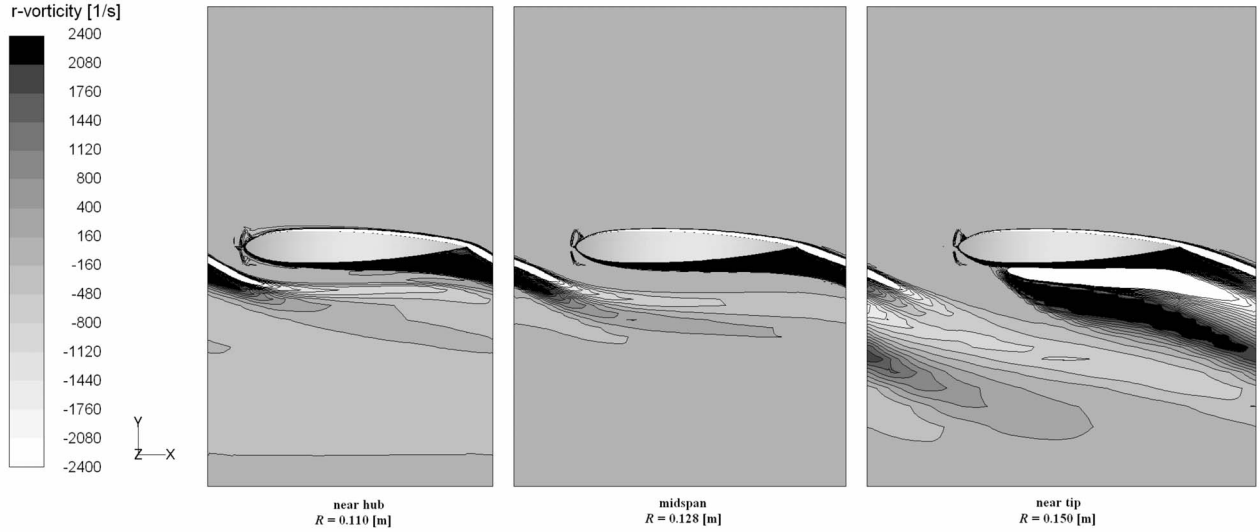

Fig. 25 Radial vorticity contours for $U^{\star}=0.218$

The contours of ω_x for $U^{\star}=0.218$ also show (a) the wakes of the adjacent blades, which are not oriented radially due to the increase in the axial velocity component toward the external radius downstream of the cascade [15]; and (b) the tip-leakage vortex generated from the adjacent blades and transported downstream; notice that the diffusion process associated with the transport leaves the positive vortex within the channel, while the negative one merges with the boundary layer developing on the case.

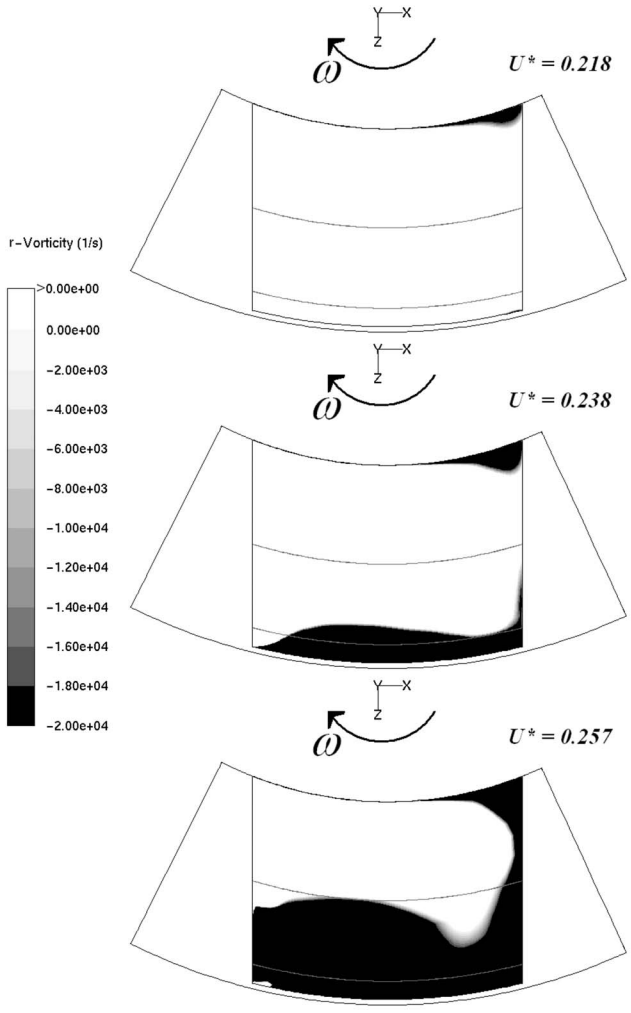

Fig. 26 Radial vorticity contours on the blade suction side

For $U^{\star}=0.238$ the flow is characterized by an incipient stall condition, as properly predicted by the numerical results. Differently from the previously discussed flow behavior, the tip-leakage flow is markedly more intense so that the tip vortex bending, along with the relief-effect, is much weaker. In fact, separation occurs at the suction-side tip, as shown in Figs. 26 and 28, while the flow is attached at midspan.

For $U^{\star}=0.257$ the deep stall condition is reached. Separation takes place already at $x=-0.03$ m at about midspan and extends on the entire chord length; see Figs. 26 and 29.

From the above description, it is evident that in such a turbine the flow begins to separate, and hence the blades begin to stall, from tip to hub region and not vice versa. Indeed, this is a peculiarity of the Wells turbine, as already observed in previous research works [11,15]. In these studies a relevant outward radial flow downstream of the rotor was observed, with a consequent decrease in the actual flow deflection toward the tip region, where the flow is more likely to separate. Such a behavior, effectively explained by means of a potential flow model based on the actuator disk theory, is due to the blade cascade effect, which decreases along with the solidity from hub to tip for Wells turbine with constant chord blades [15,25]. On the other hand, in the limiting case of vanishing solidity, the flow downstream of the rotor approaches the free vortex condition, with constant axial velocity and negligible radial flow, and the flow would more likely separate near the hub region. The blade cascade effect can be observed, at different $U^{\star}$ values, in Figs. 25, 28, and 29: Moving from hub to tip, the cascade pitch increases and the flow coming from the pressure side is less and less effective in counteracting the flow separation on the suction side of the advancing blade. Correspondingly, the pressure loading on the blades experiences a considerable change, as shown in Fig. 30. In agreement with the considerations drawn in Sec. 4.1, the pressure distribution along the blade pressure side barely varies with $U^{\star}$, whereas along the blade suction side major variations are observed resulting in a decrease in the loading with an increase in both $U^{\star}$ and R. Furthermore, the flow separation at the tip is also detectable by the presence of the pressure plateau along the suction side at $U^{\star}$

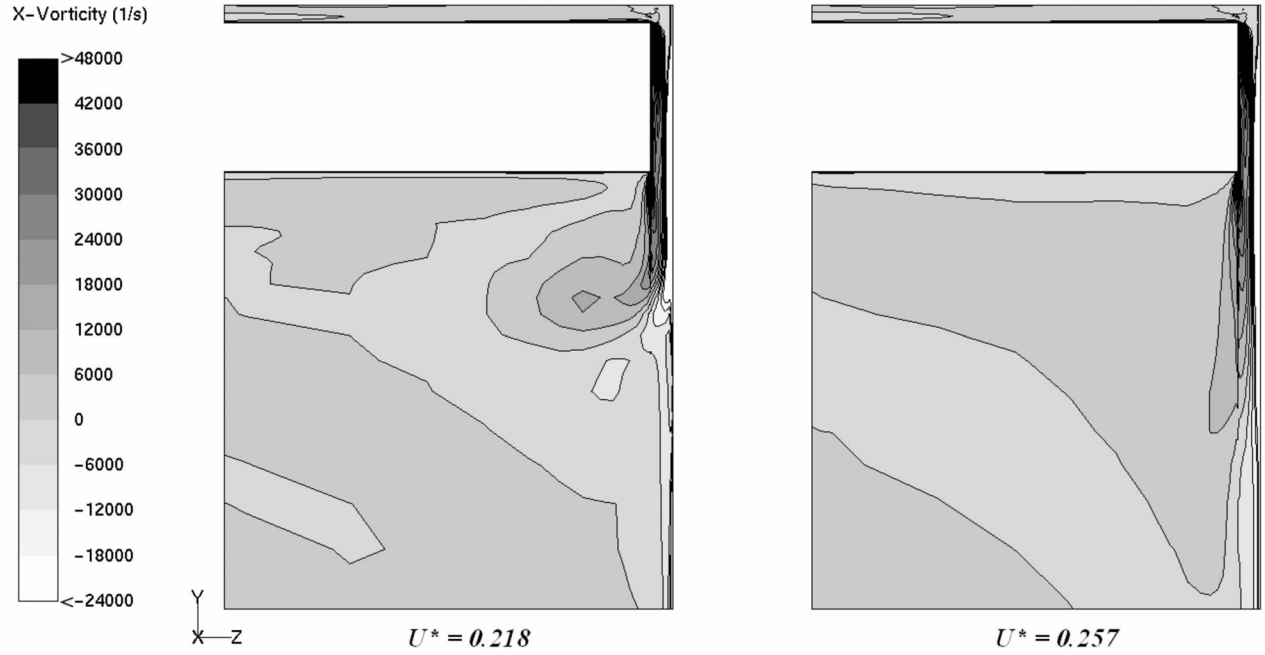

Fig. 27 Particular of the ω_x contours in the midchord plane

=0.238 and, more importantly, at $U^*=0.257$.

Finally, in order to summarize in a unique picture the considerations above, so as to provide a global view of the tip-leakage flow and its interaction with the blade suction side, pathline visualizations are presented. Two of the working conditions discussed above, namely, U^* equal to 0.218 and 0.238, are considered and the corresponding pathlines are provided in Figs. 31 and 32 in tangential and orthographic views, respectively.

5 Conclusions

In this paper the detailed performance analysis of a small prototype of a high solidity Wells turbine has been presented with particular emphasis on the incipient and deep stall conditions. This analysis has been carried out by solving the Reynolds-averaged Navier–Stokes equations together with three turbulence models, namely, the Spalart–Allmaras, the k-ω, and the Reynolds-stress models. A detailed study of the local torque contribution along the blade surface has shown that without separation the torque increases along the blade span, whereas the stall condition is observed to start from the tip section, with an abrupt torque reduction, and to move toward midspan while going in deep stall. The comparison of the numerical results with available experimental data has shown that the Reynolds-stress model appears more reliable in predicting the complex flow through the Wells turbine, for the considered range of operating conditions.

This finding has been corroborated by an anisotropy invariant analysis of the turbulence stress tensor. Thus, using the Reynolds-stress model, a detailed description of the flow-field for different

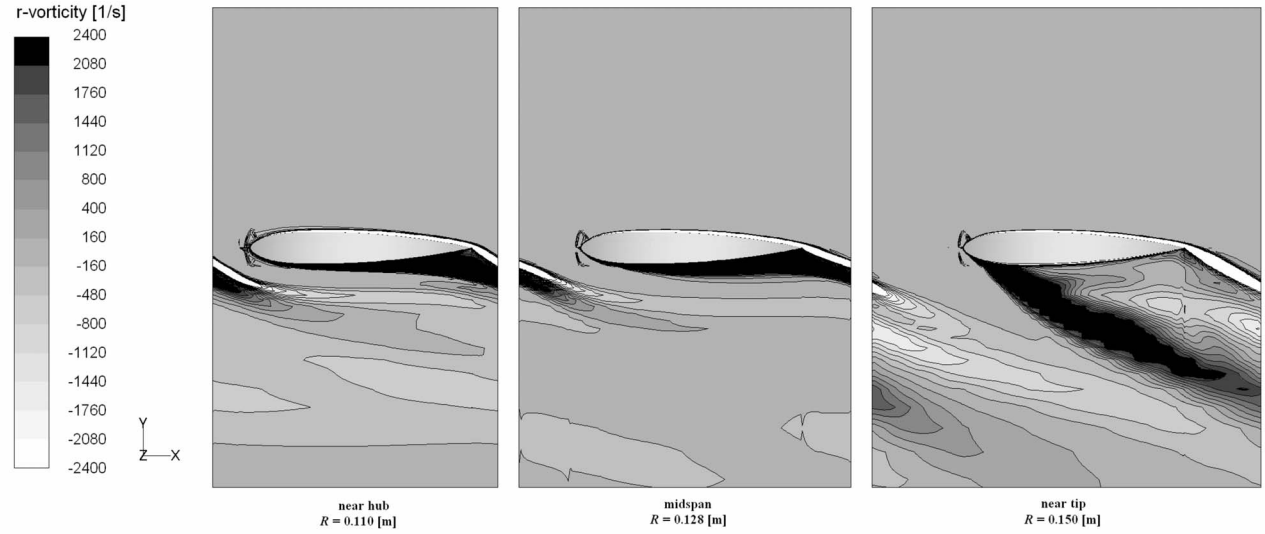

Fig. 28 Radial vorticity contours for $U^*=0.238$

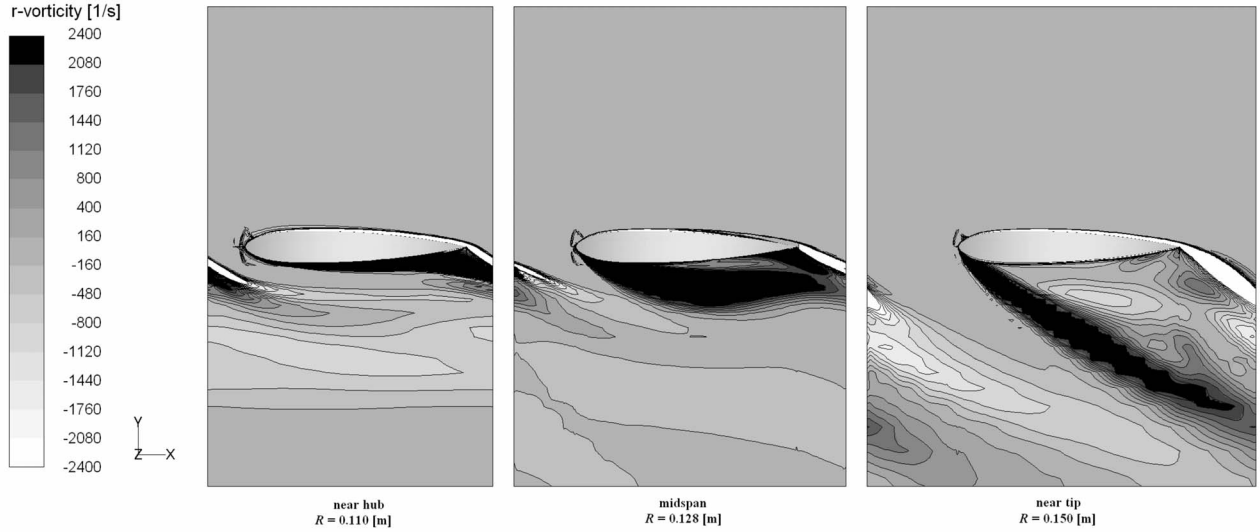

Fig. 29 Radial vorticity contours for $U^*=0.257$

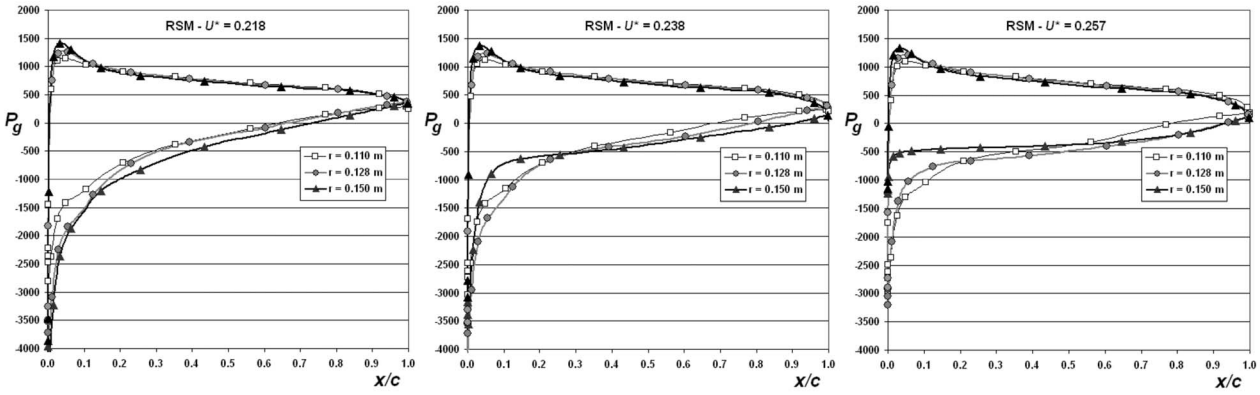

Fig. 30 Gauge pressure (N/m^2) distributions along the chord fraction at different R values obtained using the Reynolds-stress model

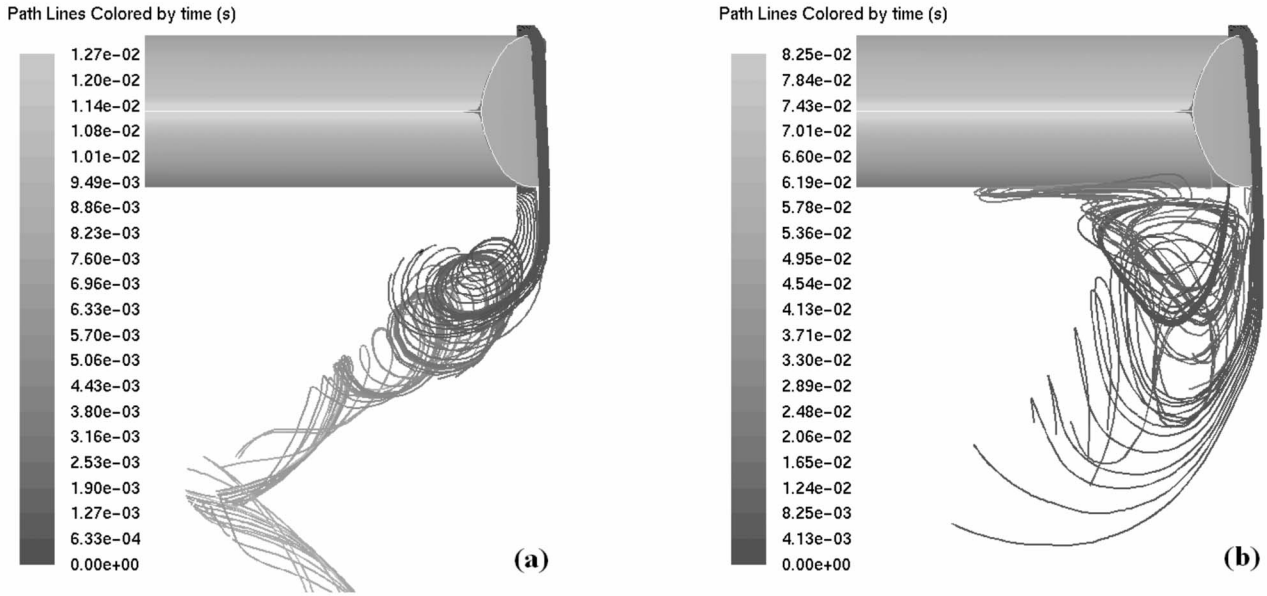

Fig. 31 Tangential view of the pathlines for (*a*) $U^*=0.218$ and (*b*) $U^*=0.238$

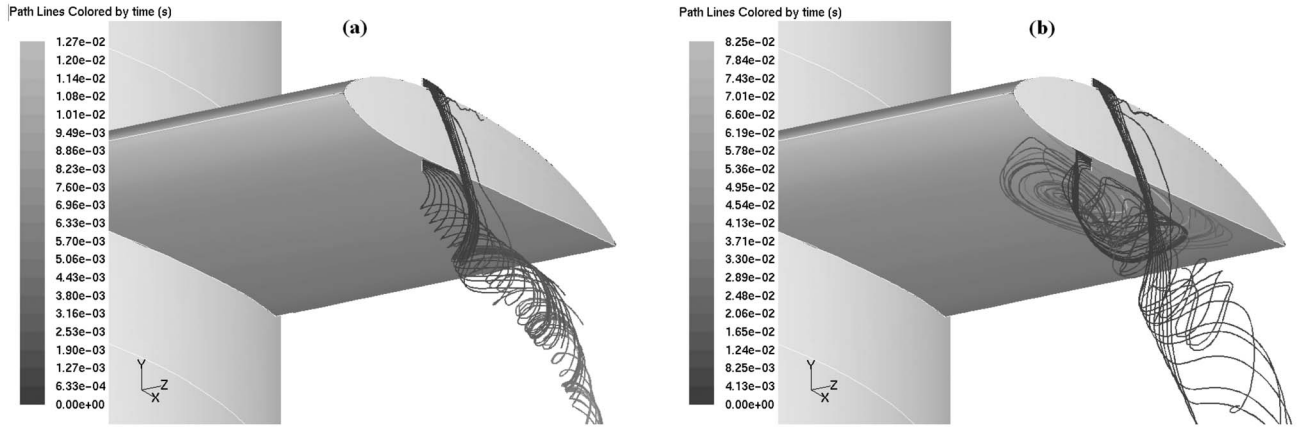

Fig. 32 Orthographic view of the pathlines for (*a*) $U^* = 0.218$ and (*b*) $U^* = 0.238$

values of the flow coefficients has been provided showing the interaction of the tip-leakage flow with the main stream and enlightening its role on the turbine performance.

References

[1] Clément, A., McCullen, P., Falcão, A., Fiorentino, A., Gardner, F., Hammarlund, K., Lemonis, G., Lewis, T., Nielsen, K., Petroncini, S., Pontes, M.-T., Schild, P., Sjöström, B.-O., Sørensen, H. C., and Thorpe, T., 2002, "Wave Energy in Europe: Current Status and Perspectives," Renewable Sustainable Energy Rev., **6**, pp. 405–431.

[2] Masuda, Y., Miyazaki, Y., Yamada, O., and Hiramoto, A., 1981, "Wave Power Generator Assembly," U.S. Patent No. 4405866.

[3] Raghunathan, S., 1995, "The Wells Air Turbine for Wave Energy Conversion," Prog. Aerosp. Sci., **31**, pp. 335–386.

[4] Brito-Melo, A., Gato, L. M. C., and Sarmento, A. J. N. A., 2002, "Analysis of Wells Turbine Design Parameters by Numerical Simulation of the OWC Performance," Ocean Eng., **29**, pp. 1463–1477.

[5] Curran, R., Stewart, T. P., and Whittaker, T. J. T., 1997, "Design Synthesis of Oscillating Water Column Wave Energy Converters: Performance Matching," Proc. Inst. Mech. Eng., Part A, **211**, pp. 489–505.

[6] Thakker, A., Frawley, P., and Bajeet, E. S., 2001, "Experimental Investigation of CA9 Blades on a 0.6 m Wells Turbine Rig," Fourth European Conference on Turbomachinery, Firenze, Italy, Paper No. ATI-CST-062/01.

[7] Cocco, D., Nurzia, F., and Puddu, P., 2001, "Analisi Fluidodinamiche su Turbina Wells: Risultati Sperimentali e Teorici Ottenuti Presso il DIMECA," *III Convegno MiniHydro*, Acquafredda di Maratea (PZ), Italy.

[8] Inoue, M., Kaneko, K., Setoguchi, T., and Raghunathan, S., 1987, "The Fundamental Characteristics and Future of Wells Turbine for Wave Power Generation," Science of Machine, **39**, pp. 275–280.

[9] Raghunathan, S., Tan, C. P., and Wells, N. A. J., 1982, "Theory and Performance of a Wells Turbine," J. Energy, **6**, pp. 157–160.

[10] Gato, L. M. C., and de O. Falcão, A. F., 1984, "On the Theory of the Wells Turbine," Trans. ASME: J. Eng. Gas Turbines Power, **106**, pp. 628–633.

[11] Thakker, A., Frawley, P., and Bajeet, E. S., 2001, "Performance Simulation of CA9 Wells Turbine Rotor Using a 3-D Navier-Stokes Explicit Solver," Fourth European Conference on Turbomachinery, Firenze, Italy, Paper No. ATI-CST-063/01.

[12] Kim, T. H., Setoguchi, T., Kaneko, K., and Raghunathan, S., 2002, "Numerical Investigation on the Effect of Blade Sweep on the Performance of Wells Turbine," Renewable Energy, **25**, pp. 235–248.

[13] Dhanasekaran, T., and Govardhan, M., 2005, "Computational Analysis of Performance and Flow Investigation on Wells Turbine for Wave Energy Conversion," Renewable Energy, **30**, pp. 2129–2147.

[14] Thakker, A., and Dhanasekaran, T. S., 2004, "Computed Effects of Tip Clearance on Performance of Impulse Turbine for Wave Energy Conversion," Renewable Energy, **29**, pp. 529–547.

[15] Torresi, M., Camporeale, S. M., Strippoli, P. D., and Pascazio, G., 2008, "Accurate Numerical Simulation of a High Solidity Wells Turbine," Renewable Energy, **33**, pp. 735–747.

[16] Boccotti, P., 2004, *Gli impianti REWEC*, Editoriale Bios, Cosenza, Italy.

[17] Boccotti, P., 2007, "Caisson Breakwaters Embodying an OWC With a Small Opening–Part I: Theory," Ocean Eng., **34**(5–6), pp. 806–819.

[18] Camporeale, S., Torresi, M., Fortunato, B., and Filianoti, P., 2003, "Design of a Self-Rectifying Hydraulic Turbine for a Sea-Wave Energy Conversion Device," 16th International Conference on Efficiency, Costs, Optimization, Simulation and Environmental Impact of Energy Systems, Copenhagen, Denmark, Jun. 30–Jul. 2.

[19] Boccotti, P., 2007, "Comparison Between a U-OWC and a Conventional OWC," Ocean Eng., **34**(5–6), pp. 799–805.

[20] Torresi, M., Camporeale, S., and Pascazio, G., 2007, "Performance of a Small Prototype of a High Solidity Wells Turbine," Seventh European Conference on Turbomachinery Fluid Dynamics and Thermodynamics, Athens, Greece, Mar. 5–9.

[21] Torresi, M., Camporeale, S., and Pascazio, G., 2007, "Experimental and Numerical Investigation on the Performance of a Wells Turbine Prototype," Seventh European Wave and Tidal Energy Conference, Porto, Portugal, Sept. 11–14.

[22] Filianoti, P., and Camporeale, S., 2007, "A Small Scale Field Experiment on a Wells Turbine Model," Seventh European Wave and Tidal Energy Conference, Porto, Portugal, Sept. 11–14.

[23] Camporeale, S., Torresi, M., Pascazio, G., and Fortunato, B., 2003, "A 3D Unsteady Analysis of a Wells Turbine in a Sea-Wave Energy Conversion Device," ASME TURBO EXPO 2003, Atlanta, GA, Paper No. GT2003-38715.

[24] Torresi, M., Camporeale, S. M., Pascazio, G., and Fortunato, B., 2004, *Fluid Dynamic Analysis of a Low Solidity Wells Turbine*, 59° Congresso ATI, Genova, Italy.

[25] Torresi, M., Camporeale, S. M., and Pascazio, G., 2006, "Studio Teorico Dell'influenza dei Parametri Geometrici Sulle Prestazioni di Turbine Wells," 61° Congresso ATI, Perugia, Italy.

[26] Spalart, P. R., and Allmaras, S. R., 1994, "A One-Equation Turbulence Model for Aerodynamic Flows," Rech. Aerosp., **1**, pp. 5–21.

[27] Menter, F. R., 1994, "Two-Equation Eddy-Viscosity Turbulence Models for Engineering Applications," AIAA J., **32**, pp. 1598–1605.

[28] Wilcox, D. C., 1998, *Turbulence Models for CFD*, DCW Industries, Inc., La Canada, CA.

[29] Launder, B. E., 1989, "Second-Moment Closure and Its Use in Modeling Turbulent Industrial Flows," Int. J. Numer. Methods Fluids, **9**, pp. 963–985.

[30] Launder, B. E., 1989, "Second-Moment Closure: Present… and Future?," Int. J. Heat Fluid Flow, **10**, pp. 282–300.

[31] Wells, A. A., 1976, "Fluid Driven Rotary Transducer," Br. Patent No. 1595700.

[32] Henriques, J. C. C., and Gato, L. M. C., 2002, "Use of a Residual Distribution Euler Solver to Study the Occurrence of Transonic Flow in Wells Turbine Rotor Blades," Comput. Mech., **29**, pp. 243–253.

[33] Horlock, J. H., 1978, *Actuator Disk Theory*, McGraw-Hill, London.

[34] Curran, R., and Gato, L. M. C., 1997, "The Energy Conversion Performance of Several Types of Wells Turbine Designs," Proc. Inst. Mech. Eng., Part A, **211**, pp. 133–145.

[35] Lumley, J. L., 1979, "Computational Modeling of Turbulent Flows," Adv. Appl. Mech., **18**, pp. 123–176.

[36] Escudié, R., and Liné, A., 2006, "Analysis of Turbulence Anisotropy in a Mixing Tank," Chem. Eng. Sci., **61**, pp. 2771–2779.

[37] Im, Y. H., Huh, H. Y., and Kim, K.-Y., 2002, "Analysis of Impinging and Countercurrent Stagnating Flows by Reynolds Stress Model," ASME Trans. J. Fluids Eng., **124**, pp. 706–718.

[38] Krogstad, P.-Å., and Torbergsen, L. E., 2000, "Invariant Analysis of Turbulent Pipe Flow," Flow, Turbul. Combust., **64**, pp. 161–181.

Assessment of Large-Eddy Simulation of Internal Separated Flow

Marco Hahn[1]
e-mail: m.hahn@cranfield.ac.uk

Dimitris Drikakis

Department of Aerospace Sciences,
Fluid Mechanics and Computational Science Group,
Cranfield University,
Bedfordshire MK43 0AL, UK

This paper presents a systematic numerical investigation of different implicit large-eddy simulations (LESs) for massively separated flows. Three numerical schemes, a third-order accurate monotonic upwind scheme for scalar conservation laws (MUSCL) scheme, a fifth-order accurate MUSCL scheme, and a ninth-order accurate weighted essentially non-oscillatory (WENO) method, are tested in the context of separation from a gently curved surface. The case considered here is a simple wall-bounded flow that consists of a channel with a hill-type curvature on the lower wall. The separation and reattachment locations, velocity, and Reynolds stress profiles are presented and compared against solutions from classical LES simulations.
[DOI: 10.1115/1.3130243]

1 Introduction

Many flows of practical importance are governed by viscous near-wall phenomena that have a major influence on the flow properties. Among those, unsteady flow separation currently poses one of the greatest challenges for numerical simulations. It appears in a wide range of applications pertinent not only to external flows but also to internal flows, such as flows around turbomachinery blades, in divergent channels and nozzles.

The flow over curved surfaces has to overcome an adverse pressure gradient as it travels along the surface. Consequently, kinetic energy is transformed into internal energy. In addition to this retarding force, the viscous shear continuously slows the fluid down as it progresses along the surface until, ultimately, the slope of the velocity profile becomes zero. Under the perpetual influence of the adverse pressure gradient the flow begins to reverse its direction and separates from the surface. These phenomena are inherently unstable; thus a well-defined point of separation cannot be accounted for. It rather results in a separation area with a downstream recirculation zone. The unsteady free shear-layer between the main-stream and the separated boundary layer rolls up into Kelvin–Helmholtz-type vortices that transfer momentum between the free-flow and the recirculation zone. The instability of this unsteady system manifests itself in the breakdown of the Kelvin–Helmholtz structures. Thus, for massively separated flow, a highly turbulent wake region dominated by the small-scale dynamics of the secondary vortices develops.

To date, no theoretical models have been developed that can deal with the complexity of this type of flow. The boundary-layer equations, a simplification of the Navier–Stokes equations, are only valid up to the point of separation. Downstream of this point, however, the separation zone thickens quickly and the approximations made in the boundary-layer equations are no longer valid. And even if they could be applied, the turbulent fluctuations render the solutions impossible to obtain without resorting to further approximations.

Implicit large-eddy simulations (ILESs) are currently used to simulate a broad variety of complex flows, e.g., flows that are dominated by vorticity leading to turbulence, flows featuring shock waves and turbulence, and the mixing of materials. However, most classical test cases for these methods belong to the group of wall-free flows, e.g., decaying isotropic turbulence [1], free jets [2,3], or Rayleigh–Taylor instabilities [4], and more insight into the ability to reproduce near-wall effects with ILES is clearly needed. A small number of investigations focusing on wall-bounded problems pertinent to practical engineering flows have emerged only more recently. Here, such problems as open cavities [5], plane channels [6], backward facing steps [7], or submarine hydrodynamics [8] have been successfully simulated.

The test case considered here consists of a channel with hill-type constrictions and periodic boundary conditions in streamwise and cross-stream directions. The simplicity of the geometry and the boundary conditions makes it an ideal testbed that has attracted a great deal of interest and produced data from classical LES [9–11], where the present simulations can be compared against.

2 Numerical Framework

2.1 Governing Equations. The physics of (Newtonian) fluid flow is governed by the Navier–Stokes equations. They are solved by considering the coupled generalized conservation laws

$$\frac{\partial \rho}{\partial t} + \nabla \cdot (\rho \mathbf{u}) = 0 \tag{1}$$

$$\frac{\partial \rho \mathbf{u}}{\partial t} + \nabla \cdot (\rho \mathbf{u}\mathbf{u}) = -\nabla \cdot \mathbf{P} + f \cdot \hat{\mathbf{x}} \tag{2}$$

$$\frac{\partial e}{\partial t} + \nabla \cdot (e\mathbf{u}) = -\nabla \cdot (\mathbf{P} \cdot \mathbf{u}) - \nabla \cdot \mathbf{q} + f \cdot \mathbf{u} \cdot \hat{\mathbf{x}} \tag{3}$$

where $\mathbf{u}$, ρ, e, and $\mathbf{q}$ stand for the velocity components, density, total energy per unit volume, and heat flux, respectively, and $\hat{\mathbf{x}}$ is the unit basis vector in x-direction. The standard form of the Navier–Stokes equations is extended by an external forcing term f similar to the one proposed by Lenormand et al. [12]. This modification is necessary because pressure-driven channel flow violates the boundary conditions for the test case considered here, namely, the periodicity in the x-direction. In the absence of a pressure drop, the forcing term acts as a driver for the flow and ensures a constant mass flow rate.

The tensor $\mathbf{P}$ for a Newtonian fluid is defined by

[1]Corresponding author.

Contributed by the Fluids Engineering Division of ASME for publication in the JOURNAL OF FLUIDS ENGINEERING. Manuscript received March 31, 2008; final manuscript received April 14, 2009; published online June 1, 2009. Assoc. Editor: Ugo Piomelli. Paper presented at the 46th AIAA Aerospace Sciences Meeting and Exhibit, 2008.

$$\mathbf{P} = p(\rho,T)\mathbf{I} + \tfrac{2}{3}\mu(\nabla\cdot\mathbf{u})\mathbf{I} - \mu[(\nabla\mathbf{u}) + (\nabla\mathbf{u})^T] \tag{4}$$

where $p(\rho,T)$ is the scalar pressure, $\mathbf{I}$ is the identity tensor, T is the temperature, and μ is the dynamic viscosity coefficient. The above system is completed by an equation of state. For a perfect gas the equation of state is given by $p=\rho RT$, where R is the gas constant.

In order to facilitate the development of numerical methods Eqs. (1)–(3) are written in a Cartesian matrix form [13] as

$$\frac{\partial\mathbf{U}}{\partial t} + \frac{\partial\mathbf{E}}{\partial x} + \frac{\partial\mathbf{F}}{\partial y} + \frac{\partial\mathbf{G}}{\partial z} = \frac{\partial\mathbf{R}}{\partial x} + \frac{\partial\mathbf{S}}{\partial y} + \frac{\partial\mathbf{L}}{\partial z} + \mathcal{F} \tag{5}$$

where $\mathbf{U}$ is the array of the conservative variables; $\mathbf{E}$, $\mathbf{F}$, and $\mathbf{G}$ are the inviscid and $\mathbf{R}$, $\mathbf{S}$, and $\mathbf{L}$ are the viscous flux vectors associated with the Cartesian x,y,z-direction, respectively, and $\mathcal{F}$ represents the external forcing

$$\mathbf{U} = [\rho,\rho u,\rho v,\rho w,e]^T \tag{6}$$

$$\mathbf{E} = [\rho u,\rho u^2 + p,\rho vu,\rho wu,(e+p)u]^T \tag{7}$$

$$\mathbf{F} = [\rho v,\rho uv,\rho v^2 + p,\rho wv,(e+p)v]^T \tag{8}$$

$$\mathbf{G} = [\rho w,\rho uw,\rho vw,\rho w^2 + p,(e+p)w]^T \tag{9}$$

$$\mathbf{R} = [0,\tau_{xx},\tau_{xy},\tau_{xz},u\tau_{xx} + v\tau_{xy} + w\tau_{xz} - \dot{q}_x]^T \tag{10}$$

$$\mathbf{S} = [0,\tau_{yx},\tau_{yy},\tau_{yz},u\tau_{yx} + v\tau_{yy} + w\tau_{yz} - \dot{q}_y]^T \tag{11}$$

$$\mathbf{L} = [0,\tau_{zx},\tau_{zy},\tau_{zz},u\tau_{zx} + v\tau_{zy} + w\tau_{zz} - \dot{q}_z]^T \tag{12}$$

$$\mathcal{F} = [0,f,0,0,fu]^T \tag{13}$$

For geometries featuring curvature, Eq. (5) has to be transformed to a generalized curvilinear coordinate given by $\xi = \xi(x,y,z,t)$, $\eta = \eta(x,y,z,t)$, $\zeta = \zeta(x,y,z,t)$, $\tau = t$. The resulting system of equations is solved in a split 1D fashion by employing a Godunov-type high-resolution method [14–16] for the advective flux derivatives (see Secs. 2.2 and 2.3), and central differences for discretizing the viscous terms [13]. In a finite volume framework, a central difference scheme for approximating the Cartesian velocity derivatives that appear in the diffusive fluxes across a cell face defined by the subscript $(i-1/2,j,k)$ can, for example, be written as

$$\left.\frac{\partial u}{\partial x}\right|_{i-1/2,j,k} = \frac{u_{i,j,k} - u_{i-1,j,k}}{\Delta x} \tag{14}$$

$$\left.\frac{\partial u}{\partial y}\right|_{i-1/2,j,k} = \frac{0.5(u_{i,j+1,k} + u_{i-1,j+1,k} - u_{i,j-1,k} - u_{i-1,j-1,k})}{2\Delta y} \tag{15}$$

$$\left.\frac{\partial u}{\partial z}\right|_{i-1/2,j,k} = \frac{0.5(u_{i,j,k+1} + u_{i-1,j,k+1} - u_{i,j,k-1} - u_{i-1,j,k-1})}{2\Delta z} \tag{16}$$

The remaining components can be calculated accordingly.

2.2 Characteristics-Based Scheme. For the sake of simplicity, only the Cartesian flux derivative $\partial\mathbf{E}/\partial x$ is considered here. The discretization at the center of the control volume (i) using the values of the intercell fluxes yields

$$\frac{\partial\mathbf{E}}{\partial x} = \frac{\mathbf{E}_{i+1/2} - \mathbf{E}_{i-1/2}}{\Delta x} \tag{17}$$

The intercell flux functions $\mathbf{E}_{i+1/2}$ and $\mathbf{E}_{i-1/2}$ are calculated according to a characteristics-based (CB) scheme [14–16], which satisfies the following criteria for high-resolution methods [17].

- Provide at least second order of accuracy in smooth areas of the flow.
- Produce numerical solutions (relatively) free from spurious oscillations.
- In the case of discontinuities, the number of grid points in the transition zone containing the shock wave is smaller in comparison with that of first-order monotone methods.

The CB scheme is a Godunov-type method that defines the conservative variables along the characteristics as functions of their characteristic values. Various reconstruction methods presented in Sec. 2.3 have been used in this investigation to compute the characteristic values from the left or right states, $\overline{\mathbf{U}}_{L/R,i-1/2}$, depending on the sign of the characteristic speed (eigenvalues).

Along each characteristic (denoted by $l=0,1,2$), the variables $\mathbf{U}_l$ are given by

$$\mathbf{U}_{l,i-1/2} = (0.5 + \phi_l)\overline{\mathbf{U}}_{L,i-1/2} + (0.5 - \phi_l)\overline{\mathbf{U}}_{R,i-1/2} \tag{18}$$

where the function ϕ_l is defined as

$$\phi_l = 0.5\frac{\lambda_{L,l} + \lambda_{R,l}}{|\lambda_{L,l}| + |\lambda_{R,l}| + \epsilon} \tag{19}$$

The parameter ϵ averts division by zero and $\lambda_{L,l}$ and $\lambda_{R,l}$ are the left and right eigenvalues at the cell face, respectively. Using the Godunov-type up-winding scheme from Eq. (18) three sets of characteristic variables are calculated

$$\mathbf{U}_{0,i-1/2} = \begin{pmatrix} \rho_0 \\ (\rho u)_0 \\ (\rho v)_0 \\ (\rho w)_0 \\ e_0 \end{pmatrix}, \quad \mathbf{U}_{1,i-1/2} = \begin{pmatrix} \rho_1 \\ (\rho u)_1 \\ (\rho v)_1 \\ (\rho w)_1 \\ e_1 \end{pmatrix}, \quad \mathbf{U}_{2,i-1/2} = \begin{pmatrix} \rho_2 \\ (\rho u)_2 \\ (\rho v)_2 \\ (\rho w)_2 \\ e_2 \end{pmatrix} \tag{20}$$

With the characteristic variables $\mathbf{U}_{l,i-1/2}$ being known, the characteristics-based variables $\hat{\mathbf{U}}_{i-1/2}$ are computed according to

$$\hat{\mathbf{U}}_{i-1/2} = \begin{pmatrix} \hat{\rho} \\ \widehat{(\rho u)} \\ \widehat{(\rho v)} \\ \widehat{(\rho w)} \\ \hat{e} \end{pmatrix} = \begin{pmatrix} \rho_0 + r_1 + r_2 \\ (\rho u)_0 + (u+s)r_1 + (u-s)r_2 \\ (\rho v)_0 + vr_1 + vr_2 \\ (\rho w)_0 + wr_1 + wr_2 \\ e_0 + (H + s\lambda_0)r_1 + (H - s\lambda_0)r_2 \end{pmatrix} \tag{21}$$

with

$$r_1 = \frac{1}{2s^2}\left[(\rho_0 - \rho_1)\left(s\lambda_0 - \frac{\gamma-1}{2}q^2\right) + ((\rho u)_0 - (\rho u)_1)((\gamma-1)u - s) + ((\rho v)_0 - (\rho v)_1)(\gamma-1)v + ((\rho w)_0 - (\rho w)_1)(\gamma-1)w - (e_0 - e_1)(\gamma-1)\right] \tag{22}$$

$$r_2 = \frac{1}{2s^2}\left[-(\rho_0 - \rho_2)\left(s\lambda_0 + \frac{\gamma-1}{2}q^2\right) + ((\rho u)_0 - (\rho u)_2)((\gamma-1)u + s) + ((\rho v)_0 - (\rho v)_2)(\gamma-1)v + ((\rho w)_0 - (\rho w)_2)(\gamma-1)w - (e_0 - e_2)(\gamma-1)\right] \quad (23)$$

and H being the total enthalpy given by

$$H = \frac{s^2}{\gamma-1} + 0.5q^2 \quad (24)$$

The velocities u, v, and w and the speed of sound s are the average values of their left and right states and $q^2=u^2+v^2+w^2$. Finally, the advective flux $\mathbf{E}_{i-1/2}$ for the CB scheme is calculated using the variables $\hat{\mathbf{U}}_{i-1/2}$, i.e.,

$$\mathbf{E}^{\mathrm{CB}}_{i-1/2} = \mathbf{E}(\hat{\mathbf{U}}_{i-1/2}) \quad (25)$$

2.3 Reconstruction Methods. High-resolution is typically accomplished by extrapolation of variables using linear or quadratic functions in a cell as opposed to the piecewise constant approach used in conjunction with first-order algorithms. Three reconstruction methods of different accuracies are investigated here: a third-order monotonic upwind scheme for scalar conservation laws (MUSCL) scheme, a fifth-order MUSCL scheme, and a ninth-order WENO method.

2.3.1 MUSCL Schemes. For a MUSCL scheme [18], the left and right states of the conservative variables at the cell faces are computed as

$$\mathbf{U}^L_{i+1/2} = \mathbf{U}_i + \frac{1}{4}\left[(1-k)\phi(r^L)(\mathbf{U}_i - \mathbf{U}_{i-1}) + (1+k)\phi\left(\frac{1}{r^L}\right)(\mathbf{U}_{i+1} - \mathbf{U}_i)\right] \quad (26)$$

$$\mathbf{U}^R_{i+1/2} = \mathbf{U}_{i+1} - \frac{1}{4}\left[(1-k)\phi(r^R)(\mathbf{U}_{i+2} - \mathbf{U}_{i+1}) + (1+k)\phi\left(\frac{1}{r^R}\right)(\mathbf{U}_{i+1} - \mathbf{U}_i)\right] \quad (27)$$

where $\mathbf{U}$ is the vector of cell averaged conserved variables, k is a free parameter, which is set to 1/3 for the third-order limiter, and the cells are labeled by the integer i. Additionally,

$$r^L_i = \frac{\mathbf{U}_{i+1} - \mathbf{U}_i}{\mathbf{U}_i - \mathbf{U}_{i-1}} \quad (28)$$

$$r^R_i = \frac{\mathbf{U}_{i+1} - \mathbf{U}_i}{\mathbf{U}_{i+2} - \mathbf{U}_{i+1}} \quad (29)$$

In this study, the following third-order MUSCL-type limiter [19] is considered:

$$\phi_{M3} = 1 - \left(1 + \frac{2Nr}{1+r^2}\right)\left(1 - \frac{2r}{1+r^2}\right)^N \quad (30)$$

$M3$ is constrained in the normal fashion to first-order accuracy at local maxima and minima and also includes a "steepening" parameter N to improve the resolution of discontinuities; in this paper, $N=2$.

The fifth-order MUSCL scheme [20] employed here is slightly more complex,

$$\phi^*_{M5,L} = \frac{-2/r^L_{i-1} + 11 + 24r^L_i - 3r^L_i r^L_{i+1}}{30} \quad (31)$$

$$\phi^*_{M5,R} = \frac{-2/r^R_{i+2} + 11 + 24r^R_{i+1} - 3r^R_{i+1} r^R_i}{30} \quad (32)$$

where monotonicity is maintained by limiting the above extrapolations using

$$\phi_{M5,L} = \max(0, \min(2, 2r^L_i, \phi^*_{M5,L})) \quad (33)$$

$$\phi_{M5,R} = \max(0, \min(2, 2r^R_i, \phi^*_{M5,R})) \quad (34)$$

2.3.2 WENO Scheme. WENO [21–24] is an extension of the original ENO concept first proposed by Harten et al. [25]. It is, in fact, an arguably simpler, more efficient, robust, and accurate approach. For a given order of accuracy the requisite polynomial is interpolated over each support stencil that includes the interface in question. The smoothness of these candidate polynomials is then assessed in such a way that a weighted convex combination of all the resulting interface values can be obtained with minimal spurious oscillations. In effect, stencils that cross a discontinuity will be assigned a near zero weight in comparison with those that do not. By including all the stencils, the order of accuracy of the reconstruction in smooth regions of the flow increases to $2r-1$ for polynomial reconstructions of rth order accuracy.

The WENO method considered in this paper is ninth-order accurate. For the sake of simplicity, however, a third-order WENO reconstruction derived from a linear interpolation with $r=2$ is presented here. For the left-hand interface value $\mathbf{U}_{i+1/2,L}$, there are two stencils (x_{i-1}, x_i) and (x_i, x_{i+1}). For each stencil, the interpolation polynomial is given by

$$P^-(x) = \mathbf{U}_i + \frac{\mathbf{U}_i - \mathbf{U}_{i-1}}{\Delta x}(x - x_i) \quad (35)$$

$$P^+(x) = \mathbf{U}_i + \frac{\mathbf{U}_{i+1} - \mathbf{U}_i}{\Delta x}(x - x_i) \quad (36)$$

The convex combination is then

$$\mathbf{U}_{i+1/2} = \frac{a_0}{a_0 + a_1}P^-(x_{i+1/2}) + \frac{a_1}{a_0 + a_1}P^+(x_{i+1/2}) \quad (37)$$

with

$$a_0 = \frac{C_0}{(\epsilon + (\mathrm{IS})^-)^2}, \quad a_1 = \frac{C_1}{(\epsilon + (\mathrm{IS})^+)^2} \quad (38)$$

and the coefficients C are determined for optimal weighting. The smoothness indicators (IS) are defined through $(\mathrm{IS})^- = (\mathbf{U}_i - \mathbf{U}_{i-1})^2$ and $(\mathrm{IS})^+ = (\mathbf{U}_{i+1} - \mathbf{U}_i)^2$. Finally, ϵ is a small number used to prevent divisions by zero in a perfectly smooth flow. The equations for higher-order methods are naturally more complex but the principle does not change [21].

2.4 Time Integration. For integrating the system of governing equations in time an explicit Runge–Kutta time-stepping method was chosen. In separated flows, high levels of turbulence are usually encountered. Thus, explicit time marching is preferred to an implicit treatment because of the need to temporally resolve the rapidly fluctuating components.

The Runge–Kutta method employed here is second-order accurate in time and consists of the following stages:

$$\frac{\mathbf{U}^1 - \mathbf{U}^n}{h} = \frac{1}{2}f(\mathbf{U}^n)$$

$$\frac{\mathbf{U}^2 - \mathbf{U}^1}{h} = \frac{1}{2}f(\mathbf{U}^1)$$

$$\frac{\mathbf{U}^{n+1} - \frac{2}{3}\mathbf{U}^2 - \frac{1}{3}\mathbf{U}^n}{h} = \frac{1}{3}f(\mathbf{U}^2) \tag{39}$$

where $h=\Delta t$ is the size and n is the number of the time step, respectively. Additionally, this method belongs to the group of strong stability preserving schemes [13] and features numerical stability for Courant–Friedrichs–Lewy (CFL) numbers of up to 2. This property significantly contributes to a reduction in the relatively high computational costs associated with time-dependent flow simulations.

3 Analysis of the Numerical Methods

The implicit approach to subgrid-scale (SGS) modeling in LES is motivated by the fact that computational solvers are always affected by both physical as well as numerical limitations and they should not be regarded separately. It is deemed more appropriate to consider the combined effects instead.

With no explicit filtering, the average originating from the finite volume formulation adopted here can be seen as a form of implicit spatial filtering. The discretization of the governing equations then leads to an additional truncation error term, which depends on the discretization scheme and the solution procedure. This numerical error term conveniently appears in the same divergence form as the subgrid-scale stress tensor [26]—hence it is assumed to have a similar effect on the solution.

High-resolution methods had originally been introduced with the intention to solve the advective part of the equations as accurately as possible. However, it was found that they not only provide a superior accuracy to classical linear methods, but they are also equipped with a built-in subgrid-scale model. In order to investigate this approach to SGS modeling analytically, the methodology of modified equation analysis (MEA) [27] can be employed to determine the leading order truncation errors arising from the combination of control volume differencing and inherently nonlinear high-resolution approximations.

For the MEA, the discrete, one-dimensional equation of the form

$$\mathbf{U}_i^{n+1} = \mathbf{U}_i^n - \frac{\Delta t}{\Delta x}[\mathbf{E}_{i+1/2} - \mathbf{E}_{i-1/2}] \tag{40}$$

where $\mathbf{U}$ and $\mathbf{E}$ are the array of dependent variables and the inviscid flux vector, respectively, can be considered [13]. The superscript n marks the time level, whereas the subscript i denotes the position in space. After the high-resolution reconstruction step, the fluxes are determined from the left and right data states by a linearized Godunov-type method according to

$$\mathbf{E}_{i+1/2} = \frac{1}{2}[\mathbf{E}_{i+1/2,R} + \mathbf{E}_{i+1/2,L}] - \frac{|\mathbf{E}'|}{2}[\mathbf{U}_{i+1/2,R} - \mathbf{U}_{i+1/2,L}] \tag{41}$$

with $\mathbf{E}'$ being the flux Jacobian $\partial\mathbf{E}/\partial\mathbf{U}$. For this general form of the modified equation, the finite volume discretization itself naturally produces a truncation term that is analogous to the effect of a scale-similarity subgrid model in conventional LES. This term, which generally enters the equation at second order, is deemed necessary for a successful ILES approach [26].

Additional error terms originate from the details of the reconstruction methods. The physical concept behind this step is the need for entropy production in under-resolved situations, i.e., near high gradients, in order to eliminate or control spurious oscillations in the solution. Effectively, the reconstruction can be seen as a sophisticated trigger for an "artificial viscosity" inherent to the nonlinear method where the character of the numerical scheme is closely related to the form of the truncation term.

In order to determine the leading order truncation term introduced by the reconstruction methods, the discrete solution incorporating the high-resolution schemes presented in Sec. 2.3 is subtracted from the exact solution [28], yielding

$$\epsilon_{M3} = -\frac{\Delta x^3}{12} s u^{(1)} u^{(3)} + \text{H.O.T} \tag{42}$$

$$\epsilon_{M5} = \frac{\Delta x^5}{60} s u^{(1)} u^{(5)} + \text{H.O.T} \tag{43}$$

$$\epsilon_{W9} = \frac{\Delta x^9}{1260} s u^{(1)} u^{(9)} + \text{H.O.T} \tag{44}$$

Here, H.O.T stands for the higher order terms, s is the speed of sound, the superscript (n) indicates the nth derivative with respect to the x-direction, the subscripts $M3$, $M5$, and $W9$ refer to the third-order MUSCL, the fifth-order MUSCL, and the ninth-order WENO scheme, respectively. It should be noted that only the optimal weights have been considered in the evaluation of ϵ_{W9}. However, based on the findings from a similar analysis for a fifth-order WENO method [29], it is assumed that including the nonlinear weights would not change the result.

All terms presented in Eqs. (42)–(44) characterize the dissipation inherent to the reconstruction methods arising from the second term of the right-hand side (RHS) of Eq. (41). The truncation terms stemming from the centered term on the RHS, on the other hand, are often referred to as the "self-similar" terms [30] and they do not appear at leading order for the schemes investigated here. This is not always the case as has been shown for a MUSCL reconstruction employing van Leer's limiter [28].

Surprisingly, the leading order truncation error for the third-order MUSCL scheme is negative, which suggests slightly antidiffusive behavior in smooth flow regions. As the accuracy is reduced to first order near extrema, however, the character of the scheme is diffusive in other areas. A previous study of the Taylor–Green vortex flow [31] has been conducted in order to quantify the effective numerical dissipation associated with the reconstruction methods employed in this investigation. It has been demonstrated that the numerical viscosity induced by the third-order MUSCL scheme is equivalent to the numerical viscosity produced by the ninth-order WENO method on a mesh with twice the grid spacing in each spatial dimension. The fifth-order MUSCL scheme lies in between the two.

4 The Geometry

The numerical investigation of high-resolution methods for large-eddy simulation has been carried out using three different computational grids. The computational domain representing the constricted channel extents $9h$ and $4.5h$, and between $2h$ and $3.035h$ in x-, y-, and z-direction, also referred to as streamwise, cross-stream, and vertical directions, respectively. Here, h is the height of the hill-type shape at the lower wall. A H-H-type topology was chosen (Fig. 1(*a*)) and no-slip boundary conditions are applied at the top and bottom walls of the channel, while periodicity was assumed in the streamwise and cross-stream directions.

Three different grid resolutions have been investigated here: (i) a highly under-resolved grid, referred to as "coarse," comprising approximately 0.65×10^6 relative uniformly distributed points; (ii) a modified version of the coarse grid with an identical number of points, referred to as "modified," featuring a finer clustering near the top and bottom walls of the channel; and (iii) a moderately finer grid consisting of 1.03×10^6 points, referred to as "medium," where the refinement mainly affects the distribution around the hill crest and a slightly better resolution near the bottom wall is achieved; see Figs. 1(*b*)–1(*d*). The coarse and medium grids are basically identical to the ones used in previous wall-modeled LES [9]. The characteristic parameters for all three grids, including z^+ values at the bottom wall, which are not sensitive to the choice of numerical discretization method, are given in Table 1. Additionally, the same parameters for a highly resolved reference simulation [10] are included.

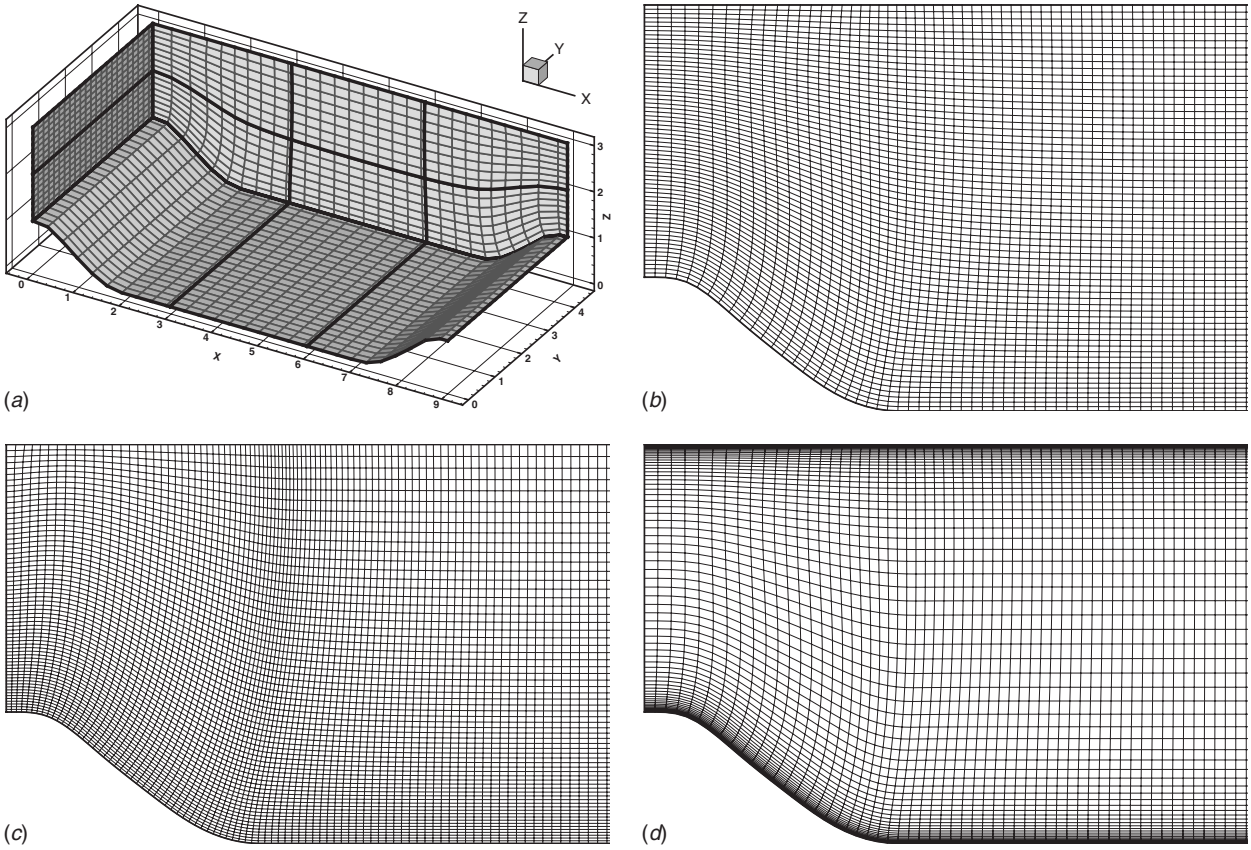

Fig. 1 The computational H-H-type grid topology and the three different grids employed in the simulations of the hill flow

5 Results

For all simulations the Reynolds number is equal to 10,595 and the Mach number is 0.2, where all values are nondimensionalized with the bulk velocity at the hill crest and the height of the constriction. The time integration has been performed exclusively by the second-order extended stability Runge–Kutta scheme and several high-resolution methods have been considered in combination with a characteristics-based Riemann solver [14]. This investigation includes the third-order MUSCL scheme [19], the fifth-order MUSCL scheme [32], and the ninth-order WENO scheme [21]. These methods are referred to as $M3$, $M5$, and $W9$, respectively, throughout the paper.

5.1 Flow Topology. Figure 2(*a*) illustrates the general flow features encountered in this test case. The averaged streamlines, although partially obscured by the vortical structures, reveal the existence of a closed recirculation area in the lee of the hill. This separation bubble originates at the convex curvature of the wall, a short distance downstream of the hill crest, and it ends after the flow has passed the region of concave curvature at the foot of the hill, i.e., in the trough between the constrictions. A highly unsteady shear-layer that is emanating from the separation line marks the transitional region between recirculation and core flow. After the turbulent shear-layer has reattached, a strongly agitated boundary layer is formed that subsequently experiences a slight recovery before it approaches the hill. The boundary layer downstream of a separation bubble is not of standard form because the influence of the shear-layer goes well beyond the line of reattachment [33]. At the windward slope, the flow is quickly accelerated and thus the boundary layer becomes thinner. As this particular case generates its own inlet conditions due to the periodicity in the x-direction, the incoming boundary layer is also very thin and contains a certain level of turbulence. Consequently, both the line of separation and reattachment exhibit significant fluctuations around their averaged positions. This behavior has also been observed for the detachment and subsequent attachment of a turbulent boundary layer [34].

The scales of coherent structures as predicted by the third-order MUSCL ($M3$), the fifth-order MUSCL ($M5$), and the ninth-order WENO ($W9$) schemes can be compared visually by applying the Q-criterion [35] to an instantaneous realization of the fully developed flow field. It has been found that more and finer structures are resolved by all methods with increasing grid resolution, but

Table 1 Characteristic parameters for the three grids employed here and for the highly resolved reference LES

Grid	$N_x \times N_y \times N_z$	Size	$\Delta x/h$	$\Delta y/h$	$\Delta z/h$	$z^+_{\min}$	$z^+_{\max}$
Coarse	$112 \times 91 \times 64$	0.65×10^6	0.08	0.049	0.032	≈ 7	≈ 14
Modified	$112 \times 91 \times 64$	0.65×10^6	0.08	0.049	0.0047	≈ 1	≈ 3
Medium	$176 \times 91 \times 64$	1.03×10^6	0.04	0.049	0.02	≈ 4	≈ 9
Reference	$196 \times 186 \times 128$	4.67×10^6	0.032	0.024	0.0033	≈ 0.5	≈ 1

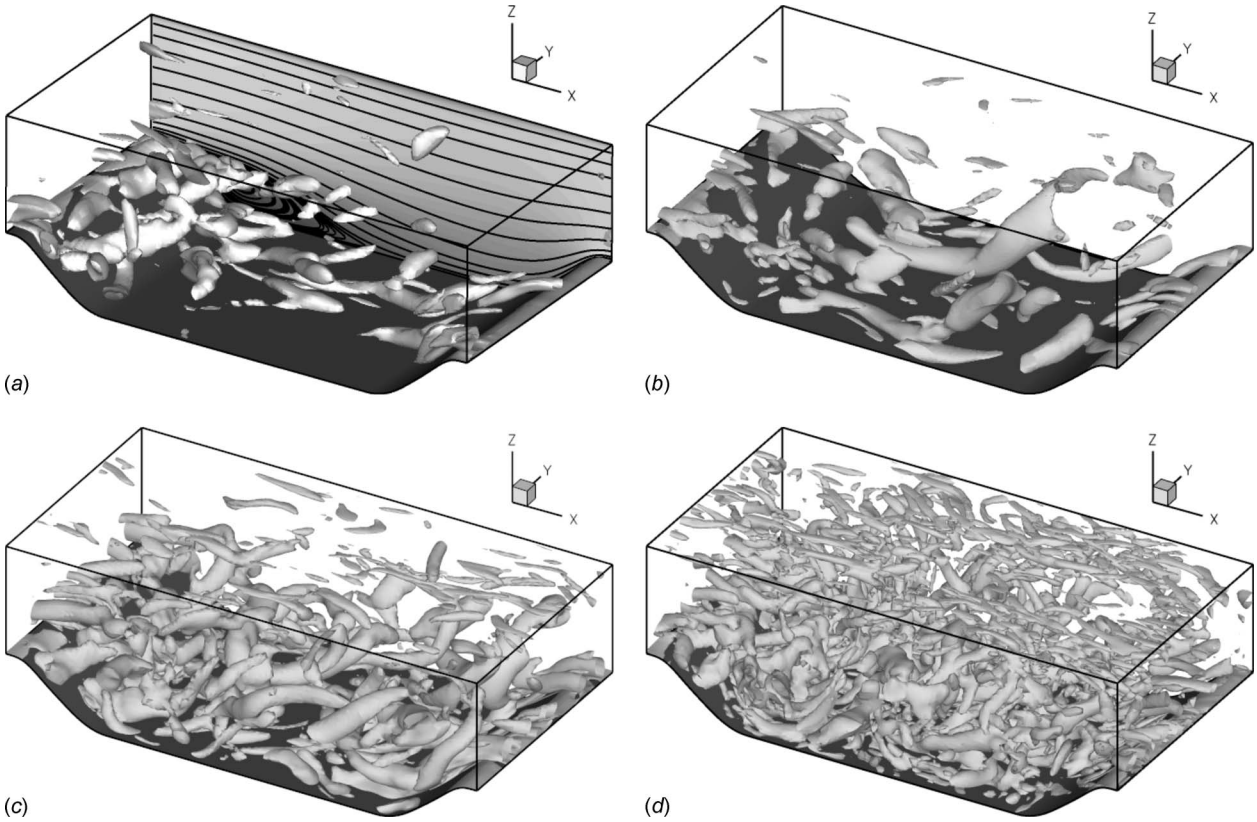

Fig. 2 Flow features in the channel visualized by time- and space-averaged streamlines and instantaneous vortical structures defined by the *Q*-criterion

the relative difference between them appear to be similar irrespective of the grid size. Therefore, only the flow fields obtained on the modified grid have been visualized in Figs. 2(*b*)–2(*d*) by using the same levels of Q for all methods. *M*5 is able to resolve smaller scales than *M*3 on identical grids and, in turn, *W*9 provides a higher resolution power than *M*5. However, the basic character of the structures does not seem to change. In the free shear-layer emanating from the separation line near the crest of the hill, the preferred axis of orientation is in cross-stream direction for all methods because of the Kelvin–Helmholtz-type instability. It should be noted that this behavior is largely obscured by the vortices in the upper portion of the channel in case of *W*9. When the shear-layer develops further downstream, the vortices break into smaller scales more rapidly with increasing order of the method. As a result, the turbulence mixing is enhanced and more unsteady activity in the core region and the recirculation zone can be observed for *M*5 and, most significantly, for *W*9. This is also the main reason for the premature reattachment of the flow predicted by *M*5 and, in particular, *W*9; see Sec. 5.2. For all methods, predominantly elongated structures aligned in streamwise direction can be observed in the trough of the channel after the shear-layer has disintegrated and in the core flow over the whole domain.

5.2 Separation Bubble. All separation and reattachment points obtained with *M*3, *M*5, and *W*9 for the coarse, the medium, and the modified grid are listed in Table 2. Additionally, previously published data [9] have been included for comparison. The results in rows labeled "LL3," "WW," and "NS" are from the classical, wall-modeled LES using the wall-adapting local eddy-viscosity (WALE) subgrid-scale model [36] on grids identical to the coarse and the medium mesh. LL3 and WW refer to simulations with a three-layer logarithmic wall model and the wall approximation of Werner and Wengle [37], respectively, whereas NS refers to a simulation with no-slip boundary conditions, i.e., no wall model, at the top and bottom walls of the channel.

From the data presented here, it is already clear that all simulations using high-resolution methods outperform the classical LES without a wall model for the highly under-resolved, coarse grid. Applying the log-law model improves the classical LES result regarding the prediction of the separation point. However, the effect on reattachment is only minor because it is not valid for separated flows. Strictly speaking, neither is the WW model, but it still yields the best result on behalf of the classical LES for the coarse grid. This can mainly be attributed to the specific implementation in cell-integrated form that leads to a higher wall shear-stress and thus favors separation. It has been found that the dependence of the results on the near-wall approximation declines for the medium grid [9]. This effect is reflected in the relatively close proximity of the separation and reattachment predicted by

Table 2 Averaged locations of separation and reattachment obtained with *M*3, *M*5, and *W*9 on the coarse, medium, and modified grids (data from Temmerman et al. [9] have also been included for comparison)

	Coarse		Medium		Modified	
Method	x_{sep}/h	x_{att}/h	x_{sep}/h	x_{att}/h	x_{sep}/h	x_{att}/h
M3	0.98	2.89	0.55	3.62	0.32	5.06
M5	1.06	2.57	0.63	3.00	0.24	4.35
W9	0.74	2.33	0.47	3.40	0.24	3.77
LL3	0.53	2.98	0.34	4.32	-	-
WW	0.46	4.00	0.32	4.56	-	-
NS	1.12	2.17	0.38	3.45	-	-
Reference	$x_{sep}/h=0.22$			$x_{att}/h=4.72$		

LL3 and WW. The local grid refinement also enhances the performance of the classical LES with no-slip condition, although the separation bubble remains too short.

Among the high-resolution methods, *W*9 gives the best result for all grids regarding the location of the separation. Yet, it underpredicts the length of the separation bubble. On the other hand, the bubble length obtained by *M*3 is closest to the reference length [10] on all grids. Most interestingly, the drastic improvement of the results for the medium grid as seen in all classical LES is not reproduced. As expected, however, a grid refinement in the wall-normal direction has the desired effect and both detachment and reattachment are in better agreement with the reference LES. It should be noted that, for a correct interpretation of the results, the different behavior of *M*3, *M*5, and *W*9 has to be assessed in combination with other parameters presented in Sec. 5.3. The position of the separation bubble alone is not very meaningful because it is strongly influenced by several factors, e.g., the grid resolution near the separation point and in the shear-layer and, above all, the characteristics of the incoming boundary layer.

5.3 Velocity Profiles and Reynolds Stresses. In order to assess the performance of the three high-resolution methods employed quantitatively, the results have been compared against highly resolved classical LES [10]. It should be noted that only the boundary layer at the bottom wall of the channel was fully resolved in the reference case. In this section, the profiles of the mean streamwise velocity, and the normal and the shear-stress are investigated. All quantities have been averaged over approximately 50 flow through cycles in time and across the spanwise extent of the domain in space. Furthermore, the turbulent stresses have been calculated according to the standard Reynolds decomposition of the flow field into mean and fluctuating components. The data have been extracted for the coarse, medium, and modified grids at four characteristic locations along the streamwise direction, which are representative of different behaviors of the flow field.

5.3.1 Incoming Flow. The profiles as obtained by *M*3, *M*5, and *W*9 shortly after the crest of the hill at a streamwise location of $x/h=0.05$ are shown in Fig. 3. The results for the three grids employed in this study are compared one at a time against the reference data from the fully wall-resolved reference LES. As a result of the turbulent reattachment and the subsequent strong acceleration along the windward slope of the hill, the flow at this position features a thin, but excited boundary layer near the hill surface. However, the sharp peak observed for the normal stress in the bottom boundary layer is mainly due to the influence of the fluctuating separation line and not a characteristic of the incoming flow [10]. The boundary layer at the upper wall is relatively thick and more gentle. For the coarse grid (Fig. 3(*a*)) all high-resolution methods overpredict the velocity maximum near the hill and underpredict the second peak near the top wall. Since this specific configuration generates its own inlet conditions, the effects of all phenomena are able to propagate through the whole flow field and thus influence each other. Therefore, this behavior will be explained in the following paragraphs. The shear-stress shown in Fig. 3(*b*) is nearly zero for all methods and the maximum normal stresses in the boundary layer are approximately one order of magnitude too low, which can be attributed to the delayed separation at the lee side of the hill. In general, both Reynolds stresses are almost uniformly distributed across the channel and the level of turbulence is very low.

Although the resolution near the wall is increased only marginally for the medium grid, approximately three points in the boundary layer as opposed to about two points for the coarse grid at this position, a drastic improvement in the results can be seen. This already indicates substantial differences in the incoming flow field. The characteristic shape of the velocity profile featuring two narrow maxima near the top and the bottom wall is approached, albeit the effect in Fig. 3(*c*) is only faint. Additionally, the peak velocity is much closer to the fully resolved LES with *W*9 yielding the best result, followed by *M*3 and then *M*5. Again, this is associated with the characteristics of the upstream flow. The shear-stress in Fig. 3(*d*) exhibits a similar shape and magnitude as the reference solution where *W*9 follows it almost exactly, except in the boundary layer. Here, the peak is less pronounced. The same holds for the maximum normal stress. *W*9 predicts about half the amount of normal stress in the boundary layer as observed in the reference LES and it is further decreasing for the lower order schemes. Furthermore, the shape of the normal stress appears more flat for all high-resolution methods when compared with the classical LES in the lower half of the channel and the level of turbulence is generally lower.

The results for the modified grid featuring a higher clustering of grid points near the walls are presented in Figs. 3(*e*) and 3(*f*). For this particular mesh, approximately 11 points lie within the boundary layer at the hill surface and the z^+ distribution along the bottom wall indicates nearly resolved conditions throughout the domain (not shown here). The averaged velocity profiles from the reference LES and the simulations performed here are virtually identical near the surface of the hill. The local minimum near the half-height of the channel at this position is slightly more pronounced for all high-resolution methods. Minor differences can also be observed at the top wall where the reference solution yields a very thick boundary layer as opposed to a much thinner boundary layer predicted by the present simulations. This can mainly be attributed to the fact that the grid employed in the reference LES was relatively coarse in this area and a wall function had been used. Additionally, the wall treatment introduces an unrealistic kink in the velocity profile, which appears at all locations along the channel. It has been reported that the near-wall approximation at the top surface is not relevant to the solution in the rest of the flow field [10]. However, this claim will be revisited for the reattached flow region.

In Fig. 3(*f*), a significant improvement can also be observed for the Reynolds stresses on the modified grid. The shape and magnitude of the shear-stresses as predicted in all simulations are in very good agreement with the reference solution. Although the minimum shear-stress in the bottom boundary layer is slightly less distinct, the peak normal stresses at the same location are very close to the reference. Both are strongly related to the movement of the separation line. With increasing grid resolution in the wall-normal direction, the high-resolution methods are able to tap their full potential. This is indicated clearly by the upstream shift of the averaged separation points. Small disturbances start to develop normal to the wall and are propagated along the surface even though the grid resolution in the streamwise direction is fairly coarse. Because the higher order methods are more sensitive to small fluctuations, they predict a separation prior to *M*3. This is reflected in the peak normal stresses shown in Fig. 3(*f*). Here, *W*9 results in the strongest maximum, followed by *M*5 and then *M*3. It should be noted that the averaged points of separation are identical for *W*9 and *M*5, but the influence of the fluctuations on the stress profiles is probably stronger for *W*9 due to its higher order of accuracy. Farther away from the hill surface, less turbulence is predicted by all high-resolution methods when compared against the classical LES [10] in the lower half of the channel, but increased levels of normal stress are observed for *M*5 and especially *M*3 in the upper half.

5.3.2 Separated Flow. The maximum turbulent intensities are reached after separation has occurred. Here, several phenomena interact with each other: the two boundary layers at the top and bottom walls of the channel; the recirculation zone, which can be seen as a shear-layer; and the highly unsteady free shear-layer emanating from the separation line and the core flow can be distinguished at the streamwise location $x/h=2$. Averaged velocity and stress profiles for this position are shown in Fig. 4.

A substantial difference between the velocity profiles from the

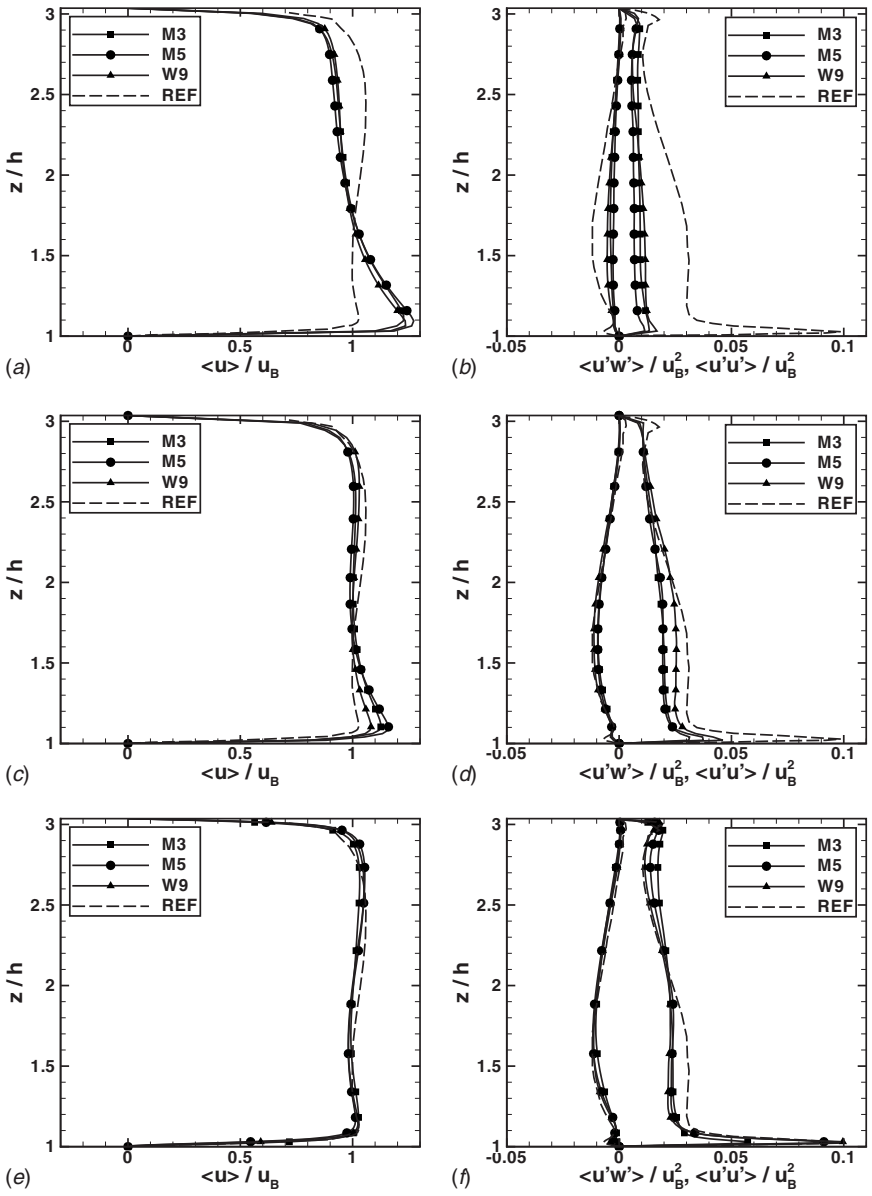

Fig. 3 Comparison of the averaged streamwise velocity and Reynolds stresses near the hill crest at $x/h=0.05$ as obtained by different high-resolution methods on the coarse, medium and modified grids with the reference LES

reference LES and the present simulations on the coarse grid is illustrated in Fig. 4(*a*). The size of the separation bubble is heavily underpredicted by all high-resolution methods due to the delayed separation and the subsequent early reattachment. Hence, the separation region covers only approximately half a hill-height in the wall-normal direction and the reversed flow is less developed. Since the same mass flow rate has to be achieved in all simulations, the core velocity is underpredicted accordingly when compared with the reference solution. This is the main reason for the relatively uniform velocity distribution above the hill crest in Fig. 3(*a*). Surprisingly, however, the stress magnitudes shown in Fig. 4(*b*) are of approximately the same order. Differences between the high-resolution methods can be observed regarding the location of the shear-layer, marked by the peak stresses, and the shape of the profiles. *M*5 yields the lowest shear-layer as late separation favors this behavior. Although *M*3 separates downstream of *W*9, the position of the shear-layer is slightly higher, which is associated with the early reattachment of *W*9. Additionally, the peak normal stresses and the spreading of the shear-layer appear to be dominated by the separation location. For the coarse grid, higher normal stresses are observed for delayed separation and the width of the shear-layer grows with the distance from its origin.

Figures 4(*c*) and 4(*d*) present the results for the medium grid at the same streamwise location. In accordance with the above, early separation and late reattachment lead to a better prediction of the separation bubble height. Thus, all methods approach the reference velocity profile in Fig. 4(*c*), albeit the reversed flow in the lower portion of the channel is still slightly underpredicted. Regarding the Reynolds stresses, more turbulence can be supported due to the grid refinement and consequently higher levels of shear-stress and normal stress are observed, both exceeding the reference [10] in the trough where the turbulence is produced. This behavior indicates that the flow is still under-resolved. Large variations of the peak stresses have also been observed in wall-modeled LES [9] and have been associated with the differences regarding the separation point. Yet, this conclusion was not consistent since different turbulence intensities had been found in simulations with similar separation points. Hence, the effect of

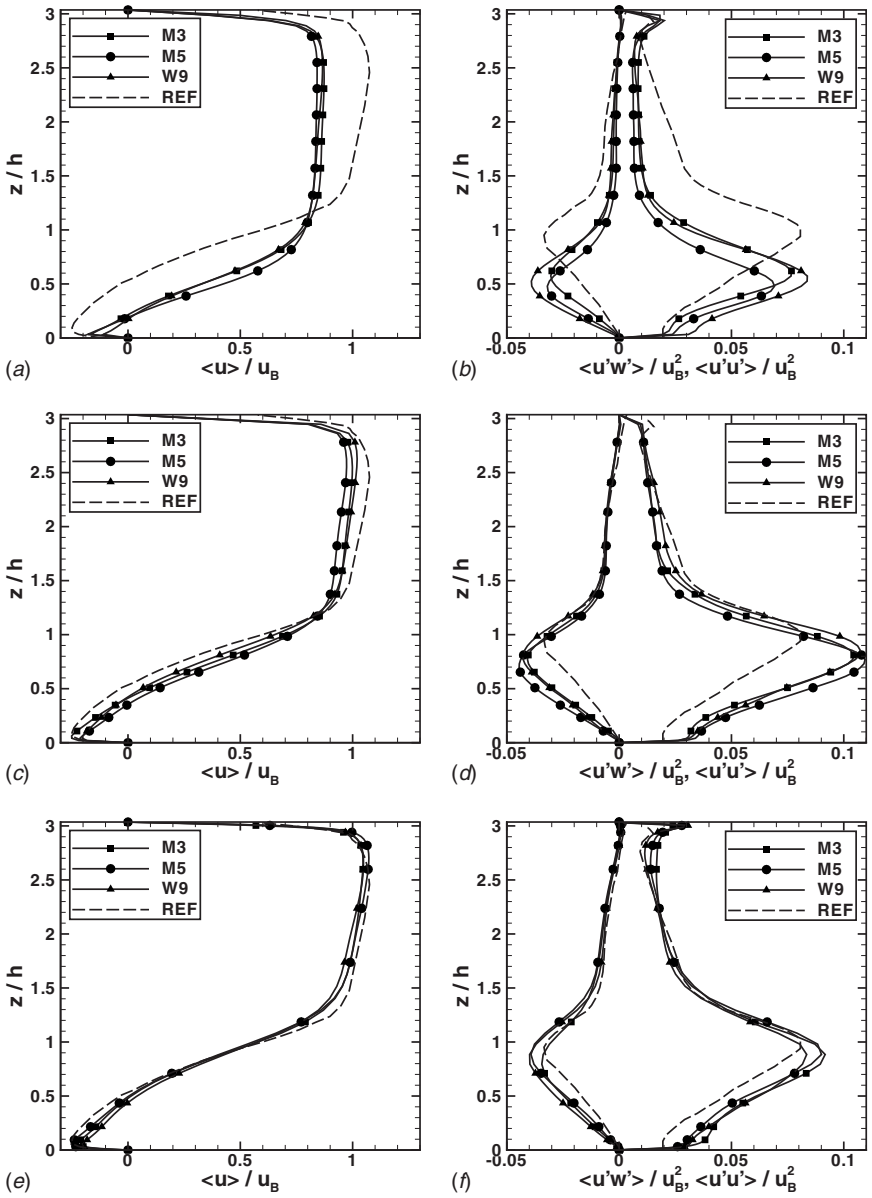

Fig. 4 Comparison of the averaged streamwise velocity and Reynolds stresses across the recirculation zone at $x/h=2$ as obtained by different high-resolution methods on the coarse, medium and modified grids with the reference LES

grid clustering in the free shear-layer cannot be disregarded. However, no information about the grid resolution in this region is available for the reference LES [10]. It should be noted that the peak stresses for the medium grid are less dependent on the exact location of detachment and reattachment at this position because the free shear-layer had more time to develop and it is still well ahead of the impingement at the bottom wall.

For the modified grid, the velocity profiles in Fig. 4(*e*) follow the reference solution more closely, with minor differences in the boundary layers at the top and bottom walls. Additionally, all high-resolution methods predict a smoother transition between the free shear-layer and the core flow. *M*5 appears to predict a stronger recirculation than *W*9, although separating at identical locations. This leads to later reattachment of the separation bubble. A strong dependence of the upper boundary layer on the grid resolution and the core flow can be observed. As expected, the boundary layer becomes thinner for higher velocities in the core of the channel. The classical LES, despite predicting slightly stronger velocities, results in a considerably thicker boundary layer than the high-resolution methods. This can mainly be attributed to the combined effect of the relatively coarse grid and the wall approximations employed in the reference solution. Good agreement for the stresses is revealed in Fig. 4(*f*). In the upper portion of the channel, both the shear and the normal stress are very close to the reference profile. Again, a slight discrepancy does exist near the boundary layer at the top wall due to the inadequate treatment in the classical LES. In the recirculation region, more turbulent energy is produced by *M*3, *M*5, and *W*9 when compared with the reference [10]. Here, all high-resolution methods yield similar Reynolds stresses. Minor differences, however, appear in the shear-layer where the maximum intensities occur. The behavior of the stresses, especially near the peaks, is influenced by a number of parameters, e.g., the location of separation and reattachment or the specifics of the numerical method, but no consistent pattern seems to emerge in the massively separated flow region.

5.3.3 Reattached Flow. The next position along the channel that has been investigated is the postreattachment region at x/h

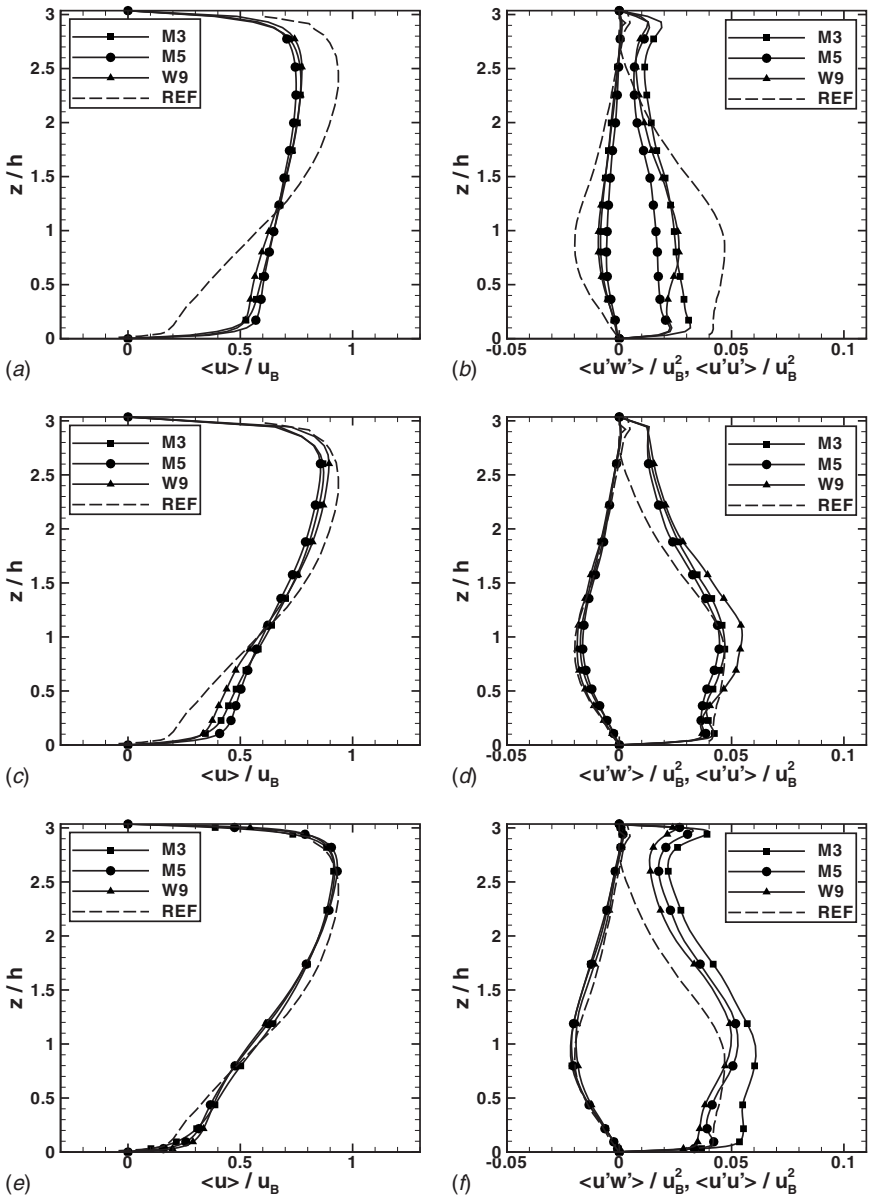

Fig. 5 Comparison of the averaged streamwise velocity and Reynolds stresses after reattachment at $x/h=6$ as obtained by different high-resolution methods on the coarse, medium and modified grids with the reference LES

=6 (Fig. 5). Here, the flow recovers to a state more typical for a plane channel geometry. The results obtained by the high-resolution methods on the coarse grids exhibit large discrepancies compared with the reference solution as the time histories of the flow differ substantially. The velocity profiles predicted by the present simulations (Fig. 5(*a*)) are already closer to the state of equilibrium. Most remarkably, however, is the qualitative difference of the normal stress profile obtained by *W*9 when compared with the lower order methods. The pronounced maximum in Fig. 5(*b*) indicates more transport of turbulence initially generated in the free shear-layer. This effect is intensified on the coarse grid because *W*9 also yields the strongest fluctuations further upstream.

As expected, the velocity profiles obtained on the medium grid (Fig. 5(*c*)) are in better agreement with the reference solution than the coarse grid solutions. In general, earlier reattachment leads to higher velocities in the trough at the same streamwise locations. This is the case indeed for all methods if applied on the modified grid, but does not hold for combinations of *W*9 and the medium or the coarse grid. Here, *W*9 reattaches prior to *M*3 and exhibits smaller velocities in the lower portion of the channel. The Reynolds stresses obtained on the medium grid are displayed in Fig. 5(*d*). Apart from the normal stresses in the vicinity of the top wall, they are relatively close to the reference profiles. Especially the shear-stresses are in very good agreement over the whole height of the channel. At about the height of the hill crest, the distinctive peak due to turbulence transport can be observed for all methods. It is most pronounced for *W*9, however, which leads to higher levels of turbulence in the lower half of the attached flow field throughout the channel.

The results for the modified grid are presented in Figs. 5(*e*) and 5(*f*). Regarding the averaged streamwise velocities, they approach the reference profiles in the main flow field. Near the bottom wall, however, the velocity is overpredicted because of the earlier reattachment. Consequently, the transition between the flow in the core of the channel and the trough is smoother. The boundary layer at the top wall thickens similar to the prediction from the classical LES [10] due to the deceleration of the core flow. However, major differences can be observed for the normal stresses

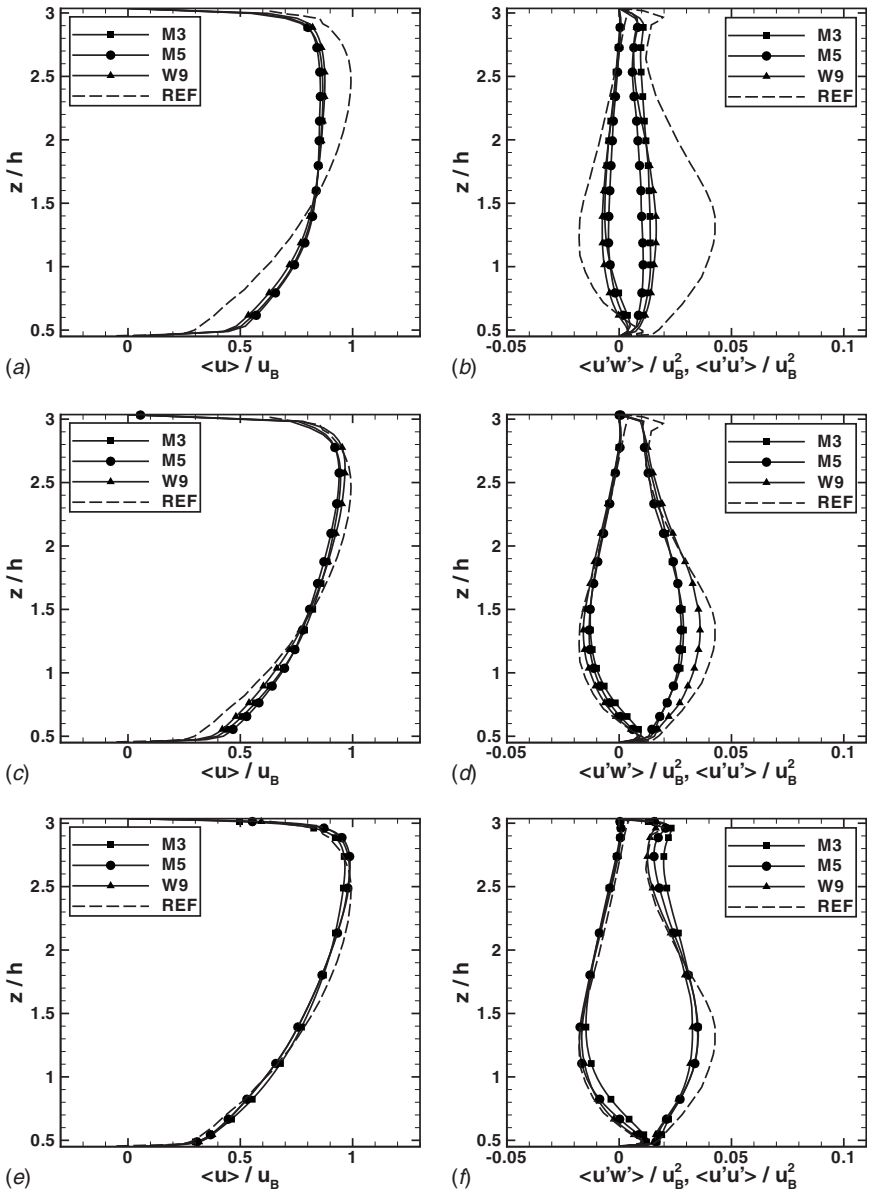

Fig. 6 Comparison of the averaged streamwise velocity and Reynolds stresses above the windward slope at $x/h=8$ as obtained by different high-resolution methods on the coarse, medium and modified grids with the reference LES

along the top wall; see Fig. 5(*f*). The normal stress seems to vanish in the reference solution, whereas all present simulations predict considerable turbulent activity. According to other fully wall-resolved LES simulations [38], the normal stress should reach a minimum of approximately 0.015 in the vicinity of the top wall and then increase again as the solid surface is approached. Thus, all high-resolution methods appear to reproduce the correct behavior. In general, the level of turbulence across the channel also reflects the location of the reattachment point because they are relatively close on the medium grid. The reattachment is delayed for the lower order methods and thus the turbulent intensity at the current location is higher for *M*3 than for *M*5, and, in turn, *M*5 than *W*9. All methods lead to virtually identical results as the reference LES regarding the shear-stress.

5.3.4 Accelerated Flow. The flow in the channel is subject to strong acceleration as it passes over the windward side of the hill. This region is represented by the averaged velocity and stress profiles at $x/h=8$. It should be noted that the slope of the geometry has not been accounted for during the extraction of the data presented in Fig. 6. Hence, in accordance with the reference solution [10], the flow variables do not represent the normal and tangential directions at the surface.

As the flow recovers and a more uniform state is achieved, the velocity profiles as predicted by the high-resolution methods are nearly indistinguishable irrespective of the grid employed. The data confirm the observations made prior to this position and no new insight can be gained. On the coarse grid the size of the separation bubble is severely underpredicted. This behavior can be improved gradually with increasing the grid resolution near the walls as shown for the medium grid in Fig. 6(*c*) and for the modified grid in Fig. 6(*e*). Additionally, the boundary layers at the top and bottom walls become thinner as the flow is accelerated in the streamwise direction.

Although less pronounced, the Reynolds stresses presented in Figs. 6(*b*)–6(*d*) bear similar features to the ones already discussed for the reattached flow at $x/h=6$. Interestingly, even at this loca-

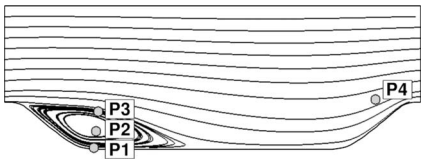

Fig. 7 Location of the four measurement points for the turbulence power spectra in relation to the flow phenomena visualized by averaged streamlines

tion, the wall approximations made in the reference LES still have a significant effect on the boundary-layer profile and the normal stresses near the top wall. Attention should be paid to the shear-stresses at the hill surface since they appear to reverse sign. However, this is only an artifact of the misalignment between the hill slope and the velocity components, which also has to be considered when interpreting the velocity profiles at this specific location.

5.4 Turbulence Kinetic Energy Spectra. In this section, power spectra of the fluctuating velocity components at characteristic locations identifying different flow regimes are presented. The length of the processed time signals corresponds to approximately 55 flow through times and the nondimensional sampling frequency based on the hill-height and the bulk velocity is $K=h/(u_B t)\approx 1$. Higher frequencies could not be considered here because the discrete point-data have not been extracted directly during the course of the simulations. In order to improve the quality of the statistics, however, all time signals across the spanwise extent of the domain have been processed and subsequently averaged.

Figure 7 illustrates the significance of the four locations investigated with respect to the flow phenomena visualized by averaged streamlines. Points 1–3 all lie in the lee of the hill at $x/h\approx 2$. P1 has been chosen at a fixed position $(x/h, z/h)\approx(2.00, 0.03)$ in the boundary layer of the recirculation zone, whereas the locations of P2 and P3 are grid-dependent near the center of the recirculation bubble and in the free shear-layer emanating from the crest of the hill, respectively. Furthermore, the signal at a fixed fourth point with $(x/h, z/h)\approx(8.00, 1.00)$ has been examined to characterize the flow near the windward slope of the hill.

Before analyzing the individual spectra shown in Figs. 8–10, certain common features should be mentioned. In general, no dominant frequency induced by the finite length of the channel can be observed. This is clearly indicated by the absence of a distinctive peak for frequencies smaller than the natural flow through frequency $K_D=1/9$, which has been marked in the graphs by a short gray line. Additionally, all power spectra more or less seem to follow Kolmogorov's $K^{-5/3}$ law for frequencies greater than K_D. This seems a reasonable result, albeit homogeneity and isotropy cannot be assumed a priori at any point in the flow. Moreover, employing Taylor's hypothesis of "frozen turbulence" to infer the spatial structure from the time spectra is subject to uncertainty as the mean flow and the velocity fluctuations are of the same order.

In the following paragraphs, the discussion will be focused on the high-end of the frequency range, i.e., $K>K_D$. Also, only selected spectra will be considered here because the trends revealed by the individual velocity components or the data sets obtained with different high-resolution methods on different grids are very similar. Thus no additional information can be gained by presenting all possible combinations.

A comparison of the one-dimensional power spectra obtained for the individual fluctuating velocity components at the four different points as predicted by *M*3 on the modified grid are shown in Fig. 8. The effect of wall blockage is most obvious in the boundary layer of the recirculation zone; see Fig. 8(*a*). Whereas the streamwise and the cross-stream components lead to nearly identical power spectra, the wall-normal fluctuations are strongly damped due to the existence of the wall, which manifests itself in

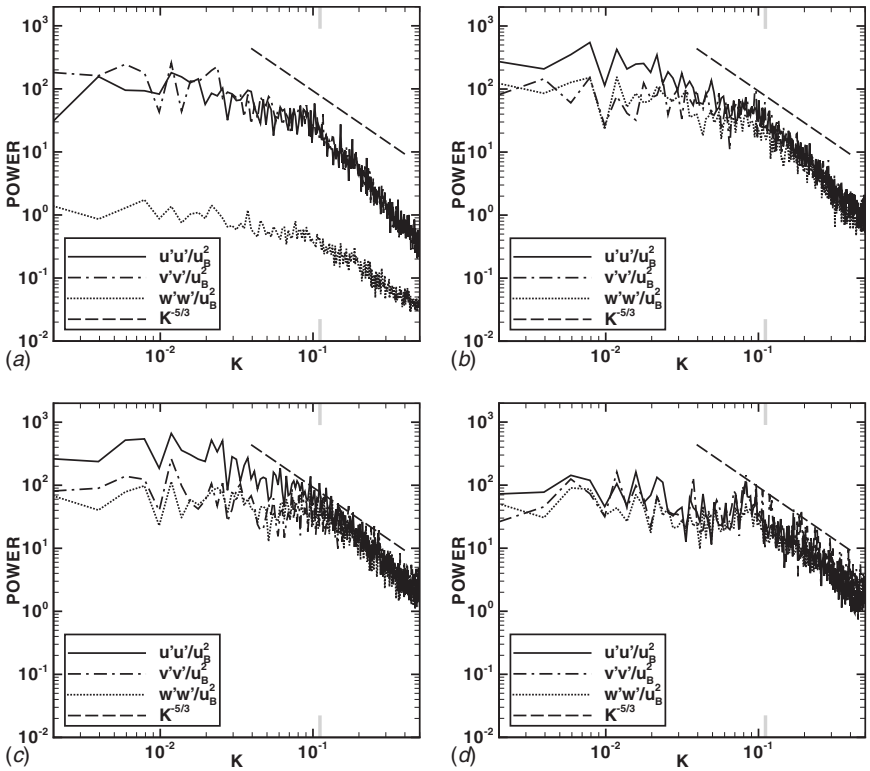

Fig. 8 Comparison of the one-dimensional turbulence power spectra as obtained by *M*3 on the modified grid

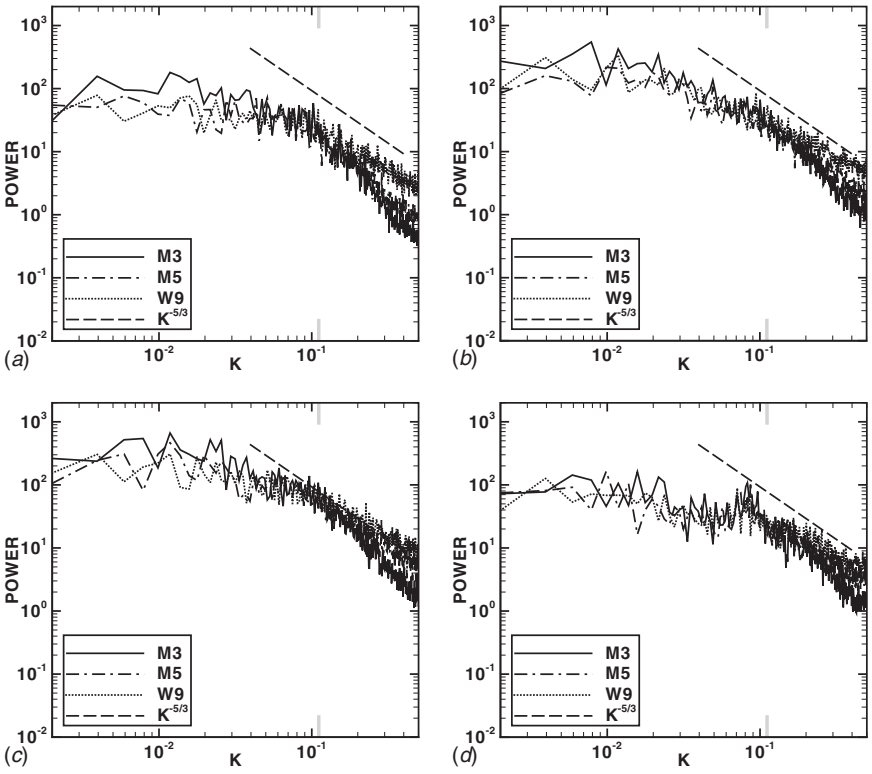

Fig. 9 Comparison of the one-dimensional turbulence power spectra as obtained by different high-resolution methods on the modified grid

a comparably low energy level of $w'w'/u_b^2$. Moving away from the bottom wall toward the center of the recirculation zone, Fig. 8(*b*), the wall-normal component recovers and the spectra almost collapse. The flow at P2 can therefore be interpreted as being more isotropic. This also holds for point P3, Fig. 8(*c*), which lies inside the free shear-layer. Here, the highest turbulence energy levels in the flow are observed. When the flow approaches the windward slope of the following hill, the fluctuating components

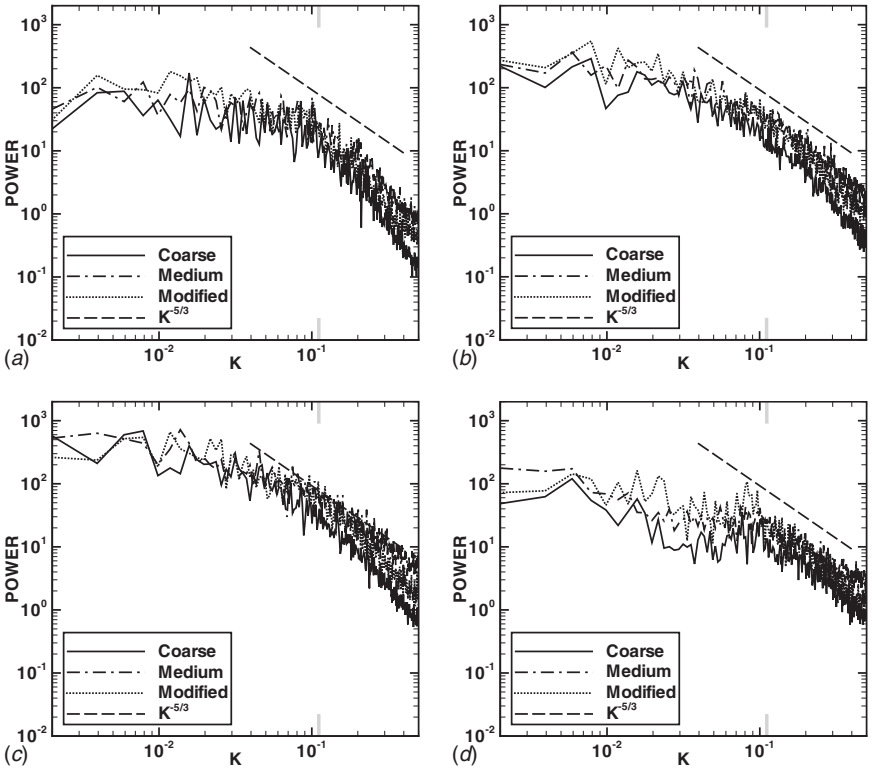

Fig. 10 Comparison of the one-dimensional turbulence power spectra as obtained by *M*3 on the coarse, medium, and modified grids

$u'u'/u_b^2$ and $w'w'/u_b^2$ appear to be slightly damped compared with $v'v'/u_b^2$ as a result of the wall blockage. Thus the components affected by the existence of the solid wall exhibit lower energy levels than the cross-stream component at P4, Fig. 8(*d*).

In Sec. 5.1, differences regarding the resolution power of the three high-resolution methods have been discussed and illustrated by means of the coherent structures observed in the instantaneous flow fields. The effect of resolution power can also be related to the turbulence kinetic energy spectra shown in Fig. 9. On identical grids, the ninth-order WENO method is able to predict smaller scales than the fifth-order MUSCL scheme and, in turn, the fifth-order MUSCL scheme results in smaller scales than the third-order MUSCL scheme. Consequently, the velocity fluctuations are most frequent for *W*9 and more frequent for *M*5 than they are for *M*3. This holds throughout the flow field and leads to differences in the spectral analysis of the data taken at points 1–4; see Figs. 9(*a*)–9(*d*), respectively. As can be seen, a consistent ranking in order of increasing power level at the high-frequency end can be assigned to the high-resolution methods: *W*9-*M*5-*M*3.

Comparisons of the turbulence kinetic energy spectra for the streamwise component $u'u'/u_b^2$ as obtained by the third-order MUSCL scheme on the coarse, medium, and modified grids are presented in Fig. 10. Again, a consistent pattern can be observed in all flow regions represented by the point measurements shown in Figs. 10(*a*)–10(*d*). The signal on the medium grid yields the highest power at all frequencies $K > K_D$ and the results for the coarse grid exhibit the lowest power in the same frequency range. This behavior can be explained by considering the Reynolds stresses from Figs. 4 and 6. The spectral energy level of the fluctuating velocity components is a direct consequence of the turbulence intensity predicted on the different grids.

6 Conclusions

The performance of three high-resolution methods has been assessed with respect to massively separated flow in the lee of a hill geometry. The unsteady flow field encountered in this test case comprises various regions where different requirements have to be met. Near the crest of the hill, the accurate prediction of the thin boundary-layer detachment from the gently curved surface is paramount to the downstream development of the flow field. After separation has occurred, the highly unsteady free shear-layer emanating from the hill challenges the turbulence modeling capabilities of the numerical method. The reattachment location at the bottom wall of the channel is strongly influenced by the representation of the free shear-layer. Reattachment itself is an unsteady process and the coherent structures originating in the shear-layer alternate between being propagated downstream or being swept back into the recirculation bubble. Thus, a feedback loop is generated that adds to the fluctuation of the separation line. In the postreattachment region, the recovery process toward a plane channel flow has to be captured. Here, the boundary layer in the trough causes additional difficulties because it is of nonstandard form and undergoes several evolution steps prior to reaching the next hill crest. Initially, it is very thick and highly turbulent. As it approaches the windward side of the following hill, it is accelerated, becomes thinner, and thus poses even more stringent requirements with respect to grid resolution.

All of the above phenomena are intimately connected to each other because the hill flow generates its own inlet condition through the periodicity constraint in streamwise direction. Therefore, it is almost impossible to isolate the effects of the numerical method on individual regions. However, it can certainly be claimed that the higher order methods yield an improvement in predicting the averaged separation point even if the boundary layer is under-resolved. It has also been found that clustering of grid points in the wall-normal direction is more beneficial than a streamwise clustering. This can be explained by the reduced influence of wall blockage on the fluid movement near the surface. Since the higher order methods are more sensitive to small disturbances, they are able to propagate the disturbances along the wall and increase the likelihood of separation—especially if the underlying nonlinear stability criteria are relaxed as for a WENO method.

In the free shear-layer, the increased sensitivity of the higher order methods *M*5 and *W*9 leads to a more rapid breakdown of the layer when compared with *M*3. Consequently, the predicted separation length becomes shorter with increasing order of the method. This is also associated with more turbulence mixing and the formation of small-scale structures whose size depends on the resolution power of the numerical scheme. No conclusive prediction can be made for the postreattachment region because the history of the flow strongly influences the results obtained here.

Acknowledgment

The authors would like to acknowledge Lionel Temmerman (NUMECA) for providing the computational grids and several stimulating discussions regarding the test case presented. They would also like to thank Ben Thornber and Vladimir Titarev from the FMaCS Group at Cranfield University for their advice on the analysis of the numerical methods.

References

[1] Margolin, L. G., Smolarkiewicz, P. K., and Wyszogrodzki, A. A., 2002, "Implicit Turbulence Modeling for High Reynolds Number Flows," ASME J. Fluids Eng., **124**, pp. 862–867.
[2] Boris, J. P., Grinstein, F. F., Oran, E. S., and Kolbe, R. L., 1992, "New Insights Into Large Eddy Simulation," Fluid Dyn. Res., **10**, pp. 199–228.
[3] Grinstein, F. F., and DeVore, C. R., 1996, "Dynamics of Coherent Structures and Transition to Turbulence in Free Square Jets," Phys. Fluids, **8**(5), pp. 1237–1251.
[4] Youngs, D. L., 1991, "Three-Dimensional Numerical Simulation of Turbulent Mixing by Rayleigh-Taylor Instability," Phys. Fluids A, **3**(5), pp. 1312–1320.
[5] Drikakis, D., 2003, "Advances in Turbulent Flow Computations Using High-Resolution Methods," Prog. Aerosp. Sci., **39**, pp. 405–424.
[6] Fureby, C., and Grinstein, F. F., 2002, "Large Eddy Simulation of High Reynolds Number Free and Wall Bounded Flows," J. Comput. Phys., **181**, pp. 68–97.
[7] Grinstein, F. F., and Fureby, C., 2002, "Recent Progress on MILES for High Reynolds Number Flows," ASME J. Fluids Eng., **124**, pp. 848–861.
[8] Fureby, C., 2006, "ILES and LES of Complex Engineering Turbulent Flows," European Conference on Computational Fluid Dynamics (ECCOMAS CFD).
[9] Temmerman, L., Leschziner, M. A., Mellen, C. P., and Fröhlich, J., 2003, "Investigation of Wall-Function Approximations and Subgrid-Scale Models in Large Eddy Simulation of Separated Flow in a Channel With Streamwise Periodic Constrictions," Int. J. Heat Fluid Flow, **24**, pp. 157–180.
[10] Fröhlich, J., Mellen, C. P., Rodi, W., Temmerman, L., and Leschziner, M. A., 2005, "Highly Resolved Large-Eddy Simulation of Separated Flow in a Channel With Streamwise Periodic Constrictions," J. Fluid Mech., **526**, pp. 19–66.
[11] Breuer, M., Kniazev, B., and Abel, M., 2007, "Development of Wall Models for LES of Separated Flows Using Statistical Evaluations," Comput. Fluids, **36**, pp. 817–837.
[12] Lenormand, E., Sagaut, P., Ta Phuoc, L., and Comte, P., 2000, "Subgrid-Scale Models for Large-Eddy Simulations of Compressible Wall Bounded Flows," AIAA J., **38**(8), pp. 1340–1350.
[13] Drikakis, D., and Rider, W. J., 2004, *High-Resolution Methods for Incompressible and Low-Speed Flows*, Springer, New York.
[14] Eberle, A., 1987, "Characteristic Flux Averaging Approach to the Solution of Euler's Equations," *Computational Fluid Dynamics* (VKI Lecture Series), Rhode-St-Genýse, Belgium.
[15] Drikakis, D., 2001, "Uniformly High-Order Methods for Unsteady Incompressible Flows," *Godunov Methods: Theory and Applications*, Kluwer Academic, Dordrecht, The Netherlands, pp. 263–283.
[16] Drikakis, D., Govatsos, P. A., and Papatonis, D. E., 1994, "A Characteristic-Based Method for Incompressible Flows," Int. J. Numer. Methods Fluids, **19**, pp. 667–685.
[17] Harten, A., 1983, "High Resolution Schemes for Hyperbolic Conservation," J. Comput. Phys., **49**, pp. 357–393.
[18] van Leer, B., 1974, "Towards the Ultimate Conservative Difference Scheme. Part II: Monotonicity and Conservation Combined in a Second Order Scheme," J. Comput. Phys., **14**, pp. 361–370.
[19] Zóltak, J., and Drikakis, D., 1998, "Hybrid Upwind Methods for the Simulation of Unsteady Shock-Wave Diffraction Over a Cylinder," Comput. Methods Appl. Mech. Eng., **162**, pp. 165–185.
[20] Kim, K. H., and Kim, C., 2005, "Accurate, Efficient and Monotonic Numerical Methods for Multi-Dimensional Compressible Flows. Part II: Multi-Dimensional Limiting Process," J. Comput. Phys., **208**, pp. 570–615.
[21] Balsara, D. S., and Shu, C.-W., 2000, "Monotonicity Preserving Weighted Essentially Non-Oscillatory Schemes With Increasingly High Order of Accuracy," J. Comput. Phys., **160**, pp. 405–452.

[22] Shu, C.-W., and Osher, S., 1988, "Efficient Implementation of Essentially Non-Oscillating Shock-Capturing Schemes," J. Comput. Phys., **77**, pp. 439–471.
[23] Shu, C.-W., and Osher, S., 1989, "Efficient Implementation of Essentially Non-Oscillating Shock-Capturing Schemes II," J. Comput. Phys., **83**, pp. 32–78.
[24] Jiang, G.-S., and Shu, C.-W., 1996, "Efficient Implementation of Weighted ENO Schemes," J. Comput. Phys., **126**, pp. 202–228.
[25] Harten, A., Engquist, B., Osher, S., and Chakravarthy, S. R., 1987, "Uniformly High Order Accurate Essentially Non-Oscillatory Schemes, III," J. Comput. Phys., **71**, pp. 231–303.
[26] Grinstein, F. F., Margolin, L. G., and Rider, W. J., 2007, "A Rationale for Implicit LES," *Implicit Large Eddy Simulation*, F. F. Grinstein, L. G. Margolin, and W. J. Rider, eds., Cambridge University Press, Cambridge, Chap. 2, pp. 39–58.
[27] Warming, R. F., and Hyett, B. J., 1974, "The Modified Equation Approach to the Stability and Accuracy Analysis of Finite-Difference Methods," J. Comput. Phys., **14**, pp. 159–179.
[28] Thornber, B., Mosedale, A., Drikakis, D., Youngs, D., and Williams, R. J. R., 2008, "An Improved Reconstruction Method for Compressible Flows With Low Mach Number Features," J. Comput. Phys., **227**, pp. 4873–4894.
[29] Titarev, V. A., and Toro, E. F., 2007, "Analysis of ADER and ADER-WAF Schemes," IMA J. Numer. Anal., **27**, pp. 616–630.
[30] Margolin, L. G., and Rider, W. J., 2007, "Numerical Regularization: The Numerical Analysis of Implicit Subgrid Models," *Implicit Large Eddy Simulation*, F. F. Grinstein, L. G. Margolin, and W. J. Rider, eds., Cambridge University Press, Cambridge, Chap. 5, pp. 195–221.
[31] Hahn, M., 2008, "Implicit Large-Eddy Simulation of Low-Speed Separated Flows Using High-Resolution Methods," Ph.D. thesis, Cranfield University, UK.
[32] Kim, K. H., and Kim, C., 2005, "Accurate, Efficient and Monotonic Numerical Methods for Multi-Dimensional Compressible Flows. Part II: Multi-Dimensional Limiting Process," J. Comput. Phys., **208**, pp. 570–615.
[33] Castro, I. P., and Epik, E., 1998, "Boundary Layer Development After a Separated Region," J. Fluid Mech., **374**, pp. 91–116.
[34] Na, Y., and Moin, P., 1998, "Direct Numerical Simulation of a Separated Turbulent Boundary Layer," J. Fluid Mech., **374**, pp. 379–405.
[35] Jeong, J., and Hussain, F., 1995, "On the Identification of a Vortex," J. Fluid Mech., **285**, pp. 69–94.
[36] Ducros, F., Nicoud, F., and Poinsot, T., 1998, "Wall-Adapting Local Eddy-Viscosity Model for Simulations in Complex Geometries," *Numerical Methods for Fluid Dynamics VI*, M. J. Baines, ed., Oxford University Computing Laboratory, Oxford, UK, pp. 293–299.
[37] Werner, H., and Wengle, H., 1991, "Large Eddy Simulation of Turbulent Flow Over and Around a Cube in a Plate Channel," *8th Symposium on Turbulent Shear Flows*, Technical University of Munich, Germany.
[38] Breuer, M., 2005, "New Reference Data for the Hill Flow Test Case," online, URL: http://www.hy.bv.tum.de/DFG-CNRS/.

Investigations of Tripping Effect on the Friction Factor in Turbulent Pipe Flows

A. Al-Salaymeh
Department of Mechanical Engineering,
Faculty of Engineering and Technology,
University of Jordan,
Amman 11942, Jordan
e-mail: salaymeh@ju.edu.jo

O. A. Bayoumi
LSTM-Erlangen,
Institute of Fluid Mechanics,
Friedrich Alexander Universität Erlangen-Nürnberg,
Cauerstrasse 4,
D-91058 Erlangen, Germany
e-mail: ossammah@gmail.com

*Tripping devices are usually installed at the entrance of laboratory-scale pipe test sections to obtain a fully developed turbulent flow sooner. The tripping of laminar flow to induce turbulence can be carried out in different ways, such as using cylindrical wires, sand papers, well-organized tape elements, fences, etc. Claims of tripping effects have been made since the classical experiments of Nikuradse (1932, Gesetzmässigkeit der turbulenten Strömung in glatten Rohren, Forschungsheft 356, Ausgabe B, Vol. **3**, VDI-Verlag, Berlin), which covered a significant range of Reynolds numbers. Nikuradse's data have become the metric by which theories are established and have also been the subject of intense scrutiny. Several subsequent experiments reported friction factors as much as 5% lower than those measured by Nikuradse, and the authors of those reports attributed the difference to tripping effects, e.g., work of Durst et al. (2003, "Investigation of the Mean-Flow Scaling and Tripping Effect on Fully Developed Turbulent Pipe Flow," J. Hydrodynam., **15**(1), pp. 14–22). In the present study, measurements with and without ring tripping devices of different blocking areas of 10%, 20%, 30%, and 40% have been carried out to determine the effect of entrance condition on the developing flow field in pipes. Along with pressure drop measurements to compute the skin friction, both the Pitot tube and hot-wire anemometry measurements have been used to accurately determine the mean velocity profile over the working test section at different Reynolds numbers based on the mean velocity and pipe diameter in the range of 1.0×10^5–4.5×10^5. The results we obtained suggest that the tripping technique has an insignificant effect on the wall friction factor, in agreement with Nikuradse's original data.* [DOI: 10.1115/1.3153364]

Keywords: pipe flow, turbulent flow, friction factor, tripping effect

1 Introduction and Aim of Study

Turbulence is a complex phenomenon, endowing fluid flows with properties that remain generally unknown, although they are directly influenced by the initial and boundary conditions. In view of the dynamical complexity, it will remain impossible to capture all relevant mechanisms that generate and maintain turbulence in realistic flows. But some of the most essential features can be captured by investigating stably measurable averaged properties of individual classes of turbulent flows. The most important instance of such properties is the spatial distributions of the time-averaged velocity components and the turbulent velocity fluctuations. Some amount of investigations on these statistical measures in classical flows, such as developed turbulent channel and pipe flows, would suggest that these measures are very well-known. A closer inspection, however, reveals questions remaining still open, even at the level of mean velocity distributions in classical wall-bounded flows. The factors determining the shape of the mean velocity profile still remain an open topic. An infinite number of equations can be derived from the governing Navier–Stokes equations, in which the mean velocity profile is coupled to other turbulence statistics, but in all cases a closure assumption would be required to produce a definite prediction for mean velocity profile.

In recent investigations, the mean flow properties of turbulent pipe flows have obtained some new attention of turbulent flows researchers. Among the questions that were forwarded through these recent studies, the question arose whether there is a difference between pipe and channel flows in comparison to the flat-plate boundary layer flow, see Refs. [1–3]. Recent publications indicated that it is unlikely that the tripping has an effect on the friction factor in turbulent pipe flows, e.g., Refs. [4–7]. This finding was a big surprise to various people active in turbulent research.

The fully developed turbulent flow represents a state of the flow in a pipe that is well-defined, and it has been the subject of numerous investigations of engineers and scientists interested in its basic properties and in understanding fully developed turbulence [8,9]. A good number of publications resulted out of studies of fully developed turbulent pipe flows, yielding the general conviction that the mean flow properties of this flow are fully understood, e.g., Refs. [10–13].

The data published by Nikuradse [14] in 1932 and by Zagarola and Smits [15] in 1998 for turbulent pipe flow experiments represent the most extensive studies of the mean flow and mean pressure gradient measurements of high Reynolds number fully developed turbulent pipe flows. Nikuradse [14] documented impressive investigations in basic turbulent flows, showing good data of mean pressure gradient measurements and Pitot tube measurements of the mean velocity distributions in pipe and channel flows. Data are made available also for high Reynolds number and the experimental test rig, and the employed measuring procedures are described with care. Recently, Zagarola and Smits [15] performed measurements of the mean velocity profile and pressure drop in a fully developed, smooth pipe flow for Reynolds numbers from 31×10^3–35×10^6. The friction factor data at high Reynolds numbers were found to be significantly larger ($>5\%$) than those predicted by Prandtl's relation. A new friction factor relation is proposed, which is within $\pm1.2\%$ of the data for Reynolds numbers between 10×10^3 and 35×10^6, and includes a term to account for the near-wall velocity profile. In the present paper, Nikuradse's pipe flow measurements and the data of Zagarola and

Contributed by the Fluids Engineering Division of ASME for publication in the JOURNAL OF FLUIDS ENGINEERING. Manuscript received August 12, 2007; final manuscript received April 19, 2009; published online June 16, 2009. Assoc. Editor: Timothy J. O'Hern.

Smits are considered in detail and are compared with the authors own results. However, the present friction factors have been calculated from the mean pressure gradient measurements and from the corresponding mean velocity distributions. The mean static pressure measurements at different pipe stations in the fully developed flow region were used to evaluate the streamwise pressure gradient dp/dx, which in turn was employed to obtain the wall shear stress and the wall friction velocity u_τ.

In order to carry out such experimental investigations, the following criteria must be fulfilled to yield reliably the information on the shape of the normalized mean velocity distribution. Shear stress measurements must be carried out with high care. The data must be averaged over a high enough number of statistically independent measurements. The mean velocity measurements must be performed with a measurement technique that provides the highest spatial resolution needed to yield local measurements even at the highest Reynolds numbers of the flows. Pitot tubes do not usually provide the required spatial resolution. The mean velocity data must be first employed to evaluate the drag coefficient.

It is the aim of the present work to carry out pipe flow measurements in order to study the tripping effects. The experimental investigations were carried out at LSTM-Erlangen by using the pipe test set up and also the hot-wire equipment employed to yield the gradients of mean velocity profiles in turbulent pipe flows. All of these measurements for turbulent pipe flow investigations are connected to the data acquisition (DAQ) system. After making wall shear stress measurements for a pipe without tripping in its entrance, the tripping percentage was changed by installing a ring at the pipe entrance in order to yield turbulent pipe flows and to study tripping effects on the friction factor. The hot-wire measurements are repeated in order to see whether the slope of the mean velocity profile in the logarithmic region will stay the same over the entire flow regime from the nontripping into the tripping flow.

The authors of this paper also carried out such investigations yielding reliable information on the tripping effects on the drag coefficient and on the shape of the normalized mean velocity distribution. This finding and other observations in their measurements have encouraged us to suggest a sequence of measurements and data evaluations for investigating fully developed pipe flows. The test rig and its employment for pressure drop and mean velocity investigation are described in this paper. The mean velocity measurements in pipe flows and their evaluation were carried out, and the results were summarized. Finally, the paper shows very good agreement for all investigations of the friction factor measurements at different tripping percentages with the measurements available from the literature. Also, a comparison of the wall friction coefficient versus friction-velocity Reynolds number for different tripping conditions with the data of Zagarola and Smits [15] has been carried out.

2 Existing Knowledge on Friction Factor of Turbulent Pipe Flow

Numerous experimental and numerical investigations have been devoted to turbulent pipe flows. Information of the mean velocity distribution in fully developed turbulent pipe flow is available in the literature, and is being continuously updated with data from measurements and numerical predictions providing higher precisions year by year, and also for higher and higher Reynolds numbers. In recent years, turbulent circular pipe flows have become again of interest to turbulence research, e.g., Refs. [15–17].

Pipe flow investigations can be considered as one of the most extensively studied flows and among the most commonly cited experiments in smooth pipes is that by Nikuradse [14]. Nikuradse's data cover a significant range of Reynolds number (three orders of magnitude) and therefore it becomes the metric by which theories have been established and judged. However, Nikuradse's data have also been the subject of intense scrutiny, and this scrutiny has revealed inconsistencies and uncertainties in his data, e.g., Refs. [15,18]. The inconsistencies and uncertainties in Nikuradse's data, which resulted from uncertainties in the measurement technique, underscore the importance of a new precise experiment that permits accurate measurements over a large range of Reynolds numbers. The results presented in this paper include measurements of the mean velocity profile and pressure drop for 15 different Reynolds numbers between 1.0×10^5 and 4.5×10^5. Nikuradse [14] reported 141 friction factor measurements, and this large number of friction factor measurements can lead to a good statistical analysis.

At high Reynolds numbers, the mean flow in the outer layer must scale with the other variables: typically D as length scale and U_m or U_c as velocity scale. In the wall shear region, the dynamics are substantially influenced by viscosity, so the relevant length scale is $\ell_c=\nu/u_\tau$, where ν is the kinematic viscosity of the fluid. The wall friction velocity, u_τ, used for normalization was deduced from the pressure gradient measurements in the downstream part of the pipe test section, where a fully developed flow exists. The mean velocity profiles were then normalized using the corresponding shear velocity to yield $U^+=U/u_\tau$ and the wall distance with the viscous length scale, $l_c=\nu/u_\tau$, to give $y^+=y/l_c$. The wall units ℓ_c and u_τ lead to the definition of a friction-velocity Reynolds number

$$\mathrm{Re}_\tau = Du_\tau/\nu = D/\ell_c \tag{1}$$

The relations between the different Reynolds numbers are monotonic in the laminar and in the developed turbulent regime. A comparison between the turbulent and laminar profile corresponding to a given flow rate leads to the definition of friction factors

$$c_f = \tau_w/(\rho U_m^2/2) = 2(u_\tau/U_m)^2 = 2(\mathrm{Re}_\tau/\mathrm{Re}_m)^2 \tag{2}$$

For the steady laminar velocity profile, an analytical relation between all these characteristics exists. For laminar circular pipe (Hagen–Poisseuille) flow, it is

$$U_m = U_c/2 \tag{3}$$

$$c_f = 16/\mathrm{Re}_m \tag{4}$$

3 Test Rig and Measurement Equipment

To answer the open question indicated in the introduction regarding the effects of tripping of turbulent pipe flows at the pipe inlet, an experimental investigation has been conducted, and the measurements were carried out, yielding additional friction factor information on turbulent pipe flow. Measurements with and without tripping devices of different blocking areas, 10%, 20%, 30%, and 40%, were carried out to see the effect of entrance condition on the developing flow field in pipe. For this purpose a test rig was set up at the Institute of Fluid Mechanics (LSTM) of the Friedrich-Alexander-University of Erlangen-Nürnberg using an open type wind tunnel and the pipe flow test section described already by Zanoun and Durst [19] to study fully developed turbulent pipe flows to yield information on the normalized mean velocity distribution. The pressure loss measurements have been performed in the Re-number range of $1\times10^5\leq\mathrm{Re}\leq4.5\times10^5$.

3.1 Wind Tunnel and Pipe Flow Test Section. To carry out fully developed turbulent pipe flows, a test rig described in detail in Refs. [7,19] was used. Measurements at moderately high Reynolds number, $\mathrm{Re}\leq500\times10^3$, have been carried out. The pipe test section was made of a high precision smooth brass tube of surface roughness measured to be approximately equal to 0.25 μm, which in terms of wall units is less than 0.03 for the maximum Reynolds number. The pipe is therefore hydrodynamically smooth at all Reynolds numbers reported in this study. The test pipe has a nominal diameter (D) of 148 mm and is 14 m long, i.e., $L/D\approx95$ and consists of three sections connected together by custom-designed couplings. A sketch of the pipe flow test section showing the pipe entrance with tripping device is shown in Fig. 1, and a schematic of the pipe test facility showing the plenum

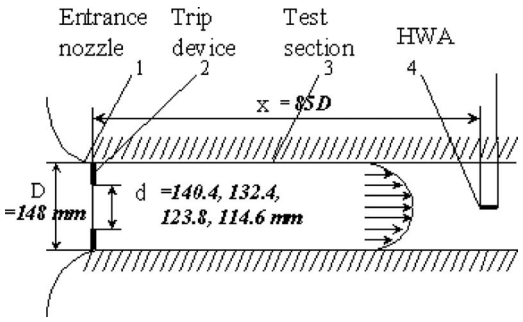

Fig. 1 Sketch of the pipe flow test section showing the pipe entrance with tripping device and measuring test section

chamber measuring test section and the pressure taps at different pipe positions is shown in Fig. 2. A contraction using a two-cubic arc profile was used between the plenum chamber and the pipe test section to assure a smooth inlet to pipe test section. This contraction has an area ratio of 11.4 and was made out of hard wood and was circular in cross section.

In this test rig the air flow was provided by a centrifugal blower which has a maximum capacity of 10 m^3/s, powered by 20 kW motor. The air is supplied through a well designed settling chamber to improve flow uniformity. The chamber is provided with two perforated plates directly downstream of the blower and then with a honeycomb of 8 mm mesh size and 160 mm length. Thereafter, four screens of 1 mm mesh size have been installed inside the chamber to get flow with high quality and of low background turbulence level, less than 0.6% at pipe entrance. The passive devices, perforated plates, honeycomb, and four screens were designed and arranged properly to minimize any flow swirling and other lateral velocities. The entire flow was setup in accordance with Ref. [20]. The flow rate for each investigated Reynolds number was controlled by changing the speed of the radial blower blades by means of a frequency converter control unit, providing impeller rotational speeds of approximately 100–2000 rpm. This corresponded to a mean velocity range of the pipe flow from 2 m/s to 45 m/s with a centerline turbulence level of less than 0.6% at the axis of the pipe inlet cross section. The mean volume flow rate is measured at the pipe entrance using a Pitot tube, which is connected to very precise pressure transducer and 16 bit DAQ card.

An inlet fence was used to trigger the turbulence development along the pipe length. The tripping devices have been used to see the effect of entrance condition on flow regime and to invoke turbulence with a shortest developing length, see, e.g., Refs. [21,22]. As shown in Fig. 2, the fence was mounted at the pipe entrance, i.e., at $x=0$, with a percentage blocked area of $(D^2-d^2)/D^2=10$, 20, 30, and 40% to trigger the flow over the circumference of the pipe cross section. The height of this tripping fence was chosen according to investigations by Fischer [23] to ensure a well-tripped turbulent pipe flow at the measuring location and also to study the effect of tripping on the friction factor and mean velocity profiles.

It ensured that turbulent flow properties were sufficiently well reached at the measuring station, i.e., at $X/D=85$, where all velocity measurements are reported. This measuring location was considered to be sufficiently far downstream to ensure a fully developed turbulent pipe flow and was far enough away from the pipe outlet, $10D$, to ensure no outlet disturbances to the flow, e.g., Ref. [14]. Patel [24] concluded that both the mean and the fluctuating velocity distributions in a turbulent pipe flow indicate full development for a downstream distance of $50-80D$. For each investigated flow in the present study, the mean flow velocity was measured at the pipe entrance using a Pitot tube.

The last station for wall pressure measurements was at the measuring station, where velocity data were acquired using a Pitot tube and a hot-wire anemometer. For each investigated flow, the mean flow velocity was obtained by measuring the pressure drop of the venturi flow nozzle installed at the blower inlet. Also, some measurements for the mean flow velocity at the pipe entrance using a Pitot-static probe were carried out. In addition, it was also obtained by integrating the velocity profile at the measuring station $(X/D=85)$ for each Reynolds number using a Pitot tube and a hot-wire anemometry to ensure a good assessment of the mean flow velocity, $\bar{U}$, for each case. The mean flow velocity was then used to compute the mean velocity based Reynolds number of the flow, $\mathrm{Re}_{\mathrm{mean}}=\bar{U}D/v$. A wide range of Reynolds numbers up to $\mathrm{Re}_{\mathrm{mean}}\approx 4.5\times 10^5$ was covered.

3.2 Measuring Equipment and Application

3.2.1 Pressure Measurements. The present pipe test section was prepared with pressure taps for wall pressure measurements along the pipe at ten different stations, one meter apart. Three static pressure taps of 300 μm inner diameter were installed at each station for pressure measurements in the streamwise direction. Care was taken to ensure that the inner surface of the top side of the pipe, where the holes were drilled, was free from drilling problems (i.e., smoothness was insured around the pressure taps). The entire investigations and the analysis of the flow are similar to that described by Zanoun [7]. The distance in the upstream direction before the first station for the pressure measurements was 3.5 m, corresponding to an $X/D\approx 24$. This distance from the inlet was found to be sufficient to ensure a full development of pressure. Observations made by Patel and Head [25] indicated that the mean pressure gradient showed an earlier state of full develop-

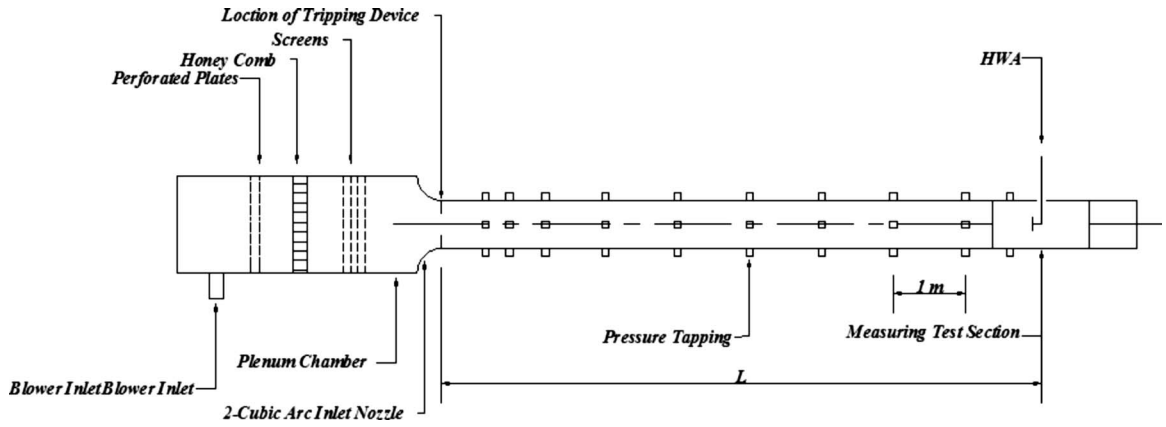

Fig. 2 Schematic of the pipe flow test setup showing the plenum chamber, measuring test section and the pressure taps at different pipe positions

ment, at $10-20D$ from the pipe inlet test section. The last station for wall pressure measurements, where hot-wire measurements were also carried out, was far enough away from the pipe outlet, i.e., $X/D=10$, to ensure that there were no outlet disturbances to the investigated flows. The pressure transducer was used for measuring the pressure with an accuracy of $\pm 0.25\%$ of the actual reading. All pressure measurement points were connected to a scan valve to facilitate switching from one point to another, and the corresponding static pressure was then measured and recorded for different air flow velocities.

3.2.2 Temperature Measurements. For temperature measurements, a special temperature sensor was used at all times during measurements within accuracy range of $\pm 0.05\,^{\circ}\mathrm{C}$ to measure the air temperature at the blower inlet, as well as before the pipe outlet, i.e., $X/D=10$.

3.2.3 Hot-wire Anemometry. The velocity profile measurements for the turbulent pipe flow investigations were carried out using a DANTEC 55M10 constant-temperature anemometer. The hot-wire measurements of the local velocity were carried out with a boundary layer probe (DANTEC, Type 55P15), equipped with a wire of 5 μm diameter and an active wire length of 1.25 mm, providing an aspect ratio, l/d, of 250. Hence the wire had a sufficiently large aspect ratio to suggest a negligible influence of the prongs on the actual velocity measurement. All calibrations and measurements were performed with a 70% overheat ratio.

Before each set of measurements, the hot-wire probe was calibrated against velocity measured with a Pitot tube at the pipe entrance where a uniform and well-defined flow field existed. The Pitot tube was installed directly at the centerline of the pipe input cross section, and its output was connected to a precision pressure transducer for both stagnation and static pressure measurements. In addition, the air temperature inside the tunnel was measured at all times during measurements within accuracy range of $\pm 0.05\,^{\circ}\mathrm{C}$. The ambient conditions were monitored before and during each test run using an electronic barometer and thermometer mounted in the same building of the laboratory. All electronic equipments were connected to an analog to digital (A/D) converter board from National Instruments (USA) with 16 bit resolution and 8 input channels. In addition, a computer-based programming system was used for acquiring and processing all the measured data.

To ensure that the original calibration curve was maintained during an entire set of hot-wire measurements, the calibration curves were rechecked after each set of measurements covering the entire range of velocities experienced in the wall region for each investigated flow case. If the deviations of the calibration were more than $\pm 1\%$, the entire set of data was rejected, and the measurements for the corresponding Re were repeated.

Hot-wire output is temperature dependent and therefore a correction for temperature drift is necessary, if the temperature of the working fluid cannot be kept constant during calibrations and measurements. Different methods are available in the literature to deal with the problem of air temperature effect on hot-wire output. A good treatment of the problem was given by Bearman [26], Bremhorst [27], and Crowell et al. [28]. For small temperature changes, i.e., approximately $\pm 5\,^{\circ}\mathrm{C}$, Bearman [26] introduced an expression to correct hot-wire output for the temperature drift. In the present study an instantaneous correction for the hot-wire output was carried out in case any temperature drift existed utilizing the relationship of Bearman [26].

The wall distance determination is of vital importance especially at high Reynolds number, where the thickness of the viscous sublayer is too small to be measured. Therefore, great care was taken to ensure a precise location of the hot wire at a reference distance from the wall. A calibration positioning procedure proposed by Bhatia et al. [29] and Durst et al. [30] was applied. The vertical location of the hot wire in the pipe was adjusted by measuring the hot-wire anemometer (HWA) output at zero flow velocity as close as possible to the pipe wall surface, and from the position calibration data close to the wall the corresponding position of the wire was estimated. The absolute error in the wire positioning was ± 20 μm.

In the present investigation, the aspect ratio of the hot wire l/d was 250, and the spatial resolution of the hot-wire probe was <25 times the viscous length scale. The measurements of Ligrani and Bradshaw [31] in the viscous sublayer of a flat-plate turbulent boundary layer in air, using single hot-wire sensors with lengths from 1–60 viscous length scales show that, at a given distance from the surface, the turbulence intensity, flatness factor, and skewness factor of the longitudinal velocity, fluctuations are nearly independent of wire length. This applies when the latter is less than 20–25 times the viscous length scale, and decreases significantly and abruptly for larger wire lengths. This is most evident for $8<y^{+}<17.5$, and the change becomes larger and more abrupt as the wall is approached. As well as defining the maximum sensor length acceptable for sublayer studies, the results of Ligrani and Bradshaw [31] show that there are significant effects of conduction on the supports for $l/d<200$; the final conclusion is that adequately accurate results for the mean-square and higher moments of the longitudinal velocity fluctuations near the wall can be obtained if $l^{+}=U_{\tau}$, $l/v<20$, and $l/d>200$.

3.2.4 Pitot Probe. The Pitot probe made a substantial contribution in early fluid dynamics research when Henri's Pitot tube was introduced in 1732. However, it has inherent problems when applied in highly sheared turbulent flows. Effects of some other factors such as turbulence, wall, compressibility, and vibration have to be accounted for when a Pitot probe is used for measurements, e.g., Ref. [32]. In the present study, the Pitot probe velocity measurements were obtained by traversing a total-head probe of 0.25 mm inner diameter over half of the pipe cross section. To obtain the dynamic head for velocity calculation, the wall static pressure was measured 6D in the downstream direction of the Pitot opening. Using the incompressible Bernoulli equation, the Pitot probe measurements were converted to velocity. Furthermore, the zero position of the Pitot probe was specified by measuring the resistance between the pipe wall and the body of the Pitot probe. The absolute error in positioning the Pitot probe was found to be less than ± 20 μm. The outlet of the Pitot tube was connected to a precision pressure transducer operated by a computer with a 16 bit DAQ card.

4 Pressure Measurements and Friction Factor Evaluations

Measurement of the local skin friction is an essential quantity in a wide range of wall-bounded shear flow applications. For instance, accurate estimation of the logarithmic skin friction law requires methods for accurate wall shear stress measurements. A wide variety of measuring techniques is available for determining the wall shear stress and therefore the skin friction factor, e.g., Refs. [33,34]. The wall shear stress measurements at the measuring location were an essential part of the present pipe flow study, and the wall friction data were obtained utilizing the mean pressure gradient measurements.

Hence, to provide the basis for the present pipe data analysis, the streamwise pressure measurements along the pipe test section were carried out for each investigated Re_m of the flow to obtain the wall shear stress, τ_w. Three static pressure taps at each measuring station were installed for pressure measurements. Several measuring techniques were employed to yield the needed friction factor and mean velocity information, and these techniques are briefly described below.

Undoubtedly, the most common and widely used method in pipe flows to get the local wall shear stress is based on mean pressure gradient measurement, which is used in the present study. To satisfy all requirements for the accurate determination of the wall skin friction coefficient, the pipe side wall effect on the wall

shear stress was determined independently of the velocity distribution using the pressure gradient measurements.

There have been numerous investigations on turbulent pipe flows and among the most studied properties of these flows is the pressure loss in the pipe or the related momentum loss to the wall

$$\tau_w = -\frac{D}{4}\frac{dp}{dx} \tag{5}$$

where τ_w is the wall shear stress, D is the pipe diameter, and dp/dx is the pressure loss. In wall-bounded turbulent flows, the wall shear stress is conventionally expressed in terms of the local skin friction coefficient, i.e., in dimensionless form, as

$$c_f = \frac{\tau_w}{1/2(\rho \bar{U}^2)} \tag{6}$$

where c_f is the friction factor, ρ is the density of fluid, and $\bar{U}$ is the cross-sectional mean velocity. The velocity scale relevant close to the wall is the friction velocity

$$u_\tau = \sqrt{\tau_w/\rho} \tag{7}$$

By introducing the definition of the wall friction velocity, Eq. (7), Eq. (6) can be rearranged to yield

$$c_f = 2\left(\frac{u_\tau}{\bar{U}}\right)^2 \tag{8}$$

Therefore, by means of Eq. (6), it was easy to determine the wall skin friction coefficient experimentally by measuring the integral flow parameters, $\bar{U}$, and dp/dx. As it was mentioned in Sec. 3.2, the hot-wire measurements have been carried out with a high level of accuracy, and the measurements were repeated if the deviations of the calibration were more than $\pm 1\%$. The inaccuracy of $\bar{U}$ was less than $\pm 1\%$ and the pressure transducer, which was used for measuring the pressure, has an accuracy of $\pm 0.25\%$ of the actual reading and therefore the error in dp/dx is $\pm 0.25\%$. The uncertainty value for the friction factor c_f has been calculated using the method of Kline and McClintock [35] and has been found to be less than $\pm 1.15\%$.

The air temperature inside the settling chamber and inside the pipe test section was measured all the time during measurements. Simultaneously to the pressure measurements and in correspondence with the air stream temperature in the pipe test section, the air density and kinematic viscosity were calculated for the purpose of normalization using the following ideal gas relations, (e.g., Ref. [18]), for density:

$$\rho = \frac{(P_{\text{atm}} + P_{\text{st}})}{\Re T} \tag{9}$$

and for the kinematic viscosity the well-known Sutherland's correlation

$$v = 1.458 * 10^{-6}\frac{T^{3/2}}{\rho(T + 110.4)} \tag{10}$$

where P_{atm} is the atmospheric pressure, P_{st} is the mean static pressure, $\Re = 279.1$ J/kg K is constant for air under the ideal gas law, and T is the temperature of the flow.

5 Pressure and Friction Factor Results

Through drilled small holes along the pipe wall in both the streamwise and the spanwise directions, pressure gradient measurements were obtained. The resultant mean wall static pressure, P_{st}, measurements at various locations in the fully developed flow region, which is shown in Fig. 3, were then used to evaluate the streamwise pressure gradient, dp/dx, which is shown in Fig. 4, and, in turn, was employed to obtain the wall shear stress and the wall friction velocity, u_τ. Figure 3 indicates that the flow field was fully developed for all cases under investigation, at least as far as the pressure distribution in the flow direction is concerned. In addition to static pressure measurements, the bulk flow velocity for each set of measurements was obtained by measuring the dynamic pressure through an inlet nozzle to the settling chamber, where a uniform and well-defined flow field existed. The pressure difference between nozzle inlet and throat of the nozzle was measured utilizing a highly precision pressure transducer whose uncertainty is $\pm 0.25\%$ of the actual reading.

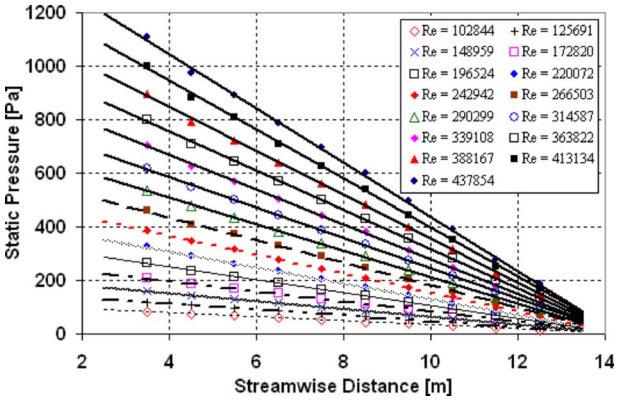

Fig. 3 Pressure gradient distribution along part of the pipe test section at different Reynolds numbers

The authors performed pressure loss measurements in the Re-number range of $1 \times 10^5 \leq \text{Re} \leq 4.5 \times 10^5$. Evaluation of the wall skin friction coefficient was conducted, and the results obtained from the streamwise pressure gradient are presented in Fig. 5 in a form of c_f as a function of Re_m.

Hence, the wall skin friction data were obtained independently of the detailed velocity data using the pressure gradient measurements provided in Fig. 4 in connection with the bulk velocity. In pipe flow, it is, however, common to express the flow pressure drop in terms of the friction factor instead of the wall friction velocity as follows:

$$\lambda = 4c_f = 4\frac{\tau_w}{1/2(\rho \bar{U}^2)} = -4\left[\frac{D}{4}\frac{dp}{dx}\right]\frac{1}{1/2(\rho \bar{U}^2)} \tag{11}$$

and by introducing the definition of the wall friction velocity, Eq. (11) could be rewritten as

$$\lambda = 8\left[\frac{u_\tau}{\bar{U}}\right]^2 \tag{12}$$

Figure 6 shows the present pipe Darcy friction factor, λ, as a function of the friction-velocity Reynolds number. As a result, the wall skin friction data were obtained independently of the velocity

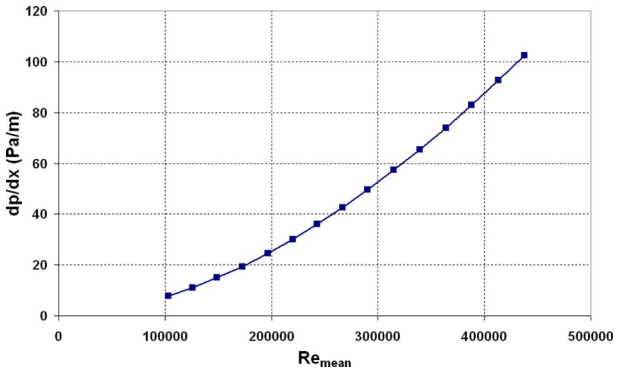

Fig. 4 The streamwise pressure gradient, *dp/dx*, as a function of the mean-based Reynolds number, Re_{mean}

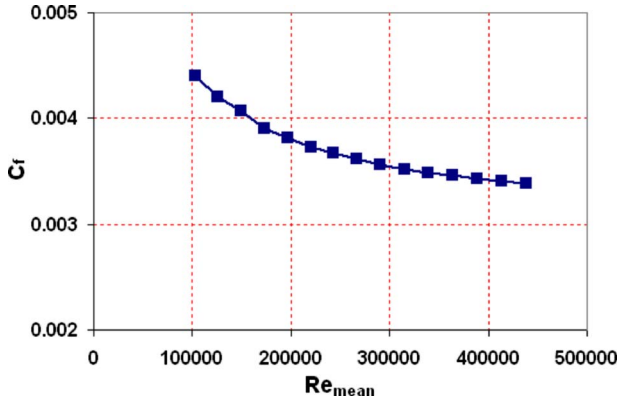

Fig. 5 Pipe wall skin friction coefficient, c_f, as a function of the mean-based Reynolds number, Re_{mean}

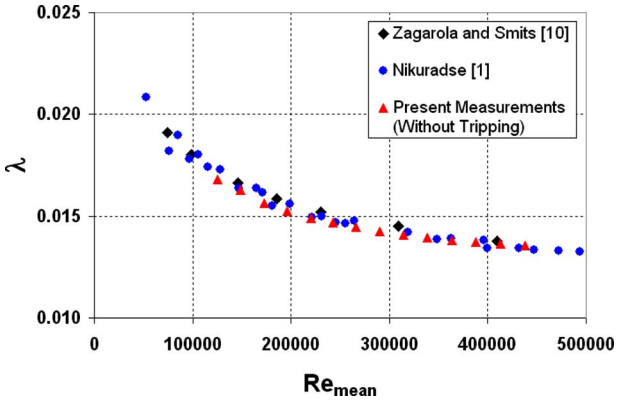

Fig. 7 Pipe Darcy friction factor, λ, for the present nontripping measurements over an intermediate range of Reynolds numbers compared with Nikuradse's data [14] and Zagarola and Smits [15]

profile using the pressure gradient measurements provided in Fig. 3. Thereafter, the wall friction velocity, u_τ, and the kinematic viscosity, v, were used for scaling all results to yield the normalized velocity distribution over the pipe radius.

The local wall shear stress is a very important quantity in both practical developments and fundamental studies. Each measurement was repeated at least three times. A good analysis of friction factor measurement of pipe flows was given by Nikuradse [14], summarizing all the work up to 1932. He contributed to the subject by carrying out detailed measurements in pipe flows of different diameter yielding $c_f(\mathrm{Re})$ in the range of $3\times10^3 \leq \mathrm{Re} \leq 3\times10^6$. To generalize the pressure drop measurements reported in Sec. 4, the pressure drop measurements were evaluated to yield the corresponding friction coefficient. Figure 7 shows the pipe skin friction coefficient as a function of the Reynolds number based on the average velocity. It also shows the pipe friction data, λ, for the investigated fully developed, turbulent pipe flows in comparison to data extracted from the literature. A quite good agreement can be observed between the results of Darcy friction factor for the present study and data reported by Nikuradse [14] and Zagarola and Smits [15].

6 Tripping Effects on the Friction Factor

As mentioned previously, tripping devices are usually installed at the entrance of laboratory-scale pipe test sections to obtain a fully developed turbulent flow sooner. Tripping can be obtained by using cylindrical wires, sand papers, well-organized tape elements, and fences.

The characterization of the mean velocity in developed turbulent pipe flow has been well understood. Detailed experimental data are available over a wide range of Reynolds numbers, including the measurements by Nikuradse [14] or the more recent "superpipe" measurements documented, e.g., in Ref. [15]. To provide the basis for the present data analysis, the streamwise pressure gradient measurements were carried out for the tripping cases to obtain the wall shear stress in the pipe for each investigated Re_m of the flow. Results of static pressure gradient measurements in the streamwise direction are presented in Fig. 8. The results show that the tripping has no effect on the mean pressure gradient. Also,

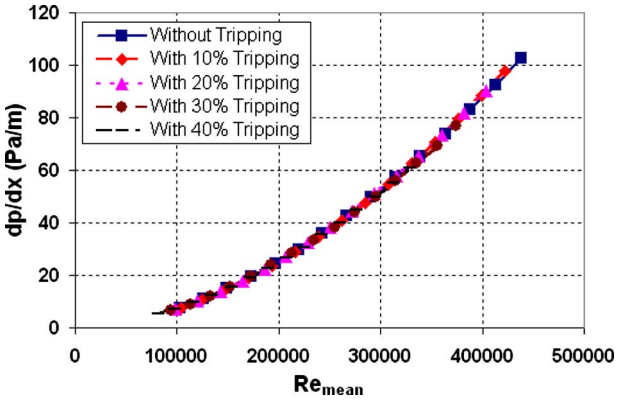

Fig. 8 The streamwise pressure gradient, *dp/dx*, as a function of Reynolds numbers for tripping and nontripping conditions

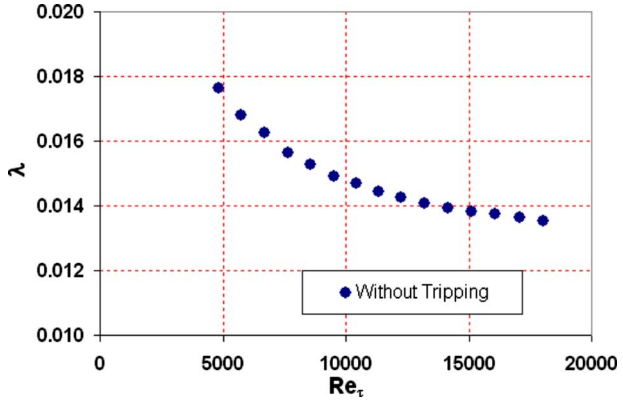

Fig. 6 Pipe Darcy friction factor, λ, as a function of the friction-velocity Reynolds number

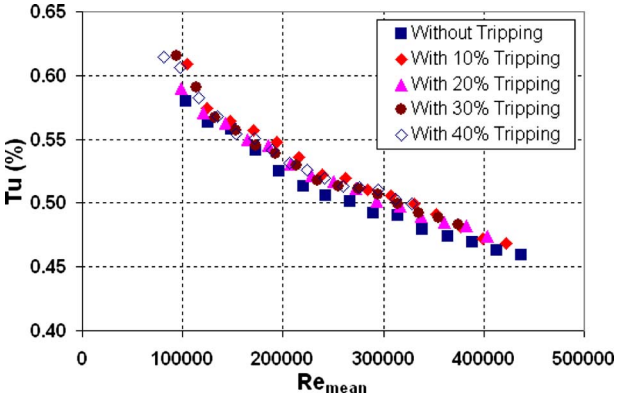

Fig. 9 Turbulence Intensity versus Reynolds number for tripping and no-tripping conditions

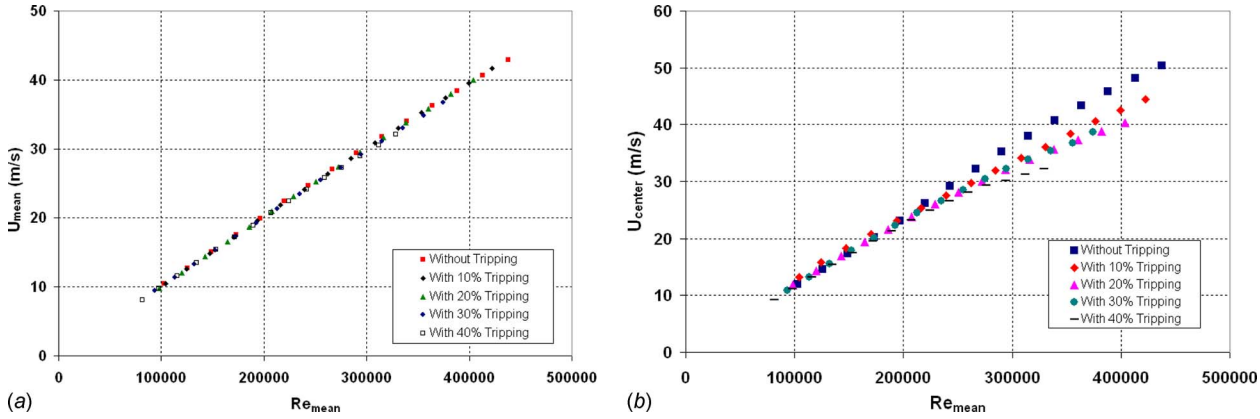

Fig. 10 Pipe mean flow velocity (*a*) and centerline flow velocity (*b*) versus Reynolds number for tripping and nontripping conditions

the tripping has very small effect on the turbulence level, which is less than 0.6% at pipe entrance for all examined cases as shown in Fig. 9. Figure 10 shows the mean and centerline flow velocities of the pipe as a function of Reynolds number for tripping and nontripping conditions. Unlike the mean pressure gradient and the turbulence intensity, the centerline velocity shows a deviation between the tripping and nontripping conditions at high Reynolds number because the presence of tripping devices at the pipe entrance works as a new resistance to the flow. Therefore, the centerline flow velocity at high Reynolds number decreases slightly as the percentage of tripping increases, as shown in Fig. 10, but the bulk flow velocity remains identical for tripping and nontripping conditions. The maximum mean flow velocity decreases as the percentage of tripping increases and the maximum value of Reynolds number at 40% tripping is 3.3×10^3. The relationship is linear and again there is no difference between tripping and nontripping conditions, but the maximum value of the mean flow velocity decreases as the tripping increases because the power of the blower fan is constant, as shown in Fig. 10(*a*).

The experimental investigations of the friction coefficients were conducted with and without tripping devices of different blocking areas, 10%, 20%, 30%, and 40%. The tripping devices were mounted at the pipe entrance to trigger the flow over the circumference of the pipe cross section, and the results obtained from the streamwise pressure gradient are presented in Fig. 11 in a form of λ as a function of Reynolds number. The procedure that was followed here for representing our experimental data is based on measuring the pressure gradient for each investigated flow velocity. As can be seen, the friction factor profile for the experimental data in the absence of tripping devices agree very well with the tripping results over the whole range of the Reynolds numbers. Figure 11 shows also a comparison between the present data and the data of Nikuradse, and a quite good agreement was observed. No difference between tripped and nontripped results and also for Nikuradse data [14] was obtained. The resultant friction factor distributions are presented in Fig. 11 over a Re-range of $1.0 \times 10^5 \leq \mathrm{Re}_m \leq 4.5 \times 10^5$.

Figure 12 shows the results of the pipe Darcy friction factor for fully developed pipe flow and comparison with tripping data as a function of the Reynolds number based on friction velocity. This figure presents similar results, as shown in Fig. 11, but the abscissa, which is the Reynolds number based on the mean velocity, has been replaced by friction-velocity Reynolds number, Re_τ. A wide range of friction-velocity Reynolds numbers up to $\mathrm{Re}_\tau \approx 20{,}000$ was covered.

The authors' fully developed, turbulent pipe flow data were also compared in the form $c_f(\mathrm{Re}_\tau)$ with the corresponding results of fully developed turbulent pipe flows. Very good agreement was obtained, and it was felt that the present measurement in the pipe flow study was sufficiently accurate to yield good τ_w-information from the pressure drop measurements to ensure a reliable normalization of the measured mean velocity measurements. Figure 13 shows the experimental data obtained with the present pipe test rig for the wall friction factor as a function of the Reynolds number that is based on friction velocity, which is in excellent agreement with the results of tripping conditions with different blocking ratios.

Figure 14 shows a comparison between the present pipe skin

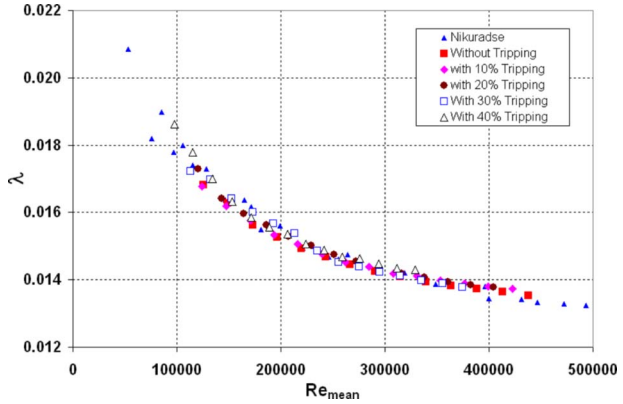

Fig. 11 Pipe Darcy friction factor versus Reynolds number based on mean velocity for tripping cases compared with Nikuradse's data

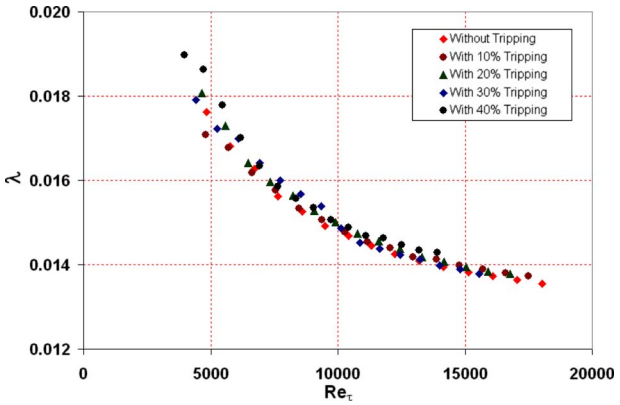

Fig. 12 Pipe Darcy friction factor versus Reynolds number based on friction velocity compared with tripping results

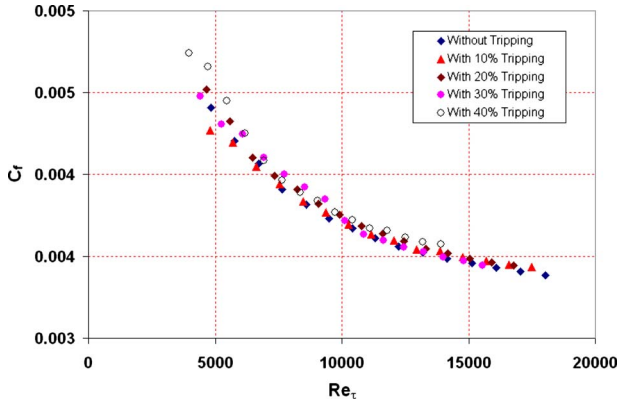

Fig. 13 The wall friction coefficient versus Reynolds number based on friction velocity compared with tripping results

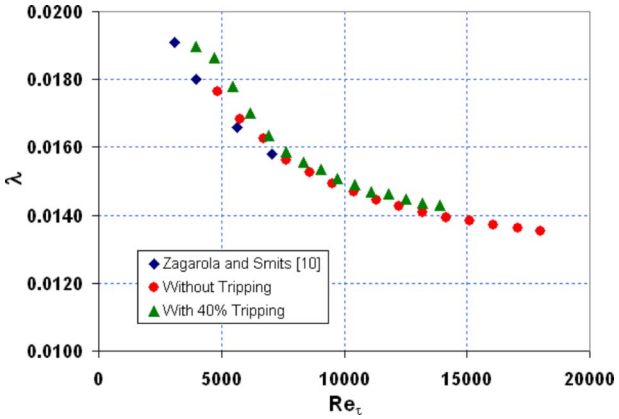

Fig. 14 The present wall friction coefficient versus friction-velocity Reynolds number compared with Zagarola and Smits [15] results

friction coefficient as a function of the friction-velocity Reynolds number and the recent results of Zagarola and Smits [15]. As can be seen in the figure, a very good agreement between the present tripping, nontripping, and Zagarola and Smits [15] results can be observed.

The present data were obtained by means of hot-wire anemometry to yield the mean velocity measurements needed to correctly deduce the corresponding c_f(Re)-relationship. The results were compared with the corresponding experimental c_f(Re)-distribution for tripping and nontripping conditions. These data yielded a c_f(Re)-relationship in good agreement with the authors experimental findings deduced from pressure drop measurements. Figure 15 shows the dimensionless mean velocity distributions $U^+ = F(y^+)$ of the present measurements, the measurements of Zagarola and Smits [15] and the comparison of the present data with those of Zagarola and Smits [15] at different values of Reynolds numbers. The data of the present measurements, which are shown in Fig. 15, are related to the nontripping conditions. Figure 16 shows the present mean velocity distribution for no tripping and 10% tripping conditions compared with the data of Zagarola and Smits [15] at two values of Reynolds numbers. A good agreement can be shown between the present data, which has been carried out at no tripping and 10% tripping conditions, with the data of Zagarola and Smits, which has been carried out at nontripping conditions. In Fig. 16, there are some differences in profiles be-

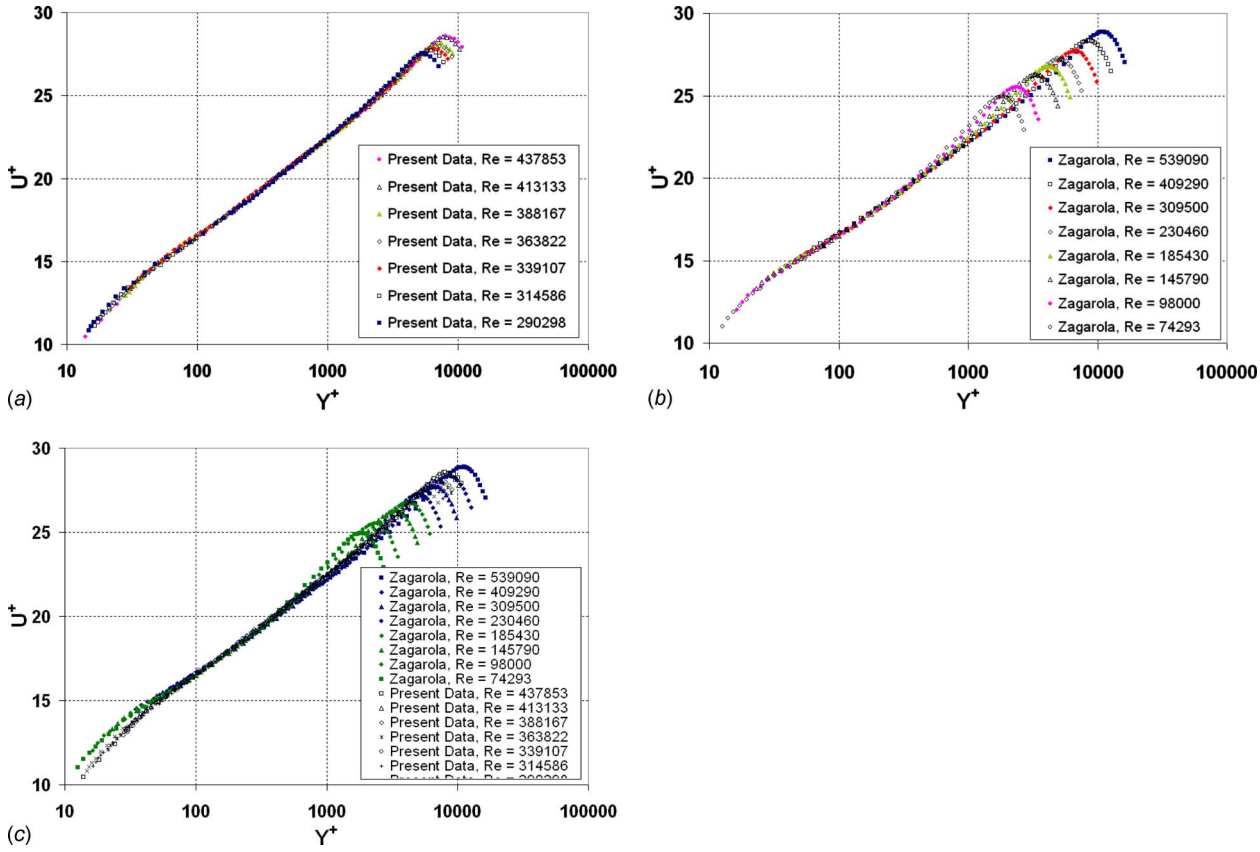

Fig. 15 The normalized mean velocity distribution as a function of the normalized channel height at different values of Reynolds numbers for both data of the present measurements and the data of Zagarola and Smits

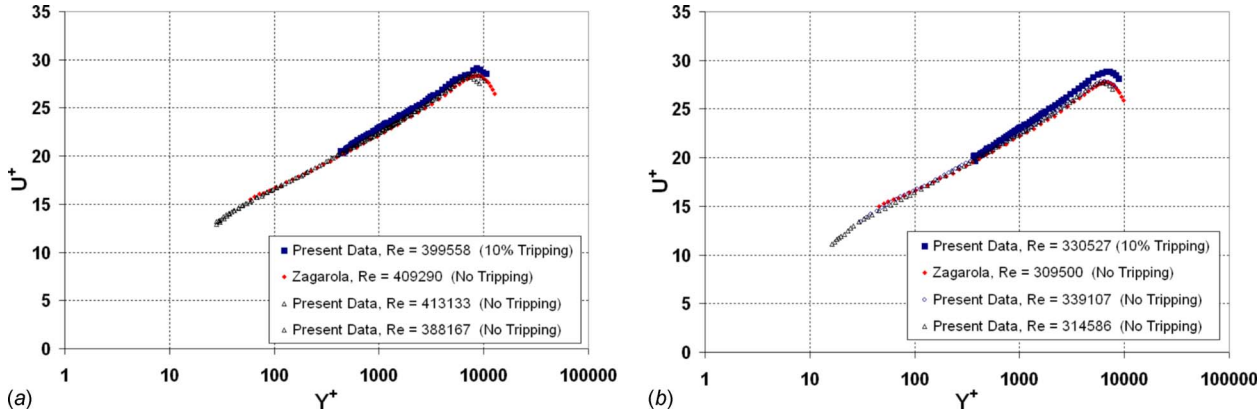

Fig. 16 The present mean velocity distribution for no tripping and 10% tripping conditions compared with the data of Zagarola and Smits at (*a*) Re=409,290 and (*b*) Re=309,500

yond $y+=1000$, and this is due to the differences in the Reynolds numbers between the current measurement at 10% tripping and those of Zagarola and Smits. The difference in profiles can be attributed also to the slight error in wall proximity in probe.

7 Conclusions

In the present study, the authors performed pressure loss measurements in the Re-number range of $1\times10^5\leq\mathrm{Re}\leq4.5\times10^5$ to determine the effect of entrance condition on the developing flow field in pipes. Using various tripping devices in cross-sectional blockages corresponding to 10%, 20%, 30%, and 40% of the cross-sectional area of the pipe employed in the present investigations; measurements with and without ring tripping devices of different blocking areas have been carried out. In addition to the pressure gradient measurements to compute the wall skin friction, both Pitot tube and hot-wire anemometry measurements have been used to accurately determine the mean velocity profile over the working test section at different Reynolds numbers. The strength of the conclusions formed from these results rests in the uncertainties in the measurements. Samples of the Darcy coefficient factor as a function of the Reynolds number for the current measurements and also for the Nikuradse data have been presented in this paper. It is clear from the results that the flow field was fully developed for all cases under investigation, at least as far as the pressure distribution in the flow direction is concerned. The measurement results of the wall friction coefficient for the fully developed turbulent pipe flow show that the tripping technique has an insignificant effect on the wall friction factor, in agreement with the original data provided by Nikuradse and the recent pipe data from Zagarola and Smits. The slight variation on the mean profiles beyond $y+\sim1000$ can be attributed to the differences in the Reynolds numbers between the current measurement and those of Zagarola and Smits in addition to the error in wall proximity in probe. Hence, the present results of the pipe Darcy friction factor show that our results for tripped and nontripped conditions are in very good agreement. Finally, the open question about the effects of tripping of turbulent pipe flows on the friction factor was clarified in the present work, and the measurements, which were carried out, yielded additional friction factor information on turbulent pipe flow.

Acknowledgment

This work has been carried out during sabbatical leave granted to the Dr. Ahmed Al-Salaymeh from the University of Jordan during the academic year 2007/2008. The authors greatly appreciate the support received from the University of Jordan, deanship of scientific research, and the faculty of engineering and technology. The experimental work has been carried at the Institute of Fluid Mechanics (LSTM), Friedrich-Alexander-University, Erlangen-Nürnberg. Dr. Al-Salaymeh was financially supported by DFG (German Research Foundation) when carrying out the experimental part of this work. The authors gratefully acknowledge much helpful advice from Prof. F. Durst and Dr. E.-S. Zanoun. Also, the authors are very grateful for the assistance of Dipl.-Ing. H. Leinhart in some of the experimental phases of this work. All kinds of support are gratefully acknowledged.

Nomenclature

c_f = friction factor $\{c_f=\tau_w/(\rho U_m^2/2)\}$
d = fence (tripping device) inner diameter/wire diameter
D = pipe nominal diameter/Length scale
ℓ_c = viscous length scale $(\ell_c=\upsilon/u_\tau)$
l^+ = nondimensional sensor length scale
L = length of pipe test section
P_{atm} = atmospheric pressure
P_{st} = static pressure
P_0 = stagnation pressure
R = pipe radius
Re = Reynolds number $\{\mathrm{Re}=DU/\upsilon\}$
Re_τ = friction-velocity Reynolds number $\{\mathrm{Re}_\tau=Du_\tau/\upsilon\}$
t = time
T = temperature
U = streamwise velocity
$\bar{U}$ = mean flow velocity
U^+ = normalized streamwise velocity $\{U^+=U/u_\tau\}$
u' = streamwise velocity fluctuations
u_τ = wall friction velocity
x = streamwise distance
y = normal wall distance
y^+ = wall distance with the viscous length scale, l_c, $\{y^+=y/l_c\}$

Subscripts

c = characteristic quantities or centerline
m = arithmetic mean
x = streamwise distance
w = at the wall surface
∞ = at infinity/Free stream

Greek Letters

$\Re$ = gas constant
λ = Darcy friction coefficient
ρ = fluid density
μ = dynamic viscosity
ν = kinematic viscosity

τ = shear stress
τ_w = wall shear stress

References

[1] Dean, R. B., and Bradshaw, P., 1976, "Measurements of Interacting Turbulent Shear Layers in a Duct," J. Fluid Mech., **78**, pp. 641–676.
[2] Durst, F., Xie, M., and Zhao, J., 2003, "Investigation of the Mean-Flow Scaling and Tripping Effect on Fully Developed Turbulent Pipe Flow," J. Hydrodynam., **15**, (1), pp. 14–22.
[3] George, W. K., and Castillo, L., 1997, "Zero-Pressure-Gradient Turbulent Boundary Layer," Appl. Mech. Rev., **50**, pp. 689–729.
[4] Eggels, G. M., 1994, "Fully Developed Turbulent Pipe Flow: A Comparison Between Direct Numerical Simulation and Experiment," J. Fluid Mech., **268**, pp. 175–209.
[5] Kim, J., 1987, "Turbulence Statistics in Fully Developed Channel Flow at Low Reynolds Number," J. Fluid Mech., **177**, pp. 133–166.
[6] Laufer, J., 1953, "The Structure of Turbulence in Fully Developed Pipe Flow," Report No. NACA TN 2954.
[7] Zanoun, E.-S., 2003, "Answers to Some Open Questions in Wall-Bounded Laminar and Turbulent Shear Flows," Ph.D. thesis, Technische Fakultät der Universität Erlangen-Nürnberg, Erlangen, Germany.
[8] Afzal, N., and Yajnik, K. S., 1973, "Analysis of Turbulent Pipe and Channel Flows at Moderately Large Reynolds Number," J. Fluid Mech., **61**, pp. 23–31.
[9] Afzal, N., 1982, "Fully Developed Turbulent Flow in a Pipe: An Intermediate Layer," Ing.-Arch., **52**, pp. 355–377.
[10] Wosnik, M., Castillo, L., and George, W. K., 2000, "A Theory for Turbulent Pipe and Channel Flow," J. Fluid Mech., **421**, pp. 115–145.
[11] Buschmann, M. H., and Gad-el-Hak, M., 2004, "Comments on Evaluating the Law of the Wall in Two-Dimensional Fully-Developed Turbulent Channel Flows," Phys. Fluids, **16**, pp. 3507–3508.
[12] Buschmann, M. H., and Gad-el-Hak, M., 2005, "New Mixing-Length Approach for the Mean Velocity Profile of Turbulent Boundary Layers," ASME J. Fluids Eng., **127**, pp. 393–396.
[13] Österlund, J. M., Johansson, A. V., Nagib, H. M., and Hites, M. H., 2000, "A Note on the Overlap Region in Turbulent Boundary Layers," Phys. Fluids, **12**, pp. 1–4.
[14] Nikuradse, J., 1932, *Gesetzmässigkeit der turbulenten Strömung in glatten Rohren, Forschungsheft 356, Ausgabe B*, Vol. 3, VDI-Verlag, Berlin.
[15] Zagarola, M. V., and Smits, A. J., 1998, "Mean-Flow Scaling of Turbulent Pipe Flow," J. Fluid Mech., **373**, pp. 33–79.
[16] McKeon, B. J., and Smits, A. J., 2002, "Static Pressure Correction in High Reynolds Number Fully Developed Turbulent Pipe Flow," Meas. Sci. Technol., **13**, pp. 1608–1614.
[17] Morrison, J. F., Jiang, W., McKeon, B. J., and Smits, A. J., 2002, "Reynolds-Number Dependence of Streamwise Velocity Statistics in Turbulent Pipe Flow," AIAA Paper No. 2002-0574.
[18] Zagarola, M. V., 1996, "Mean Flow Scaling in Turbulent Pipe Flow," Ph.D. thesis, Princeton University, Princeton, NJ.
[19] Zanoun, E.-S., and Durst, F., 2003, "Evaluating the Law of the Wall in Two-Dimensional Fully Developed Turbulent Channel Flows," Phys. Fluids, **15**(10), pp. 3079–3089.
[20] Loehrke, K. I., and Nagib, H. M., 1972, "Experiments on Management of Free-Stream Turbulence," IIT Chicago, Illinois 60616, Sept., AGARD Report No. 598.
[21] Durst, F., Fisher, M., Jovanovic, J., and Kikura, H., 1998, "Methods to Set Up and Investigate Low Reynolds Number, Fully Developed Turbulent Plane Channel Flows," ASME J. Fluids Eng., **120**, pp. 496–503.
[22] Darbyshire, A. G., 1995, "Transition to Turbulent in Constant-Mass-Flux Pipe Flow," J. Fluid Mech., **289**, pp. 83–114.
[23] Fischer, M., 1999, "Turbulente wandgebundene Strömungen bei kleinen Reynoldszahlen," Ph.D. thesis, Universität Erlangen Nürnberg, Erlangen, Germany.
[24] Patel, R. P., 1974, "A Note on Fully Developed Turbulent Flow Down a Circular Pipe," Aeronaut. J., **78**, pp. 93–97.
[25] Patel, V. C., and Head, M. R., 1969, "Some Observations on Skin Friction and Velocity Profiles in Fully Developed Pipe and Channel Flows," J. Fluid Mech., **38**, pp. 181–201.
[26] Bearman, P. W., 1971, "Corrections for the Effect of Ambient Temperature Drift on Hot-Wire Measurements in Incompressible Flow," pp. 25–30, Dansk Industri Syndikat Aktieselskab Information Report No. 11.
[27] Bremhorst, K., 1985, "Effect of Fluid Temperature on Hot-Wire Anemometers and an Improved Method of Temperature Compensation and Linearization Without Use of Small Signal Sensitivities," J. Phys. E, **18**, pp. 44–49.
[28] Crowell, G. B., Jr., Daniel, H. W., and Henery, D. B., 1988, "Comparison of Temperature Correction Methods for Hot Wire Anemometers," Trans. ASAE, **31**(5), pp. 1552–1555.
[29] Bhatia, J. C., Durst, F., and Jovanovic, J., 1982, "Corrections of Hot-Wire Measurements Near Walls," J. Fluid Mech., **122**, pp. 411–431.
[30] Durst, F., Zanoun, E.-S., and Pashtrapanska, M., 2001, "In Situ Calibration of Hot Wires Close to Highly Heat-Conducting Walls," Exp. Fluids, **31**, pp. 103–110.
[31] Ligrani, P. M., and Bradshaw, P., 1987, "Spatial Resolution and Measurement of Turbulence in the Viscous Sublayer Using Subminiature Hot-Wire Probes," Exp. Fluids, **5**, pp. 407–417.
[32] Chue, S. H., 1975, "Pressure Probes for Fluid Measurements," Prog. Aerosp. Sci., **16**(2), pp. 147–223.
[33] Winter, K. G., 1979, "An Outline of the Techniques Available for the Measurement of Skin Friction in Turbulent Boundary Layers," Prog. Aerosp. Sci., **18**, pp. 1–57.
[34] Fernholz, H. H., Janke, G., Schober, M., Wagner, P. M., and Warnack, D., 1996, "New Development and Applications of Skin-Friction Measuring Technique," Meas. Sci. Technol., **7**, pp. 1396–1409.
[35] Kline, S. J., and McClintock, F. A., 1953, "Describing Uncertainties in Single Sample Experiments," Mech. Eng. (Am. Soc. Mech. Eng.), **75**, pp. 3–8.

Annular Extrudate Swell of Newtonian Fluids Revisited: Extended Range of Compressible Simulations

Evan Mitsoulis[1]
School of Mining Engineering and Metallurgy,
National Technical University of Athens,
Zografou, 15780 Athens, Greece
e-mail: mitsouli@metal.ntua.gr

*In a recent article (Mitsoulis, 2007, "Annular Extrudate Swell of Newtonian Fluids: Effects of Compressibility and Slip at the Wall," ASME J. Fluids Eng., **129**, pp. 1384–1393), numerical simulations were undertaken for the benchmark problem of annular extrudate swell of Newtonian fluids. The effects of weak compressibility and slip at the wall were studied through simple linear laws. While slip was studied in the full range of parameter values, compressibility was confined within a narrow range of values for weakly compressible fluids, where the results were slightly affected. This range is now markedly extended (threefold), based on a consistent finite element method formulation for the continuity equation. Such results correspond to foam extrusion, where compressibility can be substantial. The new extended numerical results are given for different inner/outer diameter ratios κ under steady-state conditions for Newtonian fluids. They provide the shape of the extrudate, and, in particular, the thickness and diameter swells, as a function of the dimensionless compressibility coefficient B. The pressures from the simulations have been used to compute the excess pressure losses in the flow field (exit correction). As before, weak compressibility slightly affects the thickness swell (about 1% in the range of $0 \le B \le 0.02$) mainly by a swell reduction, after which a substantial and monotonic increase occurs for $B > 0.02$. The exit correction increases with increasing compressibility levels in the lower B-range and is highest for the tube ($\kappa = 0$) and lowest for the slit ($\kappa = 1$). Then it passes through a maximum around $B \approx 0.02$, after which it decreases slowly. This decrease is attributed to the limited length of the flow channel (here chosen to be eight die gaps).* [DOI: 10.1115/1.3155996]

Keywords: annular flow, extrudate swell, exit correction, foam extrusion, blow molding, Newtonian fluid, compressibility, linear law

1 Introduction

Annular flow occurs in many processes, such as blow molding and pipe extrusion in polymer processing [1], or in any material flow between two concentric cylinders [2]. The fully-developed flow problem of a Newtonian fluid in an annulus is one of the standard problems in fluid mechanics and transport phenomena textbooks [3]. When considering the exit of the fluid in the atmosphere and the accompanying phenomenon of extrudate swell (Fig. 1), the Newtonian problem has been solved more than 20 years ago for different inner/outer diameter ratios κ by Mitsoulis [4]. Since then, variations of the problem have been studied, including the effect of die design [5], of viscoelasticity [6], of inertia, gravity, surface tension, etc. [7,8].

On the other hand, the effects of *compressibility* (usually weak) and/or *wall slip* (through some kind of a slip law) have been studied in some key works [9–12]. The extrudate swell problem for compressible Newtonian fluids has been studied before for tubes ($\kappa = 0$) and slits ($\kappa = 1$) [9,11], while the annular swell problem has been studied in a recent work by the author [14]. Compressibility is usually assessed by a dimensionless compressibility coefficient B defined by [10,11]

$$B = \frac{\beta \mu V}{h_0} \tag{1}$$

where β is the isothermal compressibility coefficient (in Pa^{-1} units), μ is the viscosity (in Pa s units), V is a characteristic speed (usually the average velocity of extrusion at entry [9,13] or exit [10–12]), and h_0 is a characteristic length (usually the die gap or radius, see Fig. 1). In all cases, the incompressible fluid corresponds to $B = 0$. The range of B values for weakly compressible fluids is $0 \le B \le 0.02$ [9,11,13]. This limited range was dictated by considering polymeric fluids of admittedly limited compressibility [13].

However, foam extrusion [14–16] is an example where compressibility can be substantial. This led to a recent article [17], where the effects of compressibility were studied in extrusion for a much wider range of compressibility values, pushing the limits of the compressibility coefficient to $B = 0.12$ for tubes and $B = 0.24$ for slits.

It is, therefore, the purpose of the present paper to re-examine the annular extrudate swell problem and provide results for a much wider range of compressibility values. As before [13], a full parametric study of different κ–values for Newtonian fluids will be undertaken. Detailed results will be given both for the free surface location and the associated extrudate swells, as well as the excess pressure losses in the system (exit correction) as a function of a dimensionless compressibility coefficient B. The extreme cases of slits and tubes will also be included for completion.

[1]Corresponding author.

Contributed by the Fluids Engineering Division of ASME for publication in the JOURNAL OF FLUIDS ENGINEERING. Manuscript received January 15, 2009; final manuscript received May 7, 2009; published online June 24, 2009. Assoc. Editor: Neelesh A. Patankar.

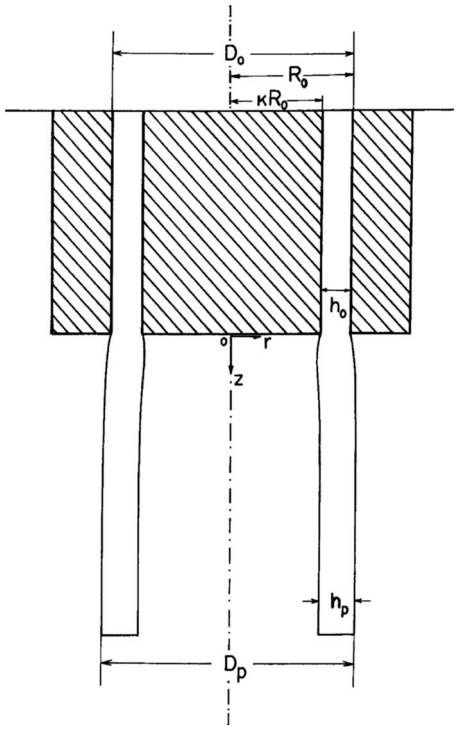

Fig. 1 Schematic representation of extrusion through an annular die and notation for the numerical analysis [2]

2 Mathematical Modeling

The problem at hand is shown schematically in Fig. 1, where an incompressible or weakly compressible Newtonian fluid is considered flowing in an annulus under steady-state conditions and exiting in the atmosphere where it acquires a free surface (annular extrudate swell) [4]. The annulus is defined by the inner/outer diameter ratio κ, while the outer radius is R_0 and the annular gap is h_0. The flow is governed by the usual conservation equations of mass and momentum under creeping isothermal flow conditions. Therefore, the effects of inertia, gravity, and surface tension are neglected, which is a good approximation for all highly viscous fluids.

The conservation of mass for compressible fluids is written as

$$\nabla \cdot (\rho \bar{u}) = 0 \tag{2}$$

where ρ is the density and $\bar{u}$ is the velocity vector. The conservation of momentum is written as

$$0 = -\nabla p(\rho) + \nabla \cdot \bar{\bar{\tau}} \tag{3}$$

where p is the pressure (a function of density ρ) and $\bar{\bar{\tau}}$ is the extra stress tensor, which is related to the velocity gradients via the Newtonian constitutive equation for compressible fluids [9,11,12] as follows:

$$\bar{\bar{\tau}} = \mu\left(\bar{\bar{\dot{\gamma}}} - \frac{2\Lambda}{3}(\nabla \cdot \bar{u})\bar{\bar{I}}\right) \tag{4}$$

where $\bar{\bar{\dot{\gamma}}} = \nabla\bar{u} + \nabla\bar{u}^T$ is the rate-of-strain tensor made up by the velocity gradient tensor $\nabla\bar{u}$ and its transpose $\nabla\bar{u}^T$, $\bar{\bar{I}}$ is the unit tensor, and Λ is a convenient coefficient, which takes the value of 0 for incompressible fluids and 1 for compressible fluids.

For isothermal flows, pressure and density are related as a first approximation via a simple thermodynamic equation of state, the linear form of which is given by [10]

$$\rho = \rho_0(1 + \beta p) \tag{5}$$

where β is the compressibility coefficient defined as

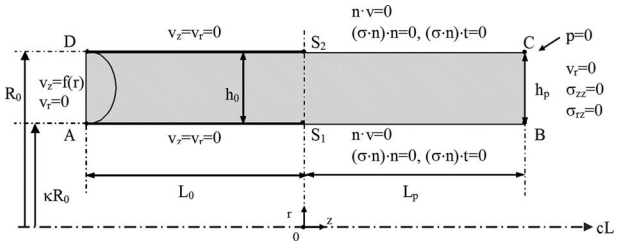

Fig. 2 Schematic of flow domain and boundary conditions

$$\beta = -\frac{1}{V_f}\left(\frac{\partial V_f}{\partial p}\right)_{p_0,T_0} \tag{6}$$

where V_f is the fluid volume at reference pressure p_0 and temperature T_0, also related to reference density ρ_0.

All lengths are scaled with the annular gap width h_0, all velocities with the inlet average velocity V, and all pressures and stresses with $\mu V/h_0$.

The constitutive equation is substituted into the momentum equation, and the system of equations must be solved after a set of appropriate boundary conditions has been applied. Figure 2 shows the solution domain and boundary conditions. Because of symmetry, only one-half of the flow domain is considered, as was done previously [4,6]. The boundary conditions are therefore as follows:

(a) no slip along the walls AS_1 and DS_2 ($v_z = v_r = 0$)
(b) along the inflow boundary DA, fully-developed velocity profile ($v_z(r) = f_1(r), \quad v_r = 0$), corresponding to a given (unit) average velocity (or constant mass flow rate)
(c) along the outflow boundary BC, zero radial velocity ($v_r = 0$) and vanishing tangential and normal stresses ($(\bar{\bar{\sigma}}\cdot\bar{n})\cdot\bar{t} = 0, \quad (\bar{\bar{\sigma}}\cdot\bar{n})\cdot\bar{n} = 0$), where $\bar{n}$ and $\bar{t}$ are the normal and tangential vectors to the surface and $\bar{\bar{\sigma}} = -p\bar{\bar{I}} + \bar{\bar{\tau}}$ is the total stress
(d) along the free surfaces S_1B and S_2C, vanishing tangential and normal stresses ($(\bar{\bar{\sigma}}\cdot\bar{n})\cdot\bar{t} = 0, \quad (\bar{\bar{\sigma}}\cdot\bar{n})\cdot\bar{n} = 0$) and no flow through the surface ($\bar{v}\cdot\bar{n} = 0$)

The reference pressure is also set to zero at point C.

The introduction of dimensionless quantities leads to the dimensionless compressibility coefficient B defined in Eq. (1), with V being the mean inlet velocity. In all cases, the incompressible fluid corresponds to $B = 0$. The range of B values in the simulations is $0 \le B \le B_{\text{lm}}$, where B_{lm} is an upper limit depending on the formulation used.

3 Method of Solution

The numerical solution is obtained with the finite element method (FEM), using the in-house program UVPTH, originally developed for multilayer flows [18], which employs as primary variables the two velocities, pressure, temperature, and free surface location (*u-v-p-T-h formulation*).

In our previous work [13] the program was modified to account for compressibility and slip. We had followed the FEM formulation for weakly compressible flows as employed by Beverly [19] and Webster et al. [20]. This formulation led to compressible solutions for very low B-values (typically in the range $0 \le B \le 0.02$) for the extrudate swell problem [9,13]. On the other hand, the FEM formulation used by Georgiou and co-workers [10–12,17] achieved solutions for much higher B-values (in the range $0 \le B \le 0.12$ for axisymmetric flows and $0 \le B \le 0.24$ for planar flows [17]). The present work was motivated, in part, by understanding these differences and extending the previous results for extrudate swell from annular dies.

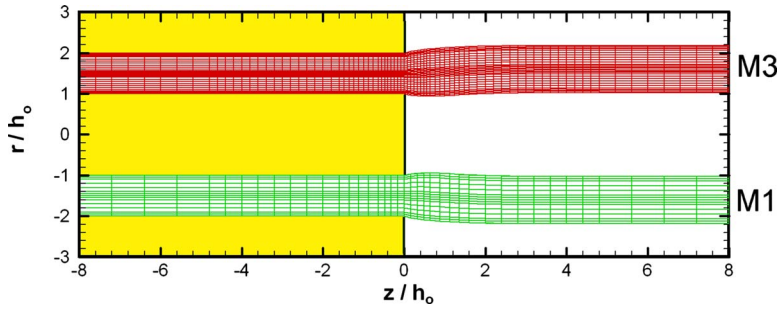

Fig. 3 Finite element meshes used in the computations. The upper half shows mesh M3 containing 2240 quadrilateral elements, while the lower half shows mesh M1 containing 560 elements.

The details of the differences in the FEM formulations (nonconsistent versus consistent) are given in the Appendix. During the course of the present work it became evident that a consistent (C-FEM) formulation for the continuity equation was needed to obtain extended results for compressible flows. With the consistent formulation the analytical solutions for the Poiseuille flow [14] showed no upper limit for any value of B. Furthermore, the convective nature of the compressible terms $\bar{u}\cdot\nabla\rho$ in the continuity equation dictates the use of streamline-upwind/Petrov–Galerkin (SUPG) integration schemes [22] to obtain smooth results for high compressibility levels.

For most of the simulations we have used three meshes of increasing density as before [13]. Figure 3 show meshes M3 (upper half) and M1 (lower half) put together for brevity, for $\kappa=0.5$ as obtained from the Newtonian incompressible solution. The entry has been set at $-8h_0$ and the die exit at 0, while the extrudate length is taken as $8h_0$. The entry length $L_0=8h_0$ is in accordance with our previous incompressible simulations [4], and is necessary in order to impose at inlet the well-known fully-developed velocity profile of a Newtonian fluid in an annulus. The entry length L_0 does play a role in compressible flows due to the convective nature of these flows [17]. The adequacy of the exit length L_p was checked by plotting the free surfaces and observing their leveling-off in the extrudate region away from the die. The less dense mesh M1 with 560 elements was used primarily for preliminary runs to gain experience with compressible annular flows and do the necessary checks and tests [13].

The initial mesh configuration was that of a rectangular domain. After an initial solution was obtained in this fixed rectangular domain, the velocities at the free surface were integrated either using Simpson's rule (decoupled approach) or using the Galerkin principle for the h-variable in the u-v-p-T-h formulation (see Appendix) with comparable results (differences less than 1% for the quantities of interest, such as extrudate swell).

The iterative scheme was direct substitution (Picard iterations), and the criteria for termination of the iterative process were for both the norm-of-the-error and the norm-of-the-residuals $<10^{-4}$, and for the maximum free surface change $<10^{-5}$. Due to the two free surfaces present in annular flows, under-relaxation for the movement of the free surface was found helpful, with the under-relaxation factor $\omega_f=0.5$. Around 25 iterations were thus needed to get the incompressible solution ($B=0$), after which continuation in the B-values was employed with changes of 0.001. Convergence for the low B-values was achieved within a few iterations (between 4 and 5), which progressively increased. While with the previous formulation [13] problems with convergence started appearing for $B_{\rm lm}>0.02$, and it was impossible to get convergence for $B=0.022$, now the same occurred for $B_{\rm lm}>0.064$, which seems to be the limiting value for the present formulation. Thus, the range of computations was extended threefold.

4 Results and Discussion

The computer program was first tested against analytical solutions for planar and axisymmetric Poiseuille flows of compressible Newtonian fluids [13]. No limiting value $B_{\rm lm}$ was found for any value of B with the consistent C-FEM formulation, in sharp contrast with the previous work [13], where it was impossible to get solutions past $B_{\rm lm}=0.2$. Convergence was achieved within at most four iterations for any B-value for which the analytical formulas given in Ref. [13] are valid.

4.1 Extrudate Swell From Tubes and Slits. Next, we repeated the runs for the axisymmetric and planar extrudate swell problem given in Ref. [17]. For this case we used an entry length $L_0=5$ and extrudate length of $L_p=10$ as in Ref. [17]. Note that here there is only one free surface and no lower wall, due to a centerline within the fluid. Thus, the boundary conditions at the centerline are altered to reflect this symmetry ($v_r=0$, $\tau_{rz}=0$). Runs were made with different meshes, ranging from 400 to 2400 elements. The results are given in terms of the following two quantities:

(i) The *extrudate swell* B_1 defined by

$$B_1=\frac{D_p}{D_0} \tag{7}$$

where D_p is the extrudate outer diameter and D_0 is the die outer diameter (Fig. 1).

(ii) The *exit correction* $n_{\rm ex}$ defined by [22,23]

$$n_{\rm ex}=\frac{\Delta P_{\rm cl}-\Delta P_{0,\rm cl}}{2\tau_w} \tag{8}$$

where $\Delta P_{\rm cl}$ is the overall pressure drop in the system (channel and extrudate regions) calculated at the centerline, $\Delta P_{0,\rm cl}$ is the pressure drop only in the channel *without* the extrudate region (distance DS_2 in Fig. 2) calculated at the centerline, and τ_w is the shear stress for fully-developed flow at the channel wall. It should be noted that the exit correction is usually calculated with the pressure values at the wall, as was done before [4,13], because pressure is measured at the wall. However, for consistency with [17] we have used here the centerline values. As will be shown later, this has a big influence on the results. In all cases the entry velocity profile is set as the fully-developed parabolic Newtonian profile, having an average velocity $V=1$, and giving $\tau_w=3$ ($\tau_w=4$) for the planar (axisymmetric) case, respectively.

We verified that the limiting value for our formulation was $B_{\rm lm}=0.11$ for the axisymmetric case and $B_{\rm lm}=0.22$ for the planar

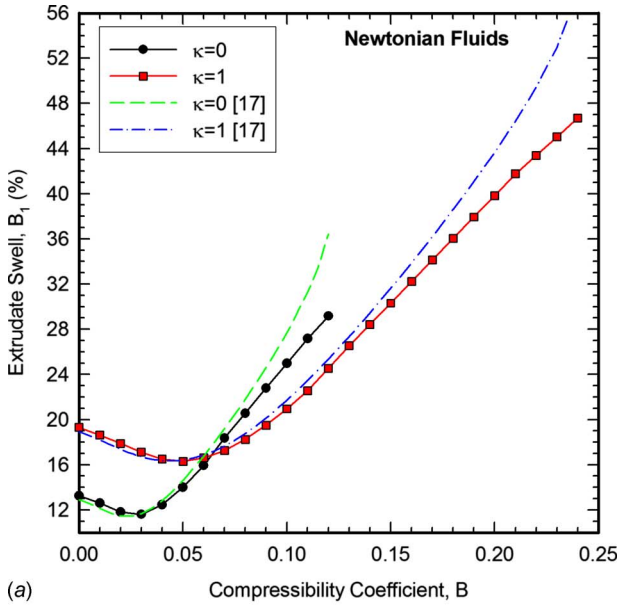

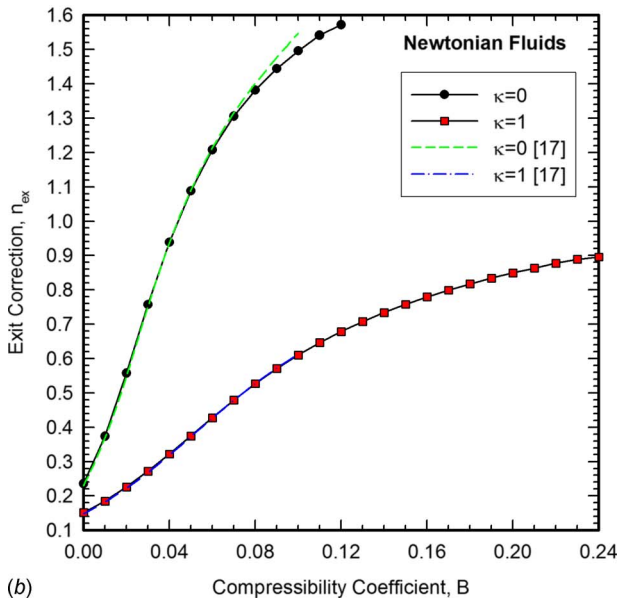

Fig. 4 Extrudate swell of compressible Newtonian fluids obeying a linear equation of state. Comparison of results with Ref. [17] for a domain with L_0=5: (*a*) extrudate swell and (*b*) exit correction based on centerline values.

one. The results for the extrudate swell are given in Fig. 4(*a*) in comparison with those from Ref. [17]. Good general agreement is obtained, especially in the range $0 \le B \le 0.08$ for the axisymmetric and $0 \le B \le 0.16$ for the planar case. Beyond these ranges, the results are more dependent on the grid used. Note that the results in Ref. [17] have been obtained with very dense grids in the order of 4000 elements, and thus they constitute an upper bound for the solution as the number of elements increases. A much better agreement has been obtained for the exit correction n_{ex} as shown in Fig. 4(*b*). It is noted that the exit correction, when calculated at the centerline, shows a monotonic increase with B, which is substantial and higher in tubes than in slits. The excellent agreement with the values given in Ref. [17] is not surprising, because the exit correction depends on pressure values in the die, while the extrudate swell is a more sensitive quantity depending on the mesh used and its density around the exit singularity.

Figure 5 shows contour results for the two geometries (κ=0, tube and κ=1, slit) for the highest B_{lm}-value for which convergence was achieved. First are shown the streamlines (contours of the stream function ψ or *STR*). The streamlines have been obtained a posteriori by solving the Poisson equation for the stream function with the known nodal vorticity values. We observe that the axisymmetric case shows less swelling but presents a more drastic rearrangement of the streamlines and the free surface than its planar counterpart. Then contours are shown for the axial velocity u_z (u_x) or U, the pressure p or P, and the shear stresses τ_{rz} (τ_{xy}) or *TXY*. The convective type of compressible flow is evident (due to the convective terms $\bar{u}\cdot\nabla\rho$ in the equation of mass conservation), and for this reason the results depend not only on the compressibility coefficient B but on the die length L_0 as well. Compressibility serves to squeeze the streamlines toward the exit and accelerate the flow there, as evidenced by the increased axial velocities and shear stresses near the exit, and to increase the pressure drop in the system compared with the incompressible values.

4.2 Extrudate Swell From Annular Dies. For all cases studied, runs were performed for $\kappa=(0,0.02,0.1,0.25,0.5,0.75,0.9,0.98,1)$ with no slip at the wall assumed as in our previous works for Newtonian fluids [4,13]. The cases of κ=0 and κ=1 correspond to the extreme cases of a round tube and a two-dimensional slit, respectively [3]. The results are given in terms of the three dimensionless swell ratios B_i (i=1,2,3) (only two of which are independent), and of the dimensionless change in pressure drop over and above the fully-developed values n_{ex}. These are defined as follows [4,5]:

(i) the (*outer*) *diameter swell* B_1 defined by

$$B_1 = \frac{D_p}{D_0} \tag{9}$$

where D_p is the extrudate outer diameter and D_0 is the die outer diameter (Fig. 1)

(ii) the *thickness swell* B_2 defined by

$$B_2 = \frac{h_p}{h_0} \tag{10}$$

where h_p is the extrudate (parison) thickness (distance BC, see Fig. 2), and h_0 is the annular gap (distance AD)

(iii) the *inner* diameter swell B_3 defined by

$$B_3 = \frac{D_p - 2h_p}{D_0 - 2h_0} \tag{11}$$

(iv) the *exit correction* n_{ex} defined by [22,23]

$$n_{ex} = \frac{\Delta P - \Delta P_0}{2\tau_{w,o}} \tag{12}$$

where ΔP is the overall pressure drop in the system (channel and extrudate regions) calculated at the outer annular wall, ΔP_0 is the pressure drop only in the channel *without* the extrudate region (distance DS_2 in Fig. 2) calculated also at the outer annular wall, and $\tau_{w,o}$ is the shear stress for fully-developed flow at the outer annular wall. Note that the pressure is set to zero at the exit outer wall in the annular Poiseuille flow without the extrudate region. In all cases the entry velocity profile is set as the fully-developed Newtonian profile for an annulus [3], having an average velocity V=1.

The calculations are pursued for compressible fluids in the extended range of $0 \le B \le 0.064$ (a threefold increase from our previous work [13]). In all cases, the previous limits are shown with a vertical line.

The results for the thickness swell (B_2) as a function of the compressibility coefficient B are given in Fig. 6 for different

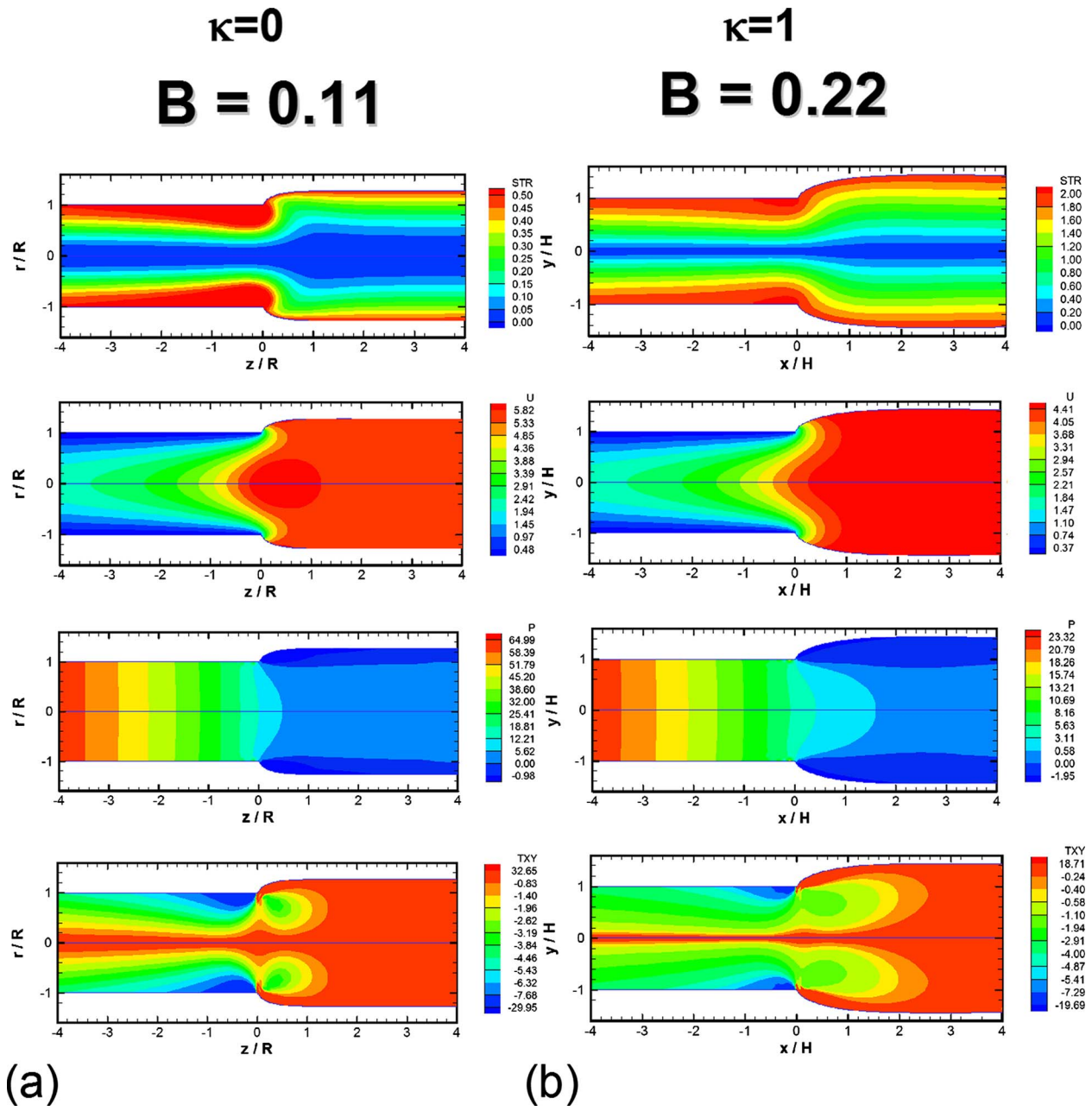

Fig. 5 Extrudate swell of compressible Newtonian fluids obeying a linear equation of state. Contour results at the limiting value B_{lm}: (*a*) tube flow ($\kappa=0$, $B=0.11$) and (*b*) slit flow ($\kappa=1$, $B=0.22$). STR=stream function, *U*=axial velocity, *P*=pressure, and *TXY*=shear stress.

κ-ratios. Interesting trends are observed. Increasing B leads to a nonmonotonic change in the thickness swell, which was also observed originally by Georgiou [11] for tubes ($\kappa=0$). The initial increase was found to be die-length dependent, i.e., for $L_0=8h_0$ used here, this increase was present, but for $L_0=4h_0$ and $L_0=5h_0$ there was no such initial increase, and the results dropped monotonically to a minimum before the upturn. The change in swell is not significant (in the order of 1%), as also found previously for tubes [9,11] and slits [9] in the limited range of weakly compressible simulations ($0\leq B\leq 0.02$). However, after the minimum is reached within this limited range of B-values, the swell takes off and reaches high values, more reminiscent of viscoelasticity [6]. All results are ordered with κ as they should, except the planar case ($\kappa=1$), which appears to need much higher B-values to reach high swelling ratios. Indeed, as it was shown in Fig. 4(*a*), swellings in the order of 40% are obtained near the limiting B-values for slits, i.e., $B_{lm}=0.22$.

The corresponding results for the diameter swell (B_1) are shown in Fig. 7, while those for the inner diameter swell (B_3) are shown in Fig. 8. Some points to notice are the smaller change in diameter swell for all B- and κ-values. In contrast to the thickness swell, the (outer) diameter swell is highest for the lower κ-value ($\kappa=0.02$), and then falls accordingly (reverse ordering with κ) reaching almost no swell for $\kappa=0.98$ (a constant value of around 0.5%). The inner diameter swell shows the biggest changes for $\kappa=0.02$ and the smallest for $\kappa=0.98$ (again small values of almost no swell). Also while B_1 follows B_2 in reverse trend, albeit with

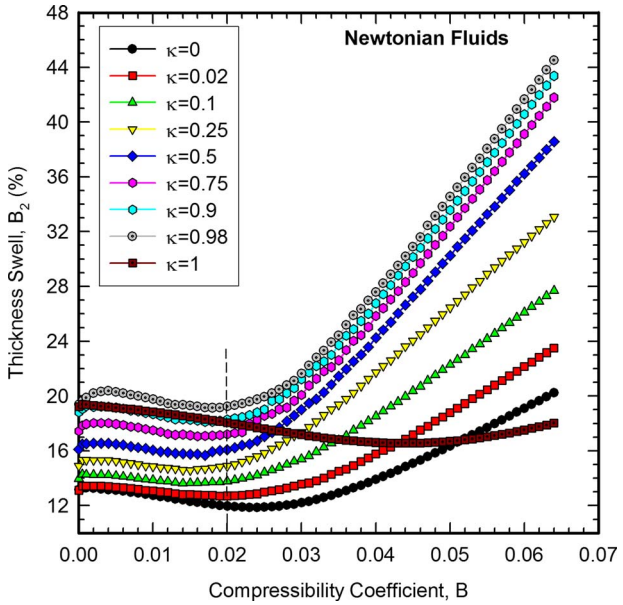

Fig. 6 Thickness swell B_2 as a function of the compressibility coefficient B for Newtonian fluids obeying a linear equation of state. The vertical line corresponds to the limit of previous calculations using the nonconsistent FEM [13].

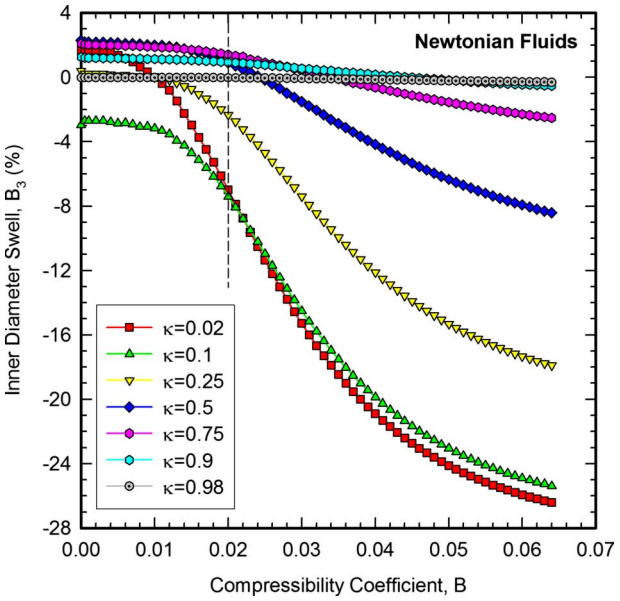

Fig. 8 Inner diameter swell B_3 as a function of the compressibility coefficient B for Newtonian fluids obeying a linear equation of state. The vertical line corresponds to the limit of previous calculations using the nonconsistent FEM [13].

smaller values, B_3 is not, not ordering with κ, especially at the lower B-range ($0 \leq B \leq 0.02$).

If the results for the thickness swell are plotted versus the diameter ratio κ (Fig. 9), we observe a sigmoidal trend, also found to exist for Newtonian incompressible fluids [4]. The curves are not monotonically ordered but are above and below the incompressible case ($B=0$) to reflect the same behavior shown in Fig. 6.

The results for the exit correction (n_{ex}) as a function of the compressibility coefficient B are given in Fig. 10 for different κ-ratios. Again, interesting trends are observed. The exit correction is an increasing function of B in the limited range of weak compressibility ($0 \leq B \leq 0.02$), after which it goes through a maximum that depends on κ, with higher κ-values giving an earlier maximum at lower B-values. After the maximum, there is a monotonic decrease with increasing B-values. It should be pointed out that this nonmonotonic behavior does depend on the die length L_0 because compressibility depends on the length as all convective flows do. A shorter die ($L_0=5$) gave always a monotonic increase with B, as evidenced in Fig. 4(*b*). The exit correction is highest for the tube ($\kappa=0$) and lowest for the slit ($\kappa=1$), with all other κ-values ordered between these two extreme cases. However, as was the case with the thickness swell, the planar geometry results present a peculiarity, showing that much higher B-values are

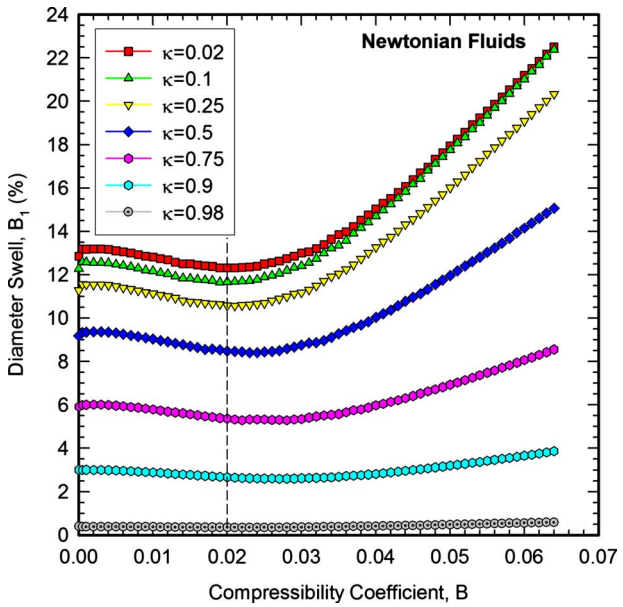

Fig. 7 Diameter swell B_1 as a function of the compressibility coefficient B for Newtonian fluids obeying a linear equation of state. The vertical line corresponds to the limit of previous calculations using the nonconsistent FEM [13].

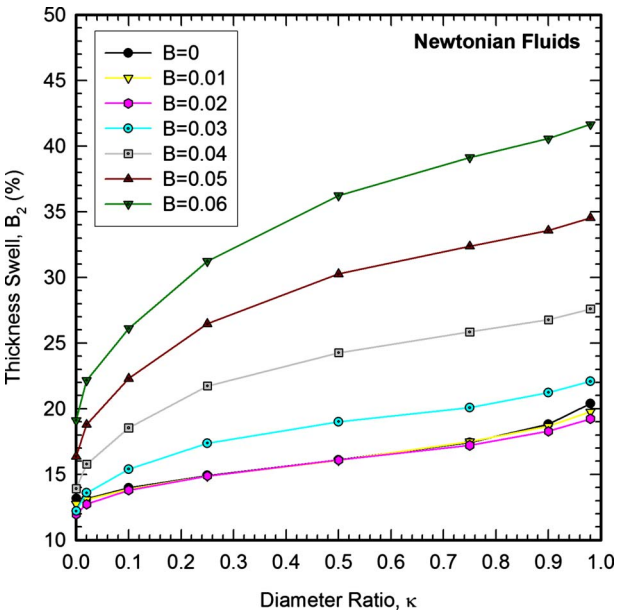

Fig. 9 Thickness swell B_2 as a function of the diameter ratio κ for various values of the compressibility coefficient B for Newtonian fluids obeying a linear equation of state

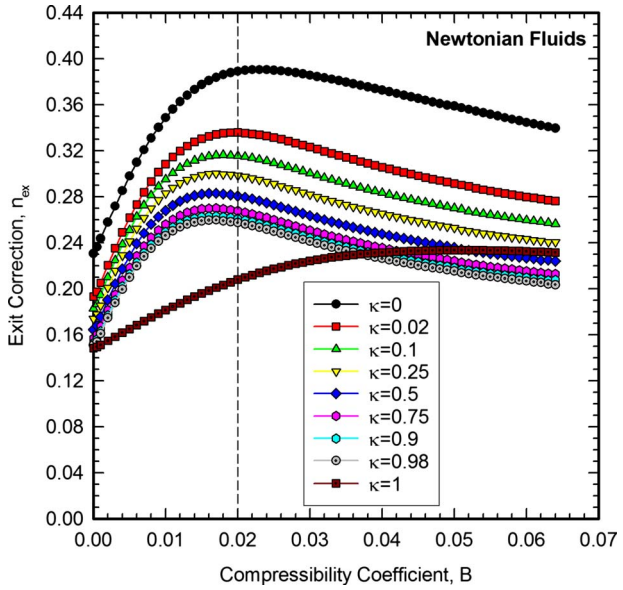

Fig. 10 Exit correction n_{ex} as a function of the compressibility coefficient *B* for Newtonian fluids obeying a linear equation of state. The vertical line corresponds to the limit of previous calculations using the nonconsistent FEM [13]. Note that the exit correction is based on pressure values calculated at the outer die wall.

needed to reach their full nonmonotonic behavior. It is important to bear in mind that the exit correction is calculated at the outer die wall, and thus it shows different trends than those of Fig. 4(*b*), where it was calculated at the centerline for tubes and slits.

If the results for the exit correction are plotted versus the diameter ratio κ (Fig. 11), we observe a monotonic decrease, also found to exist for Newtonian incompressible fluids [4]. This trend is somewhat more pronounced for higher *B* (more compressible fluids). Because of the monotonicity of the results shown in the previous graph, the curves are ordered for different *B*-values, except again at the upper limit of the computations where the results for $B=0.015$ are very close to the ones for $B=0.02$. For the same *B*-value, the effect of increasing κ is to slightly decrease the exit correction, but again the changes are not significant, and they follow those found for the incompressible case ($B=0$).

5 Conclusions

A C-FEM for compressible viscous flows has been implemented to extend numerical solutions for Newtonian fluids for higher compressibility numbers, *B*. It uses the pressure as a Lagrangian multiplier for all the terms of the continuity equation, and SUPG integration for the convective terms $\bar{u}\cdot\nabla\rho$ appearing in it due to density. The analytical solutions for Poiseuille flow in tubes and slits have been numerically reproduced for any *B*-value.

With the C-FEM, the range of simulations has been extended threefold than before [13] for the benchmark problem of annular extrusion flow of Newtonian fluids for different diameter ratios κ. The effect of compressibility has been studied by using a linear equation of state between pressure and density.

For weakly compressible fluids ($0\leq B\leq 0.02$) and as *B* increases, the extrudate swell is little affected, in the order of 1% and not in a monotonic manner, showing maxima and minima, which are affected by the die length (due to the convective nature of compressible flows). All thickness swell values range between 13% and 20%, which are the limits for tubular axisymmetric and planar flows, respectively. The exit correction (dimensionless excess pressure losses) increases for all κ-values in the low *B*-range. In the case of more compressible fluids (new results for $0.02\leq B\leq 0.064$), increasing compressibility increased substantially the (thickness) extrudate swell, in the order of 40% for $B\approx 0.06$. The exit correction showed maxima around $B\approx 0.02$, and then a gradual decrease for all κ-values. It is important to state where the exit correction is calculated, since pressure values based on the wall give different exit corrections than values calculated at the centerline, due to the compressibility of the fluid. Also it should be borne in mind that compressibility depends on the die length, due to the convective nature of compressible flows.

The present results are offered as reference solutions for researchers working with the numerical simulation of foam extrusion and parison formation in blow molding. They are the prelude for a study of combined effects together with non-Newtonian fluids, exhibiting viscoplasticity and/or viscoelasticity. Such a study is currently under way by the author.

Acknowledgment

Financial support from the National Technical University of Athens (NTUA), Greece, in the form of a basic research project, code-named "KARATHEODORI" is gratefully acknowledged.

Appendix

The FEM casts the differential equations into integral form according to the Galerkin principles [18,24]. For the primitive variable formulation *u-v-p-T-h*, FEM approximates the field variables for the velocities *u-v*, pressure *p*, temperature *T*, and free surface *h*, as follows:

$$u=\bar{\varphi}^T\bar{U}=\sum_{i=1}^{n}\varphi_i U_i \quad v=\bar{\varphi}^T\bar{V}=\sum_{i=1}^{n}\varphi_i V_i \quad p=\bar{\psi}^T\bar{P}=\sum_{i=1}^{m}\psi_i P_i$$

$$T=\bar{\varphi}^T\bar{T}=\sum_{i=1}^{n}\varphi_i T_i \quad h=\bar{\varphi}^T\bar{H}=\sum_{i=1}^{n}\varphi_i H_i$$

where $\bar{U},\bar{V},\bar{P},\bar{T},\bar{H}$ are arrays-columns of the nodal unknowns for each element, and $\bar{\varphi},\bar{\psi}$ are arrays-rows of the basis (interpolation) functions, and the superscript *T* refers to the transpose of a vector. For well-known reasons of mathematical consistency [24], the pressure basis functions ψ are of lower order than the other basis functions φ, and interpolation for pressure is carried out over *m* nodes, while for the other variables is carried over *n* nodes, with $m<n$. Nine-node Lagrangian isoparametric quadrilateral elements are used, and that choice fixes the basis functions ($n=9$, $m=4$).

For isothermal flows, the conservation of energy equation is not considered and the temperature does not enter into the system of equations. Substitution of the FEM approximations to the governing *differential* equations leads to corresponding *integral* equations to be integrated over the element area Ω or its surface boundary Γ, as shown below (Cartesian coordinates) [24].

Mass conservation. In tensor notation,

$$\nabla\cdot(\rho\bar{u})=0 \tag{A2a}$$

In long-hand notation,

$$\rho\left(\frac{\partial u_x}{\partial x}+\frac{\partial u_y}{\partial y}\right)+u_x\frac{\partial\rho}{\partial p}\frac{\partial p}{\partial x}+u_y\frac{\partial\rho}{\partial p}\frac{\partial p}{\partial y}=0 \tag{A2b}$$

$$\left(\int_\Omega\rho\frac{\partial\bar{\varphi}}{\partial x}\bar{\psi}^T d\Omega\right)\bar{U}+\left(\int_\Omega\rho\frac{\partial\bar{\varphi}}{\partial y}\bar{\psi}^T d\Omega\right)\bar{V}+\underbrace{\left(\int_\Omega\left(\frac{\partial\rho}{\partial p}\right)\frac{\partial\bar{\psi}}{\partial x}\bar{\varphi}\bar{\psi}^T d\Omega\right)\bar{U}+\left(\int_\Omega\left(\frac{\partial\rho}{\partial p}\right)\frac{\partial\bar{\psi}}{\partial y}\bar{\varphi}\bar{\psi}^T d\Omega\right)\bar{V}}_{\text{convective compressibility}}=0 \tag{A2c}$$

The above (nonconsistent) formulation uses the velocity basis functions to perform the integrations. It has been employed before for compressible flows [19,20] and led to limited results for compressible extrudate swell [9,13].

Momentum conservation. In tensor notation,

$$\rho\bar{u}\cdot\nabla\bar{u} = -\nabla p + \nabla\cdot\bar{\bar{\tau}} \tag{A3a}$$

with the total stresses $\bar{\bar{\sigma}}$ given by

$$\bar{\bar{\sigma}} = -p\bar{\bar{I}} + \bar{\bar{\tau}} \tag{A3b}$$

where

$$\bar{\bar{\tau}} = \mu(\nabla\bar{u} + \nabla\bar{u}^T) - \frac{2\mu}{3}(\nabla\cdot\bar{u})\bar{\bar{I}} \tag{A3c}$$

In long-hand notation,

$$\rho\left(u_x\frac{\partial u_x}{\partial x} + u_y\frac{\partial u_x}{\partial y}\right) = -\frac{\partial p}{\partial x} + \frac{\partial \tau_{xx}}{\partial x} + \frac{\partial \tau_{xy}}{\partial y} \tag{A3d}$$

$$\rho\left(u_x\frac{\partial u_y}{\partial x} + u_y\frac{\partial u_y}{\partial y}\right) = -\frac{\partial p}{\partial y} + \frac{\partial \tau_{yx}}{\partial x} + \frac{\partial \tau_{yy}}{\partial y} \tag{A3e}$$

$$\tau_{xx} = 2\mu\frac{\partial u_x}{\partial x} - \frac{2\mu}{3}\left(\frac{\partial u_x}{\partial x} + \frac{\partial u_y}{\partial y}\right) \tag{A3f}$$

$$\tau_{yy} = 2\mu\frac{\partial u_y}{\partial y} - \frac{2\mu}{3}\left(\frac{\partial u_x}{\partial x} + \frac{\partial u_y}{\partial y}\right) \tag{A3g}$$

$$\tau_{xy} = \mu\left(\frac{\partial u_x}{\partial y} + \frac{\partial u_y}{\partial x}\right) = \tau_{yx} \tag{A3h}$$

$$\underbrace{\left(\int_\Omega \rho\bar{\varphi}\bar{u}_m\frac{\partial\bar{\varphi}}{\partial x}^T d\Omega + \int_\Omega \rho\bar{\varphi}\bar{v}_m\frac{\partial\bar{\varphi}}{\partial y}^T d\Omega\right)\bar{U}}_{u\text{-convection}}$$

$$+\underbrace{\left(\int_\Omega \rho\bar{\varphi}\bar{u}_m\frac{\partial\bar{\varphi}}{\partial x}^T d\Omega + \int_\Omega \rho\bar{\varphi}\bar{v}_m\frac{\partial\bar{\varphi}}{\partial y}^T d\Omega\right)\bar{V}}_{v\text{-convection}} - \underbrace{\left(\int_\Omega \frac{\partial\bar{\varphi}}{\partial x}\bar{\psi}^T d\Omega + \int_\Omega \frac{\partial\bar{\varphi}}{\partial y}\bar{\psi}^T d\Omega\right)\bar{P}}_{\text{pressure}}$$

$$+\underbrace{\left(\int_\Omega 2\mu\frac{\partial\bar{\varphi}}{\partial x}\frac{\partial\bar{\varphi}^T}{\partial x}d\Omega\right)\bar{U} + \left(\int_\Omega \mu\frac{\partial\bar{\varphi}}{\partial y}\frac{\partial\bar{\varphi}^T}{\partial y}d\Omega\right)\bar{U} + \left(\int_\Omega \mu\frac{\partial\bar{\varphi}}{\partial y}\frac{\partial\bar{\varphi}^T}{\partial x}d\Omega\right)\bar{V}}_{\text{viscous terms, } x\text{-momentum}}$$

$$+\underbrace{\left(\int_\Omega \mu\frac{\partial\bar{\varphi}}{\partial x}\frac{\partial\bar{\varphi}^T}{\partial y}d\Omega\right)\bar{U} + \left(\int_\Omega 2\mu\frac{\partial\bar{\varphi}}{\partial y}\frac{\partial\bar{\varphi}^T}{\partial y}d\Omega\right)\bar{V} + \left(\int_\Omega \mu\frac{\partial\bar{\varphi}}{\partial x}\frac{\partial\bar{\varphi}^T}{\partial x}d\Omega\right)\bar{V}}_{\text{viscous terms, } y\text{-momentum}}$$

$$-\underbrace{\left(\int_\Omega \frac{2}{3}\mu\frac{\partial\bar{\varphi}}{\partial x}\frac{\partial\bar{\varphi}^T}{\partial x}d\Omega\right)\bar{U} - \left(\int_\Omega \frac{1}{3}\mu\frac{\partial\bar{\varphi}}{\partial y}\frac{\partial\bar{\varphi}^T}{\partial y}d\Omega\right)\bar{U} - \left(\int_\Omega \frac{1}{3}\mu\frac{\partial\bar{\varphi}}{\partial y}\frac{\partial\bar{\varphi}^T}{\partial x}d\Omega\right)\bar{V}}_{\text{compressible terms, } x\text{-momentum}}$$

$$-\underbrace{\left(\int_\Omega \frac{1}{3}\mu\frac{\partial\bar{\varphi}}{\partial x}\frac{\partial\bar{\varphi}^T}{\partial y}d\Omega\right)\bar{U} - \left(\int_\Omega \frac{2}{3}\mu\frac{\partial\bar{\varphi}}{\partial y}\frac{\partial\bar{\varphi}^T}{\partial y}d\Omega\right)\bar{V} - \left(\int_\Omega \frac{1}{3}\mu\frac{\partial\bar{\varphi}}{\partial x}\frac{\partial\bar{\varphi}^T}{\partial x}d\Omega\right)\bar{V}}_{\text{compressible terms, } y\text{-momentum}}$$

$$= \underbrace{\int_{\Gamma_{tr}} \bar{T}\bar{\varphi}d\Gamma}_{\text{surface tractions}} + \underbrace{\int_{\Gamma_{sl}} (\beta_{sl}\bar{t}\bar{n}:\bar{\bar{\sigma}})\bar{\varphi}d\Gamma}_{\text{slip}} \tag{A3i}$$

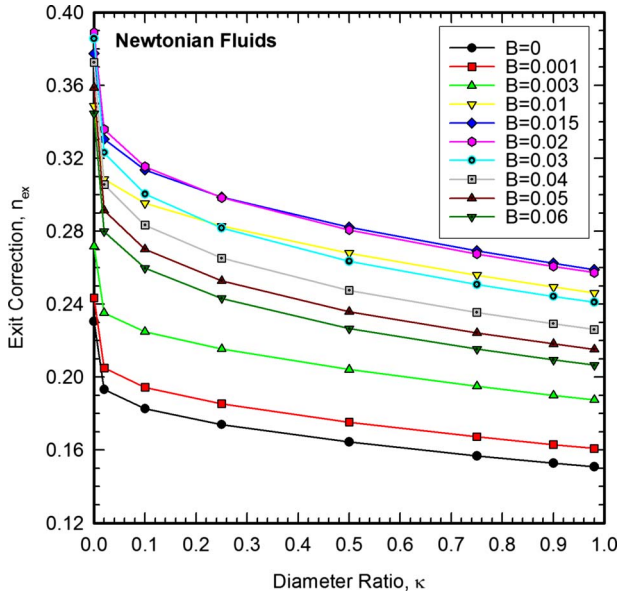

Fig. 11 Exit correction n_{ex} as a function of the diameter ratio κ for various values of the compressibility coefficient B for Newtonian fluids obeying a linear equation of state. Note that the exit correction is based on pressure values calculated at the outer die wall.

where $\bar{u}_m, \bar{v}_m$ are the velocities from the previous mth-iteration, $\bar{T}$ is the surface traction vector, β_{sl} is the slip coefficient, and $\bar{n}$ and $\bar{t}$ are the unit normal and tangential vectors to a surface.

Free surface. In tensor notation,

$$\bar{u} \cdot \bar{n} = 0 \tag{A4a}$$

$$\int_{\Gamma_{fs}} (\bar{u} \cdot \bar{n}) \bar{\varphi}^T d\Gamma = 0 \tag{A4b}$$

In the derivation of the above equations, the Green–Gauss theorem has been used for reducing the second-order diffusion terms in the momentum equation, and for reducing the pressure term into first-order terms along with surface integration. The surface integrals in the right-hand side (RHS) of the integral equations take care of the natural boundary conditions, and may contain surface tractions or momentum fluxes depending on the problem. For compressible fluids, the density has been replaced by pressure according to a state law $p(\rho)$. Thus, the density is interpolated at the same level as the pressure, i.e., with linear interpolation functions.

1 Mass and Momentum Discrete Equations (Nonconsistent Formulation). Combining the discrete forms of the conservation equations of mass and momentum into one matrix equation leads (in two dimensions) to the following system of an element (stiffness) matrix, a vector of unknowns, and a RHS (load) vector for each element as follows:

$$\begin{bmatrix} S_{11} & S_{12} & -L_1 \\ S_{21} & S_{22} & -L_2 \\ -L_{1,\rho}^T + L_3 & -L_{2,\rho}^T + L_4 & 0 \end{bmatrix} \begin{bmatrix} \bar{U} \\ \bar{V} \\ \bar{P} \end{bmatrix} + \begin{bmatrix} A_1(\bar{U}) + A_2(\bar{V}) & 0 & 0 \\ 0 & A_1(\bar{U}) + A_2(\bar{V}) & 0 \\ 0 & 0 & 0 \end{bmatrix} \begin{bmatrix} \bar{U} \\ \bar{V} \\ \bar{P} \end{bmatrix} = \begin{bmatrix} \bar{F}_1 \\ \bar{F}_2 \\ 0 \end{bmatrix} \tag{A5}$$

where

$$S_{11} = 2K_{11} + K_{22} \underbrace{- \frac{2}{3}K_{11} - \frac{1}{3}K_{22}}_{\text{compressible terms}} \tag{A6}$$

$$S_{22} = K_{11} + 2K_{22} \underbrace{- \frac{1}{3}K_{11} - \frac{2}{3}K_{22}}_{\text{compressible terms}} \tag{A7}$$

$$S_{12} = K_{12} \underbrace{- \frac{1}{3}K_{12}}_{\text{compressible}} \tag{A8}$$

$$S_{21} = K_{21} \underbrace{- \frac{1}{3}K_{21}}_{\text{compressible}}, \quad \text{with } S_{21} = S_{12} \tag{A9}$$

$$K_{11} = \int_\Omega \mu \frac{\partial \bar{\varphi}}{\partial x} \frac{\partial \bar{\varphi}}{\partial x}^T d\Omega \tag{A10}$$

$$K_{22} = \int_\Omega \mu \frac{\partial \bar{\varphi}}{\partial y} \frac{\partial \bar{\varphi}}{\partial y}^T d\Omega \tag{A11}$$

$$K_{12} = \int_\Omega \mu \frac{\partial \bar{\varphi}}{\partial y} \frac{\partial \bar{\varphi}}{\partial x}^T d\Omega \tag{A12}$$

$$K_{21} = \int_\Omega \mu \frac{\partial \bar{\varphi}}{\partial x} \frac{\partial \bar{\varphi}}{\partial y}^T d\Omega, \quad \text{with } K_{21} = K_{12} \tag{A13}$$

$$L_1 = \int_\Omega \frac{\partial \bar{\varphi}}{\partial x} \bar{\psi}^T d\Omega \tag{A14}$$

$$L_2 = \int_\Omega \frac{\partial \bar{\varphi}}{\partial y} \bar{\psi}^T d\Omega \tag{A15}$$

$$L_{1,\rho} = \int_\Omega \rho \frac{\partial \bar{\varphi}}{\partial x} \bar{\psi}^T d\Omega \quad (= L_1 \text{for incompressible fluids}) \tag{A16}$$

$$L_{2,\rho} = \int_\Omega \rho \frac{\partial \bar{\varphi}}{\partial y} \bar{\psi}^T d\Omega \quad (= L_2 \text{ for incompressible fluids}) \tag{A17}$$

$$L_3 = \int_\Omega \left(\frac{\partial \rho}{\partial p} \right) \frac{\partial \bar{\psi}}{\partial x} \bar{\varphi} \bar{\psi}^T d\Omega \quad (L_3 = 0 \text{ for incompressible fluids}) \tag{A18}$$

$$L_4 = \int_\Omega \left(\frac{\partial \rho}{\partial p} \right) \frac{\partial \bar{\psi}}{\partial y} \bar{\varphi} \bar{\psi}^T d\Omega \quad (L_4 = 0 \text{ for incompressible fluids}) \tag{A19}$$

$$A_1(\bar{U}) = \int_\Omega \rho \bar{\varphi} \bar{U} \frac{\partial \bar{\varphi}}{\partial x}^T d\Omega \tag{A20}$$

$$A_2(\bar{V}) = \int_\Omega \rho \bar{\varphi} \bar{V} \frac{\partial \bar{\varphi}}{\partial y}^T d\Omega \tag{A21}$$

$$\bar{F}_1 = \underbrace{\int_{\Gamma_{tr}} \bar{T}_x \bar{\varphi} d\Gamma}_{\text{surface tractions}} + \underbrace{\int_{\Gamma_{sl}} (\beta_{sl} \bar{t}\bar{n}:\bar{\sigma})_x \bar{\varphi} d\Gamma}_{\text{slip}} \tag{A22}$$

$$\bar{F}_2 = \underbrace{\int_{\Gamma_{tr}} \bar{T}_y \bar{\varphi} d\Gamma}_{\text{surface tractions}} + \underbrace{\int_{\Gamma_{sl}} (\beta_{sl} \bar{t}\bar{n}:\bar{\sigma})_y \bar{\varphi} d\Gamma}_{\text{slip}} \tag{A23}$$

It should be noted that in the work of Webster et al. [20], the compressible terms in Eqs. (A8) and (A9) are missing. Although this does not affect the results appreciably in Poiseuille flow when comparing with the analytical solutions, it does affect them considerably in any other 2D flow, as is the case in the extrudate swell problem.

2 Mass and Momentum Discrete Equations (Consistent Formulation). In the consistent (C-FEM) formulation, the discrete form of the continuity equation uses the pressure as a Lagrangian multiplier for all terms appearing in the equation. Thus, the discrete form becomes

$$\left(\int_\Omega \rho \frac{\partial \bar{\varphi}}{\partial x} \bar{\psi}^T d\Omega\right)\bar{U} + \left(\int_\Omega \rho \frac{\partial \bar{\varphi}}{\partial y} \bar{\psi}^T d\Omega\right)\bar{V} + \underbrace{\left(\int_\Omega \left(\frac{\partial \rho}{\partial p}\right)\left[\frac{\partial \bar{\psi}}{\partial x}\bar{U} + \frac{\partial \bar{\psi}}{\partial y}\bar{V}\right]\bar{\psi}^T d\Omega\right)\bar{P} = 0}_{\text{convective compressibility}} \tag{A24}$$

and the element (stiffness) matrix of Eq. (A5) becomes

$$\begin{bmatrix} S_{11} & S_{12} & -L_1 \\ S_{21} & S_{22} & -L_2 \\ -L_{1,\rho}^T & -L_{2,\rho}^T & S_{33} \end{bmatrix} \tag{A25}$$

where

$$S_{33} = -\underbrace{\int_\Omega \left(\frac{\partial \rho}{\partial p}\right)\left(\bar{U}\frac{\partial \bar{\psi}^T}{\partial x} + \bar{V}\frac{\partial \bar{\psi}^T}{\partial y}\right)\bar{\psi} d\Omega}_{\text{compressible terms}}$$

$$(S_{33} = 0 \text{ for incompressible fluids}) \tag{A26}$$

Note the differences above between Eqs. (A2*c*) and (A24), and between matrix Eqs. (A5) and (A25). These are the crucial differences between the two formulations.

For a linear equation of state (Eq. (5)), the term $\partial\rho/\partial p = \rho_0\beta$. Then in the above Eq. (A26) we observe the similarity between the convective term in the energy equation, $\rho c_p \bar{u}\cdot\nabla T$, and in the continuity equation, $\rho\beta\bar{u}\cdot\nabla p$. The integration of the convective terms is best carried out with the SUPG method [21], in which the basis function $\bar{\psi}$ is augmented by the term $\bar{w}\cdot\nabla\bar{\psi}$, where $\bar{w}$ is an artificial diffusivity [21]. Then Eq. (A26) is written as follows:

$$S_{33} = -\underbrace{\int_\Omega \left(\frac{\partial \rho}{\partial p}\right)\left(\bar{U}\frac{\partial \bar{\psi}^T}{\partial x} + \bar{V}\frac{\partial \bar{\psi}^T}{\partial y}\right)(\bar{\psi} + \bar{w}\cdot\nabla\bar{\psi}) d\Omega}_{\text{compressible terms}} \tag{A27}$$

The integration is carried out on bilinear quadrilaterals obtained from a 2×2 subdivision of the parent element. SUPG guarantees results which are smoother than their Galerkin counterparts, even for relatively coarser grids, and this was borne out by our calculations.

3 Final Assembly. The final assembly of the matrix Eqs. (A5) (with the consistent matrix of Eq. (A25)) from all the finite elements leads to a system of equations of the form as follows:

$$[S]\{U\} = \{F\} \tag{A28}$$

where $[S]$ is the grand coefficient (stiffness) matrix, $\{U\}$ is the global vector of unknowns, and $\{F\}$ is the global RHS (load) vector. Due to the nonlinear terms in the $[S]$ matrix (because of compressibility or inertia or a nonlinear slip law), Eq. (A28) is nonlinear, and iterations are needed. The system is then solved at each iteration by the frontal technique for unsymmetric matrices given in the book by Taylor and Hughes [25]. The nonlinear system of equations is solved by direct substitution (Picard iteration), which is most convenient for the formulation described above (no Jacobian matrices are required for such an iterative process).

References

[1] Tadmor, Z., and Gogos, C. G., 1979, *Principles of Polymer Processing* (SPE Monograph Series), Wiley, New York.
[2] Barnes, H. A., Hutton, J. F., and Walters, K., 1989, *An Introduction to Rheology* (Rheology Series), Elsevier, Amsterdam.
[3] Bird, R. B., Stewart, W. E., and Lightfoot, E. N., 1960, *Transport Phenomena*, Wiley, New York.
[4] Mitsoulis, E., 1986, "Extrudate Swell of Newtonian Fluids From Annular Dies," AIChE J., **32**, pp. 497–500.
[5] Orbey, N., and Dealy, J. M., 1984, "Isothermal Swell of Extrudate From Annular Dies; Effects of Die Geometry, Flow Rate, and Resin Characteristics," Polym. Eng. Sci., **24**, pp. 511–518.
[6] Luo, X.-L., and Mitsoulis, E., 1989, "Memory Phenomena in Extrudate Swell Simulations From Annular Dies," J. Rheol., **33**, pp. 1307–1327.
[7] Housiadas, K., Georgiou, G., and Tsamopoulos, J., 2000, "The Steady Annular Extrusion of a Newtonian Liquid Under Gravity and Surface Tension," Int. J. Numer. Methods Fluids, **33**, pp. 1099–1119.
[8] Georgiou, G., 2003, "Annular Liquid Jets at High Reynolds Numbers," Int. J. Numer. Methods Fluids, **42**, pp. 117–130.
[9] Beverly, C. R., and Tanner, R. I., 1993, "Compressible Extrudate Swell," Rheol. Acta, **32**, pp. 526–531.
[10] Georgiou, G. C., and Crochet, M. J., 1994, "Compressible Viscous Flow in Slits, With Slip at the Wall," J. Rheol., **38**, pp. 639–654.
[11] Georgiou, G. C., 1995, "The Compressible Newtonian Extrudate Swell Problem," Int. J. Numer. Methods Fluids, **20**, pp. 255–261.
[12] Georgiou, G. C., 2003, "The Time-Dependent, Compressible Poiseuille and Extrudate-Swell Flows of a Carreau Fluid With Slip at the Wall," J. Non-Newtonian Fluid Mech., **109**, pp. 93–114.
[13] Mitsoulis, E., 2007, "Annular Extrudate Swell of Newtonian Fluids: Effects of Compressibility and Slip at the Wall," ASME J. Fluids Eng., **129**, pp. 1384–1393.
[14] Naguib, H. E., Park, C. B., and Reichelt, N., 2004, "Fundamental Foaming Mechanisms Governing the Volume Expansion of Extruded Polypropylene Foams," J. Appl. Polym. Sci., **91**, pp. 2661–2668.
[15] Naguib, H. E., Park, C. B., Lee, P. C., and Xu, D., 2006, "A Study on the Foaming Behaviors of PP Resins With Talc as Nucleating Agent," J. Polym. Eng., **26**, pp. 565–588.
[16] Park, C. B., Behravesh, A. H., and Venter, R. D., 1998, "Low Density Microcellular Foam Processing in Extrusion Using CO_2," Polym. Eng. Sci., **38**, pp. 1812–1823.
[17] Taliadorou, E., Georgiou, G. C., and Mitsoulis, E., 2008, "Numerical Simulation of the Extrusion of Strongly Compressible Newtonian Liquids," Rheol. Acta, **47**, pp. 49–62.
[18] Hannachi, A., and Mitsoulis, E., 1993, "Sheet Coextrusion of Polymer Solutions and Melts: Comparison Between Simulation and Experiments," Adv. Polym. Technol., **12**, pp. 217–231.
[19] Beverly, C. R., 1992, "Finite Element Studies of Some Problems in Fluid Mechanics and Rheology," Ph.D. thesis, University of Sydney, Sydney, NSW.
[20] Webster, M. F., Keshtiban, I. J., and Belblidia, F., 2004, "Computation of Weakly-Compressible Highly-Viscous Liquid Flows," Eng. Comput., **21**, pp. 777–804.
[21] Brooks, A. N., and Hughes, T. J. R., 1982, "Streamline-Upwind/Petrov-Galerkin Formulations for Convection Dominated Flows With Particular Emphasis on the Incompressible Navier–Stokes Equations," Comput. Methods Appl. Mech. Eng., **32**, pp. 199–259.
[22] Mitsoulis, E., Vlachopoulos, J., and Mirza, F. A., 1984, "Numerical Simulation of Entry and Exit Flows in Slit Dies," Polym. Eng. Sci., **24**, pp. 707–715.
[23] Tanner, R. I., 2000, *Engineering Rheology*, 2nd. ed., Oxford University Press, Oxford, UK.
[24] Huebner, K. M., and Thornton, E. A., 1982, *The Finite Element Method for Engineers*, Wiley, New York.
[25] Taylor, C., and Hughes, T. G., 1981, *Finite Element Programming of the Navier–Stokes Equations*, Pineridge, Swansea, UK.

Tip Vortex Cavitation Inception Scaling for High Reynolds Number Applications

Young T. Shen
e-mail: young.shen@navy.mil

Scott Gowing
e-mail: scott.gowing@navy.mil

Carderock Division,
Naval Warfare Center,
Code 5800,
West Bethesda, MD 20817

Stuart Jessup
Carderock Division,
Naval Warfare Center,
Code 5030,
West Bethesda, MD 20817
e-mail: stuart.jessup@navy.mil

Tip vortices generated by marine lifting surfaces such as propeller blades, ship rudders, hydrofoil wings, and antiroll fins can lead to cavitation. Prediction of the onset of this cavitation depends on model tests at Reynolds numbers much lower than those for the corresponding full-scale flows. The effect of Reynolds number variations on the scaling of tip vortex cavitation inception is investigated using a theoretical flow similarity approach. The ratio of the circulations in the full-scale and model-scale trailing vortices is obtained by assuming that the spanwise distributions of the section lift coefficients are the same between the model-scale and the full-scale. The vortex pressure distributions and core sizes are derived using the Rankine vortex model and McCormick's assumption about the dependence of the vortex core size on the boundary layer thickness at the tip region. Using a logarithmic law to describe the velocity profile in the boundary layer over a large range of Reynolds number, the boundary layer thickness becomes dependent on the Reynolds number to a varying power. In deriving the scaling of the cavitation inception index as the ratio of Reynolds numbers to an exponent m, the values of m are not constant and are dependent on the values of the model- and full-scale Reynolds numbers themselves. This contrasts traditional scaling for which m is treated as a fixed value that is independent of Reynolds numbers. At very high Reynolds numbers, the present theory predicts the value of m to approach zero, consistent with the trend of these flows to become inviscid. Comparison of the present theory with available experimental data shows promising results, especially with recent results from high Reynolds number tests. Numerical examples of the values of m are given for different model- to full-scale sizes and Reynolds numbers. [DOI: 10.1115/1.3130245]

1 Introduction

A three-dimensional lifting surface has a vortex trailing from the tip caused by the crossover of fluid from the high pressure side to the low pressure side. The spinning motion creates regions of low pressure in the vortex core because of the balance of radial momentum. At conditions of high speed or high propeller thrust (loading), the vortex core pressure decreases to a point at which cavitation can occur. On a marine propeller, cavitation typically occurs in the trailing vortex before it occurs on the blade surface. The prediction of the onset of tip vortex cavitation is of major interest to marine engineers and ship designers because of the ensuing noise and hull vibration. The flow field in a trailing vortex is so complex that prediction of cavitation inception still relies heavily on model tests extrapolated to full-scale using cavitation scaling laws.

The report of the 19th International Towing Tank Conference Cavitation Committee [1] presented an extensive review of tip vortex cavitation and its inception. Following McCormick's approach, the report recommended testing the model at high Reynolds numbers and using an empirical formula $(\sigma_{if}/\sigma_{im} = \mathrm{K}(\mathrm{Re}_f/\mathrm{Re}_m)^m$ to scale tip vortex cavitation, in which the subscripts f and m denote full- and model-scales, respectively. The Reynolds number exponent m was found to vary around 0.35 to 0.38, and the empirical parameter K was introduced to incorporate nuclei effects on cavitation inception. Arndt and co-workers [2,3] presented a scaling formula $\sigma_{if}/\sigma_{im} = KC_l^2(\mathrm{Re}_f/\mathrm{Re}_m)^{0.4}$, in which C_l is the lift coefficient and K is an empirical parameter accounting for secondary effects such as the vortex rollup process, nuclei, flow unsteadiness, etc. The Reynolds numbers in the data of Arndt and Dugue [2] were around $2.2\times10^5-5.7\times10^5$. This range of Reynolds number can lead to inconsistent lift coefficient data for wings, however, Loftin and Smith [4] showed large Reynolds effects on lift for Reynolds numbers of 10^6 or less, but much smaller effects at Reynolds numbers greater than 3×10^6. Hence the exponent of 0.4 derived from Ref. [2] may reflect variations in foil loading at low Reynolds numbers and lead to inconsistent results for higher Reynolds number tests. A slight difference was observed in the m values derived by the ITTC and the scaling formulas of Arndt and Dugue [2], respectively.

Jessup et al. [5] compared the cavitation performance of a naval surface ship propeller tested in a 36 in. (0.91 m) water tunnel and the large cavitation channel with full-scale results. The model Reynolds number, based on inflow velocity and chord at a 0.7 propeller radius, was about 4×10^6. The corresponding full-scale Reynolds number was near 5×10^7. Applying the McCormick scaling formula using $m=0.4$ to the model results, the predicted tip vortex inception index was very different from the observed full-scale value. Very little scaling was required to match the data. The large discrepancy of the McCormick prediction was attributed to the difficulty of viewing the bottom of the propeller disk, but it is possible that the scaling methodology was simply incorrect.

Using McCormick's hypothesis that the viscous vortex core size is linearly related to the viscous boundary layer thickness via a continuity of viscous flow assumption $a_c \propto \delta$ the Reynolds effect on the vortex core pressure becomes dependent on the Reynolds variation in the boundary layer thickness. McCormick [6,7] showed that tip vortex cavitation inception indices differed noticeably when roughness was applied on the pressure side of the foil surface. He suggested that the vortex core size is related to the thickness of the boundary layer δ on the pressure side of the foil that feeds into the vortex. Visual observations by Liang and Ra-

Contributed by the Fluids Engineering Division of ASME for publication in the JOURNAL OF FLUIDS ENGINEERING. Manuscript received May 12, 2008; final manuscript received February 4, 2009; published online June 1, 2009. Assoc. Editor: Steven Ceccio.

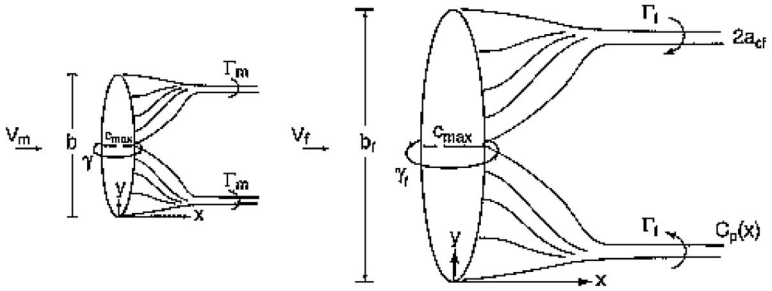

Fig. 1 Sketch of lifting surface

maprian [8] and Baker et al. [9] and the flow velocity measurements by Fruman et al. [10] also showed a strong dependency of the vortex core size on Reynolds numbers. They showed that the core size became smaller as the Reynolds number was increased. These experimental measurements agree with McCormick's hypothesis because the thinning of the boundary layer at higher Reynolds numbers should make the vortex core size smaller. Vortex cavitation can also be sensitive to incoming flow unsteadiness, foil planform/blade geometry, ship wake, the foil/blade loadings, and water quality [1,11,7]. By testing the model in a facility with high air content and high model Reynolds numbers, and by using the thrust identity method [5,12], the nuclei effects, the viscous effects on foil/blade loading, and the ship wake effects on blade loading, respectively, can be minimized. But tip vortex cavitation scaling issues can still be dominated by Reynolds effects on the tip vortex core size. Using McCormick's approach and a Rankine vortex model, viscous effects on the vortex core size and cavitation inception are investigated in this paper.

2 Problem Formulation and Approach

The process of vortex rollup in a tip vortex is complex but is well-discussed by Fruman and co-workers [10,13], Stinebring et al. [14], and Farrell and Billet [15]. To model the vortex and rollup process, consider an elliptical hydrofoil with a system of trailing vortices as shown in Fig. 1. To simplify the explanation, the large foil shown on the right is termed "full-scale" in this study. The model is set at an angle of attack α_m, velocity V_m, and local bound vorticity γ. Let b denote the foil span and c as the chord length at the midspan. Let $\Gamma(x/c)$ represent the circulation in the trailing vortex, $C_p(x/c)$ as the pressure coefficient in the vortex core, and $a_c(x/c)$ as the radius of the vortex core as a function of the downstream distance (x/c). Let subscripts m and f denote the model- and full-scale, respectively, and let λ denote the linear geometric scale ratio of full- to model-scale, namely, $b_f = \lambda\ b_m$ and $c_f = \lambda\ c_m$. Assuming both model- and full-scale have the same planform and section profiles, geometric similarity is preserved. In a uniform inflow with the same angle of attack on both full-scale and model-scale foil, namely, $\alpha_f = \alpha_m$, kinematic similarity is also satisfied. For dynamic similarity, it is assumed that the trailing edge vortex rollup process between model- and full-scale is similar.

For simplicity a Rankine vortex model will be used to relate circulation, core dimension, tangential velocity, and pressure distributions. In this process, it is assumed that the presence of nuclei in the flow does not alter the pressure distributions inside the vortex core from the single-phase flow condition. McCormick's [6,7] assumption will be applied to obtain the relationships between the full-scale and model-scale vortex core radii and pressure distributions. Reynolds scaling on vortex cavitation inception will be derived from the minimum pressure coefficients between the model- and full-scale vortices.

2.1 Trailing Vortex Pressure and Cavitation Inception. The vortex core is a region of low pressure. For sufficiently low pressures, a bubble entering a vortex core will cavitate and radiate acoustically. In some instances the bubbles can interact with the vortex and alter the pressure field from the fully wetted condition. Because the sizes of nuclei are much smaller than the vortex core diameter during the incipient stage of cavitation, it is assumed for inception scaling that the nuclei have no effect on the pressure distributions. Only the Reynolds scale effect on the vortex pressure distributions is considered here.

The Rankine vortex model has the following forms for velocity and pressure [6].

For velocity,

$$V_t(r) = \frac{\Gamma}{2\pi}\left(\frac{r}{a_c^2}\right), \quad r \le a_c$$
$$V_t(r) = \frac{\Gamma}{2\pi}\left(\frac{1}{r}\right), \quad r \ge a_c \tag{1}$$

For pressure,

$$P_0 - P(r) = \frac{\rho\Gamma^2}{4\pi^2 a_c^2}\left\{1 - \frac{r^2}{2a_c^2}\right\}, \quad r \le a_c$$
$$P_0 - P(r) = \frac{\rho\Gamma^2}{4\pi^2}\left\{\frac{1}{2r^2}\right\}, \quad r > a_c \tag{2}$$

in which V_t denotes the tangential velocity, r is the distance to the vortex center, Γ and a_c are the circulation and vortex core radius, respectively, P_0 is the ambient pressure, and ρ is the fluid density. Let $C_{p\,\min}$ denote the minimum pressure in the vortex core. From Eq. (1) we obtain

$$C_{p\,\min} = \frac{P_{(r=0)} - P_0}{1/2(\rho V_0^2)} = -\frac{(\Gamma/V_0)^2}{2\pi^2 a_c^2} \tag{3}$$

Because nuclei effects are ignored, the cavitation is assumed to occur when pressure in the vortex core reaches vapor pressure. The ratio of cavitation inception indices equals the ratio of the minimum pressure coefficients between the full-scale and the model-scale. Thus,

$$\frac{\sigma_{if}}{\sigma_{im}} = \frac{-C_{p\,\min f}}{-C_{p\,\min m}} = \left(\frac{\Gamma_f}{\Gamma_m}\right)^2\left(\frac{a_{cm}}{a_{cf}}\right)^2\left(\frac{V_{0m}}{V_{0f}}\right)^2 \tag{4}$$

where subscripts f and m denote full-scale and model-scale, respectively. Equation (4) shows that cavitation inception scaling is governed by the ratios of (Γ_f/Γ_m) and (a_{cm}/a_{cf}) if the model- and full-scale have the same speed. Now the ratios (Γ_f/Γ_m) and (a_{cm}/a_{cf}) will be derived from geometric and kinematic similarity assumptions.

2.2 Circulation Distributions (Γ_f/Γ_m) in a Trailing Vortex. The circulation rolled up in the vortex depends on the gradient of the bound vorticity in the spanwise direction,

$$\Gamma \propto \partial\gamma/\partial s \tag{5}$$

in which s is the nondimensional distance y/b. The bound vorticity depends on the local section lift as

$$\gamma(s) = l(s)/\rho V_0 \tag{6}$$

and the section lift depends on the local lift coefficient

$$l(s) = c_L(s)\frac{1}{2}(\rho V_0^2)c(s) \tag{7}$$

Because the chord distributions $c(s)$ vary between the model- and the full-scale as the linear scale ratio, the section lift, bound vorticity, and circulation shed into the vortex all scale with the linear scale ratio as well. The lift coefficient distribution stays the same from geometric and kinematic similarities (assuming that the Reynolds variation in the lift coefficient between the model- and the full-scale is small). Thus the circulation scales as

$$\Gamma_f/\Gamma_m = (c_f/c_m)(V_{0f}/V_{0m}) = \lambda(V_{0f}/V_{0m}) \tag{8}$$

The vortex circulation varies with the linear scale ratio between the model- and the full-scale.

2.3 Ratio of Vortex Core Sizes in the Trailing Vortex. From the experimental observations previously discussed and the pi theorem for nondimensional analysis of related variables, the boundary layer thickness is identified to be the proper characteristics length to normalize the size of the vortex core. Although the most direct association would be to relate the core size to the overall thickness, a better choice might be the displacement thickness (δ_1) representing the continuity deficit of the boundary layer, or momentum thickness (δ_2) representing the momentum deficit of the boundary layer. Because the viscous effects are the most apparent as a drag force, and the drag force can be represented as the momentum deficit, the momentum thickness was chosen as the boundary layer scale with which the vortex core size should scale. This choice has the added convenience that friction measurements are easy to measure and are available over a wide Reynolds number range. Additionally, experimental measurements show that the value of the shape factor $H_{12} = \delta_1/\delta_2$ on a flat plate is nearly constant and insensitive to Reynolds numbers [16]. The data of Brewer and Park [17] on the pressure side of a cambered foil also showed the shape factor to be insensitive to Reynolds numbers within the test range of 10^6–10^8. Therefore, the use of momentum thickness, displacement thickness, or boundary layer thickness as the characteristic length to normalize vortex core will give the same result in cavitation inception scaling.

McCormick's assumption is now applied in this paper. From the geometric and kinematic similarities between the model- and the full-scale, and the pi theory, the vortex core size is normalized by δ.

$$a_{cf}/a_{cm} = \delta_f/\delta_m \tag{9}$$

The next task is to express the scaling of the boundary layer thickness in geometric and kinematic variables.

2.4 Cavitation Inception Scaling Using $\frac{1}{7}$th Power Law Velocity Profile for Modeling. Experimental data analyzed by Blasius (see Ref. [16]) showed that the velocity profile on a turbulent boundary layer was well represented by the $\frac{1}{7}$th power law. For this profile the boundary layer thickness scales with Reynolds number as

$$\frac{a_{cf}}{a_{cm}} = \frac{\delta_f}{\delta_m} = \lambda\left(\frac{\mathrm{Re}_f}{\mathrm{Re}_m}\right)^{-0.2} \tag{10}$$

Based on the $\frac{1}{7}$th power law velocity profile, the ratio of vortex core size, as given in Eq. (10), is shown to decrease with an increase in Reynolds number by $\mathrm{Re}^{-0.2}$.

The flow on the surface of a rotating disk is of great importance for rotary machines such as propellers. This subject was studied by von Karman [18] and Goldstein [19]. Let ω and r denote the angular velocity and radial distance from the axis, respectively. The flow in a rotating disk becomes turbulent at large Reynolds numbers $\mathrm{Re} = r(r\omega)/\nu$ in the same way as the flow along a plate. With the balance of viscous and centrifugal forces, Schlichting [16] obtained the boundary layer thickness on a rotating disk as follows:

$$\delta = 0.526r(\omega r^2/\upsilon)^{-0.2} = 0.526r\ \mathrm{Re}^{-0.2} \tag{11}$$

Hence for a rotating disk, the Reynolds scaling of the boundary layer thickness and vortex core size is

$$\frac{a_{cf}}{a_{cm}} = \frac{\delta_f}{\delta_m} = \lambda\left(\frac{\mathrm{Re}_f}{\mathrm{Re}_m}\right)^{-0.2} \tag{12}$$

Equations (10) and (12) show that the scaling of turbulent boundary layer thickness on a rotating disk exhibits the same dependence on Reynolds scale as that of a flat plate $\mathrm{Re}^{-0.2}$. The scaling formula for a rotating propeller is therefore expected to exhibit a $\mathrm{Re}^{-0.2}$ dependence as well.

From Eq. (4), the cavitation inception scaling based on a $\frac{1}{7}$th power law velocity profile becomes

$$\frac{\sigma_{if}}{\sigma_{im}} = [\lambda(V_{0f}/V_{0m})]^2\left[\frac{1}{\lambda}(\mathrm{Re}_f/\mathrm{Re}_m)^{0.2}\right]^2 \bullet (V_{om}/V_{of})^2 = (\mathrm{Re}_f/\mathrm{Re}_m)^{0.4} \tag{13}$$

Equation (13) shows that the tip vortex cavitation inception varies with Reynolds scale by the 0.4 power because of the viscous effects on the boundary layer thickness. Experimental measurements by Fruman et al. [10] show measured cavitation inception σ_i indices that do scale with $\mathrm{Re}^{0.40}$. But this scaling law assumes a priori that the velocity profile is well-described by a $\frac{1}{7}$th power law relation. If the velocity profile varies from this, a different scaling relation will result. The problem becomes one of describing a scaling relationship that applies over as great a range of Reynolds numbers as possible, at least covering the Reynolds numbers encompassed from experiments to full-scale.

2.5 Accuracy of $\frac{1}{7}$th Power Law Assumptions. The boundary layer thickness on a flat plate derives from Prandtl's assumption that the friction coefficient is related to the boundary layer thickness to the $-\frac{1}{4}$ power and that the momentum thickness is about 1/10 of the boundary layer thickness (matches a 1/7th power law velocity profile). Using these two approximations to solve Karman's integral relation for the friction coefficient results in the -0.2 exponent. That is,

$$\delta/x = 0.37\ \mathrm{Re}^{-0.2}$$
$$\delta_1/x = 0.046\ \mathrm{Re}^{-0.2} \tag{14}$$

and the resulting friction coefficient is

$$C_f = 0.074\ \mathrm{Re}^{-0.2} \tag{15}$$

Recently, a large two-dimensional foil was tested in the Naval Warfare Center's Large Cavitation Channel. The foil has a NACA-0016 suction side and a flat surface on the pressure side after $x/c = 0.28$. The model was tested at high speeds to achieve high Reynolds numbers of 9.0×10^6–5.6×10^7. Detailed discussions of the test setup and measurements are given in the paper by Judge et al. [20]. Brewer and Park [17] obtained boundary layer profiles and friction velocities by numerical integration of the velocity profiles measured by laser doppler velocimetry (LDV). They obtained a power law curve fit for the displacement thickness versus Reynolds number for the pressure side data. These data show that the viscous effect on the boundary layer displacement thickness and friction coefficient at high Reynolds numbers is significantly weaker than the value of $\mathrm{Re}^{-0.2}$ predicted by a 1/7th power law.

The measured and computed torque coefficients on a rotating

disk are discussed in the papers by von Karman [18] and Goldstein [19]. As pointed out by Schlichting, the centrifugal force generated by the rotating disk plays an important role on boundary layer development. Even at the moderate Reynolds numbers, calculations from the $\frac{1}{7}$th power law by von Karman deviate from the measurements. Again, calculations based on the logarithmic law by Goldstein agree well with experimental data.

Velocity distributions in a trailing vortex core on a foil was measured by Fruman et al. [10] using laser Doppler velocimetry. The characteristic dimension of the viscous core region in the vortex is compared with the boundary layer on the foil. The measured vortex core size deviates progressively from the calculated turbulent boundary layer thickness as the Reynolds numbers are increased (see Fig. 10 of Ref. [10]). The pattern of deviation with Reynolds number shown on the core of a NACA foil vortex is similar to the pattern of friction coefficient shown on a flat plate. The influence of viscosity on the vortex core size is much weaker than predicted by $\frac{1}{7}$th power law assumptions as the Reynolds numbers increased.

3 Logarithmic Law and Cavitation Inception Scaling

In practical applications, the Reynolds number that ranges from model- to full-scale often exceeds the range of validity of a $\frac{1}{7}$th power law assumption. The theory of the friction coefficients on a flat plate based on the $\frac{1}{7}$th power law yields results that deviate increasingly from the measurements as Reynolds numbers are increased. Schlichting [16] fitted the friction coefficients and Reynolds numbers to give the following expression:

$$C_f = 0.455/(\log \mathrm{Re})^{2.58} \tag{16}$$

This logarithmic expression gives good agreement with flat plate experimental data even at large Reynolds numbers.

Cavitation inception scaling based on a logarithmic law will now be derived. The momentum thickness is related to the friction coefficient by

$$\delta_2/x = C_f/2 = 0.228/(\log \mathrm{Re})^{2.58} \tag{17}$$

The momentum thickness then scales as

$$\delta_{2f}/\delta_{2m} = \lambda(\log \mathrm{Re}_m/\log \mathrm{Re}_f)^{2.58} \tag{18}$$

If the vortex core size scales as the momentum thickness, then

$$\frac{a_{cf}}{a_{cm}} = \frac{\delta_{2f}}{\delta_{2m}} = \lambda(\log \mathrm{Re}_m/\log \mathrm{Re}_f)^{2.58} \tag{19}$$

Equations (4), (16), and (19) give

$$\sigma_{if}/\sigma_{im} = (-Cp_{\min f}/-Cp_{\min m}) = [\lambda(V_{0f}/V_{0m})]^2\left[\frac{1}{\lambda}(\log \mathrm{Re}_f/\log \mathrm{Re}_m)^{2.58}\right]^2 (V_{0m}/V_{0f})^2 \tag{20}$$

In short, the new scaling gives

$$\frac{\sigma_{if}}{\sigma_{im}} = (\log \mathrm{Re}_f/\log \mathrm{Re}_m)^{5.16} \tag{21}$$

The new scaling formula depends on both values of Re_f and Re_m. This contrasts the scaling given in Eq. (13) in which the scaling formula depends only on the ratio of $\mathrm{Re}_f/\mathrm{Re}_m$.

Equation (21) should be applicable from the Reynolds numbers of 3×10^5 and above. Below the Reynolds numbers of 3×10^5, the model flow may be laminar or in transition, and the friction relation of Eq. (16) may be invalid in that range. Provided that the boundary layer on the foil surface is fully turbulent, Eq. (21) should be valid.

3.1 Expression of the New Scaling in Conventional *m* Scaling Format. Numerous model tests were conducted to determine the values of m to fit the previously mentioned power law scaling.

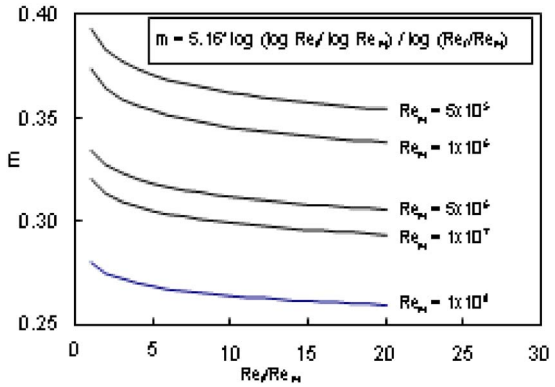

Fig. 2 Variation of *m* with Reynolds number

The new scaling $\sigma_{if}/\sigma_{im} = (\log \mathrm{Re}_f/\log \mathrm{Re}_m)^{5.16}$ can be expressed in an equivalent power law format for comparison, that is,

$$\sigma_{if}/\sigma_{im} = (\log \mathrm{Re}_f/\log \mathrm{Re}_m)^{5.16} = (\mathrm{Re}_f/\mathrm{Re}_m)^m \tag{22}$$

Hence,

$$m = 5.16 \log(\log \mathrm{Re}_f/\log \mathrm{Re}_m)/\log(\mathrm{Re}_f/\mathrm{Re}_m) \tag{23}$$

Numerical values computed from Eq. (23) are given in the following figures.

Figure 2 shows the value of m versus the ratio of $\mathrm{Re}_f/\mathrm{Re}_m$ with Re_m as a variable. At $\mathrm{Re}_m = 5\times10^5$, the value of m approaches 0.4 as the ratio $\mathrm{Re}_f/\mathrm{Re}_m$ approaches 1. The values of m decrease as the ratio $\mathrm{Re}_f/\mathrm{Re}_m$ increases for a given Re_m. Even at the same value of $\mathrm{Re}_f/\mathrm{Re}_m$, the values of m decrease as the values of Re_m increase. The value of m approaches zero at the limit of very high Reynolds numbers. This agrees with the concept that the effect of viscosity on cavitation diminishes as the Reynolds number approaches infinity, analogous to the general trend of flows to become inviscid at higher Reynolds numbers. In contrast, conventional power law scaling considers m to be a fixed value that never reaches zero, independent of Reynolds numbers.

4 Experimental Comparisons

4.1 Model-Model Comparisons. Platzer and Souders [21] conducted a series of tip vortex cavitation inception tests on an elliptical foil in a 36 in. water tunnel. Oil paint flow visualization showed that the flow was basically chordwise except in the region close to the tip, which is the outermost 10% of the span. Only in this area did the flow exhibit a noticeable spanwise flow component. Based on this, the chord length at 10% from the tip is assumed to be the characteristic length to be used to define the Reynolds number for tip vortex cavitation study. Although the boundary layer flow from the entire wing ultimately wraps up into the tip vortex, cavitation typically occurs within a fraction of the chord along the vortex axis, and only the tip flow of the foil has rolled up into the vortex at this point. From the data of Platzer and Souders [21], the Reynolds numbers based on the chord length at 10% from the tip covered the range from 1.1×10^6 to 2.2×10^6, yielding a factor of two in Reynolds number variations. Their inception data showed a Reynolds number dependency of $m = 0.36$. This data point is plotted in Fig. 3.

Tip vortex cavitation on an elliptical foil was extensively tested by Fruman and co-workers [10,13]. Within the Reynolds number range from 2.2×10^5 to 5.6×10^5 (based on 10% span), the inception data showed a Reynolds number dependency of $m = 0.40$. This data point is also shown in Fig. 3.

Arndt and co-workers [2,3] tested four different foils of the same elliptical planform. Within the Reynolds numbers of 2.18×10^5 and 5.67×10^5, the cavitation inception data exhibit strong correlation with $\mathrm{Re}^{0.4}$. This data point is also plotted in Fig. 3.

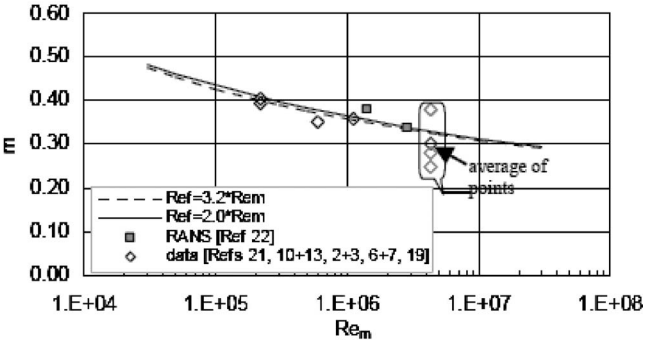

Fig. 3 Experimental values of *m*

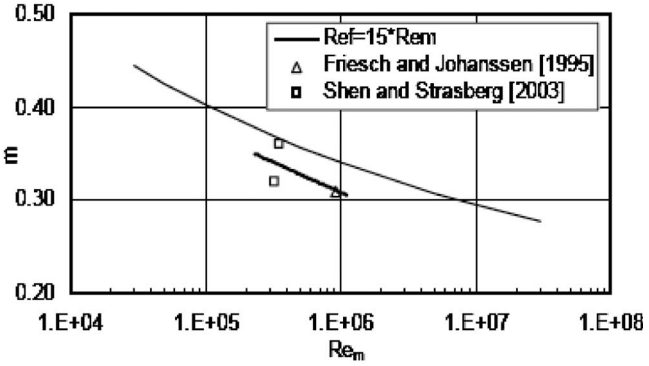

Fig. 4 Values of *m* for $\lambda=15$

Note that the Reynolds number exponent and the tested Reynolds numbers are almost identical between Arndt and Dugue [3] and Fruman and co-workers [10,13].

McCormick [6,7] conducted a series of tip vortex cavitation tests on rectangular and elliptical foils. The inception data exhibit good correlation with $\mathrm{Re}^{0.35}$ at the tested Reynolds numbers of 0.6×10^6 and 1.9×10^6. This data point is also plotted in Fig. 3.

A three-bladed propeller was recently tested in the 36 in. water tunnel. The test setup and the geometry of this propeller were discussed in the paper by Judge et al. [19]. The propeller was tested over a speed range of a factor of two using the thrust identity to set the tunnel speeds. The Reynolds numbers based on the chord at the 0.9 propeller radius were $4.3\times10^6-8.6\times10^6$. Tip vortex cavitation inception was detected visually on each blade. The best curve fit of the inception data gave the values of $m=0.38$, $m=0.28$, and $m=0.25$, respectively, for the three blades. The m values of blades 2 and 3 were almost identical within the accuracy of measurements. The variation of the m value for blade 1 from the other 2 blades was not expected nor can be explained. The averaged value of $m=0.303$ at $\mathrm{Re}=4.3\times10^6$ is plotted in Fig. 3 for comparison with the theory.

Figure 3 also shows the value of m based on values of $C_{p\,\min}$ calculated by Hsiao and Chahine [22] for two pairs of vortices with a scale ratio of 2.0.

These data were now compared with the theoretical values of m versus Re_m for the cases of $\mathrm{Re}_f/\mathrm{Re}_m=2.0$ and $\mathrm{Re}_f/\mathrm{Re}_m=3.2$, which are the limits of the Reynolds ratios in this data set. The m values are not sensitive to this small a variation in ratio as seen by the closeness of the lines. At $\mathrm{Re}_m=3\times10^5$, for example, theoretical m varies between 0.383 and 0.377, a variation of less than 2%, for $2.0<\mathrm{Re}_f/\mathrm{Re}_m<3.2$. The variations of m caused by variations of test conditions (nuclei, manufacturing, etc.) were larger than those from variations of the Reynolds number from which the scaling exponent is predicted.

For Fig. 3, the theory gives $m=0.40$ for $\mathrm{Re}_m=3\times10^5$ (barely turbulent) and $m=0.274$ for $\mathrm{Re}_m=1\times10^8$. Overall the measured values of m show a decrease with increasing Reynolds numbers as predicted by the theory. The good agreement exhibited in Fig. 3 between the available experimental data and the present theory is encouraging.

4.2 Model-Full-Scale Comparisons. The model- and full-scale data comparisons are difficult because model data are typically based on visual inception and full-scale data are more often based on acoustic or accelerometer signals. These techniques can show variations of a few knots in inception speed for the same propeller, making determination of the scaling exponent difficult. Whereas errors in estimates of the model- and full-scale Reynolds numbers cause small variations of the predicted exponent m, a 1 kn variation in inception speed for a 12 kn full-scale condition changes σ over 15%. These variations for inception speed prevent assessment of the scaling exponent with reasonable precision. There are some comparisons, however, based on visual inception at both scales.

Friesch and Johannsen [12] conducted a series of full-scale propeller tip vortex cavitation observations. They also conducted corresponding tests in the Hamburgische Schiffbau Versuchanstalt (HSVA's) large tunnel, HYKAT, with $\frac{1}{15}$ scale models. Tip vortex cavitation was observed visually for both tests. They converted the full-scale operating curve to model values and obtained the power index in McCormick's scaling formula of $m=0.31$, which is substantially smaller than $m=0.4$ used widely today. The model propeller Reynolds number at $r/R=0.9$ is estimated to be around 0.92×10^6, based on similar values of Reynolds numbers from HYKAT tests of the Sydney Express propeller reported by Weitendorf [23], and a corresponding full-scale Reynolds number of 1.4×10^7 assuming the kinematic viscosity in the model- and full-scale tests were the same. The present theory based on these Reynolds numbers gives $m=0.34$, which is 10% higher than the index derived in the paper. This result is shown in Fig. 4.

Measurements made long ago of the underwater noise associated with propeller tip vortex cavitation on a WW II submarine are now available for comparison in Refs. [24,25]. USS HAKE was a four-bladed twin screw submarine with a propeller diameter of 2.50 m. The noise levels at various speeds were measured by four hydrophones at two depths over frequencies from 10 kHz to 30 kHz. Corresponding model tests were carried out in a towing basin using a wooden model with a small hydrophone placed inside the hull. The model had a geometric scale ratio of $\frac{1}{14.5}$, close to $\frac{1}{15}$. The propeller rotation speed was adjusted to simulate self-propelled conditions using an advanced ratio determined from speed trials of the prototype submarine. The noise curves for the model- and full-scale data showed that the propeller had a quiet and a noisy speed range. The transition from quiet to noisy operation was marked by a sudden increase in noise level with speed, and at higher speeds, the noise changed little. Assuming that the noise increase was caused by vortex cavitation and using the juncture of quiet and noisy speeds as the inception speed, a power index of $m=0.315$ would be obtained for a corresponding model Reynolds number of 3.32×10^5. Using a criterion of 3 dB above the background to define inception, an index of $m=0.36$ would be obtained with a corresponding model Reynolds number of 3.54×10^5. The results are shown in Fig. 4. The line shown for these three data is a linear fit of the points.

These data are encouraging, but more experimental data are needed to validate the theory, especially at high Reynolds numbers.

5 Conclusions

The scaling of tip vortex cavitation inception was derived assuming geometric and kinematic similarities between the model- and the full-scale. Using the momentum thickness of the boundary layer near the tip to correlate with the scaling of the vortex core

size, previously derived results for friction factors over a wide range of Reynolds numbers allow the momentum thickness variation to be predicted. In the absence of nuclei effects, the resulting cavitation inception scaling due to viscosity effects is given by

$$\sigma_{if}/\sigma_{im} = (\log \mathrm{Re}_f/\log \mathrm{Re}_m)^{5.16}$$

This new scaling can be expressed in the conventional power law format as

$$\sigma_{if}/\sigma_{im} = (\mathrm{Re}_f/\mathrm{Re}_m)^m$$

and

$$m = 5.16 \log(\log \mathrm{Re}_f/\log \mathrm{Re}_m)/\log(\mathrm{Re}_f/\mathrm{Re}_m)$$

The values of m are variable and are dependent on Re_f and Re_m. This is in contrast with the conventional tip vortex cavitation inception scaling where m is treated as a fixed value.

The value of m approaches zero as the values of Re_f and Re_m approach infinity. Thus the viscous effect on tip vortex cavitation inception becomes weaker as the Reynolds number increases, approaching inviscid flow at very high Reynolds numbers.

In typical test facilities with the capability to vary Reynolds numbers by a factor of 2, the present theory gives $m=0.398$, $m=0.327$, and $m=0.313$ at $\mathrm{Re}_m=3\times10^5$, 5×10^6, and 10^7, respectively.

The present theory shows reasonable agreement with available experimental data. Nevertheless, more experimental data are needed, especially at high Reynolds numbers, to fully validate the theory.

Acknowledgment

This work was supported by NAVSEA 93R, Program Element No. 63561N under the direction of Doug Dahmer. We appreciate very much the technical support and discussions by Mr. Jude Brown.

Nomenclature

a_c = vortex core radius
c = foil chord length
C_F = flat plate friction drag coefficient
C_L = lift coefficient
c_l = section lift coefficient
C_M = torque coefficient of a rotating disk
$C_{p\,\min}$ = minimum pressure coefficient in the vortex core
G = nuclei effect on cavitation inception
L = foil lift
$P(r)$ = local pressure in the trailing vortex
P_o = reference (ambient) pressure
m = exponent used in Reynolds scale formula
r = radial distance from the vortex core center
Re = Reynolds number based on the chord length
s = nondimensional spanwise coordinate variable
V_o = reference velocity
V_t = tangential velocity of the trailing vortex
Γ = circulation along the vortex core
ρ = fluid density
σ = cavitation number
σ_i = cavitation inception number
γ = bound vortex on the foil surface
λ = linear scale ratio between full-scale and model-scale
δ = boundary layer thickness
δ_1 = displacement thickness of the boundary layer
δ_2 = momentum thickness of the boundary layer

References

[1] Cavitation Committee, 1990, 19th ITTC, Madrid, Spain.
[2] Arndt, R., and Dugue, C., 1992, "Recent Advances in Tip Vortex Cavitation Research," International Symposium on Propulsors and Cavitation, Hamburg, Germany.
[3] Maines, B. H., and Arndt, R. E. A., 1993, "Viscous Effects on Tip Vortex Cavitation," FED (Am. Soc. Mech. Eng.), **177**, pp. 125–132.
[4] Loftin, L. K., and Smith, H. A., 1949, "Aerodynamic Characteristics of 15 NACA Airfoil Sections at Reynolds Numbers From 0.7×10^6 to 9.0×10^6," Paper No. NACA TN 1945.
[5] Jessup, S. D., Remmers, K. D., and Berberich, W. G., 1993, "Comparative Cavitation Performance of a Naval Surface Propeller," ASME Symposium on Cavitation Inception, New Orleans, LA.
[6] McCormick, B. W., 1954, "A Study of the Minimum Pressure in a Trailing Vortex System," Ph.D. dissertation, Penn State University, State College, PA.
[7] McCormick, B. W., 1962, "On Cavitation Produced by a Vortex Trailing From a Lifting Surface," J. Basic Eng., **84**, pp. 369–379.
[8] Liang, X., and Ramaprian, B. R., 1991, "Visualization of the Wing-Tip Vortex in Temporal and Spatial Pressure Gradients," ASME J. Fluids Eng., **113**, pp. 511–515.
[9] Baker, G. R., Barker, S. J., Bofat, K. K., and Saffman, P. G., 1974, "Laser Anemometer Measurements of Trailing Vortices in Water," J. Fluid Mech., **65**(2), pp. 325–336.
[10] Fruman, D. H., Dugue, C., and Cerruti, P., 1991, "Tip Vortex Roll-Up and Cavitation," FED (Am. Soc. Mech. Eng.), **109**, pp. 43–48.
[11] Arndt, R. E. A., 2002, "Cavitation in Vortical Flows," Annu. Rev. Fluid Mech., **34**, pp. 143–175.
[12] Friesch, J., and Johannsen, C., 1995, "Study on Tip Vortex Cavitation Inception for Navy Propellers," International Symposium on Cavitation, CAV 1995, Deauville, France.
[13] Fruman, D., Dugue, C., Pauchet, A., Cerruti, P., and Briancon-Marjolet, L., 1994, "Tip Vortex Roll-Up and Cavitation," 19th Symposium of Naval Hydrodynamics, ONR, Washington, DC.
[14] Stinebring, D. R., Farrell, K. J., Billet, M. L., 1991, "The Structure of a Three-Dimensional Tip Vortex at High Reynolds Numbers," ASME J. Fluids Eng., **113**(3), pp. 496–503.
[15] Farrell, K. J., and Billet, M. L., 1994, "A Correlation of Leakage Vortex Cavitation in Axial-Flow Pumps," ASME J. Fluids Eng., **116**, pp. 551–557.
[16] Schlichting, H., 1979, *Boundary Layer Theory*, McGraw-Hill, New York.
[17] Brewer, J. H., and Park, J. T., 2001, "High Reynolds Number Boundary Layer Scaling on a Large Hydrofoil (HIFOIL)," Paper No. NSWCCD-50-TR-2001/08.
[18] von Karman, Th., 1921, "Laminar and Turbulent Friction," Z. Angew. Math. Mech., **1**(4), pp. 233–252.
[19] Goldstein, S., 1935, "On the Resistance to the Rotation of a Disc Immersed in a Liquid," Proc. Cambridge Philos. Soc., **31**, pp. 232–241.
[20] Judge, C., Oweis, G., Ceccio, S., Jessup, S., Chesnakas, C., and Fry, D., 1991, "Tip-Leakage Vortex Inception on a Ducted Rotor," Fourth International Symposium on Cavitation, CAV 2001, Pasadena, CA.
[21] Platzer, G. P., and Souders, W. G., 1980, "Tip Vortex Cavitation Characteristics and Delay on a Three-Dimensional Hydrofoil," 19th ATTC Conference, Madrid, Spain.
[22] Hsiao, C.-T., and Chahine, G. L., 2005, "Scaling of Tip Vortex Cavitation Inception Noise With a Bubble Dynamics Model Accounting for Nuclei Size Distribution," ASME J. Fluid Eng., **127**, pp. 55–65.
[23] Weitendorf, E. A., 1979, Conclusions From Full Scale and Model Investigations of the Free Air Content and of the Propeller-Excited Hull Pressure Amplitudes Due to Cavitation, ASME International Symposium on Cavitation Inception, New York.
[24] Strasberg, M., 1977, "Propeller Cavitation Noise After 35 Years of Study," Proceedings of the ASME Symposium on Noise and Fluids Engineering, Atlanta, GA.
[25] Shen, Y. T., and Strasberg, M., 2003, "The Effect of Scale on Propeller Tip Vortex Cavitation Noise," Paper No. NSWCCD-50-TR-2003/057.

A New Method for Numerical Prediction of Liquid Column Separation Accompanying Hydraulic Transients in Pipelines

Adam Adamkowski

Mariusz Lewandowski

Department of Hydraulic Machinery,
Szewalski Institute of Fluid-Flow Machinery,
Polish Academy of Sciences,
Gdansk 80-231, Poland

This paper presents a new method for calculating pressure fluctuations in pipelines during a water hammer with liquid column separation. The method is based on the discrete-vapor-cavity model (DVCM). Such kind of models assumes that vaporous cavities are formed in each computational section of the pipeline whenever the pressure drops to the vapor pressure at a given temperature. The proposed new model (new DVCM) brings a significant improvement in the reliability of predictions compared with existing DVCMs. The calculation method based on it eliminates some disadvantages of basic methods used in practice, as shown by comparisons between calculations made for simple hydraulic system under theoretical frictionless conditions using various DVCMs. Additionally, the authors present preliminary verification of the proposed model based on experimental results. The positive results of this verification, and the advantages of the new DVCM, could lead to incorporating them into commercial codes. [DOI: 10.1115/1.3153365]

1 Introduction

Under certain conditions, the temporary drop of fluid pressure in a pipeline to the level of the vapor pressure can cause the appearance of vapor-gas filled cavities. These cavities are responsible for discontinuities in the stream of liquid. Such a situation may occur during quick valve opening or closing, or the starting and stopping of hydraulic machines, as a result of a water hammer pressure surge. After some time, these vapor-gas cavities reduce in size or collapse, generating sudden high-pressure peaks. Usually these cavities repeatedly grow and shrink, or collapse. Cavity zones large enough to fill the whole pipe cross section are the most important from a practical point of view, as the liquid column loses its continuity. Sudden and significant pressure peaks accompanying this phenomenon often cause hydraulic system breakdown or even complete destruction of such systems [1–3].

The liquid column separation accompanying a water hammer has been the subject of much research conducted worldwide [4–16]. An extensive review of this research was performed by Bergant et al. [17]. The phenomenon discussed here was observed, and its physical aspects were explained for the first time by Joukovsky in 1898 [18]. Until the 1960s, models using graphic prediction of water hammer with liquid column separation were used. Then, a model designed especially for computer algorithms was created based on the method of characteristics (MOC). Afterward, many alternative numerical models have been developed [5,7,19–22].

Discrete vapor cavity models (DVCMs) play a dominant role among all methods used for predicting the course of water hammer with liquid column separation. They consider only vapor cavities and neglect gas cavitation, even though in reality the cavity zones created are always filled with both vapor and gas volumes. The release of gas from a liquid when its pressure drops beneath the value of the saturation pressure for the gas is a slow process in comparison with the very quick vapor cavitation phenomenon, neglecting the release to simplify the model seems to be reasonable. Vaporous zones are taken into consideration by incorporating internal boundary conditions into algorithms for solving equations describing the unsteady flow of liquid in closed conduits [23,24]. The main assumptions for these models are as follows (Fig. 1).

(a) Vaporous zones are concentrated at computational cross sections of the pipe, and they appear when the static pressure at such sections drops to or below the vapor pressure p_v at a given temperature.
(b) The pressure of the fluid in cross sections with a vaporous zone is equal to the saturated vapor pressure while the cavity persists.
(c) The vaporous zone is filled with vapor, causing discontinuity in the primal liquid stream and dividing it into two separate and continuous regions of liquid. Assuming that the vaporous cavity fills the whole area of a pipe cross section results from a 1D model used for describing the unsteady pipe flow.
(d) The cavity volume depends on parameters describing the motion of the liquid outside the vaporous zone and does not depend on the physicochemical characteristics of the liquid.

Calculation of cavity volume is based on the flow continuity equation

$$V_{\text{cav}} = \int_{t_o}^{t} (Q^+ - Q^-)dt \tag{1}$$

where t_o represents the time moment of the cavity appearance and is defined as a moment when the calculated pressure in the specific cross section drops to the level equal or below p_v. $Q^+ = AV^+$ and $Q^- = AV^-$ are the volume flow rates of liquid on the right and left sides of the vaporous zone, respectively. V is the average velocity in the pipe and A equals the pipe cross-section area.

So far, there are no satisfactory results from using computational methods to simulate liquid column separation phenomenon based on such discrete models. The classic model of a vapor cavity most often used in commercial codes assumes that vaporous zones are created in every computational cross section, where

Contributed by the Fluids Engineering Division of ASME for publication in the JOURNAL OF FLUIDS ENGINEERING. Manuscript received December 3, 2007; final manuscript received May 12, 2009; published online June 19, 2009. Assoc. Editor: Malcolm J. Andrews. Paper presented at the 2007 ASME Fluids Engineering Division Summer Meeting and Exhibition (FEDSM2007), San Diego, CA, July 30–August 2, 2007.

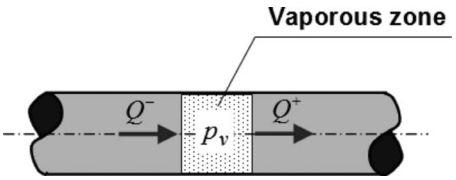

Fig. 1 The discrete model of a pipe flow with column separation

pressure drops to or below p_v level. The main disadvantage of this model is that it usually gives results different from those observed in reality, in particular, there may occur "numerical" pressure peaks as artifacts of the discontinuities spread over several computational cross sections. Such peaks may even cause instabilities in a calculation, including its termination. It is believed that these peaks result from the superimposition of many pressure waves generated by the sudden collapse of the many discontinuity zones simulated in the pipe flow. Attempts to avoid this effect have been made [15,16]. In one method, a small amount of undissolved air is introduced into all the computational cross sections where a cavity volume grows. The main reason for this was to attenuate the pressure peaks mentioned above [16,20], but still these peaks were not eliminated completely.

Another approach assumes that the discontinuity zone is created only in one particular cross section [22,25]. Usually the section adjacent to the flow control device (valve) or located at the highest point of the pipeline is chosen. Calculations conducted using this approach do not result in artificial pressure peaks. According to some authors [26], its main disadvantage is the necessity to determine the cross section where the vaporous zone appears during calculations [26]. However, additional and far more important weaknesses of this model are described later in the present paper. It will be shown that pressure courses calculated using the model with a single vaporous zone are characterized by the excessive attenuation of pressure oscillations that result from a failure to satisfy the mass and energy conservation laws.

In the new model described here, it is assumed that cavity volumes calculated in several computational cross sections are shifted toward a single cross section without breaking these basic conservation laws. The results are devoid of artificial numerical attenuation and free of the artificial pressure peaks observed while using the classical model. The method has been subjected to a preliminary verification using the experimental results obtained at a test rig designed and erected at the Szewalski Institute of Fluid-Flow Machinery of the Polish Academy of Sciences (IMP PAN) in Gdansk, Poland.

2 Unsteady Fluid Flow in Pipelines: Assumptions and Basic Equations

The computational method is based on the classic theory of water hammer (hydraulic transients). The main assumptions are as follows.

- Fluid flow is one dimensional. Quantities describing the flow are averaged over pipe cross sections and depend on time and the distance measured along the pipe axis.
- The liquid is assumed to be a low-compressible fluid; that is, it deforms elastically under pressure surges with insignificant change in density.
- The pipeline wall is deformed by pressure surges according to the theory of elastic deformation. The dynamic interactions between fluid and pipeline wall are neglected.
- Fluid velocity is small compared with the pressure wave speed.

The following equations are used for the mathematical description of unsteady liquid flows in pipelines [24,27].

- For continuity equation,

$$\frac{\partial H}{\partial t} + \frac{a^2}{gA} \cdot \frac{\partial Q}{\partial x} = 0 \tag{2}$$

- For momentum equation,

$$\frac{\partial H}{\partial x} + \frac{1}{gA}\frac{\partial Q}{\partial t} + J = 0 \tag{3}$$

Equations (2) and (3) form a closed system of partial differential equations of hyperbolic type with unknown functions of piezometric head, $H=H(x,t)$, and volumetric flow rate, $Q=Q(x,t)$ ($Q=VA$). Elasticity of pipe walls and liquid is represented by the pressure wave speed a in Eq. (2).

The quantity J in Eq. (3) stands for head loss per unit of pipe length and represents hydraulic resistance caused by both internal friction within the liquid and friction at the pipe wall. According to the quasisteady hypothesis, the hydraulic losses in an unsteady flow are calculated using formulas valid for steady flows. Such an approach may be the main source of discrepancies between experimental and numerical results for the pressure wave damping effect.

An alternative approach is to include the unsteady friction losses in the mathematical description of unsteady fluid flow in closed conduits. In the relevant literature, a large variety of unsteady friction models can be found. In general, they assume that the quantity J is a sum of the quasisteady flow pipeline resistance, the active resistance resulting from viscous friction at the pipe wall, J_q, and the pipeline inertance, reactance accounting for liquid inertia, J_u:

$$J = J_q + J_u \tag{4}$$

Modeling quantity J_q is based on the quasisteady flow hypothesis and usually based on the Darcy–Weisbach equation

$$J_q = \frac{f_q}{DA^2} \cdot \frac{Q|Q|}{2g} \tag{5}$$

where the quasisteady friction coefficient f_q is calculated using the Hagen–Poiseuille law for laminar flows or the Colebrook–White formula for turbulent flows.

The models of unsteady friction losses focus on the J_u quantity. They can be classified into three groups according to the method of calculating the friction factor in the one-dimensional momentum equation.

- The friction term is related to the instantaneous velocity derivatives in the pipe cross section [28].
- The friction term is related to the past velocity changes in a given cross section [29–32].
- The friction term is calculated according to the irreversible thermodynamic theory [33,34].

The first group of models enables simple numerical calculations of friction losses. Hence, they are most frequently used for simulating water hammer courses. Models belonging to the second group demand much more effort when developing algorithms and require more computer storage. Knowledge of the flow history in a given pipe cross section is essential for enabling calculations of flow parameters in the next time step of simulation and requires storing very large sets of data. This considerably slows the calculations and makes the models from this group less attractive. However, these models have the virtue of conforming to theory, as are models belonging to the third category. On the other hand, models derived from the irreversible thermodynamic theory are still in a preliminary state of development and require many empirically determined coefficients. For further considerations, the Vardy and Brown model [29] was used. It is one of a group of

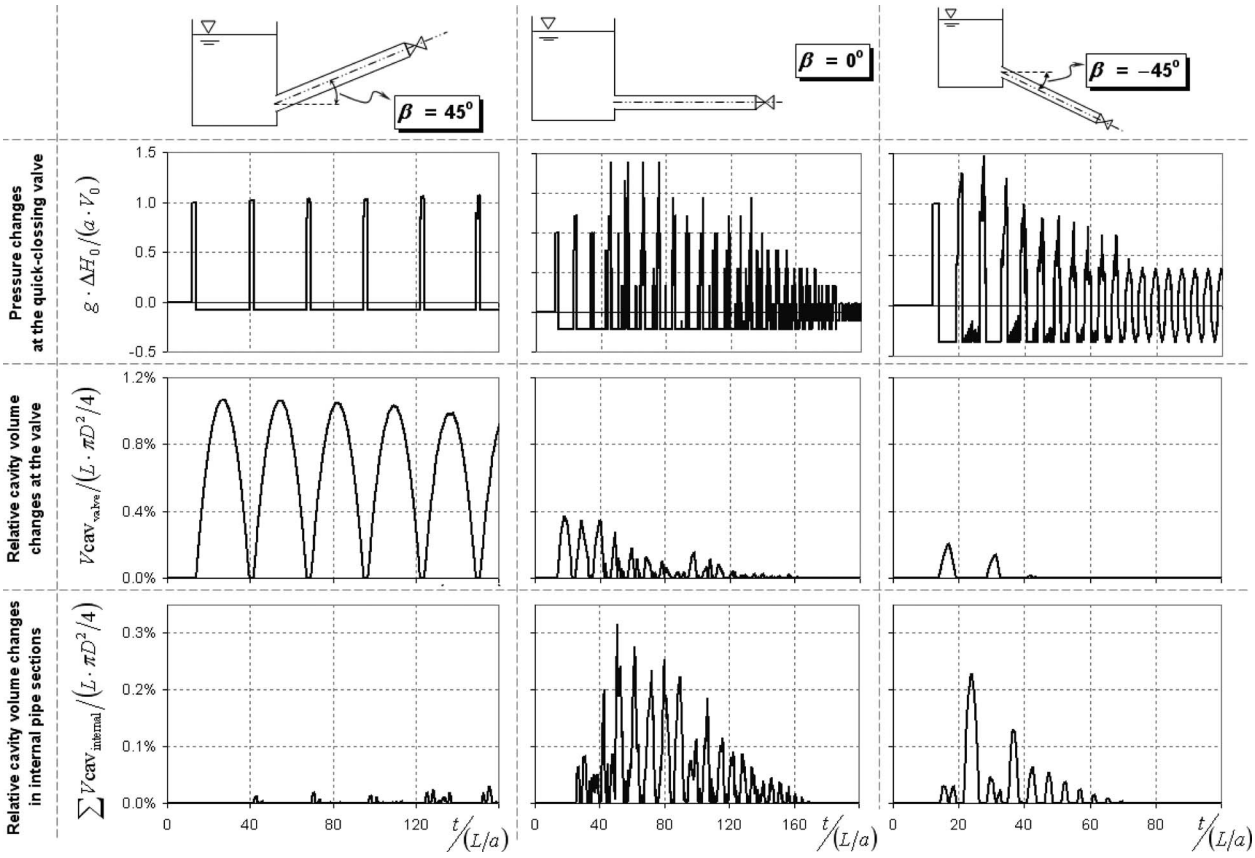

Fig. 2 Calculated pressure changes (cross section at the valve) and cavity volumes (V_{cav}) referred to the volume of the whole pipeline ($L \cdot \pi D^2/4$) obtained using the classic DVCM—calculation results for three different pipeline slopes

models that use past velocity changes to calculate the unsteady friction in turbulent unsteady flows. To solve the system of Eqs. (2) and (3), the MOC was applied [24,35,36].

3 The Origin and Essence of the New Model and the Resulting Calculation Method

The method presented below predicts liquid column separation during a water hammer course and is based on the DVCM. The vapor cavity is the only cavity type considered in this model. Gas cavitation is neglected as a phenomenon poorly recognized and showed small influence on the predicted maximal pressure amplitudes (the most important computational result in practical applications).

As in the classical model, vaporous zones are included by internal boundary conditions used when solving the system of Eqs. (2) and (3). The fluid flow within the continuous zones is described by these equations, and the assumption of a constant pressure $p=p_v$ or $H=H_v$ allows the calculation of all the required parameters of this flow averaged over the pipe cross section. As the gas cavities are neglected, the system of Eqs. (2) and (3) is solved for constant pressure wave speed a.

The main assumptions are similar to assumptions (a)–(d) presented in the Introduction. To calculate the cavity volumes in the computational sections of a pipeline, the following form of Eq. (1) is used:

$$V_{\mathrm{cav}_{t+\Delta t}} = V_{\mathrm{cav}_t} + [\psi \cdot (Q^+_{t+\Delta t} - Q^-_{t+\Delta t}) + (1-\psi) \cdot (Q^+_t - Q^-_t)] \cdot \Delta t \tag{6}$$

The ψ symbol in Eq. (6) stands for the weighting factor with a "normal" value of 0.5. This factor is confined to $0 \le \psi \le 1$ and is introduced into the finite difference scheme applied for integrating the cavity volume. According to Wylie [16], it is strongly recommended to choose a value within the range 0.5–1.0 because it eliminates numerical instabilities that appear during simulation of the transient. Additionally, we have found that ψ in some cases may be used to control the correctness of calculations of cavity volume changes in the proposed numerical method.

During liquid column separation, the cavity volume at a given cross section first expands and then contracts, resulting in a complete collapse of the cavity. If, during the simulation, the volume V_{cav} achieves a value equal to 0 or less, the condition for complete disappearance is fulfilled, and starting from this moment, in that particular cross section, calculations should be continued for the case without liquid column separation.

The authors initially used the classic DVCM in their analyses. This model assumes that vaporous zones arise in all computational cross sections of a pipe where static pressure drops to or below the saturated vapor pressure p_v. Figure 2 shows three examples of calculations performed using this model. A simple hydraulic system was chosen: an open reservoir with an infinite volume, a straight pipeline with a constant diameter, and a fast-closing valve. The following geometry and initial conditions were assumed: length of the pipeline $L=50$ m, internal diameter $D=0.25$ m, initial value of flow velocity under steady-state conditions $V_o=2$ m/s, head in the upper reservoir $H_o=44.6$ m and constant during the analyzed phenomenon, and the pressure wave speed $a=1200$ m/s. The numerical scheme used in these calculations consists of 33 cross sections along the pipeline axis and is based on a diamond shaped staggered grid [28]. The water hammer was caused by a sudden stepwise valve closure. To simplify further considerations, the hydraulic resistance was neglected. The configurations of the hydraulic systems differ in the pipe slope angle β. In general, the computational results are not satisfactory.

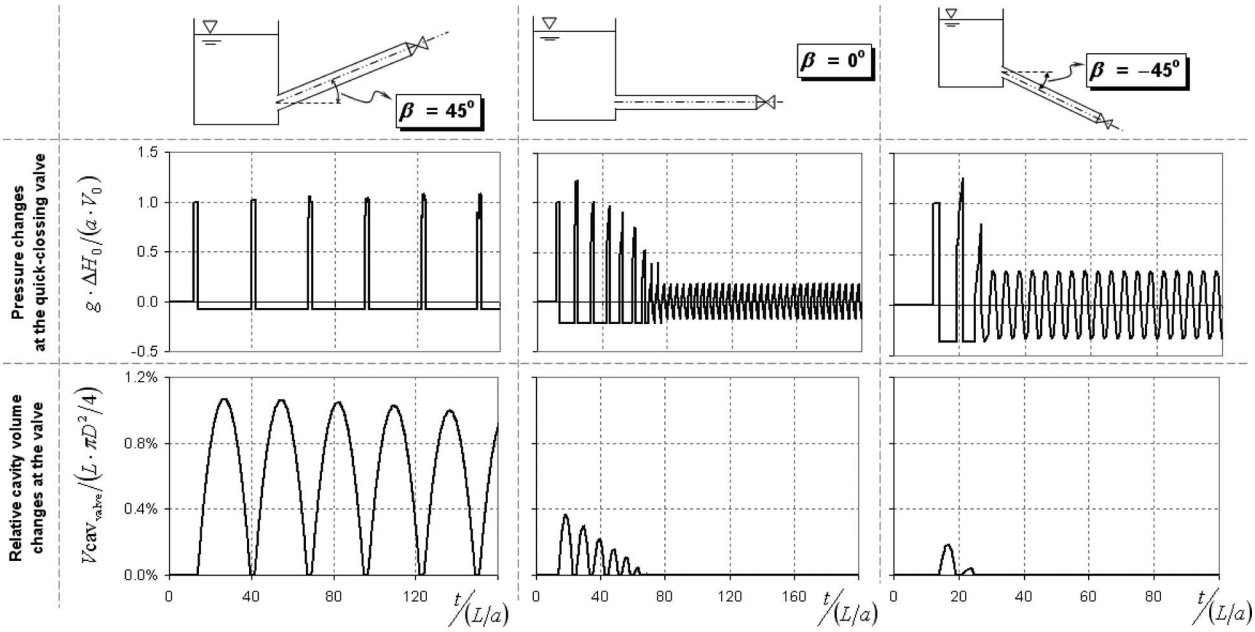

Fig. 3 Calculated pressure changes (cross section at the valve) and cavity volumes (V_{cav}) referred to the volume of the whole pipeline ($L \cdot \pi D^2/4$) obtained using the single-zone DVCM—calculation results for three different pipeline slopes

The artificial "numerical" pressure peaks are clearly apparent and, moreover, the pressure amplitudes decrease over time although the hydraulic resistance was neglected.

Having demonstrated the disadvantages of the classic DVCM, the authors studied the model with a single vaporous zone (single-zone DVCM). The original, developed by Safwat and Van Den Polder [22], was improved by introducing an automatic determination of the cross section where a vaporous zone is formed. This cross section is where the earliest pressure drop to or below the saturated vapor pressure (p_v) is observed. In the other cross sections, where $p \leq p_v$, the average value of volumetric flow rate is calculated using the formula $Q=0.5(Q^+ + Q^-)$, with Q^+ and Q^- denoting flow rates referring to the right and to the left sides of the discontinuity zone, respectively, calculated using the fixed value of $p=p_v$. The results of calculations conducted for the same hydraulic system with the same slopes to the pipeline are presented in Fig. 3.

In contrast to the classic DVCM, numerical pressure peaks were not observed in the results obtained using the single-zone DVCM. But despite neglecting the hydraulic resistance, the calculation results obtained using the single-zone DVCM show an attenuation of pressure amplitudes. As for the classic DVCM, the intensity of attenuation is clearly dependent on the angle β. One of the reasons for this undesirable feature is that the model leaves out cavity volumes created in cross sections other than the one in which the main vaporous zone is formed. Thus, the main cavity volume and also the pressure amplitudes decrease during the following cycles of the repeated column separations (Fig. 3). When we remove the hydraulic resistance from consideration, all calculated cycles of the analyzed liquid column separation phenomenon should be the same and should last infinitely. It may be stated that the single-zone DVCM does not meet basic conditions following from the mass and energy conservation laws.

To show the essence of the new proposed model, consider an idealized, straight pipe segment filled with liquid and vapor zones discretely distributed in two sections—k and $j \neq k$ (Fig. 4). Similar to the single-zone DVCM, the intermediate cross sections and the one with the main cavity volume are considered. Cross section k in Fig. 4 is the one where the earliest drop of pressure to or below the saturated vapor pressure (p_v) is observed, so the developing cavity is considered the main one.

In accordance with the principal assumption of the new model, a segment with two vaporous zones may be replaced with a segment with only one vaporous zone, that is, equivalent with regard to the mass and energy conservation laws. When pressure at a given cross section is assumed constant and equal to p_v, the mass conservation law requires equality between the cavity volume in the corresponding pipe segment and the sum of the cavity volumes in the original pipe segment. This law also requires the wave period along the pipe length to be preserved. In the intermediate cross sections of the pipeline, j, two streams of liquid flowing with velocities V_j^+ and V_j^- may be replaced with one continuous stream flowing with the velocity V_j. The energy conservation law requires that the sum of the kinetic and potential energies of elementary liquid masses separated by a vaporous zone has to be equal to the total energy following the reconnection of the two separate liquid streams. Thus it might be written as follows:

$$dm \cdot [(V_j^+)^2/2 + gz_j^+ + (V_j^-)^2/2 + gz_j^-] = dm \cdot [(V_j)^2/2 + gz_j^- + (V_j)^2/2 + gz_j^-] \quad (7)$$

For simplicity, it was assumed that the mass of the vapor filling the vaporous zone is negligible compared with the mass of liquid filling the same volume. According to the assumptions, velocity V_j should be calculated as follows:

$$V_j = \sqrt{0.5[(V_j^+)^2 + (V_j^-)^2] + g(z_j^+ - z_j^-)} \quad (8)$$

In Eq. (8) z_j^+ and z_j^- represent the altitudes of the centers of cross-sectional surfaces limiting the cavity within the computational cross section j from the right and left sides, respectively.

In the case of the horizontal pipeline, the difference $\Delta z_j = z_j^+ - z_j^-$ is equal to 0, whereas in general cases it can be calculated from the cavity volume:

$$\Delta z_j = (z_j^+ - z_j^-) = \frac{V_{\text{cav}_j}}{A_j} \sin \beta_j \quad (9)$$

where A_j stands for the cross-sectional area.

It is important to move the cavity volumes formed in the intermediate cross sections starting with those which are the most distant from the main vaporous zone located in the cross section k and to proceed in the same way at both sides of this cross section,

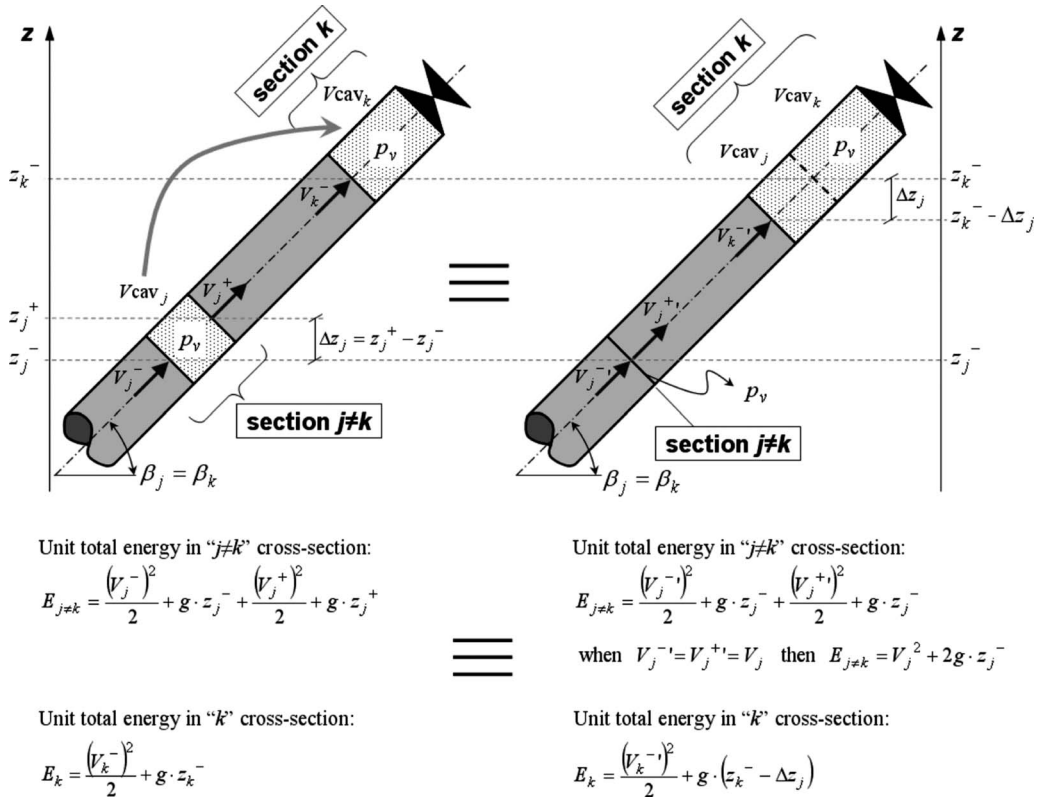

Fig. 4 The liquid flow and idealized vaporous zones in simple pipeline segments equivalent to each other as regards the mass and energy conservation laws

that is, for $j<k$ and for $j>k$. This means that the cavity volumes calculated in each time step at the intermediate cross sections most distant from k cross section are the first shifted into intermediate sections located by Δx closer to the main vaporous zone. This procedure is repeated until the total sum of all intermediate cavity volumes is added to the cavity volume in the main vaporous zone, cross section k.

As cavity volumes are moved from intermediate cross sections j to the main vaporous zone, velocity V_k^- in cross section k should be transformed into $V_k^{-\prime}$ to preserve the total energy of the liquid in these pipe segments (Fig. 4). This velocity should be calculated using the following equation:

$$V_k^{-\prime} = \sqrt{(V_k^-)^2 + 2g \cdot \Delta z_j} \tag{10}$$

The velocity at the right hand side of the main vaporous zone, at the cut-off valve, is equal to zero, $V_k^+=0$.

In the more general situation, with an idealized pipe segment filled with liquid and vaporous zones discretely distributed along its length in several sections (Fig. 3), after shifting cavity volumes from intermediate zones to the main vaporous zone and introducing appropriate signs for flow velocities V, Eq. (8) should be presented as follows.

- For $j<k$,

$$V_j = \mathrm{sgn}\left[0.5(V_j^+|V_j^+| + V_j^-|V_j^-|) + g\sum_{i=1}^{j}\frac{V_{\mathrm{cav}_i}}{A_i}\sin\beta_i\right] \cdot \sqrt{\left|0.5[(V_j^+)^2 + (V_j^-)^2] + g\sum_{i=1}^{j}\frac{V_{\mathrm{cav}_i}}{A_i}\sin\beta_i\right|} \tag{11}$$

- For $j>k$,

$$V_j = \mathrm{sgn}\left[0.5(V_j^+|V_j^+| + V_j^-|V_j^-|) + g\sum_{i=n}^{j}\frac{V_{\mathrm{cav}_i}}{A_i}\sin\beta_i\right] \cdot \sqrt{\left|0.5[(V_j^+)^2 + (V_j^-)^2] + g\sum_{i=n}^{j}\frac{V_{\mathrm{cav}_i}}{A_i}\sin\beta_i\right|} \tag{12}$$

For the pipeline segments presented in Fig. 5, the velocities at the left and right sides of the main vapor cavity in cross section k should be calculated based on the following equations with sign changes in flow velocities taken into account:

$$V_k^{-\prime} = \mathrm{sgn}\left(V_k^-|V_k^-| + 2g\sum_{j=1}^{k-1}\frac{V_{\mathrm{cav}_j}}{A_j}\sin\beta_j\right) \cdot \sqrt{\left|(V_k^-)^2 + 2g\sum_{j=1}^{k-1}\frac{V_{\mathrm{cav}_j}}{A_j}\sin\beta_j\right|} \tag{13}$$

$$V_k^{+\prime} = \mathrm{sgn}\left(V_k^+|V_k^+| + 2g\sum_{j=k+1}^{n}\frac{V_{\mathrm{cav}_j}}{A_j}\sin\beta_j\right) \cdot \sqrt{\left|(V_k^+)^2 + 2g\sum_{j=k+1}^{n}\frac{V_{\mathrm{cav}_j}}{A_j}\sin\beta_j\right|} \tag{14}$$

where j represents the index of an intermediate cross section where the liquid column separation has occurred; k represents the index of computational cross section where the earliest drop of pressure to or below p_v has been observed and assumed to be location of the main vaporous zone formation; i is the index of the subsequent intermediate cross sections where column separation

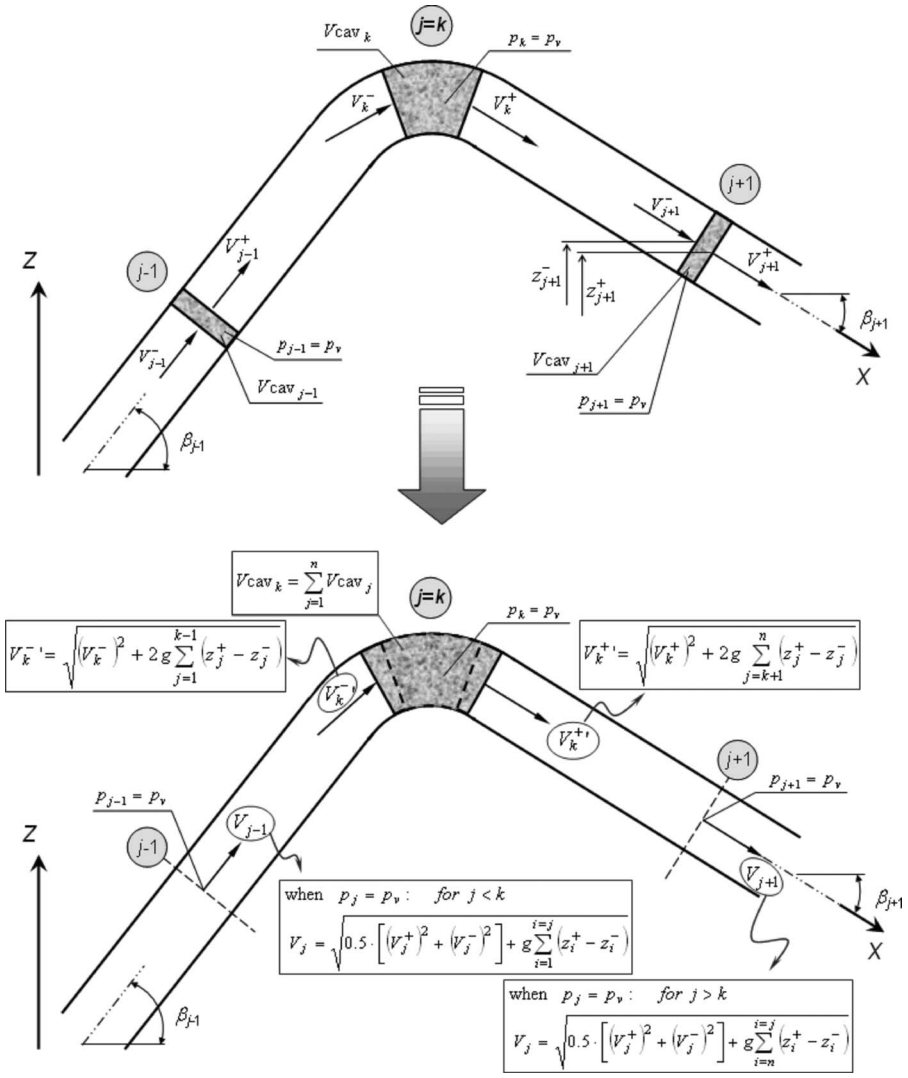

Fig. 5 Schematic diagram of the new DVCM for general case

has occurred, but with distance from the k cross section not less than the distance between j and k cross sections; and n is the total number of computational cross sections along the pipeline length.

All the relationships presented above result from the assumptions that form the basis of the new model. The relationships were incorporated into the authors' own computer code. To perform some preliminary tests of the new computational method, calculations for the same hydraulic configurations as those for the classic DVCM and the single-zone DVCM were conducted (Fig. 4). They show the correctness of the proposed model—the method does not generate unrealistic attenuation of pressure amplitudes, and the cavity volumes (Fig. 6) are not decreasing in any cycle, as was the case for both the classic DVCM and the single-zone DVCM. It is worthwhile to mention that the proposed new model, in which the "de facto" cavity volumes that arise at many cross sections along the pipeline are taken into account, seems to be transparent and simple.

4 Preliminary Experimental Verification of the New Model

The calculation method developed using all assumptions presented in this paper has been the subject of preliminary experimental verification. The experiment used in this case was conducted at a test rig specially prepared to investigate the water hammer phenomenon (Fig. 7). It was erected in the laboratory of the IMP PAN in Gdansk, Poland. Its main component is the $L=98.11$ m copper pipe with an internal diameter of $D=0.016$ m and a wall thickness of $e=0.001$ m. The pipe is spirally coiled on a steel cylinder with a diameter of about 1.7 m and is rigidly mounted to the steel cylinder coating in order to minimize vibration. The inclination angle of the pipe (β) is not larger than 0.5 deg. A fast-closing ball valve is installed at one end of the pipe. The special spring drive of this valve enables an almost stepwise complete flow cutoff. This has been confirmed by the records of valve closure with a duration not exceeding 0.003 s, about 1% of the pressure wave propagation period in this pipe.

The test rig is equipped with four absolute pressure semiconductor transducers, mounted every $L/4$ section along the pipeline. The measuring range of these transducers is 0–4 MPa with a transmitted frequency band of 0–2 kHz and a precision class of 0.2%. The transmitted frequency band of the transducers, 0–2 kHz, indicates that the rise time of the output signal for up to 4 MPa stepwise change in pressure (measuring range) is shorter than 0.0005 s (1/2000 Hz). This time is shorter than about 0.17% of the pressure wave period ($4L/a \cong 0.3$ s) or, in other words, the transmitted frequency band for each transducer is at least 600 times wider than the pressure wave frequency equal to about 3.3 Hz ($a/(4L)$). A turbine flowmeter with the range of 1.5 m^3/h ($\sim 4.2 \times 10^{-4}$ m^3/s) and a precision class of 1% is used for the indirect measurement of flow velocity in the pipeline.

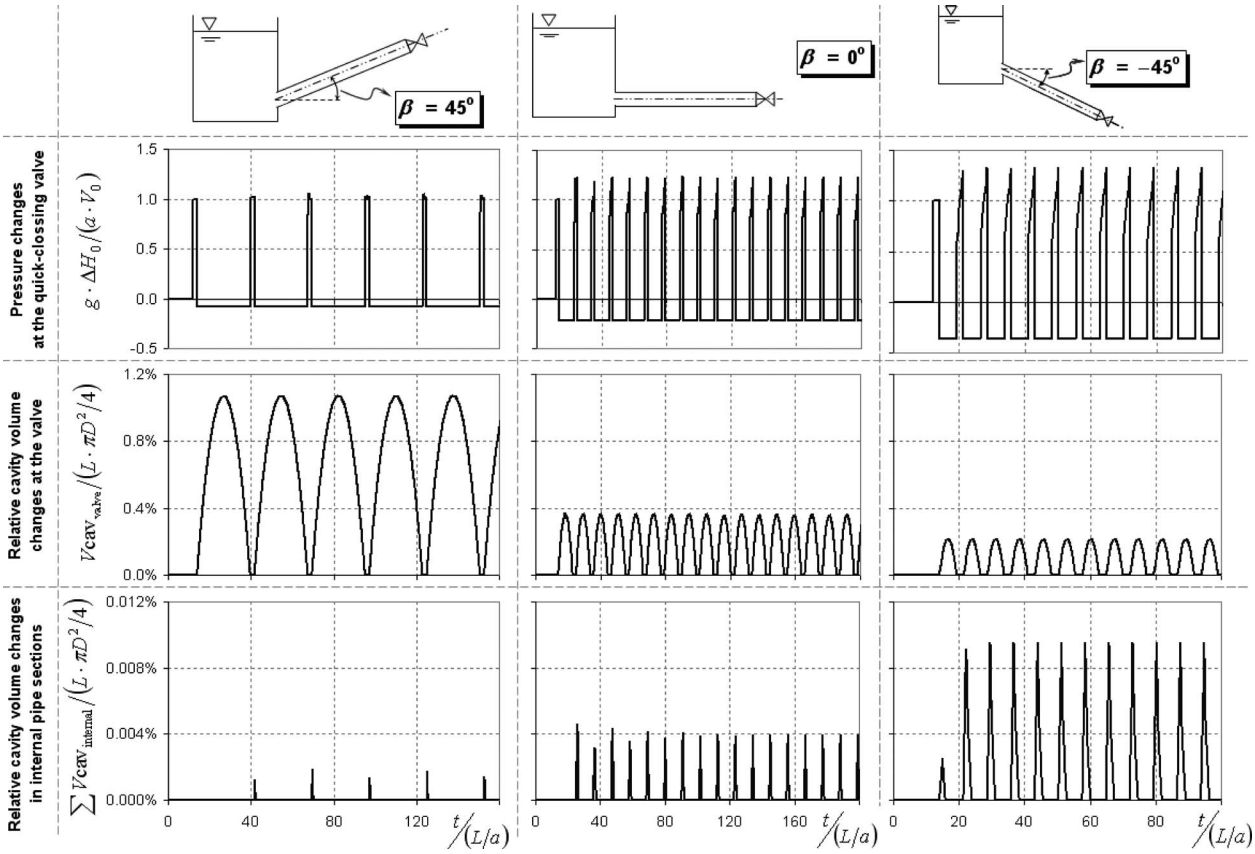

Fig. 6 Calculated pressure changes (cross section at the valve) and cavity volumes (V_{cav}) referred to the volume of the whole pipeline ($L \cdot \pi D^2/4$) obtained using the new DVCM—calculation results for three different pipeline slopes

Before starting the experiments, the hydraulic system was filled with water and left for a few days to remove as much undissolved air from the liquid as possible to minimize the influence of undissolved air bubbles. Naturally, such an operation did not assure removing air released under low pressure conditions occurring during the liquid column separation phenomenon, that is, gas cavitation.

The experimental test consisted of several runs of unsteady

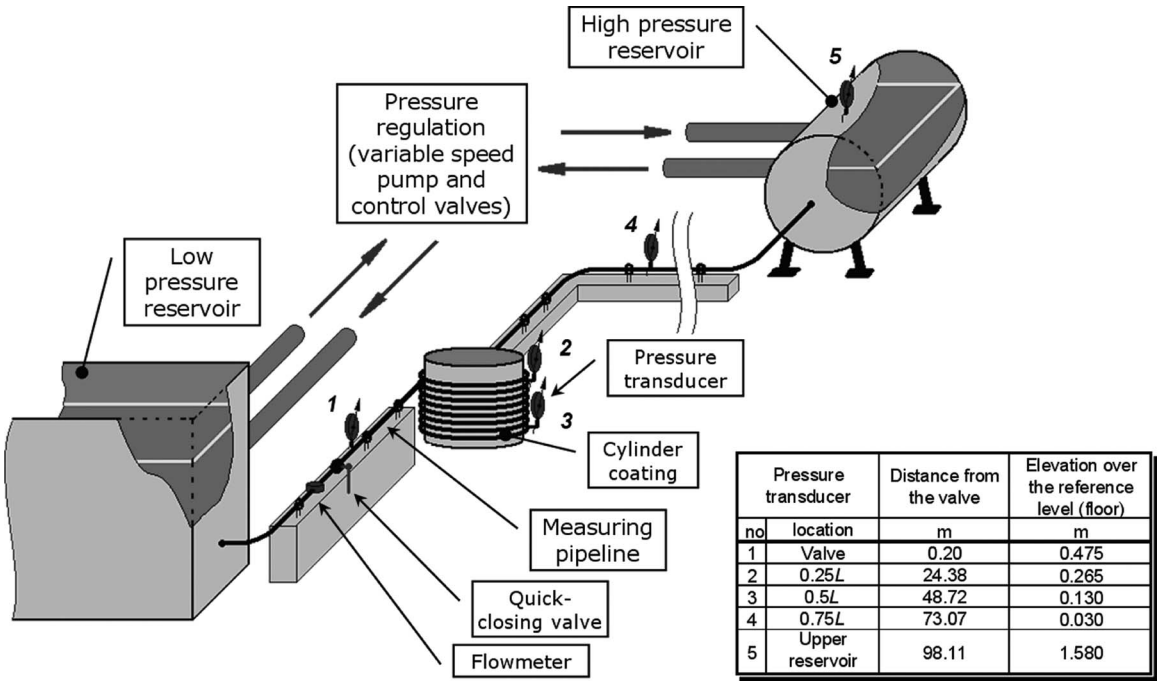

Pressure transducer		Distance from the valve	Elevation over the reference level (floor)
no	location	m	m
1	Valve	0.20	0.475
2	0.25*L*	24.38	0.265
3	0.5*L*	48.72	0.130
4	0.75*L*	73.07	0.030
5	Upper reservoir	98.11	1.580

Fig. 7 Layout of the test stand

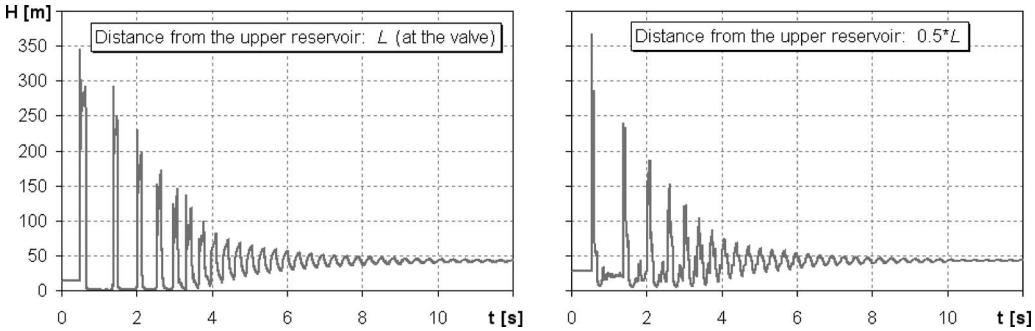

Fig. 8 Pressure changes measured at the valve and at the cross section located in the middle of the pipe

flow after sudden valve closure. Water hammer with or without accompanying water column separation was generated depending on the initial flow conditions: velocity V_o (Re_o) and free water surface level H_o in the high-pressure reservoir. Because of the limited value of H_o, the test stand was enabled to generate water hammer without column separation phenomenon at the initial conditions of Reynolds numbers up to $\mathrm{Re}_o \cong 16{,}000$. The kinematic viscosity coefficient of $\nu = 9.493 \times 10^{-7}$ m^2/s was determined for the water temperature of about 22.6°C, kept during tests.

Figure 8 presents a selected sample of pressure variations measured for the case of water hammer with column separation where $H_o = 42.3$ m and $V_o = 1.82$ m/s ($\mathrm{Re}_o \cong 30{,}600$). This pressure is the absolute pressure head referred to the floor of the laboratory hall taken as the reference level. After the first pressure peak, caused by a stepwise flow cutoff, the pressure measured at the valve falls to the critical value close to the saturated vapor pressure and remains at this level for a time period longer than the pressure wave period duration. For all this time, the vapor zone occurs and when it collapses, an instant pressure increment of high value appears. Such a pressure pulse repeats cyclically with decreasing amplitude and increasing frequency. These pressure changes are accompanied by intensive acoustic effects resembling a knocking noise. After some time the pressure peaks are transformed into oscillatory changes typical for water hammer without water column separation. It is worthwhile to mention that the high frequency pressure spikes superimposed on the water hammer-originated pressure changes are the effect of the dynamic interaction between fluid and the pipeline structure. The fluid-structure interaction phenomenon is the subject of much research, but it is neglected in this contribution.

For further analysis, the pressure wave speed a was calculated from the data recorded. For each investigated run, the value of the wave period, $4L/a$, was determined based on 20 pressure oscillations, and the calculated pressure wave speed based on selected test runs was equal to $a = 1280$ m/s. This value is very close, within 1.5%, to the theoretical value of a determined from the following formula [37]:

$$a = \sqrt{\frac{E_l}{\rho\left(1 + \frac{E_l}{E}\frac{D}{e}c_1\right)}} = 1298.4 \text{ m/s} \tag{15}$$

In Eq. (15) coefficient c_1 was calculated as for the pipeline anchored against longitudinal movement $c_1 = 1 - \upsilon^2$, where $\upsilon = 0.35$ for copper, $E_l = 2100$ MPa for water, and $E = 120$ GPa for copper.

Figures 9 and 10 show comparisons between the measured pressure courses and the results of calculations obtained using all three DVCMs, the classic, the single-zone, and the new DVCM described here. The calculations were conducted for two different cases of friction modeling.

- Quasisteady friction based on the Hagen–Poiseuille law and the Colebrook–White formula, shown in Fig. 9.
- Unsteady friction based on the Vardy and Brown friction model [29], shown in Fig. 10.

The results of these calculations confirm all the features of the discrete-vapor-cavity models discussed in this paper. The pressure courses calculated using the classic DVCM show numerous numerical peaks. In spite of numerical instabilities the new model that uses the quasisteady friction shown in Fig. 9 yields results close to experimental values for a few initial pressure peaks. For further pressure head oscillations, free of water column separation in this particular case, the two compared courses differ significantly concerning pressure wave amplitude attenuation; the measured pressure course is characterized by much more intense pressure amplitude damping than the calculated values. However, the same model applied with the Vardy and Brown unsteady friction model [29] in Fig. 10 gives results far more different from the experimental data. In this case, the calculated course shows completely contradistinctive pressure traces at the beginning of the analyzed run.

Although the single-zone DVCM does not generate numerical pressure peaks, as far as the initial pressure amplitudes are concerned, there is unexpectedly good conformity between the measured pressure courses and those calculated based on the quasisteady friction model. Further calculated oscillations are characterized by less effective pressure amplitude damping than in the experimental pressure course. In a cursory analysis these results can be interpreted as an advantage of the classic and the single-zone DVCMs, but the good agreement between the measurements and calculations for these models is a consequence of uncontrolled dissipation generated by the models themselves. This is evidently the result of nonconformity with the energy and mass conservation laws, as was shown for the frictionless cases in Figs. 2 and 3.

When we consider the unsteady friction model in Fig. 10, the damping effect for the single-zone DVCM model has a completely different nature. The amplitude attenuation is much closer to that shown by the experimental course, but the initial pressure peaks in these two courses differ from each other significantly.

The new DVCM applied with quasisteady friction does not show such good conformity with experimental data as the two models discussed previously. But this is consistent with expectations: numerous investigations, including those performed by the authors [33,34], confirm that the quasisteady hypothesis is a source of disparity between measured and calculated pressure courses for cases of a simple water hammer without liquid column separation. Logically, this disadvantage would also be expected to exist in the case of water hammer with liquid column separation. The results obtained using the new DVCM with the quasisteady friction assumption lead to this conclusion. In general, we can observe differences between compared pressure courses through-

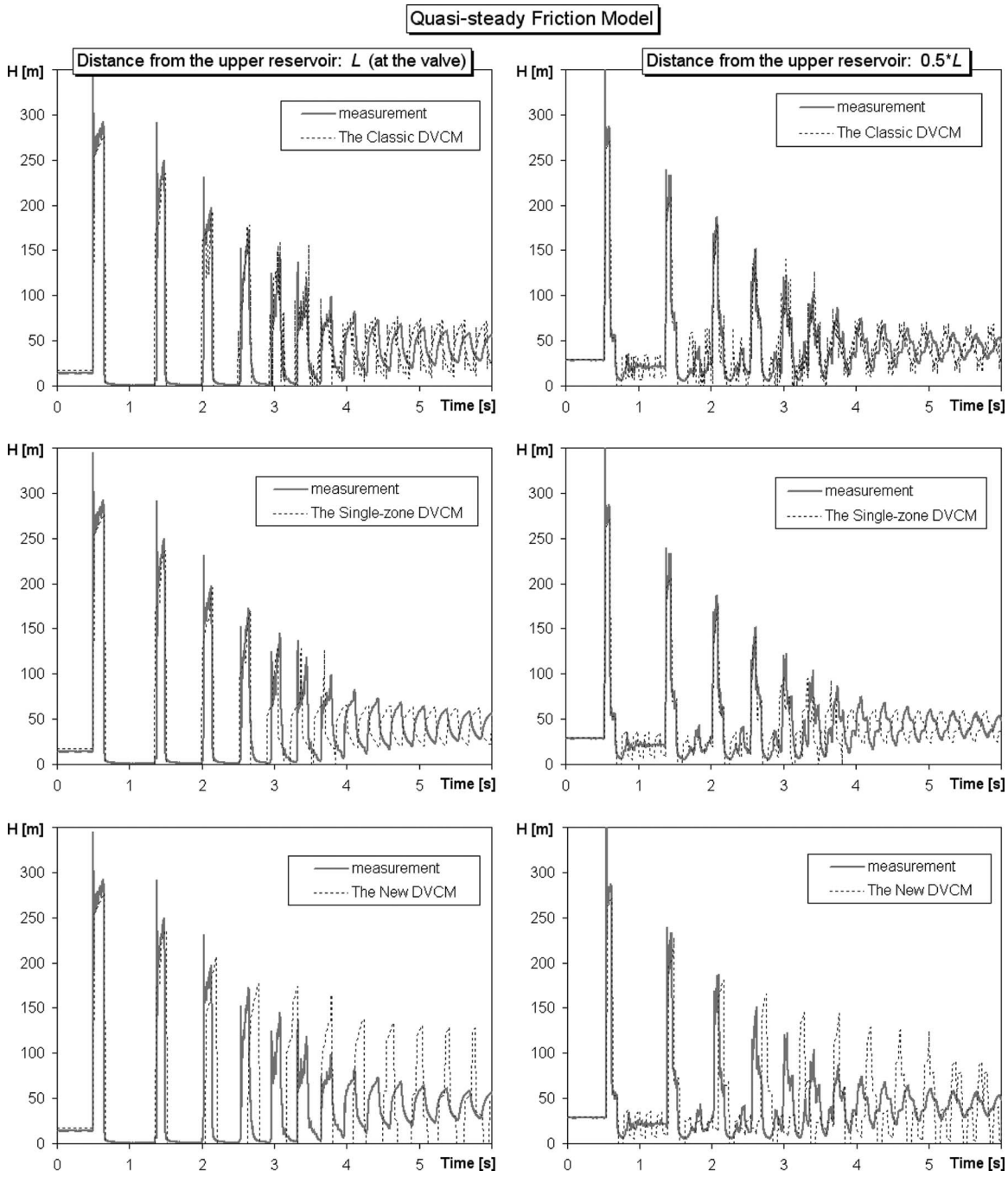

Fig. 9 Comparison of measured and calculated pressure surges at the valve and in the middle of the pipeline obtained using different DVCMs and the quasisteady friction model—the test run with $Re_o \cong 30{,}600$

out the whole time period. In this case, calculated pressure oscillations cease to decay after about 5 s while keeping constant pressure oscillation amplitude. The situation is completely different in the case of calculations conducted with the unsteady friction model, where there is very good agreement between the compared measured and calculated courses. This conformity exists for both pressure amplitudes at the beginning of the course when the liquid column separation phenomenon plays a dominant role and for further pressure oscillations without vapor cavities arising inside the pipe when the amplitude damping effect together with preservation of the frequency is of the highest significance.

5 Conclusions

A calculation method used to predict water hammer with liquid column separation was developed and presented in this paper. The method is based on the new DVCM that assumes vaporous zones at computational cross sections of the pipeline. The proposed new model shows significant advantages compared with similar models known from the literature. Based on calculations conducted for cases with neglected hydraulic resistance, it was proved that the proposed method eliminates substantial disadvantages of the methods most commonly used in engineering practice. Moreover, the proposed new model is of similar simplicity, a distinct advantage of this new approach.

Based on data gathered experimentally, a preliminary verification of the new model was conducted. Cursory analysis of comparison between the pressure courses measured and calculated using the classic DVCM and the single-zone DVCM, with quasisteady friction modeling, shows that these methods give acceptable results predicting water hammer with column separation,

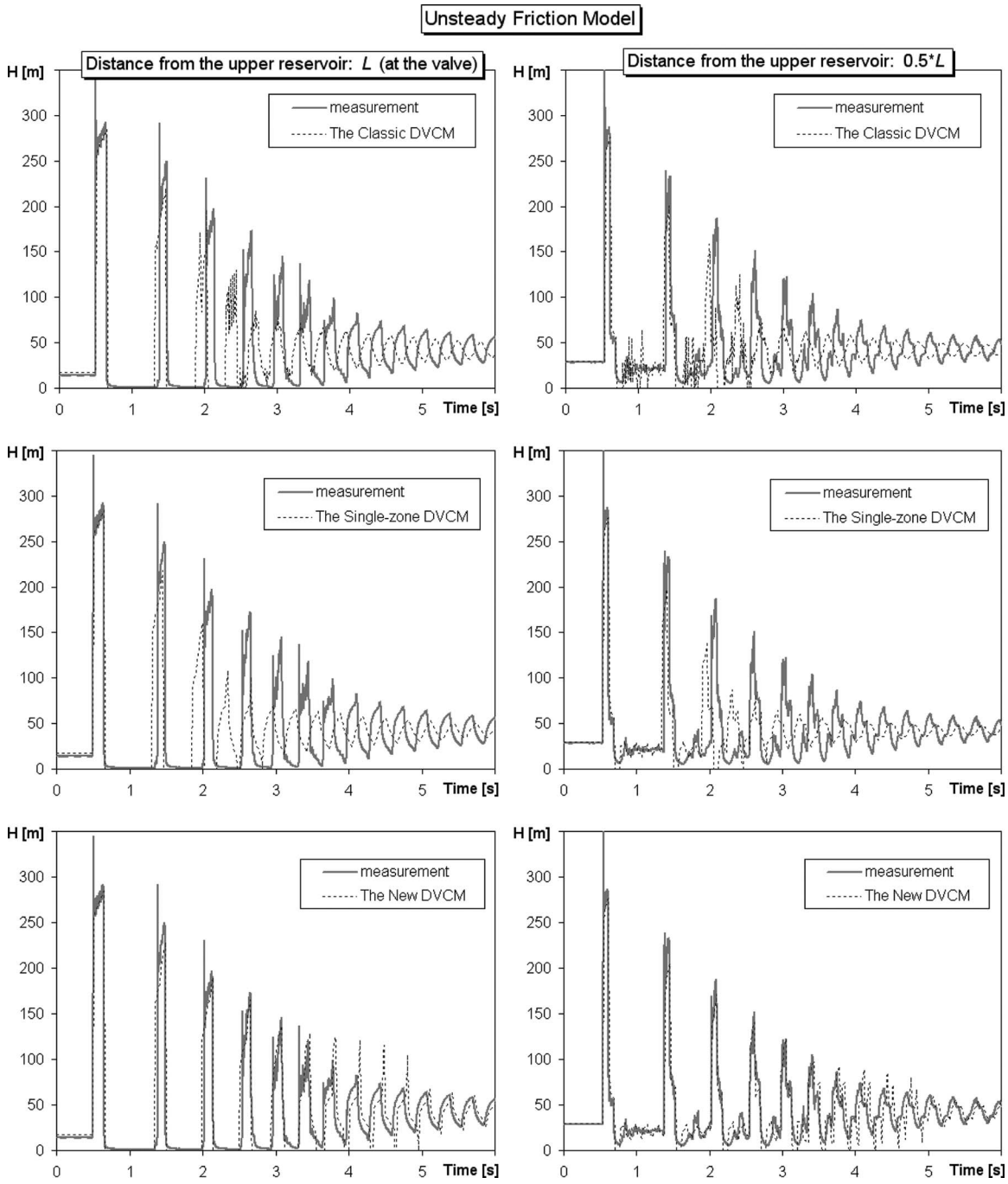

Fig. 10 Comparison of measured and calculated pressure surges at the valve and in the middle of the pipeline obtained using different DVCMs and the unsteady friction model—the test run with $Re_o \cong 30{,}600$

and especially the pressure peaks at the beginning of the analyzed course. After careful analysis it became clear that this good agreement resulted mainly from an unrealistic energy dissipation, incorporated in an implicit and uncontrolled way into these two models. In particular, calculations made for the frictionless cases clearly prove that both the standard models are incorrect methods for describing a liquid column separation during hydraulic transients in pipelines because they do not satisfy energy and mass conservation laws. The proposed new model is free of this disadvantage and therefore it tends to underpredict dissipation when quasisteady friction is used in calculations. This stands in agreement with prior research and theoretical considerations that have already demonstrated. The quasisteady hypothesis for describing friction losses is one of the basic causes of significant differences between measurements and calculations. Making use of the unsteady friction modeling verifies the new DVCM and tested calculation method. The other models, the classic and the single-zone DVCMs combined with the unsteady friction model, overpredict pressure wave damping significantly. This is also a direct result of the unrealistic energy dissipation characteristic for these two models.

With the positive results of experimental verification of the new DVCM, the correctness of the results obtained for frictionless case, and the simplicity of the method, the possibility exists to incorporate this model into commercial codes used for simulation of water hammer with column separation phenomenon.

Acknowledgment

This paper was prepared in the Szewalski Institute of Fluid-Flow Machinery of the Polish Academy of Sciences under Research Project No. N504 029 31/2026, which is funded by the Government of Poland from financial resources for science for the period 2006–2009. Some parts of the paper were presented at the Fifth Joint ASME/JSME Fluids Engineering Conference, San Diego, CA, July 30–August 2, 2007 and at the Tenth International Conference on Pressure Surges, Edinburgh, UK, May 14–16, 2008.

Nomenclature

a = pressure wave speed (m/s)
A = area (m^2)
D = internal diameter of a pipeline (m)
e = thickness of pipe walls
E = Young's modulus (modulus of elasticity) (Pa)
E_l = bulk modulus of liquid (Pa)
g = acceleration of gravity (m/s^2)
H = absolute pressure head (m)
J = head loss per pipe length unit
L = pipe length (m)
m = total number of computational cross sections of a pipeline
p = pressure (Pa)
Q = volumetric flow rate (m^3/s)
t = time (s)
V = average flow velocity in a pipe (m/s)
V_{cav} = volume filled with vapor (cavity volume) (m^3)
x = distance along pipe axis (m)
z = vertical coordinate of pipe cross section location (m)
Δt = time step (s)
β = slope angle of pipe axis (deg)
ρ = liquid density (kg/m^3)
υ = Poisson ratio
ψ = weighting coefficient

Indices Concern

bar = atmospheric pressure
cav = cavity head
internal = intermediate cross sections for straight pipe ended with quick-closing valve
j,k,i = numbers of computational cross sections of pipe
$j<k$, $j>k$ = intermediate cross sections with existing cavity volumes
o = initial value
v = vaporization of liquid
valve = cut-off valve

References

[1] Bonin, C. C., 1960, "Water-Hammer Damage to Oigawa Power Station," ASME J. Eng. Power, **82**, pp. 111–119.
[2] Parmakian, J., 1985, "Water Column Separation in Power and Pumping Plants," Hydro Rev., **4**(2), pp. 85–89.
[3] De Almeida, A. B., and Koelle, E., 1992, *Fluid Transients in Pipe Networks*, CMP/Elsevier, Southampton/London.
[4] Bergant, A., and Simpson, A. R., 1999, "Pipeline Column Separation Flow Regimes," J. Hydraul. Eng., **125**, pp. 835–848.
[5] Chaiko, M. A., 2006, "A Finite-Volume Approach for Simulation of Liquid-Column Separation in Pipelines," ASME J. Fluids Eng., **128**(6), pp. 1324–1335.
[6] Fan, D., and Tijsseling, A., 1992, "Fluid-Structure Interaction With Cavitation in Transient Pipe Flows," ASME J. Fluids Eng., **114**, pp. 268–274.
[7] Kojima, E., Shinada, M., and Shindo, K., 1984, "Fluid Transient Phenomena Accompanied With Column Separation in Fluid Power Pipeline," Bull. JSME, **27**(233), pp. 2421–2429.
[8] Martin, C. S., 1983, "Experimental Investigation of Column Separation With Rapid Closure of Downstream Valve," Proceedings of the Fourth International Conference on Pressure Surges, BHRA, Bath, UK, pp. 77–88.
[9] Mitosek, M., 2000, "Study of Transient Vapor Cavitation in Series Pipe Systems," J. Hydraul. Eng., **126**, pp. 904–911.
[10] Shinada, M., and Kojima, E., 1987, "Fluid Transient Phenomena Associated With Column Separation in the Return Line of a Hydraulic Machine Press," JSME Int. J., **30**(268), pp. 1577–1586.
[11] Shinada, M., 1994, "Influence of Gas Diffusion on Fluid Transient Phenomena Associated With Column Separation Generated During Decompression Operation," JSME Int. J., Ser. B, **37**(3), pp. 457–466.
[12] Simpson, A. R., and Wylie, E. B., 1991, "Large Water-Hammer Pressures for Column Separation in Pipelines," J. Hydraul. Eng., **117**, pp. 1310–1316.
[13] Shu, J.-J., 2003, "Modelling Vaporous Cavitation on Fluid Transients," Int. J. Pressure Vessels Piping, **80**, pp. 187–195.
[14] Simpson, A. R., and Bergant, A., 1994, "Developments in Pipeline Column Separation Experimentation," J. Hydraul. Res., **32**, pp. 183–194.
[15] Streeter, V. L., 1983, "Transient Cavitating Pipe Flow," J. Hydraul. Eng., **109**(11), pp. 1407–1423.
[16] Wylie, E. B., 1984, "Simulation of Vaporous and Gaseous Cavitation," ASME J. Fluids Eng., **106**, pp. 307–311.
[17] Bergant, A., Simpson, A. R., and Tijsseling, A. S., 2006, "Water Hammer With Column Separation: A Historical Review," J. Fluids Struct., **22**, pp. 135–171.
[18] Evangelisti, G., 1969, "Waterhammer Analysis by the Method of Characteristics," L'Energ. Elettr., Nos. 10,11,12.
[19] Baltzer, R. A., 1967, "Column Separation Accompanying Liquid Transients in Pipes," ASME J. Basic Eng., **89**, pp. 837–846.
[20] Brown, R. J., 1968, "Water-Column Separation at Two Pumping Plants," ASME J. Basic Eng., **90**, pp. 521–531.
[21] Kranenburg, C., 1974, "Gas Release During Transient Cavitation in Pipes," J. Hydr. Div., **100**, pp. 1383–1398.
[22] Safwat, H. H., and Van Den Polder, J., 1973, "Experimental and Analytic Data Correlation Study of Water Column Separation," ASME J. Fluids Eng., **95**, pp. 91–97.
[23] Wylie, E. B., and Streeter, V. L., 1978, *Fluid Transients*, McGraw-Hill, New York.
[24] Streeter, V. L., and Wylie, E. B., 1967, *Hydraulic Transients*, McGraw-Hill, New York.
[25] Safwat, H. H., Arastu, A. H., and Husaini, S. H., 1986, "Generalized Applications of the Method of Characteristics for the Analysis of Hydraulic Transients Involving Empty Sections," Proceedings of the Fifth Conference on Pressure Surges, BHRA, Hanover, Germany, pp. 157–167.
[26] Simpson, A. R., and Bergant, A., 1994, "Numerical Comparison of Pipe Column-Separation Models," J. Hydraul. Eng., **120**, pp. 361–377.
[27] Adamkowski, A., 2003, "Analysis of Transient Flow in Pipes With Expending or Contracting Sections," ASME J. Fluids Eng., **125**(4), pp. 716–722.
[28] Brunone, B., Golia, U. M., and Greco, M., 1991, "Some Remarks on the Momentum Equations for Fast Transients," International Meeting on Hydraulic Transients With Column Separation, Ninth Round Table, IAHR, Valencia, Spain.
[29] Vardy, A. E., and Brown, J. M., 2003, "Transient Turbulent Friction in Smooth Pipe Flows," J. Sound Vib., **259**(5), pp. 1011–1036.
[30] Zarzycki, Z., and Kudźma, S., 2005, "Computation of Transient Turbulent Flow of Liquid in Pipe Using Unsteady Friction Formula," Transactions of the Institute of Fluid-Flow Machinery, **116**, pp. 27–42.
[31] Zielke, W., 1968, "Frequency-Dependent Friction in Transient Pipe Flow," ASME J. Basic Eng., **90**(1), pp. 109–114.
[32] Schohl, G. A., 1993, "Improved Approximate Method for Simulating Frequency-Dependent Friction in Transient Laminar Flow, ASME Trans. J. Fluids Eng., **115**, pp. 420–424.
[33] Axworthy, D. H., Ghidaoui, M. S., and McInnis, D. A., 2000, "Extended Thermodynamics Derivation of Energy Dissipation in Unsteady Pipe Flow," J. Hydraul. Eng., **126**, pp. 276–286.
[34] Bilicki, Z., Giot, M., and Kwidzynski, R., 2002, "Fundamentals of Two-Phase Flow by the Method of Irreversible Thermodynamics," Int. J. Multiphase Flow, **28**, pp. 1983–2005.
[35] Adamkowski, A., and Lewandowski, M., 2006, "Experimental Examination of Unsteady Friction Models for Transient Pipe Flow Simulation," ASME J. Fluids Eng., **128**(6), pp. 1351–1363.
[36] Adamkowski, A., and Lewandowski, M., 2004, "Unsteady Friction Modelling in Transient Pipe Flow Simulation," Transactions of the Institute of Fluid-Flow Machinery, **115**, pp. 83–97.
[37] Wylie, E. B., and Streeter, V. L., 1993, *Fluid Transients in Systems*, Prentice-Hall, Englewood Cliffs, NJ.

Experimental Study of Liquid Slosh Dynamics in a Partially-Filled Tank

Guorong Yan[1]
e-mail: guorong_yan@hotmail.com

Subhash Rakheja

Kamran Siddiqui

Concave Research Centre,
Concordia University,
1455 de Maiosnneuve West,
Montréal, QC, H3G 1M8, Canada

This article reports on an experimental study conducted to investigate slosh forces and moments caused by fluid slosh within a partly-filled tank subjected to lateral and longitudinal excitations applied independently. The experiments were performed on a scale model cleanbore and a baffled tank with laterally placed single- and multiple-orifice baffles. The experiments were conducted for three different fill volumes and different types of excitations: continuous harmonic and single-cycle sinusoidal excitations of different amplitudes and discrete frequencies. The dynamic forces and moments caused by fluid slosh with the baffled and cleanbore tank configurations were measured for different fill volumes and excitations using three-axis dynamometers. It is shown that the resulting forces and moments comprise many spectral components that can be associated with the excitation, resonance, and vibration and beat frequencies. Modulation of excitation frequency with the resonant frequency was also evident for all fill conditions and tank configurations when the two were in close proximity. The results also showed that the peak amplifications of forces and moments occur in the vicinity of the resonant frequency. At higher frequencies, the peak magnitudes of the forces, however, reduced significantly to values lower than the inertial forces developed by an equivalent rigid mass. At a given excitation condition, the slosh force amplitude increased with a decrease in the fill volume. It was also observed that the presence of baffles has negligible effect on the lateral slosh force and the corresponding resonant frequency. However, it caused a significant increase in the longitudinal mode resonant frequency. The baffles greatly reduced the amplifications in longitudinal force and pitch moment under longitudinal acceleration excitations. [DOI: 10.1115/1.3059585]

Keywords: liquid slosh, slosh frequency, slosh force, slosh moment, fluid-structure interaction, baffled tank

1 Introduction

Slosh dynamics is an important area that is associated with the stability of liquid-transporting vehicles. Slosh could be induced within a partly-filled container when subject to external disturbances, such as variable acceleration field during a vehicle maneuver. Large-amplitude slosh may significantly reduce the stability limits of a partly-filled tank vehicle [1]. The study of slosh dynamics is thus quite critical in many engineering applications from the safety aspect that is associated with the liquid cargo transportation by road trucks, trains, and ships [1–3], as well as the flight of rockets, aircrafts, and other vehicles that are equipped with large liquid fuel tanks [4]. The large-size ground-based liquid storage facilities may also be at risk of damage due to violent liquid slosh inside the containers during an earthquake [5].

The forces resulting from the slosh are dependent on the fill level, tank geometry, and excitation amplitude, which are known to directly influence the stability of vehicles [1,6]. Tank trucks involved in general-purpose transportation of bulk liquids may encounter partial fill conditions due to local regulations on the axle loads and variations in the product weight density. The dynamic slosh forces inside moving road tank vehicles arising from either lateral or longitudinal acceleration fields or a combination of the two during a steering and/or braking maneuver have been mostly evaluated using quasistatic fluid flow [7–9]. A few studies have investigated the transient slosh response within rectangular and circular containers [2,6,10,11]. These studies concluded that the magnitudes of transient slosh forces and moments are significantly larger than those derived from the steady-state or quasistatic analysis. The amplification factor of forces and moments, defined as the ratio of the peak dynamic forces and moments to the corresponding steady-state values, could reach as large as 2 under a steady-turning maneuver. It was further shown that the peak transient force and moment amplification factors occur in the vicinity of the medium fill level (ratio of fill depth to the characteristic length) for the rectangular container but at relatively smaller fill level for the circular tanks [2].

Strandberg [1] experimentally studied liquid slosh in different scale model tanks to determine the overturning tendencies of various tank vehicles under steady cornering and transient lane-change maneuvers. The results showed that the overturning limit of a 50%-filled elliptic tank vehicle could be half of that of the completely-filled vehicle. Yan et al. [6] numerically studied the effect of transient lateral slosh on rollover threshold of a partly-filled tractor-tank-semitrailer under steady-turning maneuvers and concluded that the rollover threshold under transient slosh forces and moments was 20% lower than that predicted using the steady-state slosh forces.

The natural frequency of slosh is a parameter of prime consideration in the design stage of liquid containers because the coincidence of the excitation frequency with the natural frequency could yield large-amplitude slosh, and thus the forces and moments [12]. The frequency of liquid slosh has been investigated for the containers of various common shapes, such as rectangular [13–15], circular [4,16–20], spherical [16–18], and elliptical [21]. It is known that the slosh natural frequency depends on fill depth,

[1]Corresponding author.

Contributed by the Fluids Engineering Division of ASME for publication in the JOURNAL OF FLUIDS ENGINEERING. Manuscript received April 30, 2007; final manuscript received November 1, 2008; published online June 22, 2009. Assoc. Editor: Timothy J. O'Hern.

tank geometry, and the excitation amplitude [4,12,16–20,22]. For the tanks of common shapes, the slosh natural frequencies have been derived from the linear flow field equations based on hydrodynamic potential theory [16,17], and solutions of the wave equation [23] or the Navier–Stokes equations [24].

Budiansky [16] analytically studied the natural modes and frequencies of small-amplitude liquid slosh within horizontal cylindrical and spherical tanks in the roll plane and concluded that the fundamental frequency increases in a monotonic manner as the liquid fill ratio (i.e., the ratio of fill depth to radius) increases. This trend, however, was not observed in frequencies corresponding to the second and third modes. Mciver [17] also presented similar results for these two tanks. Kobayashi et al. [19] predicted the longitudinal mode natural frequency of slosh in horizontal circular tanks and showed that the longitudinal natural frequencies corresponding to the first three modes increase with the fill depth. Romero et al. [21] analyzed the natural frequencies in tanks of complex cross-sectional geometries using the wave equation and concluded that the lateral mode slosh frequencies in circular tanks are higher than those in elliptical tanks. Cho et al. [15] used linear potential theory and finite element approach to investigate the two-dimensional (2D) resonant slosh response in a rectangular tank with longitudinal baffles subject to lateral harmonic excitation.

The slosh frequencies for rectangular and circular tanks have been analyzed in a number of studies [13–20]. However, only limited efforts have been made to evaluate slosh frequencies and forces arising from dynamic slosh within baffled tanks of different geometries used in freight vehicles [1,2,25,26]. Strandberg [1] reported that the addition of three longitudinal baffles could yield significant increase (by 163%) in the overturning limit for a 50%-filled elliptical tank vehicle. Longitudinal baffles in large-size highway tanks, however, add considerable weight and may pose hindrance while cleaning the tanks. Lloyd et al. [25] performed measurements of the slosh damping effect of different baffles in a scaled circular tank and concluded that a perforated baffle could yield most effective slosh damping compared with the solid dished, oblique, spiral, and round baffles. Another experimental study of free slosh in a baffled rectangular cross-sectional tank showed that the size and location of lateral baffles significantly influence the hydrodynamic damping [26].

The fluid slosh phenomenon has also been investigated using various analytical (e.g., Refs. [16,27,28]) and numerical (e.g., Refs. [2,6,10,29]) techniques. These methodologies have been thoroughly reviewed by Ibrahim et al. [30]. The majority of previously reported studies, irrespective of the methods used, have mostly analyzed 2D slosh. A partly-filled road tanker, however, exhibits 3D slosh caused by simultaneous application of braking and steering maneuvers. Although only a few studies have investigated 3D fluid slosh [10,11], the validity of the analyses has not been adequately demonstrated. When the excitation is in the neighborhood of the resonant frequency, the swirling motion may be induced and superimposed on the normal slosh motion caused by either a lateral or a longitudinal acceleration field [4]. Abramson et al. [4] also mentioned the possible beating phenomenon in fluid oscillations that may add further complexities in dynamic slosh forces and moments. Miles [27] studied free oscillations of different liquid slosh modes and reported that modulations in amplitude and phase may occur due to coupled modes.

The majority of experimental investigations of fluid slosh have been conducted using very small-size model tanks. Moreover, some of the studies were limited to measurements of hydrodynamic pressure at given points or only one component of the slosh forces [19,31]. However, the stability of a road tank vehicle is strongly dependent on all the components of the resultant slosh forces and moments. In the present study, the 3D fluid slosh is experimentally investigated in a relatively large-size laboratory test tank with and without baffles. The measured data are analyzed to evaluate the fundamental slosh frequencies and dynamic slosh forces and moments under different types and amplitudes of lateral and longitudinal acceleration fields. The conditions of beating phenomenon and swirling motion of the free surface together with magnitudes of slosh forces developed and the influencing factors are discussed.

2 Experimental Method

2.1 Experimental Setup. The experiments were conducted using a scale model tank of cross section, similar to the "Reuleaux triangle" with variable arc widths, as shown in Fig. 1(*a*). The tank cross section was realized on the basis of the optimal tank geometry proposed by Kang et al. [32] with the goal of suppressing liquid slosh in the roll plane. The test tank was designed with a total length of 1.85 m, a cross-sectional area of 0.426 m^2, and a volume capacity of 760 l, which is considerably larger than those employed in the earlier studies [1,4,19,21]. The transverse width of the tank was approximately 1/3 of a typical road vehicle tank. The tank was made of 12.7 mm thick transparent Plexiglas material to facilitate flow visualization. The design consisted of three modular sections of equal length such that two baffles could be conveniently inserted between the flanges of the modular sections (see Fig. 1(*a*)). Two different baffle designs were considered: (i) single-orifice baffle (245.5 mm diameter orifice) and (ii) multiple-orifice baffle with a 101.6 mm diameter orifice at the geometric center and 34 smaller orifices (38.1 mm diameter with centers located 177.8 mm, 241.3 mm, and 368.3 mm from the geometric center), as shown in Fig. 1(*b*). The porosity of the two baffles was approximately 11% of the entire cross-sectional area. The selection of baffle porosity was based on the Code of Federal Regulations (CFR) [33], which recommends porosity of less than 20%. The baffles were made of 6.35 mm thick transparent rigid polyvinyl chloride (PVC). The experiments were conducted using cleanbore (without baffles) and baffled tanks. For simplicity, hereinafter, the cleanbore tank is denoted as "T0," while those with single-orifice and multiple-orifice baffles are denoted as "T1" and "T2," respectively.

The tank (with or without baffles) was mounted on an aluminum plate that was fixed on a horizontal shake table through three three-axis force dynamometers to measure dynamic forces developed along the longitudinal (X), lateral (Y), and vertical (Z) axes. The three dynamometers were installed in a triangular manner, as shown in Fig. 2. Two of the dynamometers (D2 and D3) were mounted in the rear end of the plate, while a single dynamometer (D1) was placed along the longitudinal axis (X) near the leading edge of the plate. The forces acquired by the dynamometers could be manipulated to compute roll, pitch, and yaw moments. The shake table, connected to a 40 cm stroke hydraulic actuator, was placed on a granite slip table. The motion of the slip table was constrained by a pair of guides on the sides of the table. During the experiments, the surface of the slip table was fully covered with oil to achieve smooth motion of the shake table with minimal friction. The oil film was maintained on the table surface through an oil circulation system. The hydraulic actuator was controlled by a servo controller (MTS 407). The tank with its support structure could be mounted either along or normal to the actuator axis in order to realize either longitudinal or lateral excitation to the tank. Water was used as the test liquid within the tank and a food dye was added to visualize the flow.

2.2 Test Conditions. The experiments were designed to measure three components of the dynamic force arising from the liquid slosh within the test tank with or without baffles. The test matrix included three fill volumes (30%, 50%, and 70% of the tank volume) and various amplitudes and frequencies of acceleration excitation. The fill depth corresponding to each fill volume was computed from the tank geometry and summarized in Table 1, while the test matrix used is illustrated in Table 2. For the single-orifice baffle configuration (T1), the 30% fill volume was

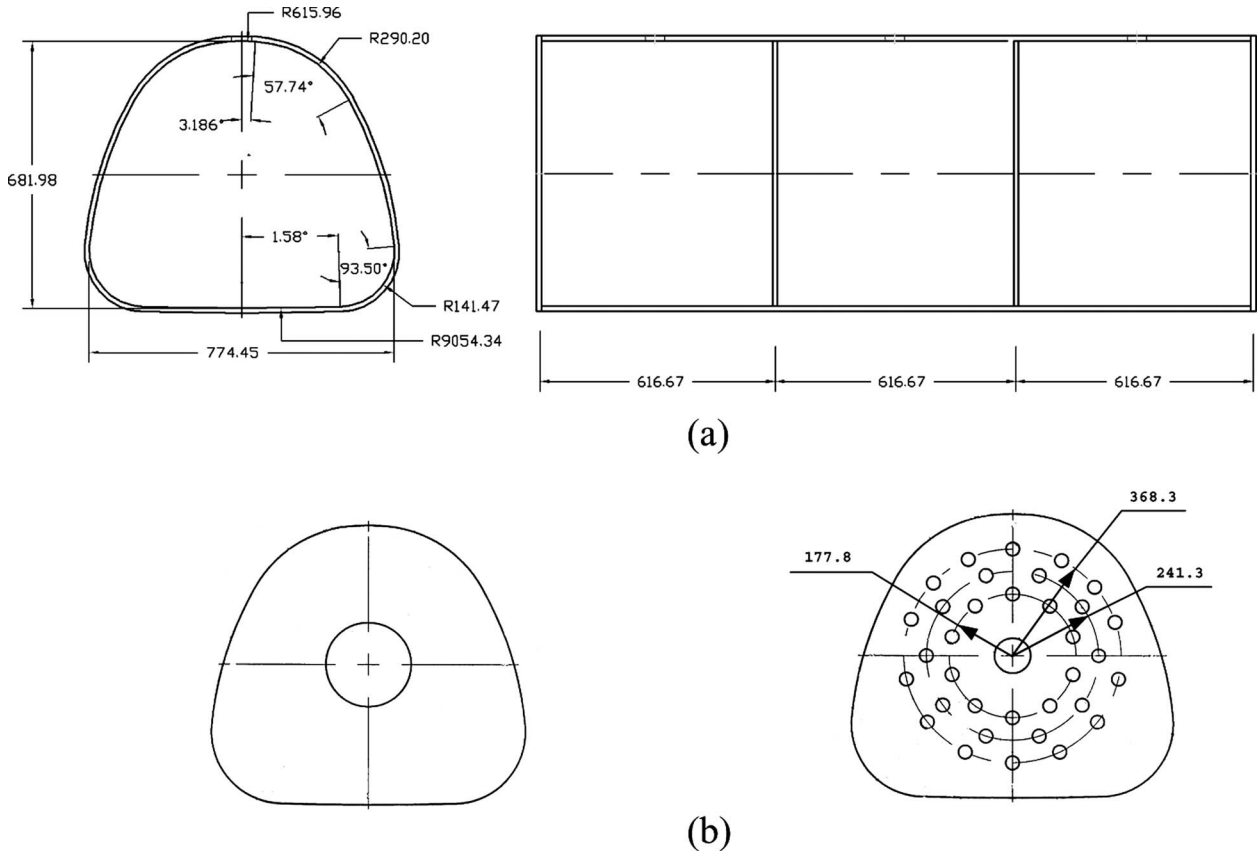

Fig. 1 Schematic of (*a*) test tank (all dimensions are in millimeters) and (*b*) single-orifice (T1) and multiple-orifice (T2) baffles

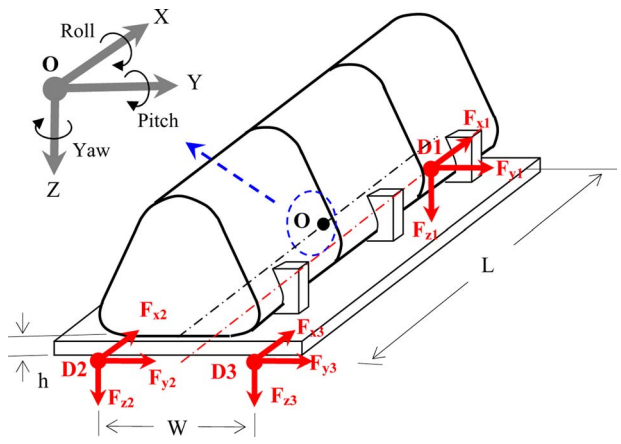

Fig. 2 Schematic of the tank illustrating local and global coordinate systems and locations of the three dynamometers (D1, D2, and D3)

excluded from the test matrix due to entrapment of the fluid within segments of the tank between the baffles. This was attributed to the absence of equalizers in the baffles used.

The experiments were performed under different amplitudes (0.5 m/s^2, 1 m/s^2, 2 m/s^2, and 3 m/s^2) of harmonic acceleration excitations at various discrete frequencies in 0.5–3 Hz range in order to study the dependency of slosh on the excitation frequency and amplitude. The ranges of excitation frequencies were selected on the basis of expected fundamental slosh frequencies, which were estimated using the methodology presented by Romero et al. [21]. The higher acceleration amplitudes at lower frequencies, however, were not attempted in order to limit the peak displacement of the tank assembly within the safe limits of the actuator stroke, as evident in Table 2. The longitudinal excitations were synthesized to yield three different amplitudes of acceleration (0.25 m/s^2, 0.5 m/s^2, and 1 m/s^2) in the frequency range of 0.25–1.5 Hz, as summarized in Table 2. Considering different longitudinal mode resonant frequencies for different tank configurations, T0 tank was subject to excitations in 0.25–1 Hz frequency range, while T1 and T2 tanks were subject to excitations in 0.5–1.5 Hz range.

Table 1 Test matrix including tank configurations and types of the lateral (*Y*) and longitudinal (*X*) excitations

	Percent fill volume (fill depth) (cm)			Type and direction of excitation	
Tank configuration	30% (17.96)	50% (29.39)	70% (41.79)	Harmonic (continuous)	Single cycle
T0 (unbaffled)	♦	♦	♦	*Y*,*X*	*Y*
T1 (single-orifice baffle)	–	♦	♦	*Y*,*X*	*Y*
T2 (multiple-orifice baffle)	♦	♦	♦	*Y*,*X*	*Y*

Table 2 Test matrix illustrating frequencies and amplitudes of continuous lateral and longitudinal excitations

A_Y (m/s^2)	Lateral acceleration excitation frequency (Hz) 0.5	0.6	0.7	0.8	0.9	1	1.1	1.2	1.3	1.5	2	2.5	3
0.5	♦	♦	♦	♦	♦	♦	♦	♦	♦	♦	♦	♦	♦
1	♦	♦	♦	♦	♦	♦	♦	♦	♦	♦	♦	♦	♦
2			♦	♦	♦	♦	♦	♦	♦	♦	♦	♦	♦
3					♦	♦	♦	♦	♦	♦	♦	♦	♦

A_X (m/s^2)	Longitudinal acceleration excitation frequency (Hz) 0.25	0.3	0.36	0.4	0.45	0.5	0.55	0.6	0.65	0.7	0.8	0.9	1	1.1	1.2	1.3	1.4	1.5
0.25	♦	♦	♦	♦	♦	♦	♦	♦	♦	♦	♦	♦	♦	♦	♦	♦	♦	♦
0.5			♦	♦	♦	♦	♦	♦	♦	♦	♦	♦	♦	♦	♦	♦	♦	♦
1						♦	♦	♦	♦	♦	♦	♦	♦	♦	♦	♦	♦	♦

Apart from the harmonic excitations, a single-cycle sinusoidal acceleration excitation was synthesized to study the transient lateral slosh behavior. It has been suggested that the centrifugal acceleration encountered during a path change can be approximated by a single-sinusoid [34]. Figure 3 shows the time history of the single-sinusoidal lateral acceleration and its corresponding displacement signal at 1 Hz and 1.5 Hz.

2.3 Test and Data Analysis Methodology. Two series of measurements were conducted under lateral excitations involving steady-state and transient slosh responses to harmonic and single-sinusoidal excitations, respectively. The measurements were initially performed with the empty tank structure with and without baffles, and the resulting forces along the three orthogonal axes were acquired and applied for the inertial correction of the total forces measured due to fluid and the tank. The dynamic responses of the tank and structure alone were measured for each excitation, which revealed a constant mass of the assembly, approximately equal to 347 kg.

For each fill condition and configuration, the tank was filled to the desired liquid fill level and the slip table was positioned in its midstroke. For each harmonic excitation, the data acquisition was initiated when steady-state motion of the free surface was observed. The data were acquired for a long duration (40 s) in order to capture the low frequency swirling slosh behavior observed for excitations in the vicinity of the fundamental slosh frequency. Under single-cycle sinusoidal excitations, the data acquisition was started prior to the initiation of the excitation in order to track the starting instant of the tank motion and to acquire the transient slosh response.

The data acquired by the three dynamometers were analyzed to determine the resultant slosh forces and moments. The measured forces for each excitation frequency revealed the presence of a 13 Hz component in both lateral and longitudinal directions, which was attributed to the natural frequency of the fixture comprising the slip table, the actuator, and the tank structure. This frequency was judged to be sufficiently high compared with the highest excitation frequency of interest (3 Hz). The acquired data were low pass filtered using an eighth order Butterworth digital low-pass filter with the cutoff frequency of 6 Hz. The filtered data showed variations in the amplitudes of different cycles of oscillations. The steady-state amplitudes were thus calculated using a confidence treatment to reduce the uncertainty. The steady-state signal over a period of 20 s was extracted and the peak amplitude was identified over the 96% confidence interval. The peak slosh forces developed under single-cycle sinusoidal inputs were taken directly from the filtered signal.

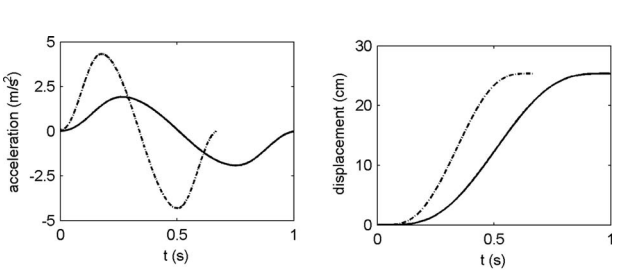

Fig. 3 The lateral single-cycle sinusoidal acceleration functions and the corresponding displacement at frequencies: solid line, 1 Hz and dash-dotted line, 1.5 Hz

For the excitations along the lateral direction, the resultant slosh forces developed along the three axes were computed by the summation of force components measured from the three dynamometers, such that

$$F_X(t) = \sum_{i=1}^{3} F_{xi}^f(t), \quad F_Z(t) = \sum_{i=1}^{3} F_{zi}^f(t)$$

$$F_Y(t) = \sum_{i=1}^{3} F_{yi}^f(t) - m_e \cdot a_Y(t), \quad i = 1,2,3 \tag{1}$$

where F_X, F_Y, and F_Z are resultant dynamic forces due to sloshing fluid; F_{xi}, F_{yi}, and F_{zi} are three force components measured by the ith dynamometer; and $i=1$, 2, and 3 refer to front, rear-left, and rear-right dynamometers, as illustrated in Fig. 2. The superscript f represents the case of liquid filled tank, m_e is the mass of rigid structure including the empty tank and its mounting plate identified from the empty tank tests, and a_Y is the lateral excitation acceleration. The subscripts X, Y, and Z indicate the global coordinate system of the tank with origin "O" located at the geometric center of the tank projected at its base (Fig. 2), while x, y, and z represent the local coordinate system of dynamometers. It should be noted that each dynamometer was zeroed prior to each experiment. The measured lateral slosh force due to fluid and the tank structure was corrected by subtracting the contribution from the rigid structure, including the platform and empty tank. The magnitude of the inertial force component measured in the X direction was found to be significantly small. In the vertical (Z) direction the inertial force equaled the fluid and structure weight, which was zeroed prior to measurements. The inertial force correction in X and Z directions was thus not attempted.

The roll (M_X), pitch (M_Y), and yaw (M_Z) moments due to fluid slosh were computed from the measured force components in the following manner:

Table 3 Comparisons of the measured and computed natural frequencies of lateral and longitudinal fluid slosh in the cleanbore tank (T0) for different fill volumes

Fill (%)	Lateral			Longitudinal		
	Measured	Computed	% Difference	Measured	Computed	% Difference
30	0.813	0.796	2.14	0.344	0.357	−3.64
50	1.000	0.955	4.71	0.453	0.445	1.80
70	1.125	1.075	4.65	0.531	0.512	3.71

$$M_X(t) = \left(\frac{W}{2}N_Y\right)K - hF_Y, \quad M_Y(t) = \frac{L}{2}N_X + hF_X$$

$$M_Z(t) = \frac{L}{2}(F_{y1} - F_{y2} - F_{y3}) + \frac{W}{2}(F^f_{x2} - F^f_{x3}) \tag{2}$$

where L is the longitudinal distance between the front dynamometer and the lateral axis passing through the center of each rear dynamometer, W is the lateral distance between the two rear dynamometers, h is the height of the origin O from the top surface of the dynamometers, and K is a calibration factor for the resultant roll moment that was determined through calibration performed with the empty tank. This calibration factor was used to account for the spacing of individual force sensors within each dynamometer. In the case of an empty tank, the roll moment could be calculated using two methods: (i) inertia force along the lateral axis and the center of gravity (cg) height of the tank structure and (ii) from the vertical forces measured by the dynamometers D2 and D3. The resulting difference was used to obtain the value of the calibration factor K ($K=1.37$). In the above equations, N_Y and N_X are the lateral and longitudinal slosh load shifts, respectively, determined from

$$N_Y(t) = (F^f_{z3} - F^f_{z2}) - N^e_Y \quad \text{and} \quad N_X(t) = (F^f_{z2} + F^f_{z3}) - F^f_{z1} \tag{3}$$

where N^e_Y is the lateral load shift for the empty tank and structure, which was calculated from the lateral force, the cg height of the tank structure, and the lateral spacing between the dynamometers D2 and D3.

Under longitudinal excitations (a_X), the resultant slosh forces are derived in a similar manner, where the inertial force correction is applied only in the longitudinal direction, such that

$$F_X(t) = \sum_{i=1}^{3} F^f_{xi}(t) - m_e \cdot a_X(t), \quad F_Y(t) = \sum_{i=1}^{3} F^f_{yi}(t)$$

$$F_Z(t) = \sum_{i=1}^{3} F^f_{zi}(t), \quad i = 1,2,3 \tag{4}$$

The moments due to fluid slosh are derived from Eq. (2), where the lateral and longitudinal load shifts are computed in the following manner:

$$N_Y(t) = F^f_{z3} - F^f_{z2} \quad \text{and} \quad N_X(t) = (F^f_{z2} + F^f_{z3} - F^f_{z1}) - N^e_X \tag{5}$$

where N^e_X is the longitudinal load shift for the empty tank and structure, which was derived in a manner similar to that of N^e_Y.

The dynamic responses of the partly-filled tank to excitations in the lateral and longitudinal directions were assessed in terms of the resultant normalized slosh forces and moments. Under a lateral acceleration excitation, the resultant lateral force F_Y is normalized with respect to that developed by an equivalent rigid load, such that

$$M_{Fy} = \frac{F_Y}{m_l A_Y} \tag{6}$$

where m_l is the liquid mass, A_Y is the amplitude of lateral excitation, and M_{Fy} is the normalized lateral slosh force that has been termed as an amplification factor of lateral slosh force [11].

The resultant forces developed along the X and Z directions were normalized with respect to the weight of the liquid alone:

$$M_{Fx} = \frac{F_X}{m_l g}, \quad M_{Fz} = \frac{F_Z}{m_l g} \tag{7}$$

The roll, pitch, and yaw moments were normalized by the roll moment developed by the equivalent rigid "frozen" liquid:

$$M_{Mi} = \frac{M_i}{m_l A_Y h_0} \quad (i = x,y,z) \tag{8}$$

where h_0 is the cg height of the "frozen liquid."

The amplification factors in slosh forces and moments under longitudinal excitations were defined in a similar manner by considering longitudinal acceleration amplitudes.

The free oscillations of the water surface were used to investigate the natural frequencies of the fluid slosh. For this purpose, the signals from the dynamometers were acquired after the acceleration excitation was stopped. The data revealed slowly decaying magnitudes of slosh forces occurring near the fundamental slosh frequencies. The fundamental natural frequencies of fluid slosh in the lateral and longitudinal directions were computed from the frequency spectra of the forces measured under the free oscillations. The spectra invariably revealed a single dominant peak, and the corresponding frequency was considered as the fundamental slosh natural frequency.

3 Results and Discussions

3.1 Slosh Frequencies. Table 3 shows the fundamental natural frequencies obtained from the frequency spectra of measured forces in both lateral and longitudinal directions for the cleanbore tank (T0) for three fill volumes. The results show that the slosh frequency increases with the fill volume. This trend is consistent with those reported by Budiansky [16], Lamb [13], and Kobayashi et al. [19] for cylindrical and rectangular tanks. The fundamental frequencies corresponding to different fill levels of the same tank dimensions were also computed using the analytical method presented by Romero et al. [21]. The slosh natural frequency (f) was derived from the wave speed c and wavelength λ ($f=c/\lambda$). For ideal and incompressible fluids with small rotational motions and sufficiently large wavelengths, the speed of surface wave is a function of the wavelength, fill depth h, and acceleration due to gravity g, such that

$$c = \left(\frac{g\lambda}{2\pi}\tanh\left(\frac{2\pi h}{\lambda}\right)\right)^{0.5} \tag{9}$$

The wavelength of the nth mode can be determined from the free surface length L_h, such that $\lambda = 2L_h/n$. The fundamental slosh frequencies estimated from the wave speed and wavelength for three fill depths are compared with the measured frequencies in Table 3, which shows reasonably good agreements between the measured and computed frequencies for both directions and three fill levels. The measured frequencies, however, tend to be slightly higher than the calculated ones for the lateral mode at the higher fill volume. The maximum difference in measured and computed frequencies for both lateral and longitudinal modes was observed to

Table 4 Fundamental longitudinal mode natural frequencies of the baffled and unbaffled tanks under different fill volumes

Fill (%)	Unbaffled (T0)	Baffled (T2)	% Frequency increase
30	0.344	0.938	173
50	0.453	1.078	138
70	0.531	1.141	115

be less than 5%.

Table 4 compares the longitudinal mode natural frequencies of the baffled and unbaffled tanks and summarizes the percent increase in the frequency due to transverse baffles. The results show that the addition of baffles yields significantly higher natural frequencies, irrespective of the fill volume. The spectral analysis of the longitudinal slosh force showed identical longitudinal mode natural frequency for the two baffled tanks (T1 and T2) under 50% and 70% fill volumes. This suggests that both types of baffles yield identical gains in the longitudinal mode natural frequencies. The results also show that the natural frequency increases with the fill level, as observed for the cleanbore tank (T0). The measured data further revealed that baffles do not affect the lateral mode natural frequency.

The frequency spectra of the slosh forces also revealed a number of important spectral components, as evident from the power spectral density (PSD) of the forces shown in Fig. 4. The figure shows the PSD of slosh forces ($\Phi_{Fi}; i=x,y,z$) measured for the 50%-filled baffled and unbaffled tanks subject to 1 m/s^2 lateral excitation at 0.7 Hz. The results for the baffled T1 tank are similar to those of T2 tank, and thus not presented in this figure. The tank configurations T0 and T2 revealed similar magnitudes of the spectral energy of lateral and vertical slosh forces, while considerable differences could be seen for the longitudinal force responses. Two predominant peaks near the excitation frequency ($f_e \approx 0.7$ Hz) and the lateral mode fundamental frequency ($f_{n,y} \approx 1$ Hz) are observed in the spectrum of the lateral force (see Fig. 4(*a*)). The spectrum of the longitudinal force (Fig. 4(*b*)) shows prominent peaks near the excitation (f_e), longitudinal mode resonance ($f_{n,x} \approx 0.45$ Hz), and the lateral mode resonance ($f_{n,y} \approx 1$ Hz) frequencies. The longitudinal mode resonance of the baffled T2 tank is approximately 1.1 Hz, close to the lateral mode resonance. The low magnitude high frequency peaks observed in the spectra may be related to higher slosh modes and structural modes.

The spectrum of the vertical force (Fig. 4(*c*)) also shows several prominent peaks. The peak near the low frequency of 0.3 Hz corresponds to the beat frequency (f_b), which is equal to the difference between the fundamental mode resonance frequency ($f_{n,y}$) and the excitation frequency (f_e). The presence of a possible beat frequency was also stated by Abramson et al. [4]. The spectral energy of the peak at the beat frequency, however, is relatively small compared with other peaks under higher excitation amplitudes. The peak corresponding to the beat frequency is not evident in the spectrum of the lateral force. This is due to the fact that the beating is reflected less apparently in the lateral force than in the vertical force. This is also evident in the time histories of lateral and vertical forces, as shown in Fig. 5. The vertical force spectrum also shows peaks at the excitation (f_e) and resonance ($f_{n,y}$) frequencies, and in 1–2 Hz range, which correspond to twice the

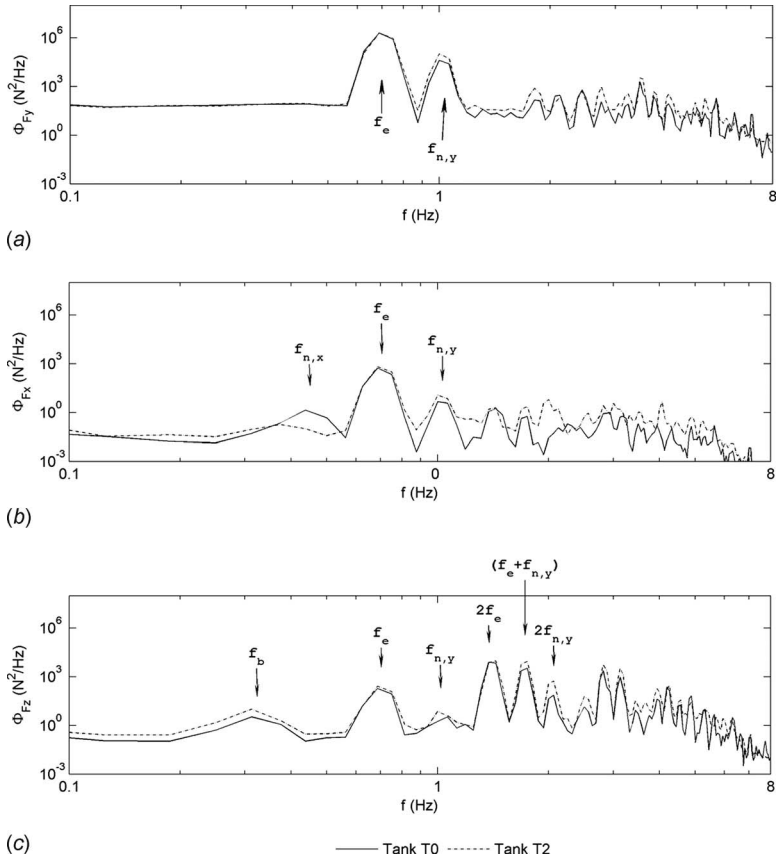

Fig. 4 Frequency spectra of slosh force components for 50%-filled unbaffled (T0) and baffled (T2) tanks subject to 1 m/s^2 lateral acceleration excitation at 0.7 Hz: (*a*) lateral force, (*b*) longitudinal force, and (*c*) vertical force

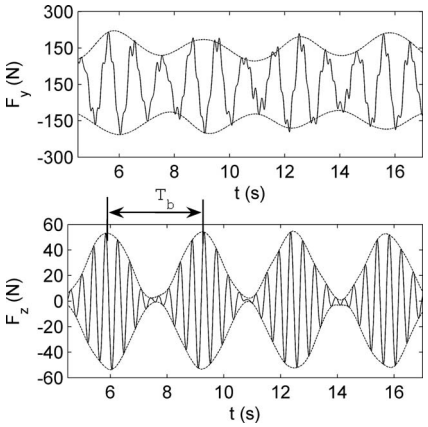

Fig. 5 Time histories of lateral (F_y) and vertical (F_z) slosh forces developed in 50%-filled cleanbore tank (T0) under 0.5 m/s^2 lateral acceleration excitation at 1.3 Hz. The dashed line illustrates the wave envelope attributed to beating phenomenon in slosh.

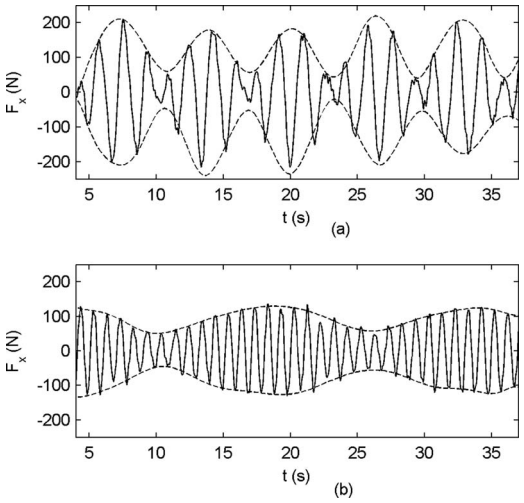

Fig. 7 Time histories of longitudinal slosh force (F_x) developed in 50%-filled cleanbore tank subject to longitudinal acceleration excitations: (*a*) A=0.5 m/s^2 at 0.6 Hz and (*b*) A=0.5 m/s^2 at 1 Hz

excitation and lateral mode frequencies. The largest peak in this range occurs at twice the excitation frequency (≈1.4 Hz), suggesting that the liquid oscillates like a pendulum. A peak near twice the resonant frequency (≈2 Hz) is also evident. The peak near 1.7 Hz corresponds to twice of the mean of excitation and resonance frequency ($f_e+f_{n,y}$) and has been referred to as the vibration frequency in the presence of beating [35]. The frequency spectrum of the vertical force at excitation amplitudes greater than 1 m/s^2 also revealed identical trends. However, at the lower excitation amplitude of 0.5 m/s^2, the largest peak in vertical force occurred at the vibration frequency, as opposed to twice the excitation frequency observed at higher amplitude excitations. This suggests that more pronounced beating is likely to occur at lower excitation amplitudes.

The largest peak in a given frequency spectrum represents the dominant mode of the corresponding slosh force component. The results in Fig. 4 show that the dominant mode frequency is not identical for all components of the slosh force. The relationship between the dominant mode frequency and the excitation frequency was thus investigated. Figures 6(*a*) and 6(*b*) illustrate variations in the dominant mode frequency (f_p) with the excitation frequency observed from the lateral and vertical force spectra, respectively, for the 50%-filled T1 tank subject to two different lateral acceleration amplitudes (0.5 m/s^2 and 2 m/s^2). The results clearly show that the dominant mode of the lateral forces occurs at the excitation frequency (i.e., $f_p=f_e$), whereas the dominant mode of the vertical force occurs at twice the excitation frequency (i.e., $f_p=2f_e$) for the higher excitation amplitude. The dominant modes corresponding to the lower excitation of 0.5 m/s^2, however, generally occur near the resonant frequency ($f_{n,y}$) for the lateral force and near the vibration frequency ($f_e+f_{n,y}$) for the vertical force.

The frequency spectra in Fig. 4 indicated the presence of the beating phenomenon, attributed to modulation of the excitation frequency with the resonant frequency [35]. The beat frequency is evident from the time histories of slosh forces shown in Fig. 5 for the 50%-filled T0 tank subject to 0.5 m/s^2 lateral excitation at 1.3 Hz. The figure shows the presence of beat frequency, $f_b=|f_e-f_{n,y}|$, with period T_b of approximately 3.3 s.

Similar trends can also be observed in the slosh forces under longitudinal excitations. Figure 7(*a*) presents variations in the longitudinal slosh force for the 50%-filled cleanbore tank (T0) under a 0.5 m/s^2 longitudinal excitation at 0.6 Hz in the vicinity of the first mode near 0.45 Hz. The results clearly show beat frequency near 0.16 Hz. The longitudinal force response under 1 Hz excitation also exhibits the beat phenomenon with frequency near 0.063 Hz, as seen in Fig. 7(*b*), although f_e is well above the first mode frequency. It was speculated that this beat frequency is associated with the second longitudinal mode resonance of the 50%-filled tank. The second mode frequency was computed as 1.09 Hz using the formulations by Kobayashi et al. [19] for an equivalent rectangular tank with identical fill level. The difference between this frequency and f_e is close to the observed beat frequency of 0.063 Hz. Considering that the pitch plane formulation derived for the rectangular tank in Ref. [19] is most likely applicable for the test tank cross section, the results suggest that the second mode frequency is close to 1 Hz.

To further explain the relationship between the beat frequency and the excitation frequency, the variations in the beat frequency are plotted against the excitation frequency in Fig. 8 for the 50%-

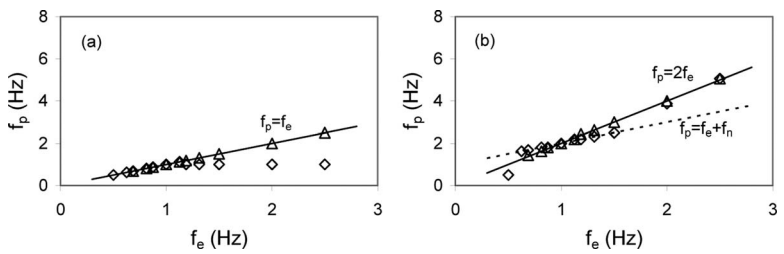

Fig. 6 Dominant mode frequency of the slosh force (f_p) versus the excitation frequency (f_e) for 50%-filled baffled tank (T1): (*a*) lateral force and (*b*) vertical force (open diamond, A=0.5 m/s^2 and open triangle, A=2 m/s^2)

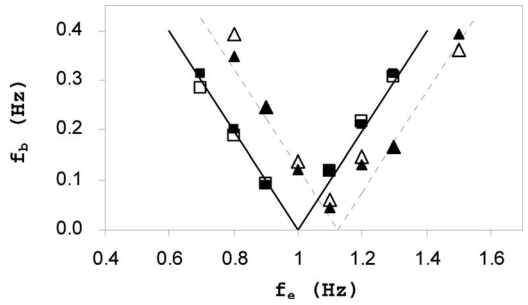

Fig. 8 Beating frequency (f_b) versus the excitation frequency (f_e) for the cleanbore tank subjected to the lateral acceleration excitation of 0.5 m/s^2. Open square, 50% fill volume; open triangle, 70% fill volume; open symbols, lateral force; and solid symbols, vertical force. The computed values are shown by continuous lines: solid line, 50% fill volume and dashed line, 70% fill volume.

and 70%-filled T0 tanks subject to a 0.5 m/s^2 lateral acceleration excitation. The beat frequency estimated from the relation $f_b = |f_e - f_{n,y}|$ is also plotted in the figure for comparison. The results clearly show good agreements between the estimated and measured beat frequencies, irrespective of the fill volume and excitation frequency considered. The results revealed that the beating phenomenon could be clearly observed for $|f_e - f_n| \leq 0.4$ Hz. It has been reported that the steering frequency in a path-change maneuver is typically in the order of 0.3 Hz and may approach as high as 0.5 Hz in an emergency type of directional maneuver [36]. Considering that the fundamental lateral mode slosh frequencies for a partly-filled full size tank employed in highway transportation lie in the 0.5–0.6 Hz range in the roll plane [11], the fluid oscillation within the tank may yield beating phenomenon. Similar degrees of agreements (not shown here) were also observed for the longitudinal acceleration excitation. The intensity of beating, however, was considerably smaller for the 30% fill volume in both lateral and longitudinal excitations. Moreover, the beating phenomenon was not clearly observable under higher amplitudes of excitations, where the slosh forces along longitudinal and lateral axes primarily oscillate at the excitation frequency.

3.2 Slosh Forces and Moments. The influences of excitation amplitude and frequency on the fluid slosh were investigated in terms of normalized amplification factors in forces and moments, using Eqs. (7)–(9). The results attained for the three tank configurations and three fill conditions under lateral and longitudinal excitations are discussed below.

3.2.1 Lateral Harmonic Excitations. Figure 9 shows variations in force and moment amplification factors for the 50%-filled T0 tank subject to lateral harmonic excitations of different amplitudes at various frequencies. The figure shows that the maxima of all three normalized force components lie in the vicinity of the lateral mode natural frequency ($\approx$1 Hz), irrespective of the excitation amplitude. Abramson and Garza [22] reported that the slosh resonance frequency decreases as the excitation amplitude increases for the compartmented upright cylindrical tanks. However, this dependence is not evident in the present study for the excitations and fill conditions considered. This could be attributed to the resolution of the test frequencies selected in the experiments.

Since the lateral force is normalized by the inertial force generated by an equivalent rigid weight, the responses can be inter-

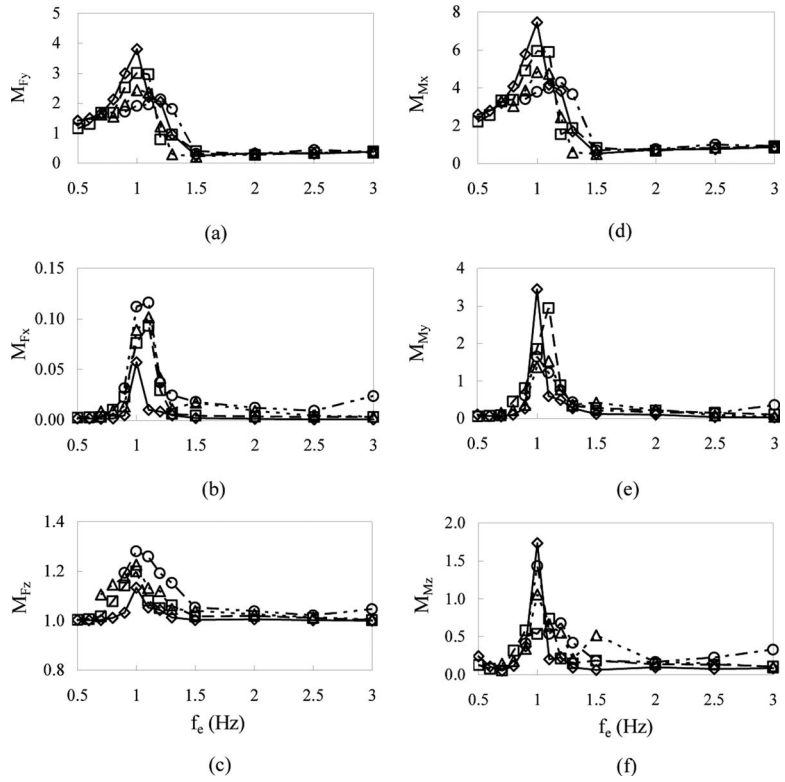

Fig. 9 Normalized slosh force and moment components versus the excitation frequency for 50%-filled cleanbore tank under lateral acceleration excitations (open diamond, A=0.5 m/s^2; open square, A=1 m/s^2; open triangle, A=2 m/s^2; and open circle, A=3 m/s^2: (*a*) lateral force, (*b*) longitudinal force, (*c*) vertical force, (*d*) roll moment, (*e*) pitch moment, and (*f*) yaw moment (note that the scales vary for different parameters)

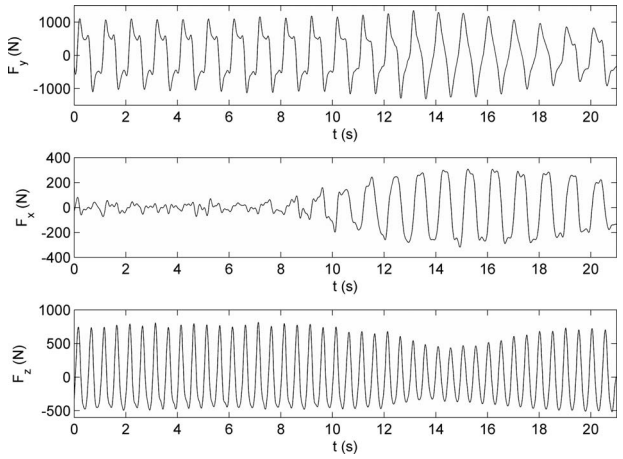

Fig. 10 Time histories of three slosh force components developed in 50%-filled cleanbore tank subjected to 1 m/s^2 lateral acceleration excitation at 1 Hz

preted as the amplification factor arising from the dynamic slosh effect. The results show that the peak amplification factor in lateral force could reach as high as 4. This factor decreases as the excitation amplitude increases, which is attributed to the boundary effects and the normalization. It is interesting to note that the amplification factor approaches a value less than unity at frequencies above 1.4 Hz, suggesting that the lateral slosh force magnitude under higher frequency excitations would be smaller than that due to an equivalent rigid mass.

The peak magnitudes of the normalized vertical slosh force also occur in the vicinity of the resonance frequency and increase with the excitation amplitude. The normalized magnitude, however, remains slightly above 1.0 at frequencies greater than 1.4 Hz, suggesting small magnitude of fluid slosh. The peak amplification factor is observed to be near 1.3 for the 3 m/s^2 lateral acceleration excitation. This indicates that the variations in the vertical force arising from dynamic slosh are up to 30% greater than the liquid weight under the excitations considered. Figure 9(*b*) shows that the magnitude of the normalized longitudinal force M_{Fx} is significantly smaller than the other force components, indicating that the amplification in longitudinal force is small in lateral excitation. The peak M_{Fx} occurs in the vicinity of the resonance frequency as observed for M_{Fy}, while the peak magnitude increases with the excitation amplitude. The results suggest that the slosh behaves in the 2D manner when the excitation frequency is distant from the resonance frequency. A sharp increase in longitudinal force is observed when the excitation approaches the natural frequency, suggesting the presence of 3D swirling motion. The results also show that the maximum force developed in the longitudinal direction is less than 13% of the liquid weight for the given excitations.

To further investigate the 3D swirling motion of the liquid, the time histories of slosh forces measured at 1 m/s^2 lateral acceleration excitation at 1 Hz (near resonance) are plotted in Fig. 10. The figure shows that the lateral and vertical force components had approached nearly steady state when the data acquisition was initiated. The magnitude of the longitudinal force component is almost negligible for $t \leq 8$ s and approaches a relatively higher magnitude thereafter. This increase after a time lag is attributed to the swirling motion of the free surface in the *x*-*y* plane, which was also observed visually during the experiments. Such 3D flows also cause variations in the magnitudes of vertical and lateral forces. The oscillations in the lateral and longitudinal forces exhibit considerable distortion in the harmonic shape, which can be attributed to large-amplitude slosh. The oscillations in F_x and F_y seem to be symmetric about the zero mean force, while those in the vertical force are asymmetric due to inertia effect. The magnitude of vertical force along the downward direction (positive) is greater than that in the upward direction (negative). The variations in magnitudes of F_y and F_z with that of F_x suggest the presence of strong coupling among the three force components.

The roll and pitch moments (Figs. 9(*d*) and 9(*e*)) exhibit trends similar to those in lateral and longitudinal forces, respectively. The maxima of the normalized roll and pitch moments are 7.5 and 3.4, respectively, for the excitation amplitude of 0.5 m/s^2 at the resonance. Figure 9(*f*) shows that the yaw moment also reaches the peak value of 1.7 near the resonance, which is mostly caused by the swirling fluid motion in the vicinity of the resonance. The influence of excitation amplitude on the peak lateral fluid slosh force and roll moment is further evaluated for all tank configurations with 30%, 50%, and 70% fill volumes in terms of peak amplification factors, as shown in Fig. 11. It should be noted that the peak responses were attained in the vicinity of the lateral mode resonance. The results show that 30% fill volume yields the highest values of M_{Fy} and M_{Mx}, while these factors are the lowest for 70% fill volume, irrespective of the excitation amplitude and tank configuration. The results also show that for a given fill volume, M_{Fy} and M_{Mx} decreased with an increase in the acceleration amplitude. The peak lateral force and roll moment tend to be the largest for 50% fill volume and lowest for 30% fill volume when fluid mass effect is taken into account. Few studies on rectangular and cylindrical tanks have also concluded that the largest slosh forces occur in the proximity of 50%-fill condition [2,10]. The figure further shows a larger amplification factor in roll moment than in lateral force, especially for the lower fill volume. For example, at 30% fill volume, the peak M_{Mx} is more than three times M_{Fy} for any excitation amplitude considered. This is because the roll moment is contributed not only by lateral force but also by the load shift caused by liquid cg oscillation and vertical slosh force. It was, however, observed that the peak values of M_{Fx} and M_{Fz} increase with an increase in the excitation amplitude, irrespective of the fill volume and tank configuration. This is attributed to the normalization with respect to the weight of the fluid ($m_l g$).

The maxima of the normalized longitudinal and vertical slosh forces as well as pitch and yaw moments measured under lateral harmonic excitations of different amplitudes are presented in Fig. 12 for the three fill volumes and tank configurations. The maxima generally occurred in the vicinity of the fundamental natural slosh frequency corresponding to the three fill levels considered, irrespective of the excitation amplitude. The results show that the peak forces and moments vary with the fill level in a manner similar to that observed for lateral force and roll moment (Fig. 11). The results also suggest a considerably larger amplification factor in pitch moment than in the longitudinal force. The peak normalized longitudinal forces developed in both baffled and unbaffled tanks are largest for 30% fill volume, but remained well below 0.2 for the given experimental conditions, while the peak normalized pitch moment approached as high as 4. This is attributed to the fact that the peak moment is mostly caused by the longitudinal load shift, which tends to be higher due to fluid swirl. The results also show that the baffled tanks yield lower normalized pitch moment (M_{My}) than the cleanbore tank, suggesting that the baffles help to suppress the longitudinal load shift due to lateral excitations. The results further show small effect of the baffles on the variations in the peak normalized vertical forces. The peak yaw moments are also considerably smaller than the pitch moment.

3.2.2 Longitudinal Harmonic Excitations. Figure 13 shows the amplification factors of the longitudinal and lateral forces and pitch moment for the 50%-filled T0 and T2 tanks subject to longitudinal harmonic excitations of different frequencies and amplitudes. The results reveal that the peak normalized longitudinal force (M_{Fx}) occurs in the vicinity of the longitudinal mode natural frequencies (i.e., 0.45 Hz and 1.08 Hz for the unbaffled and

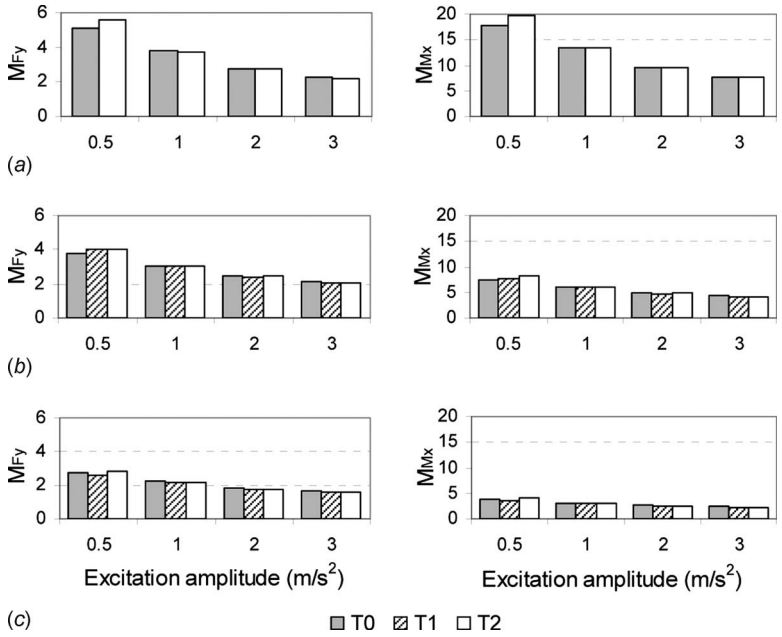

Fig. 11 Peak amplification factors of lateral force (M_{Fy}) and roll moment (M_{Mx}) versus the lateral acceleration excitation amplitude for all tank configurations: (*a*) 30%, (*b*) 50%, and (*c*) 70% fill volumes

baffled tanks, respectively). However, the baffled tank (T2) yields considerably lower peak force than the unbaffled tank (T0), confirming that the baffles could effectively suppress longitudinal slosh. The results in Fig. 13(*a*) show that the peak longitudinal force tends to decrease as the excitation amplitude increases for the T0 tank, as it was observed for M_{Fy} with lateral harmonic excitations. This trend, however, is not evident for the T2 tank in Fig. 13(*b*). An identical trend was also observed for the T1 tank (results not shown). The results further suggested that the magnitude of the longitudinal slosh force is nearly linearly dependent on the acceleration magnitude for the baffled tanks. Figure 13 also shows that the magnitudes of M_{Fx} tend to be less than unity when the excitation frequency is larger than the resonance frequency for both baffled and unbaffled tanks.

The amplification factor, M_{Fy}, shown in Fig. 13 suggests that the peak lateral force occurs in the vicinity of the longitudinal mode resonant frequency, irrespective of the excitation amplitude for both the unbaffled and baffled tanks. The largest peak value approaches 0.15 for both tanks, suggesting that the peak lateral force is approximately 15% of the liquid weight. The peak occurring at the frequency of 1 Hz is due to the lateral mode resonance, confirming the presence of coupling between the longitudinal and lateral motions of the fluid, as discussed in Sec. 3.2.1. For the baffled tank, the peak occurs near the fundamental longitudinal mode resonance frequency ($\approx$1.08 Hz), which is quite close to the lateral mode resonance. Very little variations in the normalized

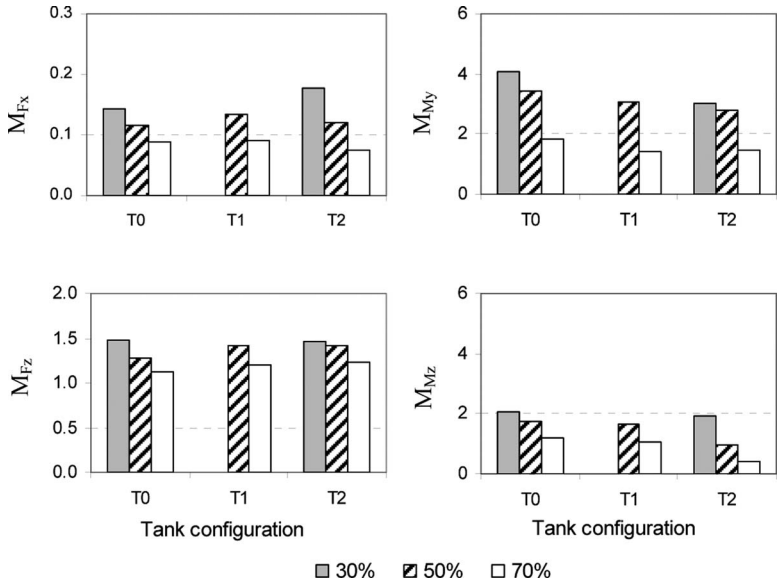

Fig. 12 Peak amplification factors of longitudinal (M_{Fx}) and vertical (M_{Fz}) slosh forces, and pitch (M_{My}) and yaw (M_{Mz}) moments versus the tank configuration for all fill volume cases

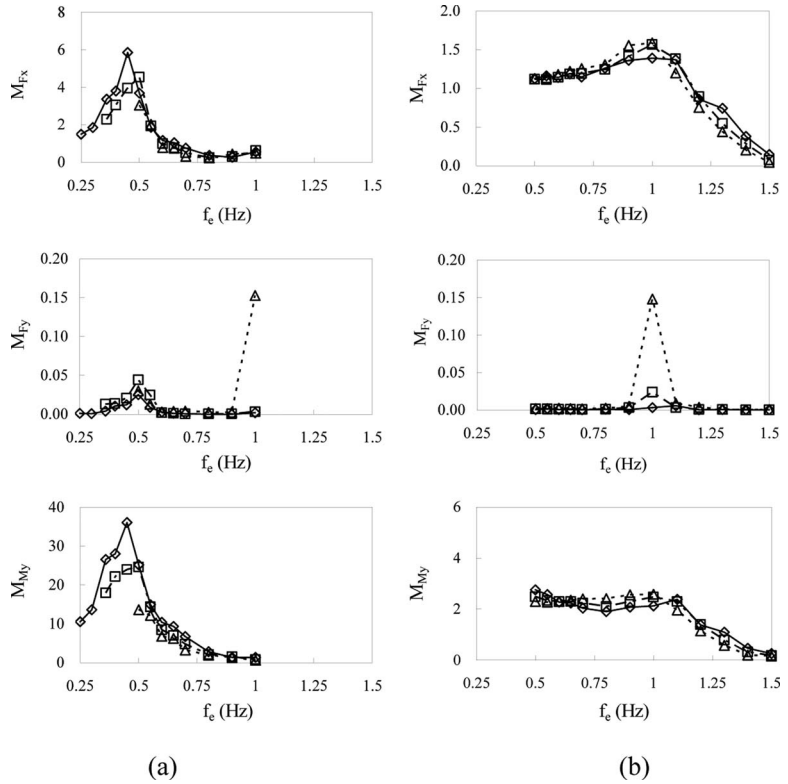

Fig. 13 Peak amplification factors of longitudinal and lateral forces, and pitch moment versus the excitation frequency for 50%-filled tanks: (*a*) "T0" tank and (*b*) "T2" tank (open diamond, =0.25 m/s^2; open square, =0.5 m/s^2; and open triangle, =1 m/s^2)

vertical force M_{Fz} were observed under longitudinal excitations for all tank configurations and fill volumes considered. The peak amplification factors in longitudinal force and pitch moment at different longitudinal excitation amplitudes are plotted in Fig. 14 for all the fill volumes and tank configurations. It should be noted that the peak forces developed in the 30%-filled T0 tank could not be derived under the excitation amplitude of 1 m/s^2 since the lowest excitation frequency was limited to 0.5 Hz, which was well above the resonant frequency of 0.36 Hz (see Table 2). The results thus show relatively lower M_{Fx} for the T0 tank under 30% fill condition.

Similar to the longitudinal force, the baffles greatly suppress the peak pitch moment caused by the fluid slosh. Figure 13 shows that the peak values of M_{My} due to fluid motion in T0 tank are significantly greater than those for T2 tank, irrespective of the excitation amplitude. This is attributed to greater longitudinal load shift in T0 tank under a longitudinal excitation, which tends to be the largest for lower fill volume of 30% (Fig. 14(*a*)). The T2 tank yields nearly constant magnitude of M_{My} at frequencies up to 1.1 Hz, irrespective of the excitation amplitude, which is mostly caused by relatively small load shifts in the baffled tank. The magnitudes of M_{My}, however, decrease rapidly at frequencies greater than the respective resonant frequencies for both tanks. The single-orifice baffle tank also reveals similar degree of effectiveness in suppressing the peak magnitude of M_{My}, as evident in Figs. 14(*b*) and 14(*c*) for 50% and 70% fill volumes, respectively. The results for the 70%-filled tank further show that multiple-orifice baffles could provide relatively greater suppression of the longitudinal force and pitch moment.

The maxima of the normalized roll and yaw moments measured under longitudinal harmonic excitations of different amplitudes are presented in Fig. 15 for the three fill volumes and tank configurations. The results show that M_{Mx} and M_{Mz} decrease as the fill volume increases, irrespective of the tank configuration, which is consistent with the trend observed in lateral excitations. The higher longitudinal load shift coupled with greater swirling motion of the fluid in T0 tank results in significantly larger yaw moment amplification (M_{Mz}). The magnitude of M_{Mz}, however, tends to be significantly lower for both the baffled tanks, irrespective of the fill volume. These results indicate that the baffles also help in suppressing the roll and yaw moments due to longitudinal excitations. For 50% fill volume, the roll and yaw moments developed by fluid slosh in the baffled T2 tank are 65.7% and 49.6% lower than those generated in the unbaffled T0 tank, respectively.

3.2.3 Lateral Single-Cycle Sinusoidal Excitations. Figure 16 shows the transient peak normalized lateral and vertical slosh forces for all the tank configurations and fill volumes subject to two lateral single-cycle sinusoidal excitations: (i) 1.9 m/s^2 peak acceleration at 1 Hz (Fig. 16(*a*)) and (ii) 4.3 m/s^2 peak acceleration at 1.5 Hz (Fig. 16(*b*)). The corresponding amplification factors in roll, pitch, and yaw moments (M_{Mx}, M_{My}, and M_{Mz}) are illustrated in Fig. 17. It should be noted that the former excitation is in the vicinity of the lateral mode resonance for the 50%-filled tank. The results show negligible effect of tank configuration and fill volume on the peak value of M_{Fz} for both the excitations. The variations in M_{Fx} (not shown here) were also found to be small, suggesting 2D liquid slosh under these conditions. The peak M_{Fy}, however, tends to be significantly higher under the 1 Hz excitation than under the 1.5 Hz excitation, irrespective of the fill volume. The higher frequency excitation (1.5 Hz) yields the peak magnitude of M_{Fy} less than unity. Furthermore, the 30% fill volume yields slightly higher peak values of M_{Fy}, similar to that observed in lateral harmonic excitation (Fig. 11). The amplification in roll moment, M_{Mx}, however, is considerably large for the 30% fill volume under both excitations, and the contribution of baffles is

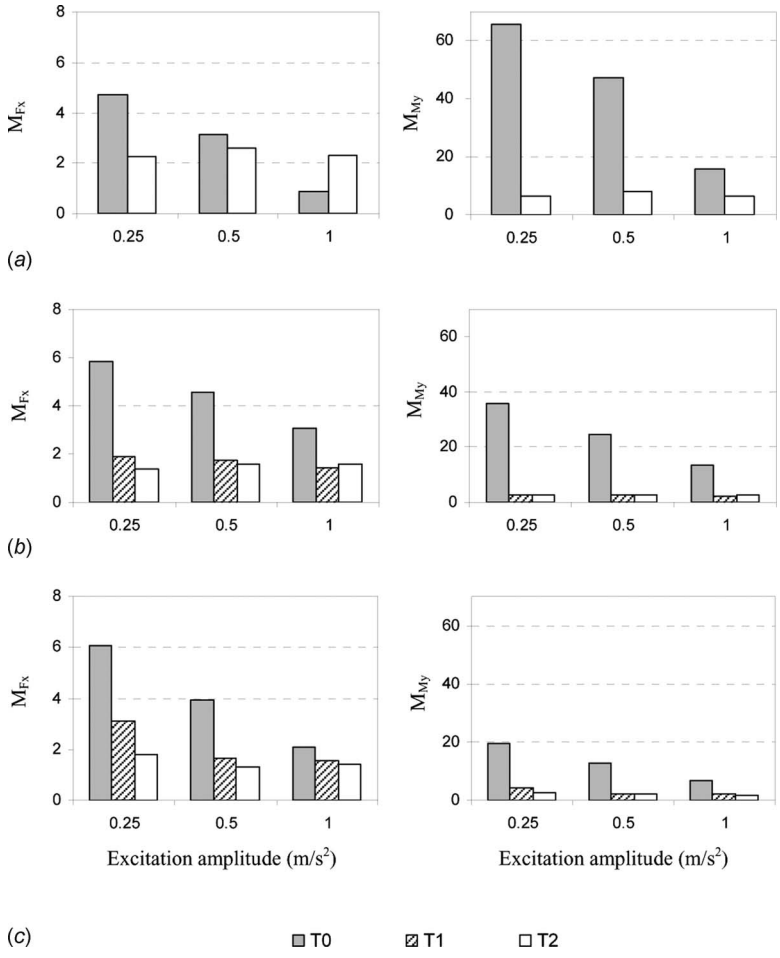

Fig. 14 Peak amplification factors of longitudinal slosh force and pitch moment versus the excitation amplitude for three tank configurations under longitudinal acceleration excitations: (*a*) 30%, (*b*) 50%, and (*c*) 70% fill volumes

very small. The magnitudes of M_{My} and M_{Mz} are also relatively small but tend to be higher for the 30% fill volume. These trends are comparable with those obtained with lateral harmonic excitations.

4 Conclusions

Liquid slosh in a scaled tank with cross section similar to a Reuleaux triangle has been investigated in the laboratory for unbaffled and baffled configurations with three fill conditions. The experiments involved the analyses of slosh frequencies, forces, and moments under lateral and longitudinal acceleration excitations of different amplitudes and frequencies. The results have shown that the slosh is a complex phenomenon, containing a number of spectral components. The predominant peak in the spectrum of a slosh force component may occur in the vicinity of the excitation frequency, the natural frequency, or the vibration frequency. The lateral and longitudinal force components generally oscillate at a frequency close to the excitation or the natural frequency, whereas the oscillations in the vertical force invariably occur at a frequency twice the excitation or natural frequency. The spectra of force components also show the presence of beating

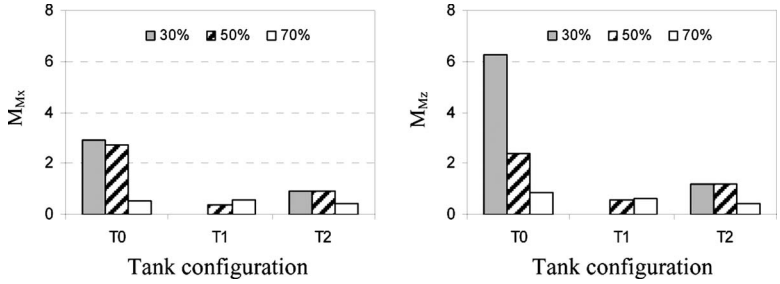

Fig. 15 Peak amplification factors of roll and yaw moments versus tank configurations for three fill volumes subjected to longitudinal acceleration excitations

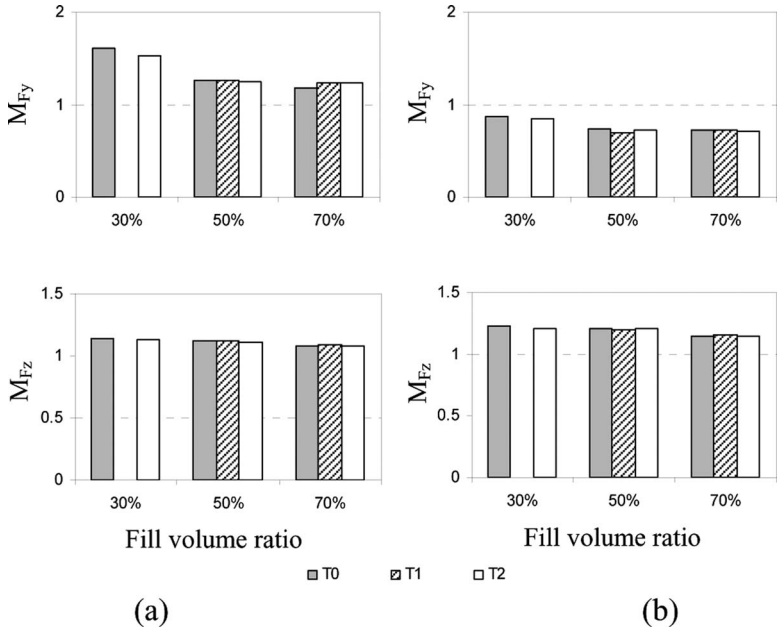

Fig. 16 Peak amplification factors of lateral and vertical slosh forces versus the fill volumes for the three tank configurations subjected to single-cycle lateral acceleration excitations: (*a*) 1.9 m/s^2 at 1 Hz and (*b*) 4.3 m/s^2 at 1.5 Hz

frequency when the excitation frequency is close to the natural frequency of slosh, which is more evident under lower excitation amplitudes.

The fundamental frequencies of fluid slosh estimated from the spectra of the dominant force component under free oscillation agreed reasonably well with those estimated using the reported method based on the wavelength and wave speed of the free surface. The fundamental natural frequency of slosh was observed to be dependent on the fill level and the tank configuration. This frequency, in both lateral and longitudinal modes, increased with the fill level for all three tank configurations considered. The addition of transverse baffles caused a significant increase in the longitudinal mode natural frequency, while the lateral mode frequency was not affected by the baffles. For the 50% fill volume, the longitudinal mode frequency increased from 0.45 Hz for the unbaffled tank to 1.08 Hz for the baffled tanks.

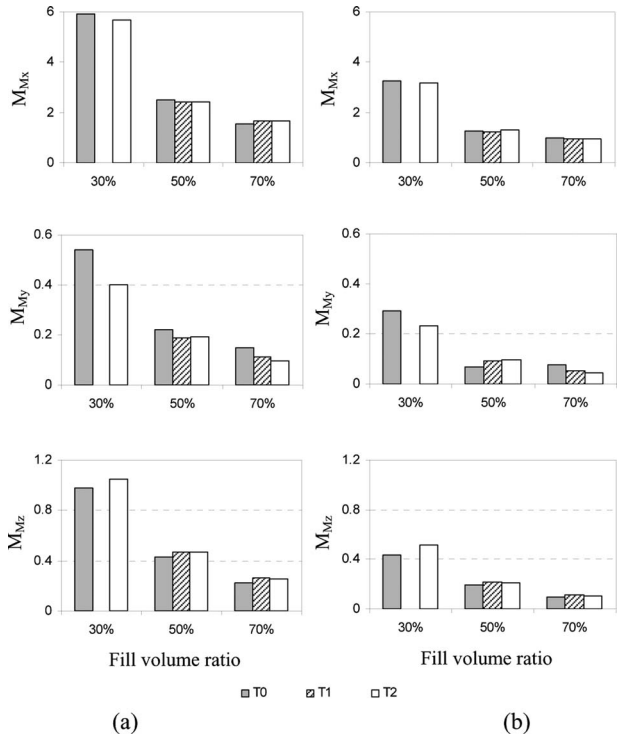

Fig. 17 Peak amplification factors of roll, pitch, and yaw moments versus the fill volumes for three tank configurations subjected to single-cycle lateral acceleration excitations: (*a*) 1.9 m/s^2 at 1 Hz and (*b*) 4.3 m/s^2 at 1.5 Hz

The measured data and flow visualization revealed the three-dimensional nature of the fluid motion under excitations along either lateral or longitudinal axis of the tank for both baffled and unbaffled configurations, which suggests a coupling between the lateral and longitudinal fluid slosh. The peak slosh forces and moments generally occurred in the vicinity of slosh natural frequency in the respective mode, which was manifested under continuous as well as single-cycle sinusoidal excitations. The dynamic slosh could yield largely amplified resulting forces and moments near the resonance when compared with those of the equivalent rigid mass. The slosh amplification factors in lateral and longitudinal forces under respective excitations, however, decreased as the fill level or excitation amplitude increased. The slosh amplification effect was reflected more significantly in roll and pitch moments than in the forces. The amplification factors in both longitudinal and lateral forces at an excitation frequency above the resonant frequencies are generally below unity, which suggests that the magnitude of fluid slosh force is less than the inertial force developed by an equivalent rigid mass subject to the same excitation. The transient lateral slosh measured under single-cycle lateral acceleration excitation revealed predominantly two-dimensional motion of the free surface for all tank configurations considered.

The peak magnitudes of longitudinal slosh force and pitch moment developed under a longitudinal acceleration excitation decreased significantly in the presence of lateral baffles. This was clearly evident for both single-orifice and multiple-orifice baffles, although multiple-orifice baffles resulted in slightly greater reduc-

tions in peak force and moment. The baffles also helped to reduce the magnitudes of corresponding roll moment. The addition of lateral baffles, however, did not affect the peak magnitudes of lateral slosh force or roll moment under lateral acceleration excitations.

Acknowledgment

This work was supported by the Ministère des Trasnport due Québec and the Natural Sciences and Engineering Research Council of Canada.

References

[1] Strandberg, L., 1978, "Lateral Stability of Road Tankers," National Road and Traffic Research Institute, Report No. 138A.
[2] Popov, G., Sankar, S., and Sankar, T. S., 1993, "Dynamics of Liquid Sloshing in Baffled and Compartmented Road Containers," J. Fluids Struct., **7**, pp. 803–821.
[3] Solaas, F., and Faltinsen, O. M., 1997, "Combined Numerical and Analytical Solution for Sloshing in Two-Dimensional Tanks of General Shape," J. Ship Res., **41**, pp. 118–129.
[4] Abramson, H. N., Chu, W. H., and Kana, D. D., 1966, "Some Studies of Nonlinear Lateral Sloshing in Rigid Containers," ASME Trans. J. Appl. Mech., **33**(4), pp. 777–784.
[5] Chen, W., Haroun, M. A., and Liu, F., 1996, "Large Amplitude Liquid Sloshing in Seismically Excited Tanks," Earthquake Eng. Struct. Dyn., **25**, pp. 653–669.
[6] Yan, G., Siddiqui, K., Rakheja, S., and Modaressi, K., 2005, "Transient Fluid Slosh and Its Effect on the Rollover-Threshold Analysis of Partially Filled Conical and Circular Tank Trucks," Int. J. Heavy Vehicle Systems, **12**(4), pp. 323–343.
[7] Rakheja, S., Sankar, S., and Ranganathan, R., 1988, "Roll Plane Analysis of Articulated Tank Vehicles During Steady Turning," Veh. Syst. Dyn., **17**, pp. 81–104.
[8] Ranganathan, R., Rakheja, S., and Sankar, S., 1990, "Influence of Liquid Cargo Shift on the Dynamic Response of Articulated Tank Vehicles," Veh. Syst. Dyn., **19**, pp. 177–200.
[9] Kang, X., Rakheja, S., and Stiharu, I., 2002, "Cargo Load Shift and Its Influence on Tank Vehicle Dynamics Under Braking and Turning," Int. J. Heavy Vehicle Systems, **9**(3), pp. 173–203.
[10] Modaressi-Tehrani, K., Rakheja, S., and Sedaghati, R., 2006, "Analysis of the Overturning Moment Caused by Transient Liquid Slosh Inside a Partly Filled Moving Tank," Proc. Inst. Mech. Eng., Part D (J. Automob. Eng.), **220**, pp. 289–301.
[11] Modaressi-Tehrani, K., Rakheja, S., and Stiharu, I., 2007, "Three-Dimensional Analysis of Transient Slosh Within a Partly-Filled Tank Equipped With Baffles," Veh. Syst. Dyn., **45**(6), pp. 525–548.
[12] Abramson, H. N., Chu, W. H., and Garza, L. R., 1963, "Liquid Sloshing in Spherical Tanks," AIAA J., **1**(2), pp. 384–389.
[13] Lamb, S. H., 1945, *Hydrodynamics*, 6th ed., Dover, New York.
[14] Silvermann, S., and Abramson, H., 1966, "Lateral Sloshing in Moving Containers," NASA, Report No. SP-106.
[15] Cho, J. R., Lee, H. W., and Ha, S. Y., 2005, "Finite Element Analysis of Resonant Sloshing Response in 2-D Baffled Tank," J. Sound Vib., **288**, pp. 829–845.
[16] Budiansky, B., 1960, "Sloshing of Liquids in Circular Canals and Spherical Tanks," J. Aerosp. Sci., **27**(3), pp. 2601–2606.
[17] Mciver, P., 1989, "Slosh Frequencies for Cylindrical and Spherical Containers Filled to Arbitrary Depth," J. Fluid Mech., **201**, pp. 243–257.
[18] McCarty, J. L., and Stephens, D. G., 1960, "Investigation of the Natural Frequencies of Fluids in Spherical and Cylindrical Tanks," NASA Technical Note No. TN D-252.
[19] Kobayashi, N., Mieda, T., Shibata, H., and Shinozaki, Y., 1989, "A Study of the Liquid Slosh Response in Horizontal Cylindrical Tanks," ASME J. Pressure Vessel Technol., **111**, pp. 32–38.
[20] Bauer, H. F., 1963, "Liquid Sloshing in a Cylindrical Quarter Tank," AIAA J., **1**(11), pp. 2601–2606.
[21] Romero, J. A., Hildebrand, R., Martinez, M., Ramirez, O., and Fortanell, J. M., 2005, "Natural Sloshing of Liquid Cargo in Road Tankers," Int. J. Heavy Vehicle System, **12**(2), pp. 121–138.
[22] Abramson, H. N., and Garza, L. R., 1965, "Liquid Frequencies and Damping in Compartmented Cylindrical Tanks," AIAA J., **2**(3), pp. 453–455.
[23] Evans, D. V., and Mciver, P., 1987, "Resonant Frequencies in a Container With a Vertical baffle," J. Fluid Mech., **175**, pp. 295–307.
[24] Popov, G., Sankar, S., Sankar, T. S., and Vatistas, G. H., 1993, "Dynamics of Liquid Slosh in Horizontal Cylindrical Road Containers," Proc. Inst. Mech. Eng., Part C: J. Mech. Eng. Sci., **207**, pp. 399–406.
[25] Lloyd, N., Vaiciurgis, E., and Langrish, T. A. G., 2002, "The Effect of Baffle Design on Longitudinal Liquid Moment in Road Tankers: An Experimental Investigation," Process Saf. Environ. Prot., **80**, pp. 181–185.
[26] Younes, M. F., Younes, Y. K., El-Madah, M., Ibrahim, I. M., and El-Dannanh, E. H., 2007, "An Experimental Investigation of Hydrodynamic Damping Due to Vertical Baffle Arrangements in a Rectangular Tank," Proc. IMechE, Part M: J. Engineering for the Maritime Environment, " , **221**, pp. 115–123.
[27] Miles, J. W., 1984, "Internally Resonance Surface Waves in a Circular Cylinder," J. Fluid Mech., **149**, pp. 1–14.
[28] Faltinsen, O. M., 1974, "A Nonlinear Theory of Sloshing in Rectangular Ranks," J. Ship Res., **18**(4), pp. 224–241.
[29] Morand, H. J. P., and Ohayon, R., 1989, "Finite Element Method Applied to the Prediction of the Vibrations of Liquid-Propelled Launch Vehicle," PVP (Am. Soc. Mech. Eng.), **176**, pp. 75–84.
[30] Ibrahim, R. A., Pilipchuk, V. N., and Ikeda, T., 2001, "Recent Advances in Liquid Slosh Dynamics," Appl. Mech. Rev., **54**(2), pp. 133–199.
[31] Rhee, S. H., 2005, "Unstructured Grid Based Reynolds-Averaged Navier-Stokes Method for Liquid Sloshing," ASME J. Fluids Eng., **127**, pp. 572–582.
[32] Kang, X., Rakheja, S., and Stiharu, I., 1999, "Optimal Tank Geometry to Enhance Static Roll Stability of Partially Filled Tank Vehicles," SAE Truck and Bus Meeting and Exhibition, Detroit, MI, Nov. 14–17, Proceedings Vol. SP-1486, SAE Paper No. 1999-01-3730.
[33] Code of Federal Regulations (CFR), 2006, Title 49, Pt. 178.
[34] El-Gindy, M., 1995, "An Overview of Performance Measures for Heavy Commercial Vehicles in North America," Int. J. Veh. Des., **16**(4/5), pp. 441–463.
[35] Graham, K. S., 2000, *Fundamentals of Mechanical Vibrations*, 2nd ed., McGraw-Hill, New York.
[36] Winkler, C. B., and Ervin, R. D., 1999, "Rollover of Heavy Commercial Vehicles," The University of Michigan Transportation Research Institute, Final Report No. UMTRI-99-19.

Analysis of Laminar Falling Film Condensation Over a Vertical Plate With an Accelerating Vapor Flow

A.-R. A. Khaled[1]
e-mail: akhaled@kau.edu.sa

Abdulhaiy M. Radhwan

S. A. Al-Muaikel

Department of Thermal Engineering and
Desalination Technology,
King AbdulAziz University,
P.O. Box 80204,
Jeddah 21589, Saudi Arabia

Laminar falling film condensations over a vertical plate with an accelerating vapor flow is analyzed in this work in the presence of condensate suction or slip effects at the plate surface. The following assumptions are made: (i) laminar condensate flow having constant properties, (ii) pure vapor with a uniform saturation temperature in the vapor region, and (iii) the shear stress at the liquid/vapor interface is negligible. The appropriate fundamental governing partial differential equations for the condensate and vapor flows (continuity, momentum, and energy equations) for the above case are identified, nondimensionalized, and transformed using nonsimilarity transformation. The transformed equations were solved using numerical, iterative, and implicit finite-difference methods. It is shown that the freestream striking angle has insignificant influence on the condensation mass and heat transfer rates, except when slip condition is present and at relatively small Gr_l/Re^2 *values. Moreover, it is shown that increasing the values of the dimensionless suction parameter* (V_S) *results to an increase in dimensionless mass of condensate* ($\Gamma(L)/(\mu_l Re)$) *and Nusselt number* ($Nu(L)/Re^{1/2}$). *Thus, it results in an increase in condensation mass and heat transfer rates. Finally, it is found that the condensation and heat transfer rates increase as Jakob number, slip parameter, and saturation temperature increase. Finally, the results of this work not only enrich the literature of condensation but also provide additional methods for saving thermal energy.*
[DOI: 10.1115/1.3155992]

Keywords: condensation, mass transfer, buoyancy driven flow, laminar, gas-liquid, heat transfer

1 Introduction

Condensation is the process by which a saturated vapor is converted into a liquid by means of removing the latent heat of evaporation. From a thermodynamic point of view, condensation occurs when the enthalpy of the vapor is reduced below its enthalpy when it is at a saturated vapor phase at the same pressure. Among condensation mechanisms is the filmwise condensation, which is of interest to this work. In filmwise condensation, the condensate drops initially form on a cold surface, and then it quickly coalesces to produce a continuous film of liquid on that surface as more heat is transferred to it. Falling film condensations over vertical surfaces are encountered in many types of heat/mass transfer equipments such as those consisting of vertical tubes and vertical plane surfaces. The condensation process is extremely important in the industry. It is an essential process in petroleum refinery industrials, as well as in many of the thermal desalination systems.

Condensation over a vertical plate occurs when vapor comes in contact with a surface at a lower temperature. As the condensate falls down on the surface due to the influence of gravity, the thickness of the falling film increases. The latent heat released due to condensation is transferred to the surface. Three consequent regions can be identified in the condensate volume: (i) laminar region, where the falling film is the thinnest, it occurs near the top of the plate; (ii) transition region, which comes after the laminar region where the condensate flow becomes thicker and unstable; and (iii) turbulent region, where the flow of the condensate becomes inhomogeneous.

The original theory of gravity induced laminar film condensation was developed by Nusselt [1]. In his theory, the following assumptions have taken on:

(a) Laminar flow and constant properties are considered for liquid film.
(b) The vapor is considered a pure vapor having a uniform saturation temperature.
(c) The shear stress at the liquid interface is negligible.
(d) The momentum and thermal energy transfers by advection in the condensate film are assumed negligible.

The Nusselt film condensation theory was first improved by Bromley [2] who assumed linear temperature distribution in the Nusselt model [1] and introduced a correction to account for the effect of liquid subcooling. His study showed a small increase in heat transfer at higher Jakob numbers. However, the Jakob number is normally very small in most of the engineering applications. Bromley's model [2] was improved by Rohsenow [3]. He analyzed the effect of nonlinear temperature distribution and included the effect of cross flow within the film. Rohsenow's [3] improvement was only important at high values of liquid subcooling, that is, at large Jakob numbers. Because small Jakob numbers are usual in engineering applications, this improvement had little contribution. In fact, it exactly agrees to the results of Bromley [2] for small Jakob numbers, which is more practical.

Sparrow and Gregg [4] included the momentum effects and energy convection in the Nusselt model [1]. They adopted the

[1]Corresponding author.

Contributed by the Fluids Engineering Division of ASME for publication in the JOURNAL OF FLUIDS ENGINEERING. Manuscript received August 16, 2008; final manuscript received April 10, 2009; published online June 23, 2009. Assoc. Editor: Ian Eames.

boundary layer theory as a mathematical technique. They studied Jakob numbers between 0 and 2 for Prandtl numbers between 0.003 and 100. They found that for Prandtl numbers greater than 1, momentum effects can be neglected with no more than 5% error at Jakob number of 2 and the error is less for smaller Jakob numbers. This led to the conclusion that momentum has little effect on condensation heat transfer. However, momentum effects become very important for low Prandtl numbers (liquid metals). Similar results were obtained by Yang [5], who used boundary layer analysis, and Mabuchi [6], who used approximate integral method.

Later on, Koh et al. [7] extended the research in the film condensation by accounting for the shear forces at the liquid-vapor interface, which were neglected before. They solved the simultaneous flow problem in the vapor and the liquid regions. They found that the influence of the interfacial shear on the heat transfer is very small for fluids with a Prandtl number of 1, and it becomes smaller as the Prandtl number increases. At a Prandtl number equal to 10, it becomes negligible. Another solution for the same problem using integral methods was later on solved by Koh [8] and Chen [9]. Their results were similar to those which were already mentioned before.

Saturated vapor is assumed in all of the previous studies. It was also assumed that the heat transfer at the liquid-vapor interface is with zero thermal resistance and that thermodynamic and transport properties are constants. The Nusselt model [1] was extended by Stender [10] in 1925 to the situation where the vapor is superheated. He assumed that the only important vapor motion is in the direction of the condensing surface (i.e., one-dimensional flow). In addition, he neglected the interfacial thermal resistance. As such, he considered that the temperature at the interface to be equal to the saturation temperature at the vapor pressure.

The Stender model [10] in the presence of superheated vapor was extended by Silver [11], who accounted for the interfacial thermal resistance. His results show that this resistance has an important influence on the rate of heat transfer at low pressure. However, at moderate and high pressures, the influence is not important. His results showed that the temperature of the condensate surface drops below the saturation temperature because of the effect of the interfacial resistance. As such, the rate of heat transfer decreased, which contradicts with the results of Stender [10]. The effect of interfacial resistance when the vapor is saturated is given by Sukhatme and Rohsenow [12]. Their results were similar to those of Silver and Simpson [13].

Using of the boundary layer theory, the problem of condensation of superheated vapor was re-examined by Sparrow and Eckert [14]. They neglected the effect of the free convection within the vapor in predicting heat transfer rate. Moreover, they neglected the effect of the thermal resistance of the interface. Their findings were found to be similar to those predicted by Stender [10]. They have also shown that only a small increase in heat flux was due to the superheat. Chisholm [15] also analyzed the problem of condensation of superheated steam.

Sparrow and Eckert [14] discussed qualitatively the consequence of noncondensable gases on the heat transfer during condensation. They concluded that a fully predictive theory for the effect of noncondensable gases must include free convection effects. Later on, Sparrow and Lin [16] devised a theory based only on the conservation principles for predicting condensation heat transfer in the presence of noncondensable gases and including the free convection effects. After that, Chen [9] considered the vapor to be stagnant far from the interface while considering it to be dragged downward by the falling film of the condensate near the interface. The values of Nusselt numbers reported by Chen [9] were found to be smaller than these reported by Sparrow and Gregg [4] and agree better with experimental data.

There are numbers of very important applications in which falling film condensations have been analyzed. Falling film over a spherical surface is analyzed in the works of Lienhard and coworker [17,18]. Shekriladze and Gomelauri [19] analyzed film condensation on the outside surface of a horizontal cylinder in cross flow. The problem of laminar condensation over an elliptical cylinder has been analyzed by several researchers (e.g., Mosaad [20], Memory et al. [21], and Yang and Hus [22]). They found that the elliptical section tube improved the vapor condensation over horizontal cylinder. Recently, several works have discussed numerically and experimentally the stability of the condensing flows [23–27]. Through a long search in the available literature, the effect of the freestream vapor-striking angle on the condensation over a vertical plate could not be located. As such, this topic is the interest of this work.

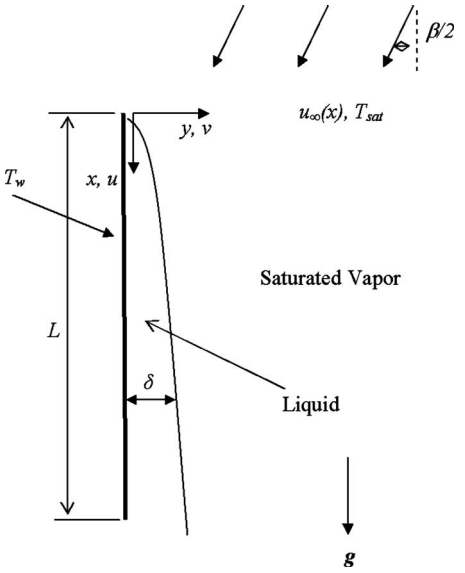

Fig. 1 Schematic diagram

In this work, the problem of laminar falling film condensation over a vertical plate with accelerating vapor flow is theoretically formulated. The developed model is considered to account for condensate blowing/suction at the plate surface and fluid slip at the wall. The governing equations for this problem are transformed using a nonsimilar transformation. Then, they are solved using an iterative and implicit finite-difference method. The Nusselt number and the dimensionless mass flow rate are obtained for various representing values of the obtained controlling dimensionless parameters. These parameters are Jakob number, dimensionless slip parameter, dimensionless suction parameter, Grashof number, Prandtl number, Reynolds number, and vapor to liquid density ratio.

2 Problem Formulation

Consider a vertical plate with a length L; the x-axis is taken along the length of the plate while the y-axis is normal to the plate, as shown in Fig. 1. The axial velocity of the condensate is u, which is along the x-axis, while its normal velocity along the y-axis is v. The plate is kept at a uniform temperature T_w, which is lower than the temperature of the surrounding vapor (assumed to be saturated vapor). As such, a falling condensate film with thickness $\delta(x)$ is formed along the plate length. The freestream velocity of the surrounding vapor is $u_\infty(x)$, which is considered variable.

The governing continuity, momentum, and energy equations for falling condensate film are [28]

$$\frac{\partial u}{\partial x} + \frac{\partial v}{\partial y} = 0 \tag{1}$$

$$\rho_l\left(u\frac{\partial u}{\partial x} + v\frac{\partial u}{\partial y}\right) = -\frac{dP'}{dx} + (\rho_l - \rho_v)g + \mu_l\frac{\partial^2 u}{\partial y^2} \tag{2}$$

$$\rho_l (c_p)_l \left(u\frac{\partial T}{\partial x} + v\frac{\partial T}{\partial y} \right) = k_l \frac{\partial^2 T}{\partial y^2} \tag{3}$$

From the inviscid theory, the pressure gradient in the flow passage is

$$\frac{dP'}{dx} = -\rho_v u_\infty(x) \frac{d}{dx}(u_\infty(x)) \tag{4}$$

The boundary conditions are

$$u(x,0) = \beta_s \left.\frac{\partial u}{\partial y}\right|_{x,0} \tag{5a}$$

$$v(x,0) = -v_o \tag{5b}$$

$$\left.\frac{\partial u}{\partial y}\right|_{x,\delta} = 0 \tag{5c}$$

$$T(x,0) = T_w \tag{6a}$$

$$T(x,\delta) = T_{\text{sat}} \tag{6b}$$

$$k_l \left.\frac{\partial T}{\partial y}\right|_{x,\delta} = \rho_l \left(u\frac{d\delta}{dx} - v \right) \Big|_{x,\delta} h_{fg} \tag{7}$$

In the boundary condition equation (5*a*), slip condition is assumed between the wall and the condensate. The slip velocity at the wall is assumed proportional to the strain rate at the wall according to Navier's model [29]. This model is taken in this work for general characterization of the present problem. The coefficient β_S is the slip coefficient; h_{fg} is the enthalpy of vaporization for the fluid. It is worth noting that the vapor shear stress at the interface is considered negligible (Eq. (5*c*)) as when μ_v/μ_l is very small or when freestream velocity is small. Also, it is indicated before that Koh et al. [7] found that the interfacial shear stress has a very small effect on the heat transfer with a Prandtl number of 1 or more.

Nondimensionalizing Eqs. (1)–(4) and (5*a*)–(7) utilizing the following variables:

$$\bar{x} = \frac{x}{L} \tag{8a}$$

$$\bar{y} = \frac{y}{L} \tag{8b}$$

$$\bar{u} = \frac{u}{u_\infty|_{x=L}} \tag{8c}$$

$$\bar{v} = \frac{v}{u_\infty|_{x=L}} \tag{8d}$$

$$\theta = \frac{T - T_{\text{sat}}}{T_W - T_{\text{sat}}} \tag{8e}$$

$$\bar{p}' = \frac{p'}{\rho_l \left(\frac{u^2_{\infty_l}}{L} \right)} \tag{8f}$$

results in the following dimensionless equations:

$$\frac{\partial \bar{u}}{\partial \bar{x}} + \frac{\partial \bar{u}}{\partial \bar{y}} = 0 \tag{9}$$

$$\bar{u}\frac{\partial \bar{u}}{\partial \bar{x}} + \bar{v}\frac{\partial \bar{u}}{\partial \bar{y}} = \frac{\rho_v}{\rho_l}\bar{u}_\infty(\bar{x})\frac{d}{d\bar{x}}(\bar{u}_\infty(\bar{x})) + \frac{\text{Gr}_l}{\text{Re}^2} + \frac{1}{\text{Re}}\frac{\partial^2 \bar{u}}{\partial \bar{y}^2} \tag{10}$$

$$\bar{u}\frac{\partial \theta}{\partial \bar{x}} + \bar{v}\frac{\partial \theta}{\partial \bar{y}} = \frac{1}{\text{Re}\ \text{Pr}_l}\frac{\partial^2 \theta}{\partial \bar{y}^2} \tag{11}$$

$$\frac{d\bar{P}'}{d\bar{x}} = -\frac{\rho_v}{\rho_l}\bar{u}_\infty \frac{d\bar{u}_\infty}{d\bar{x}} \tag{12}$$

where

$$\text{Re} = \frac{\rho_l u_\infty|_{x=L} L}{\mu_l} \tag{13a}$$

$$\text{Gr}_l = \frac{\rho_l(\rho_l - \rho_v) g L^3}{\mu_l^2} \tag{13b}$$

The dimensionless boundary conditions are

$$\bar{u}(\bar{x},0) = \frac{\beta_S}{L} \left.\frac{\partial \bar{u}}{\partial \bar{y}}\right|_{\bar{x},0} \tag{14a}$$

$$\bar{v}(\bar{x},0) = -\frac{v_o}{u_\infty(L)} \tag{14b}$$

$$\left.\frac{\partial \bar{u}}{\partial \bar{y}}\right|_{\bar{x},\bar{\delta}} = 0 \tag{14c}$$

$$\theta(\bar{x},0) = 1.0 \tag{14d}$$

$$\theta(\bar{x},\bar{\delta}) = 0 \tag{14e}$$

$$-\left(\frac{\text{Ja}_l}{\text{Re}\ \text{Pr}_l}\right)\left(\frac{\partial \theta}{\partial \bar{y}}\right)\Big|_{\bar{x},\bar{\delta}} = \left(\bar{u}\frac{d(\delta/L)}{d\bar{x}} - \bar{v}\right)\Big|_{\bar{x},\bar{\delta}} \tag{14f}$$

$$\text{Ja}_l = \frac{(c_p)_l (T_{\text{sat}} - T_W)}{h_{fg}} \tag{15}$$

where Ja_l is the Jakob number.

When the freestream vapor flow strikes the vertical plate with an angle $\beta/2$ relative to the vertical, as shown in Fig. 1, the axial freestream velocity will have the following form [28]:

$$\bar{u}_\infty(\bar{x}) = \bar{x}^m \tag{16}$$

$$m = \frac{\beta}{2\pi - \beta} \tag{17}$$

The following nonsimilar variables are used:

$$\xi = \bar{x}; \quad \eta = \frac{\bar{y}}{\left[\frac{(m+1)}{2}\text{Re}\right]^{-1/2} \bar{x}^{(1-m)/2}}; \quad f'(\xi,\eta) = \frac{\partial f}{\partial \eta} = \frac{\bar{u}(\bar{x},\bar{y})}{\bar{x}^m} \tag{18}$$

From the dimensionless continuity equation (9), the dimensionless normal velocity ($\bar{v}$) can be found to be functions of f, f' according to the following relation:

$$\bar{v} = \left[\frac{(m+1)}{2}\text{Re}\right]^{-1/2} \bar{x}^{(1-m)/2}\left[-m\bar{x}^{(m-1)} f - \bar{x}^m\left(\frac{\partial f'}{\partial \xi} - f'\frac{\partial \eta}{\partial \bar{x}}\right)\right] \tag{19}$$

The applications of variables in Eqs. (18) and (19) on Eqs. (10) and (11) result in the following nonsimilar equations:

$$f''' + ff'' + \frac{2m}{m+1}\left[\frac{\rho_v}{\rho_l} - f'^2\right] + \frac{2\xi^{1-2m}}{m+1}\left(\frac{\text{Gr}_l}{\text{Re}^2}\right) = \frac{2\xi}{m+1}\left(f'\frac{\partial f'}{\partial \xi} - f''\frac{\partial f}{\partial \xi}\right), \quad m < \frac{1}{2} \tag{20}$$

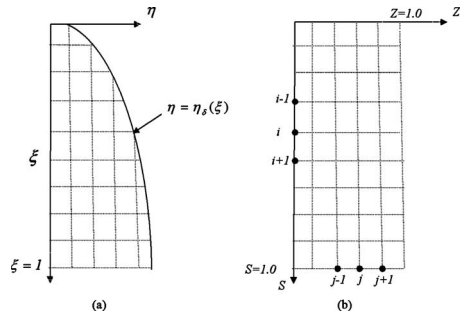

Fig. 2 (*a*) Grid with variable thickness and (*b*) uniform thickness grid

$$\frac{1}{\mathrm{Pr}_l}\theta'' + f\theta' = \frac{2}{m+1}\xi\left[f'\frac{\partial\theta}{\partial\xi} - \theta'\frac{\partial f}{\partial\xi}\right] \tag{21}$$

where

$$f'' = \frac{\partial^2 f}{\partial\eta^2}, \quad f''' = \frac{\partial^3 f}{\partial\eta^3}, \quad \theta' = \frac{\partial\theta}{\partial\eta}, \quad \theta'' = \frac{\partial^2\theta}{\partial\eta^2}$$

The transformed boundary conditions are

$$B_S f''(\xi,0) = \sqrt{\frac{2}{m+1}}\xi^{(1-m)/2} f'(\xi,0) \tag{22a}$$

$$f(\xi,0) = V_s\sqrt{\frac{m+1}{2}}\xi^{(1-m)/2} \tag{22b}$$

$$\theta(\xi,0) = 1.0 \tag{22c}$$

$$f''(\xi,\eta_\delta) = 0 \tag{22d}$$

$$\theta(\xi,\eta_\delta) = 0 \tag{22e}$$

$$\frac{\mathrm{Ja}_l}{\mathrm{Pr}_l}\theta'(\xi,\eta_\delta) = -\frac{2\xi}{m+1}\frac{\partial f(\xi,\eta_\delta)}{\partial\xi} + f(\xi,\eta_\delta) + \left(\frac{2}{m+1}\right)f'\xi\frac{d\eta_\delta}{d\xi} \tag{22f}$$

where

$$V_S = \left(\frac{v_O\rho_l L}{\mu_l}\right)\left(\frac{m+1}{2}\mathrm{Re}\right)^{-1/2} \tag{22g}$$

$$B_S = \frac{\beta_S}{L(\mathrm{Re})^{-1/2}} \tag{22h}$$

The local Nusselt number $\mathrm{Nu}(x)$ is defined as

$$\mathrm{Nu}(x) = \frac{h(x)x}{k_l} = \mathrm{Re}^{1/2}\left(\frac{x}{L}\right)^{(m+1)/2}\sqrt{\frac{m+1}{2}}\theta'(\xi,0) \tag{23}$$

The condensate mass flow rate per unit width at a given x is defined as

$$\Gamma(x) = \mu_l\,\mathrm{Re}^{1/2}\left(\frac{x}{L}\right)^{(m+1)/2}\sqrt{\frac{2}{m+1}}f(\xi,\eta_\delta) \tag{24}$$

3 Numerical Method

The nonsimilar governing equations (20) and (21) are valid when $0<\xi<1.0$ and when $0<\eta<\eta_\delta$. In order to avoid a numerical mesh with variable thickness η_δ (see Fig. 2(*a*)), these equations are transformed from (ξ,η) domain to (S,Z) domain where

$$S = \xi, \quad Z = \frac{\eta}{\eta_\delta} \tag{25}$$

The transformed momentum equation becomes

$$F''' + \eta_\delta f F'' + \frac{2m}{m+1}\left[\left(\frac{\rho_v}{\rho_l}\right)\eta_\delta^3 - \eta_\delta F'^2\right] + \frac{2S^{1-2m}}{m+1}\eta_\delta^3\left(\frac{\mathrm{Gr}_l}{\mathrm{Re}^2}\right) = \frac{2S\eta_\delta}{m+1}\left(F'\frac{\partial F'}{\partial S} - F''\frac{\partial f}{\partial S}\right) \tag{26}$$

where $F' = \partial f/\partial Z$. Define g as $g = F'$. Therefore, Eq. (26) may be written as

$$g'' + \left[\eta_\delta f + \frac{2S\eta_\delta}{(m+1)}\frac{\partial f}{\partial S}\right]g' + \left[\frac{-\eta_\delta 2m}{m+1}g - \frac{2\eta_\delta S}{(m+1)}\frac{\partial g}{\partial S}\right]g = \frac{-2m}{m+1}\left(\frac{\rho_v}{\rho_l}\right)\eta_\delta^3 - \frac{2S^{1-2m}}{m+1}\eta_\delta^3\frac{\mathrm{Gr}_l}{\mathrm{Re}^2} \tag{27}$$

Let the following parameters represent the coefficient g:

$$\pi_1 = 1.0 \tag{28}$$

$$\pi_2 = \left[\eta_\delta f + \frac{2S\eta_\delta}{(m+1)}\frac{\partial f}{\partial S}\right] \tag{29}$$

$$\pi_3 = \left[\frac{\eta_\delta 2m}{m+1}g + \frac{2\eta_\delta S}{(m+1)}\frac{\partial g}{\partial S}\right] \tag{30}$$

$$\pi_4 = \frac{-2m}{m+1}\left(\frac{\rho_v}{\rho_l}\right)\eta_\delta^3 - \frac{2S^{1-2m}}{m+1}\eta_\delta^3\frac{\mathrm{Gr}_l}{\mathrm{Re}^2} \tag{31}$$

Accordingly, Eq. (27) is arranged in the following form:

$$\pi_1 g'' + \pi_2 g' + \pi_3 g = \pi_4 \tag{32}$$

For Eq. (21), let us define

$$\Phi' = \frac{\partial\theta}{\partial Z}, \quad \Phi'' = \frac{\partial^2\theta}{\partial Z^2} \tag{33}$$

Thus, Eq. (21) reduces to

$$\frac{1}{\mathrm{Pr}_l}\Phi'' + \eta_\delta f\Phi' = \frac{2S\eta_\delta}{(m+1)}\left(F'\frac{\partial\theta}{\partial S} - \Phi'\frac{\partial f}{\partial S}\right) \tag{34}$$

Utilizing the variables in Eq. (25), the boundary conditions are reduced as follows:

$$f(S,0) = V_S\sqrt{\frac{m+1}{2}}S^{(1-m)/2} \tag{35a}$$

$$\theta(\xi,0) = 1 \tag{35b}$$

$$\left.\frac{\partial^2 f}{\partial Z^2}\right|_{s,1} = 0 \Rightarrow F''|_{s,0} = 0 \tag{35c}$$

$$\theta|_{s,0} = 0 \tag{35d}$$

Table 1 Comparison between the exact Nusselt number and the Nusselt number obtained from the adopted numerical method

Ja_l	Pr_l Gr_l	Nu_x analytical solution, Eq. (36)	Nu_x present study	Percent difference
0.08	1.35×1000	8.1665	8.14815	0.2247
	1.35×10	2.5825	2.57644	0.2347
0.1	1.35×1000	7.7483	7.72917	0.2469
	1.35×10	2.4502	2.44396	0.2547

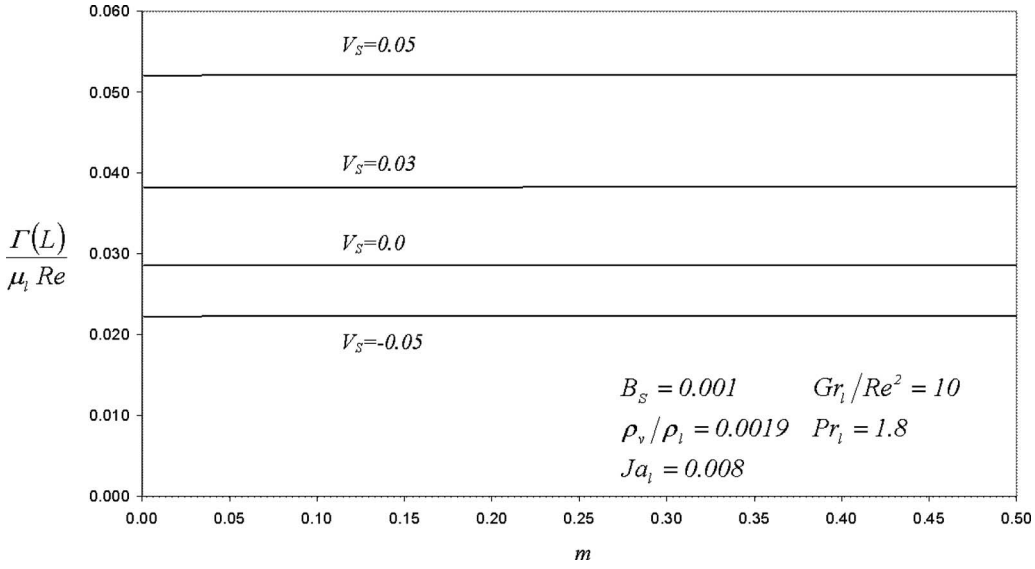

Fig. 3 Effects of m and the dimensionless suction parameter V_S on the dimensionless condensation flow rate Γ at the end of the plate

$$\eta_\delta = -\frac{\frac{\mathrm{Ja}_l}{\mathrm{Pr}_l}\left.\frac{\partial\theta}{\partial Z}\right|_{S,1}}{\left[f|_{S,1} + \frac{2S}{m+1}\left.\frac{\partial f}{\partial S}\right|_{S,1}\right]} \tag{35e}$$

The set of the dimensionless partial differential equations are approximated by finite-difference forms; the grid system shown in Fig. 2(*b*) is used, with the *i*-lines aligned along the *S*-direction and the *j*-lines along the *Z*-direction. For simplicity, uniform grid spacing in ΔS as ΔZ is used. Three point central difference approximation is used to approximate the first and second derivatives at points (i,j) in the *Z*-direction. However, two point backward-difference approximation is used to express the first derivative in the *S*-direction. The resulting equations represent a tridiagonal system of algebraic equations, which can be solved by the Thomas algorithm [30]. The solution procedure is summarized according to the following.

(a) The value of $(\eta_\delta)_{i=1}$ is assumed.
(b) The system of algebraic equations obtained by discretizing Eqs. (24) and (25) along with the boundary conditions except for Eq. (35*e*) is solved simultaneously at $i=1(S=0)$.
(c) The value of $(\eta_\delta)_{i=1}$ is corrected using Eq. (35*e*).
(d) Steps (a)–(c) are repeated until $|[(\eta_\delta)_{i=1}^{\mathrm{new}} - (\eta_\delta)_{i=1}^{\mathrm{old}}]/(\eta_\delta)_{i=1}^{\mathrm{new}}| < 10^{-4}$.
(e) Steps (a)–(d) are repeated for $S=0$ up to $S=1$.

3.1 Validation of the Numerical Results. The exact closed form solution for Nusselt number for the problem of film condensation over a vertical plate subjected to accelerating flow can be reduced to the following form according to Ref. [31], when $m=0$, $V_S=0$, and $B_S=0$:

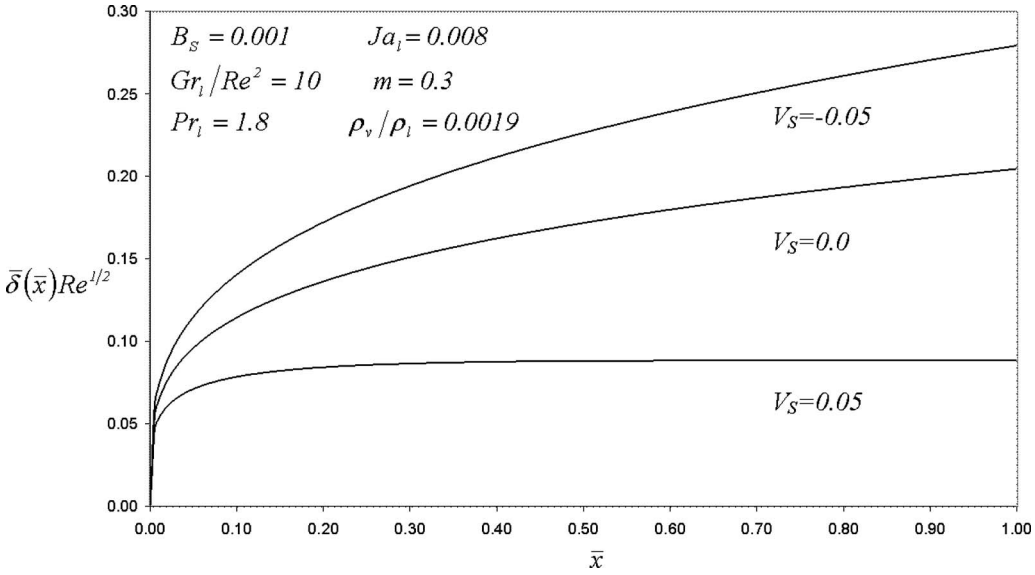

Fig. 4 Effects of $\bar{x}$ and the dimensionless suction parameter V_S on the dimensionless film condensation thickness $\bar{\delta}(\bar{x})$

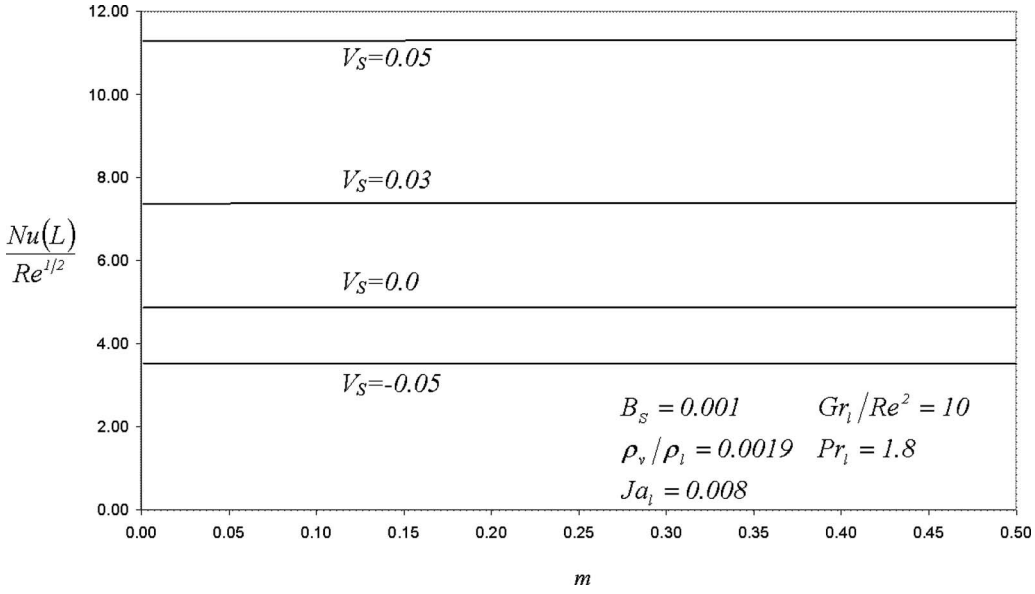

Fig. 5 Effects of m and the dimensionless suction parameter V_S on the Nusselt number Nu at the end of the plate

$$\mathrm{Nu}_x = (4\ \mathrm{Ja}_l)^{-1/4}(1 + 0.68\ \mathrm{Ja}_l)^{1/4}(\mathrm{Gr}_l\ \mathrm{Pr}_l)^{1/4} \tag{36}$$

Table 1 shows comparison between the exact solution and the results of the numerical solution. It is noticed that there is an excellent agreement between both results. This led to good confidence in the used numerical method.

4 Discussion of the Results

4.1 Effect of the Dimensionless Suction Velocity. Figure 3 shows the relationship between the inclination index m and $\Gamma(L)/(\mu_l\ \mathrm{Re})$, at different dimensionless suction parameter V_S when B_S=0.001, $\mathrm{Gr}_l/\mathrm{Re}^2$=10, ρ_v/ρ_l=0.0019, Pr_l=1.8, and Ja_l =0.008. This figure illustrates that the index m has a negligible effect on $\Gamma(L)/(\mu_l\ \mathrm{Re})$ at specific values of V_S. It is also clearly shown that an increase in the values of V_S results in an increase in $\Gamma(L)/(\mu_l\ \mathrm{Re})$. Note that negative values of V_S indicate conditions where the condensate at the plate surface is being blown far away from the plate. This includes situations where some of the liquid water is injected into the condensate film from the plate surface.

Figure 4 shows the relationship between the dimensionless axial distance $\bar{x}$ and $(\bar{\delta}(\bar{x})\mathrm{Re}^{1/2})$ at different dimensionless suction parameter V_S when B_S=0.001, $\mathrm{Gr}_l/\mathrm{Re}^2$=10, ρ_v/ρ_l=0.0019, Pr_l =1.8, and Ja_l=0.008. Note that $\bar{\delta}(\bar{x})$ is the dimensionless thickness of the condensate film along the plate. This figure illustrates that the condensate film thickness increases as $\bar{x}$ increases. It is noticed that the thickness of the condensation film decreases as V_S increases, which consequently result in enhancing the heat transfer as the condensate temperature approaches the wall temperature at a shorter distance. That is why $\mathrm{Nu}(L)/\mathrm{Re}^{1/2}$ increases as V_S increases, as shown in Fig. 5. This figure shows also that the effect of m on $\mathrm{Nu}(L)/\mathrm{Re}^{1/2}$ is negligible. The reason behind this negli-

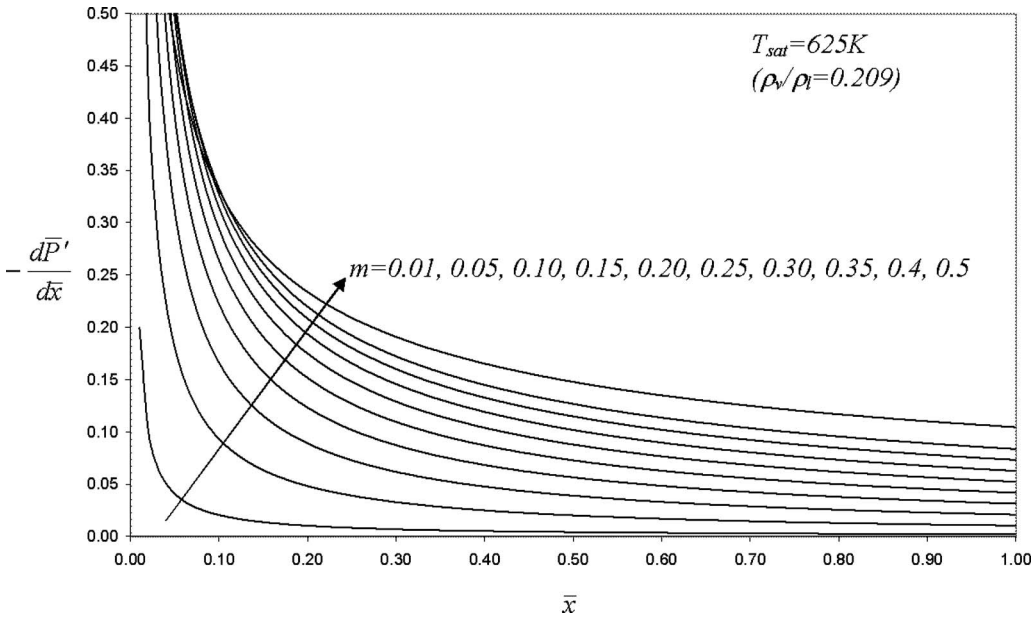

Fig. 6 Effect of m on the dimensionless freestream longitudinal pressure gradient

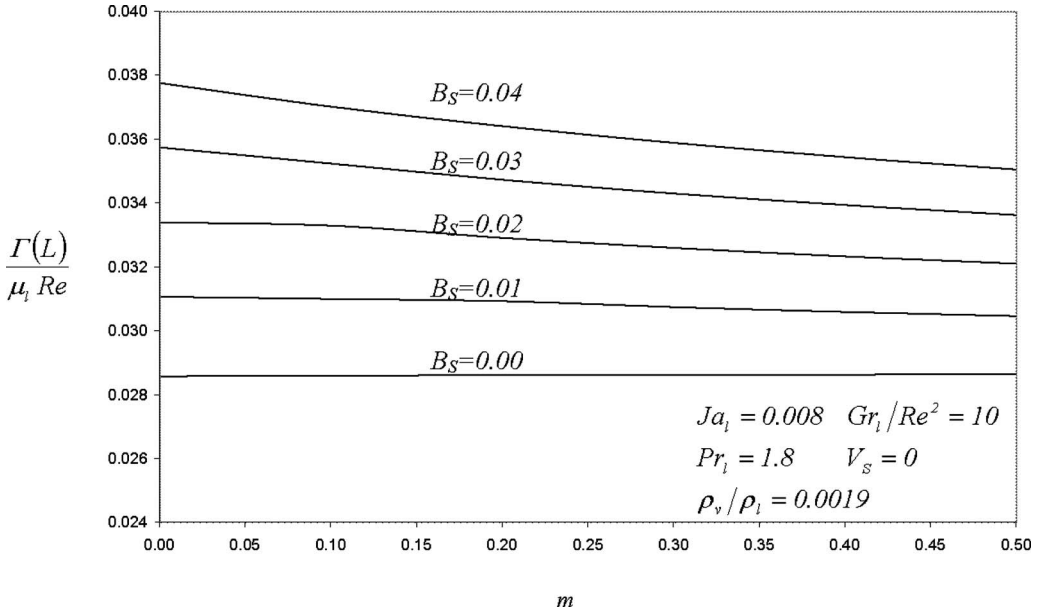

Fig. 7 Effects of m and the slip coefficient parameter B_S on the dimensionless condensation flow rate Γ at the end of the plate

gible effect of the index m can be shown in Fig. 6, where the dimensionless dynamic pressure gradient is negligible as compared with the selected value of $\mathrm{Gr}_l/\mathrm{Re}^2$.

4.2 Effect of the Condensate Slip at Plate. Figure 7 illustrates the relationship between the index m and $\Gamma(L)/(\mu_l\ \mathrm{Re})$ at different values of the slip parameter when $V_S=0$, $\mathrm{Gr}_l/\mathrm{Re}^2=10$, $\rho_v/\rho_l=0.0019$, $\mathrm{Pr}_l=1.8$, and $\mathrm{Ja}_l=0.008$. This figure illustrates that the index m has a negligible effect on $\Gamma(L)/(\mu_l\ \mathrm{Re})$ at lower values of B_S. As the value of B_S increases, $\Gamma(L)/(\mu_l\ \mathrm{Re})$ starts to decrease apparently as the m increases. This is due to the fact that for large slip coefficient, the condensate inertia effects become more apparent and its speed will approach the value $(\rho_v/\rho_l)u_\infty$ as B_S approaches infinity. Note that u_∞ decreases as m increases before x reaches the value L. It is also concluded from this figure that the condensation rate increases as B_S increases. The thickness of the condensation film is expected to decrease as B_S increases, which enhances the heat transfer due to the fact that the condensate temperature approaches the wall temperature at a shorter distance. That is why $\mathrm{Nu}(L)/\mathrm{Re}^{1/2}$ increases as B_S increases, as shown in Fig. 8.

4.3 Effect of Grashof Number. Figure 9 illustrates the relationship between the index m and $\Gamma(L)/(\mu_l\ \mathrm{Re})$ for different values of $\mathrm{Gr}_l/\mathrm{Re}^2$ $(\mathrm{Gr}_l/\mathrm{Re}^2=0.1,1,10)$ when $V_S=0$, $B_S=0.001$, $\rho_v/\rho_l=0.0019$, $\mathrm{Pr}_l=1.8$, and $\mathrm{Ja}_l=0.008$. This figure illustrates that the index m has negligible effect on $\Gamma(L)/(\mu_l\ \mathrm{Re})$ as the dimensionless dynamic pressure is negligible compared with the values of $\mathrm{Gr}_l/\mathrm{Re}^2$ (as seen from Fig. 6). In addition, it is noticed that the dimensionless condensation rate parameter $\Gamma(L)/(\mu_l\ \mathrm{Re})$ in-

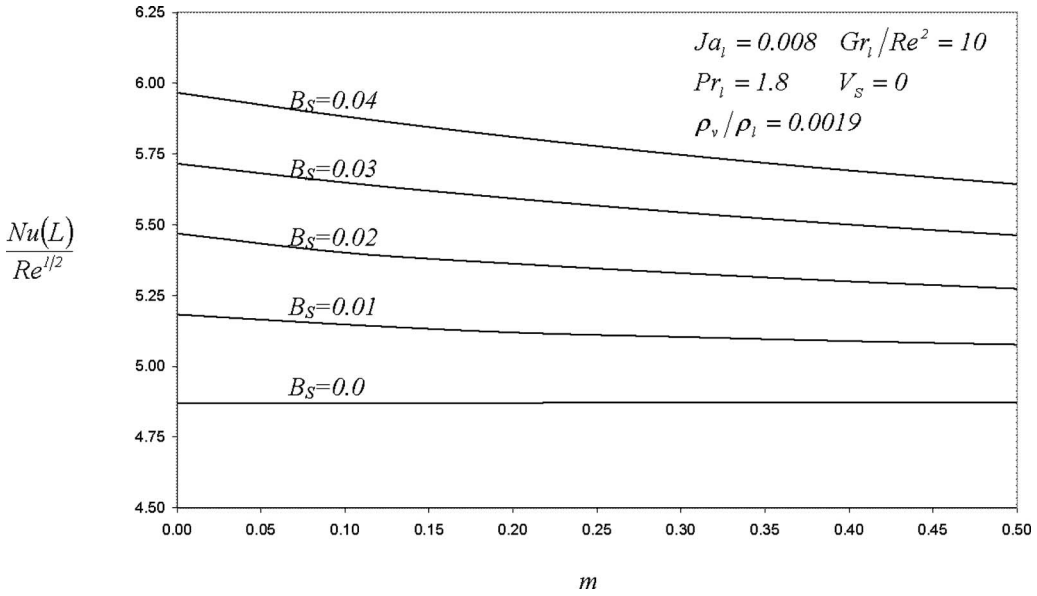

Fig. 8 Effects of m and the slip coefficient parameter B_S on the Nusselt number Nu at the end of the plate

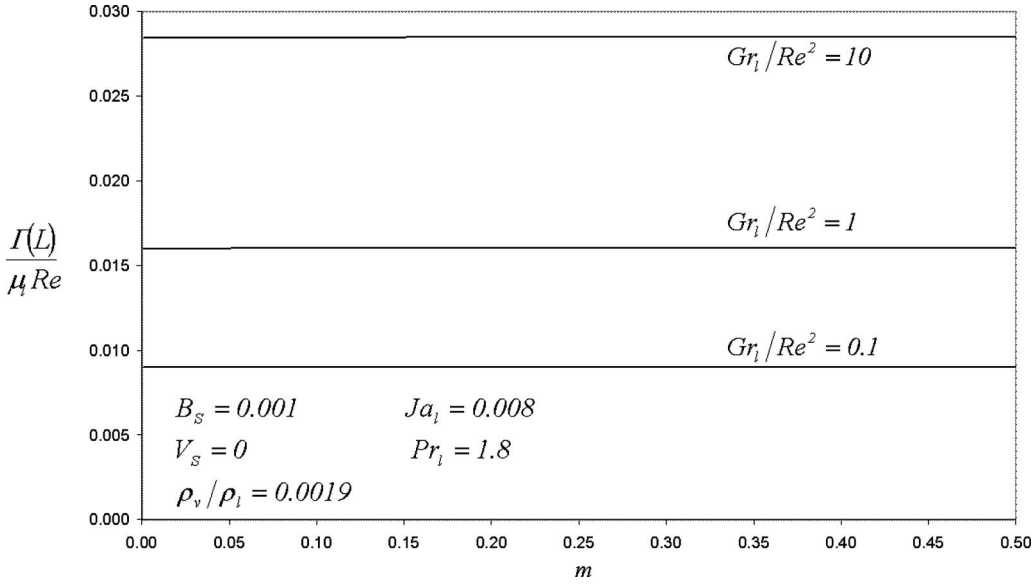

Fig. 9 Effects of *m* and the Grashof number Gr_l on the dimensionless condensation flow rate Γ at the end of the plate

creases as the value of Gr_l/Re^2 increases. The values of $Nu(L)/Re^{1/2}$ can be obtained from correlation (36) as *m*-effects are negligible for the selected range of Gr_l/Re^2.

4.4 Effect of Varying the Saturation Temperature. Figure 10 illustrates the relationship between the index *m* and for different values of pure water saturation temperature (T_{sat}) when $V_S=0$, $Gr_l/Re^2=0$, $B_S=0$, and $T_{sat}-T_w=4.28$ K. The Grashof number is set to zero to situations involving high Reynolds number or, most appropriately, the situations plate is horizontal having favorable pressure gradients. When the vapor stream velocity is very large, the value of Gr_l/Re^2 is very small and it approaches zero as u_∞ approaches infinity. For the previous cases, the driving force for the condensate flow rate is the pressure gradient in the vapor flow, which is proportional to *m*, ρ_v/ρ_l, and $u_\infty(L)$. This figure illustrates that the index *m* has a clear influence on $\Gamma(L)/(\mu_l\ \mathrm{Re})$ especially when $m \leq 0.15$. This finding is ascribed to the fact that the longitudinal pressure gradient increases at larger gradients as the index *m* increases (when $m<0.15$), as can be seen from Fig. 6. Moreover, as the value of T_{sat} increases, the dimensionless condensation parameter $\Gamma(L)/(\mu_l\ \mathrm{Re})$ increases at a given value of *m*.

Figure 11 illustrates the relationship between *m* and $Nu(L)/Re^{1/2}$ for different values of T_{sat} when $V_S=0$, $Gr/Re^2=0$, $B_S=0$, and $T_{sat}-T_w=4.28$ K. This figure illustrates that as either *m* or T_{sat} increases, the value of $Nu(L)/Re^{1/2}$ increases.

4.5 Design Correlations. The numerical plots shown in Figs. 10 and 11 can be presented by the following correlations:

$$\frac{\Gamma(L)}{\mu_l\ \mathrm{Re}} = 0.943[1+0.33(1-2m)^{1.25}]\sqrt[4]{\left(\frac{\mathrm{Ja}_l}{\mathrm{Pr}_l}\right)^3\left(\frac{\rho_v}{\rho_l}\right)m} \quad (37)$$

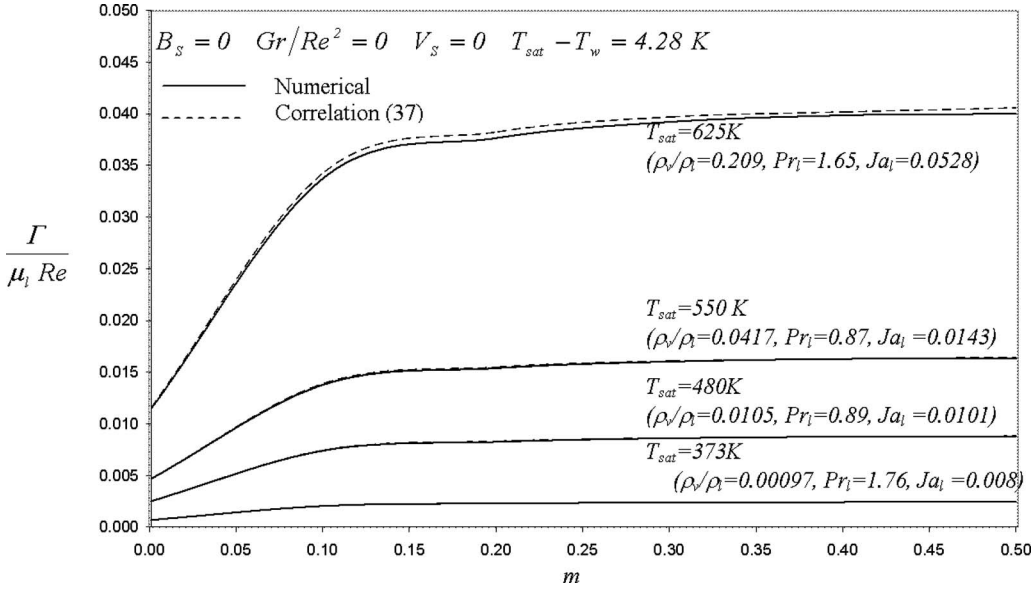

Fig. 10 Effects of the saturated temperature T_{sat} on the dimensionless condensation flow rate Γ at the end of the plate

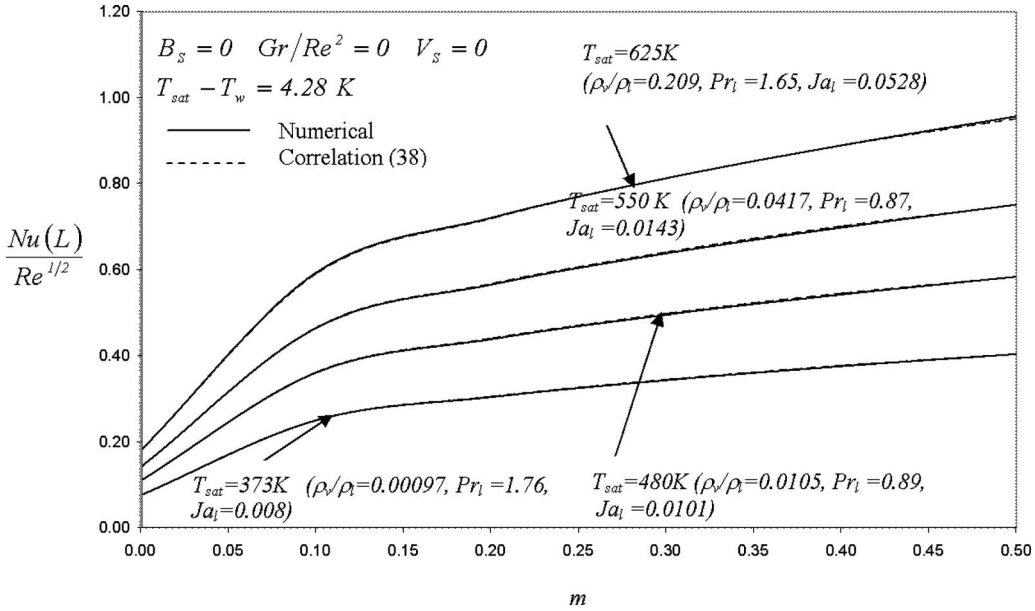

Fig. 11 Effects of the saturated temperature T_{sat} on the Nusselt number Nu at the end of the plate

$$\frac{\mathrm{Nu}(L)}{\mathrm{Re}^{1/2}} = [1 - 0.095(1-2m)^{1.25}]\sqrt[4]{\left(\frac{\mathrm{Pr_l}}{\mathrm{Ja}_l}\right)\left(\frac{\rho_v}{\rho_l}\right)m} \qquad (38)$$

The maximum error between the obtained results and the correlations is found to be around 8.0%. The plots of the correlations (37) and (38) are added to Figs. 10 and 11.

5 Conclusions

The problem of laminar falling film condensation over a vertical plate with accelerating vapor flow conditions was studied. The free vapor stream is considered to have a specific striking angle relative to the vertical plate. The effect of varying the inclination angle on the heat transfer rate and condensation rate was investigated. Additional effects were also considered in this work such as the presence of condensate suction or slip effects at the cold plate surface. The condensate film flow was assumed to be laminar and having constant properties. The vapor was assumed to have a uniform saturation temperature and assumed to be homogenous. Moreover, the shear stress on the vapor liquid interface was neglected. The governing partial differential equations for the analyzed problem were derived. The equations were nondimensionalized and transformed using nonsimilarity transformation. The transformed equations were solved using a numerical implicit, iterative, and finite-difference method.

It was found that the vapor stream striking angle on the plate has no effect on the condensation rate or heat transfer rate except when apparent slip condition is present and at $\mathrm{Gr}_l/\mathrm{Re}^2$ values comparable with the dimensionless condensate dynamic pressure gradient. It was also shown that an increase in the dimensionless suction parameter (V_S) results in an increase in the dimensionless condensation rate $\Gamma(L)/(\mu_l\ \mathrm{Re})$ and Nusselt number $\mathrm{Nu}(L)/\mathrm{Re}^{1/2}$. In addition, it was found that the condensation rate and the heat transfer rate increase as Grashof number, Jakob number, slip parameter, and saturation temperature increase. Finally, the model developed, as well as the results obtained of this work, not only enrich the literature of condensation but also provide additional solutions for saving thermal energy.

Nomenclature

c_p = specific heat
B_S = dimensionless slip number
g = gravitational acceleration
Gr_l = Grashof number
h_{fg} = latent heat of evaporation
Ja_l = liquid Jakob number
k_l = liquid thermal conductivity
L = length of the plate
m = inclination index
P' = dynamic pressure
Pr_l = liquid Prandtl number
Re = Reynolds number
T_{sat} = saturation temperature
T_w = wall temperature
u_∞ = freestream velocity of the surrounding vapor
u = condensate velocity component along the x-axis
v = velocity component along the y-axis
V_S = dimensionless suction velocity number

Symbols

β = twice the freestream inclination angle
β_s = slip coefficient
Γ = mass flow rate per unit width
δ = condensate film thickness
η = similarity parameter
θ = dimensionless temperature
μ_l = condensate dynamic viscosity
ξ = coordinate transformation for x
ρ_l = condensate density
ρ_v = vapor density

References

[1] Nusselt, W., 1916, "Die Oberflächenkondensation des Wasserdampfes," Z. Ver. Dtsch. Ing., **60**, pp. 541–569.
[2] Bromley, L. A., 1952, "Heat Transfer in Condensation—Effect of Heat Capacity Condensate," Ind. Eng. Chem., **44**, pp. 2966–2969.
[3] Rohsenow, W. M., 1956, "Heat Transfer and Temperature Distribution in Laminar-Film Condensation," Trans. ASME, **78**, pp. 1645–1648.
[4] Sparrow, E. M., and Gregg, J. L., 1959, "A Boundary-Layer Treatment of Laminar-Film Condensation," ASME J. Heat Transfer, **81**, pp. 13–18.
[5] Yang, S., 1957, "Heat Transfer Theory of Film Condensation of Saturated Vapor at Rest," Chin. J. Mech. Eng., **5**, pp. 41–53.
[6] Mabuchi, I., 1960, "Heat Transfer by Film Condensation," Trans. Jpn. Soc. Mech. Eng., **26**, pp. 1134–1138.
[7] Koh, J. C. Y., Sparrow, E. M., and Hartnett, J. P., 1961, "The Two-Phase Boundary Layer in Laminar Film Condensation," Int. J. Heat Mass Transfer, **2**, pp. 69–82.

[8] Koh, J. C. Y., 1961, "An Integral Treatment of Two-Phase Boundary Layer in Film Condensation," Trans. ASME, Ser. C: J. Heat Transfer, **83**, pp. 359–361.
[9] Chen, M. M., 1961, "An Analytical Study of Laminar Film Condensation Part I—Flat Plates," ASME J. Heat Transfer, **83**, pp. 48–54.
[10] Stender, W., 1925, "Heat Transmission During Condensation of Superheated Steam," Z. Ver. Dtsch. Ing., **69**, pp. 905–909.
[11] Silver, R. S., 1946, "Heat Transfer Coefficients in Surface Condensers," Engineering (London), **161**, pp. 505–507.
[12] Sukhatme, S. P., and Rohsenow, W. M., 1964, "Heat Transfer During Film Condensation of a Liquid Metal Vapor," Sc.D. thesis, Massachusetts Institute of Technology, Cambridge, MA.
[13] Silver, R. S., and Simpson, H. C., 1961, "The Condensation of Superheated Steam," *Proceedings of a Conference Held at the National Engineering Laboratory*, East Kilbride, Glasgow, pp. 14–15.
[14] Sparrow, M. E., and Eckert, E. R. G., 1961, "Effects of Superheated Vapor and Noncondensable Gases on Laminar Film Condensation," AIChE J., **7**, pp. 373–477.
[15] Chisholm, D., 1961, "A Survey of the Condensation of Superheated Steam," *Proceedings of a Conference Held at the National Engineering Laboratory*, East Kilbride, Glasgow, pp. 14–15.
[16] Sparrow, E. M., and Lin, S. H., 1964, "Condensation Heat Transfer in the Presence of a Noncondensable Gas," Trans. ASME, Ser. C: J. Heat Transfer, **86**, pp. 430–436.
[17] Dhir, V. K., and Lienhard, J. H., 1971, "Laminar Film Condensation on Plane and Axisymmetric Bodies in Non-Uniform Gravity," ASME J. Heat Transfer, **93**, pp. 97–100.
[18] Lienhard, J. H., 1987, *Heat Transfer Textbook*, 2nd ed., Prentice-Hall, Englewood Cliffs, pp. 400–402.
[19] Shekriladze, I. G., and Gomelauri, V. I., 1966, "Theoretical Study of Laminar Film Condensation of Flowing Vapor," Int. J. Heat Mass Transfer, **9**, pp. 581–591.
[20] Mosaad, M., 2001, "Mixed Convection Laminar Film Condensation on an Inclined Tube," ASME J. Heat Transfer, **123**, pp. 294–300.
[21] Memory, S. B., Adams, V. H., and Marto, P. J., 1997, "Free Forced Convection Laminar Film Condensation on Horizontal Elliptical Tubes," Int. J. Heat Mass Transfer, **40**, pp. 3395–3406.
[22] Yang, S., and Hus, C., 1997, "Mixed Convection Laminar Film Condensation on a Horizontal Elliptical Tube With Uniform Surface Heat Flux," Numer. Heat Transfer, Part A, **32**, pp. 85–95.
[23] Phan, L., Wang, X., and Narain, A., 2006, "Exit Condition, Gravity, and Surface-Tension Effects on Stability and Noise-Sensitivity Issues for Steady Condensing Flows Inside Tubes and Channels," Int. J. Heat Mass Transfer, **49**, pp. 2058–2076.
[24] Narain, A., Kurita, J. H., Kivisalu, M., Kulkarni, S. D., Siemionko, A., Ng, T. W., Kim, N., and Phan, L., 2007, "Internal Condensing Flows Inside a Vertical Pipe—Experimental/Computational Investigations of the Effects of Specified and Unspecified (Free) Conditions at Exit," ASME J. Heat Transfer, **129**, pp. 1352–1372.
[25] Phan, L., and Narain, A., 2007, "Non-Linear Stability of the Classical Nusselt Problem of Film Condensation and Wave-Effects," ASME J. Appl. Mech., **74**, pp. 279–290.
[26] Narain, A., Liang, O., Yu, G., and Wang, X., 2004, "Direct Computational Simulations for Internal Condensing Flows and Results on Attainability/Stability of Steady Solutions, Their Intrinsic Waviness, and Their Noise-Sensitivity," ASME J. Appl. Mech., **71**, pp. 69–88.
[27] Liang, O., Wang, X., and Narian, A., 2004, "Effect of Gravity, Shear and Surface Tension in Internal Condensation Flows—Results From Direct Computational Simulations," ASME J. Heat Transfer, **126**, pp. 676–686.
[28] Bejan, A., 1995, *Convection Heat Transfer*, 2nd ed., Wiley, New York, p. 405.
[29] Navier C. L. M. H., 1823, "Royale des Sciences de I'Institut de France," Mem. Acad. Sci. Inst. Fr., **1**, pp. 414–416.
[30] Blottner, F. G., 1970, "Finite-Difference Methods of Solution of the Boundary-Layer Equations," AIAA J., **8**, pp. 193–205.
[31] Oosthuizen, P. H., and Naylor, D., 1999, *Introduction to Convective Heat Transfer Analysis*, McGraw-Hill, New York, pp. 109–110.

Equation-Free/Galerkin-Free Reduced-Order Modeling of the Shallow Water Equations Based on Proper Orthogonal Decomposition

Vahid Esfahanian
Department of Mechanical Engineering,
University of Tehran,
North Kargar Avenue,
Tehran 11365-4565, Iran
e-mail: evahid@ut.ac.ir

Khosro Ashrafi[1]
Faculty of Environment,
University of Tehran,
Enghelab Avenue,
Tehran 14155-6135, Iran
e-mail: khashrafi@ut.ac.ir

In this paper, two categories of reduced-order modeling (ROM) of the shallow water equations (SWEs) based on the proper orthogonal decomposition (POD) are presented. First, the traditional Galerkin-projection POD/ROM is applied to the one-dimensional (1D) SWEs. The result indicates that although the Galerkin-projection POD/ROM is suitable for describing the physical properties of flows (during the POD basis functions' construction time), it cannot predict that the dynamics of the shallow water flows properly as it was expected, especially with complex initial conditions. Then, the study is extended to applying the equation-free/Galerkin-free POD/ROM to both 1D and 2D SWEs. In the equation-free/Galerkin-free framework, the numerical simulation switches between a fine-scale model, which provides data for construction of the POD basis functions, and a coarse-scale model, which is designed for the coarse-grained computational study of complex, multiscale problems like SWEs. In the present work, the Beam & Warming and semi-implicit time integration schemes are applied to the 1D and 2D SWEs, respectively, as fine-scale models and the coefficients of a few POD basis functions (reduced-order model) are considered as a coarse-scale model. Projective integration is applied to the coarse-scale model in an equation-free framework with a time step grater than the one used for a fine-scale model. It is demonstrated that equation-free/Galerkin-free POD/ROM can resolve the dynamics of the complex shallow water flows. Moreover, the computational cost of the approach is less than the one for a fine-scale model.
[DOI: 10.1115/1.3153368]

Keywords: shallow water equations (SWEs), equation-free/Galerkin-free, proper orthogonal decomposition (POD), Galerkin-projection, projective integration

1 Introduction

The proper orthogonal decomposition (POD) method is a model reduction technique for complex nonlinear problems. The need for faster numerical weather forecast motivates us to apply the POD approach in the field of meteorology. However, such an approach has become promising in other fields recently [1]. Since the shallow water equations (SWEs) are the first prototype for developing and testing numerical algorithms and often used by atmospheric modelers, this prototype is chosen to verify the reduced-order modeling (ROM) based on the POD basis functions.

In the use of the POD basis functions it is valuable to note that the selection of the POD basis functions is not just appropriate, but optimal, in a sense to be described in Sec. 3. In the POD method, analytical, empirical, or numerical data are correlated together to construct the POD basis functions. These POD basis functions are orthogonal and the best linear combination of data. The POD method was first proposed by Karhunen [2] and Loeve [3] independently; for this reason sometimes the POD basis functions are known as the Karhunen–Loeve (KL) expansion. In the field of fluid mechanics, utilizing the POD basis functions to study the turbulent flow was pioneered by Lumley [4]. Sirovich [5] who incorporated the snapshot method to the POD framework made the most progress in the POD method.

For ROM using the POD basis functions, Galerkin-projection is a common implementation method. It uses the POD basis as projection functions to convert original partial differential equations (PDEs) to a small set of nonlinear ordinary differential equations (ODEs) [6]. Galerkin-projection POD/ROM method has been used in the field of fluid mechanics to simulate incompressible and compressible flows for different purposes [7–9,1]. In the field of meteorology, the low-order atmospheric models are applied for long range prediction of climate [10–12], in which the data of a general circulation model or observation data are used to construct the POD basis functions. However, in the present study, the data used to obtain the reduced-order model are generated using numerical simulation of the governing equations, i.e., SWEs.

The equation-free/Galerkin-free method was proposed by Sirisup et al. [13] to simulate the incompressible flows. Equation-free [14–16] and projective integration [17–19] frameworks are employed in this technique. The equation-free framework is designed for the efficient coarse-grained computational study of complex, multiscale problems. This computational study has two levels: In the first level, a fine-scale model is employed to provide short-time numerical data, and in the second level, the numerical data obtained from the first level are used to estimate quantities for the coarse-grained system behavior [15,16]. Thus, coarse-scale model is estimated by acting on the data of fine-scale model directly and it is called equation-free. This framework has been applied to

[1]Corresponding author.

Contributed by the Fluids Engineering Division of ASME for publication in the JOURNAL OF FLUIDS ENGINEERING. Manuscript received March 1, 2008; final manuscript received April 16, 2009; published online June 23, 2009. Assoc. Editor: Dimitris Drikakis.

many fields, ranging from bifurcation analysis of complex systems to homogenization of random media [17,20,16,21–23].

In this context, two categories of the POD/ROM including traditional Galerkin-projection and equation-free/Galerkin-free POD/ROM are applied to the SWEs in order to decrease the degrees of freedom associated with discretized SWEs. Applying the Galerkin-projection POD/ROM to the one-dimensional (1D) SWEs shows the ability and disability of the approach for predicting the dynamics of shallow water flows. As it will be shown, the traditional Galerkin-projection POD/ROM cannot resolve the dynamics of complex flow as it was expected. However, this method can be used to describe the physics of flow field. Therefore, as an alternative method, the equation-free/Galerkin-free POD/ROM of the 1D and 2D SWEs are performed. This has been achieved by dividing a global time step into two substeps. In the first substep, the Beam & Warming and semi-implicit numerical time integration schemes are applied to the 1D and 2D SWEs, respectively, as fine-scale models to provide numerical data to construct the POD basis functions. In the second substep, the dependent variables are expanded in terms of the POD basis functions and coefficients of the POD basis functions make the coarse-scale model. The coarse-scale equations can be integrated with a larger time step than the original Beam & Warming and semi-implicit fine-scale models. Subsequently, the dependent variables are computed using the POD basis functions and their coefficients. This time marching algorithm is continued for the required time period.

The paper is organized as follows. The 1D and 2D SWEs and their computational formulation as fine-scale models are discussed in Sec. 2. In Sec. 3, the POD method is presented. The Galerkin-projection POD/ROM of the 1D SWEs and its numerical results are presented in Sec. 4. In Sec. 5, the equation-free/Galerkin-free POD/ROM method and the numerical results are discussed. Finally, in Sec. 6, the paper is concluded with some keynotes and summary results.

2 Fine-Scale Models of the 1D and 2D SWEs

The SWEs are the basic equations in the atmospheric, oceanic, and river flows. These equations involve the gravity waves and in a rotating frame (e.g., Earth) they also contain the Rossby waves.

2.1 The 1D Case. In the 1D case, the rotation of the coordinates is neglected; hence the primitive 1D SWEs are [24]

$$\frac{\partial h}{\partial t} + u\frac{\partial h}{\partial x} + h\frac{\partial u}{\partial x} = 0 \tag{1}$$

$$\frac{\partial u}{\partial t} + u\frac{\partial u}{\partial x} + g\frac{\partial h}{\partial x} = 0 \tag{2}$$

where h is the fluid height, u is the fluid velocity, and g is the gravitational acceleration. Equations (1) and (2) can be rewritten in the vector form as

$$\frac{\partial \mathbf{U}}{\partial t} = f(t, \mathbf{U}(x,t)) \tag{3}$$

where $\mathbf{U}$ is the vector field of the height and velocity.

The Beam & Warming numerical scheme is applied to the 1D SWEs as a fine-scale model to generate numerical data in fine scale. The spatial discretization is sufficiently fine to guarantee resolution-independent solution. Such a method defines a discrete version of equations, which are

$$\mathbf{U}(x,t^{n+1}) = \mathbf{U}(x,t^n) + \delta t\tilde{f}(t^n, \delta t, \Delta x, \mathbf{U}^n, \mathbf{U}^{n+1}, \ldots) \tag{4}$$

where δt and Δx are the time step size and the spatial grid size, respectively, $t^n = n\delta t$ and $\tilde{f}$ is the numerical approximation of f. The consistency of the discrete scheme requires that

$$\lim_{\delta t, \Delta x \to 0} \tilde{f}(t^n, \delta t, \Delta x, \mathbf{U}^n, \mathbf{U}^{n+1}, \ldots) = f(t^n, \mathbf{U}^n) \tag{5}$$

Also, the local truncation error of the Beam & Warming scheme is order of $O(\delta t^2, \Delta x^2)$. The details of the Beam & Warming method are not given here, but one can refer to Beam & Warming's paper [25].

2.2 The 2D Case. The 2D rotating SWEs in f-plane, which are the 2D model of the atmosphere, still retain the important dynamic interactions of the atmosphere and are written as [26]

$$\frac{\partial u}{\partial t} + u\frac{\partial u}{\partial x} + v\frac{\partial u}{\partial y} + g\frac{\partial h}{\partial x} - f_0 v = 0 \tag{6}$$

$$\frac{\partial v}{\partial t} + u\frac{\partial v}{\partial x} + v\frac{\partial v}{\partial y} + g\frac{\partial h}{\partial y} + f_0 u = 0 \tag{7}$$

$$\frac{\partial h}{\partial t} + u\frac{\partial h}{\partial x} + v\frac{\partial h}{\partial y} + h\left(\frac{\partial u}{\partial x} + \frac{\partial v}{\partial y}\right) = 0 \tag{8}$$

where u and v are the components of the horizontal wind in the x and y directions, respectively, h is the layer depth variation, f_0 denotes the Coriolis parameter, and g is the gravitational acceleration. The momentum forms (6)–(8) have the disadvantage that the components of the velocity are not true scalars (their values depend on the coordinate system chosen). Thus, Heikes and Randall [27] and others advocate using vorticity and divergence instead. To do so, we introduce the vorticity ξ, divergence δ, stream function ψ, and velocity potential χ satisfying

$$\xi = \frac{\partial v}{\partial x} - \frac{\partial u}{\partial y}, \quad \delta = \frac{\partial u}{\partial x} + \frac{\partial v}{\partial y}, \quad \nabla^2\psi = \xi, \quad \nabla^2\chi = \delta$$

Bypassing some manipulation the vorticity and divergence equations become

$$\frac{\partial \zeta}{\partial t} = -\nabla(\zeta\nabla\chi) + J(\zeta,\psi) \tag{9}$$

$$\frac{\partial \delta}{\partial t} + c_0\nabla^2\eta = \nabla\cdot(\zeta\nabla\psi) + J(\zeta,\chi) - \nabla^2 K \tag{10}$$

$$\frac{\partial \eta}{\partial t} + \nabla^2\chi = -\nabla\cdot(\eta\nabla\chi) + J(\eta,\psi) \tag{11}$$

where

$$\zeta = \xi + f_0, \quad J(\alpha,\beta) = \frac{\partial\alpha}{\partial x}\frac{\partial\beta}{\partial y} - \frac{\partial\alpha}{\partial y}\frac{\partial\beta}{\partial x}, \quad c_0 = gH_0$$

$$\eta = \frac{h}{H_0} - 1, \quad K = \frac{1}{2}(\mathbf{u}\cdot\mathbf{u}), \quad \mathbf{u} = (u,v)$$

in which H_0 is the mean layer depth. The hyper diffusion term must be added to the right hand side of Eq. (9) as $-\nu(-\nabla^2)^l\zeta$ in order to guarantee the numerical stability [28]. In this paper, $l=2$ and ν is defined as

$$\nu = \frac{C(H_0 Q)}{k_{\max}^{2l}} \tag{12}$$

in which C is a dimensionless constant, $k_{\max} = n_g/2$ denotes the highest resolved wavenumber where n_g is the grid size, and Q is defined by

$$Q = \max_{x,y}\left|q - \frac{f_0}{H_0}\right| \tag{13}$$

where q is the potential vorticity that plays an important role in geophysical fluid dynamics and is defined by

$$q = \frac{\xi + f_0}{h} = \frac{\zeta}{h} \tag{14}$$

The value of ν defined by Eq. (12) efficiently dissipates the smallest features, i.e., those comparable to the grid scale. In order to compute solutions as free of dissipation as possible, the value of C must be chosen as small as possible without producing small-scale noise. We have used $C=1$ for this purpose.

Semi-implicit discretization of Eqs. (9)–(11) and using the relation between χ and δ ($\delta=\nabla^2\chi$) and bypassing some manipulation, equations for numerical simulation are obtained as [28]

$$\xi^{n+1} = Z^n \tag{15}$$

$$\nabla^2 \eta^{n+1} + \alpha \eta^{n+1} = G^n \tag{16}$$

$$\delta^{n+1} + \Delta t c_0 \nabla^2 \eta^{n+1} = D^n \tag{17}$$

where n denotes the time level and

$$Z^n = \Delta t[-\nabla \cdot (\zeta \nabla \chi) + J(\zeta, \psi) - \nu(\nabla^4 \zeta)]^n + \xi^n \tag{18}$$

$$D^n = \Delta t[\nabla \cdot (\zeta \nabla \psi) + J(\zeta, \chi) - \nabla^2 K]^n + \delta^n \tag{19}$$

$$F^n = \Delta t[-\nabla \cdot (\eta \nabla \chi) + J(\eta, \psi)]^n + \eta^n \tag{20}$$

$$G^n = \alpha(F^n - \Delta t D^n), \quad \alpha = -\frac{1}{\Delta t^2 c_0} \tag{21}$$

subsequently the numerical algorithm of the 2D SWEs' simulation has the following steps:

1. calculating Z^n, D^n, F^n, and G^n from Eqs. (18)–(21), respectively
2. calculating ξ^{n+1} from Eq. (15)
3. solving Helmholtz equation for η^{n+1} (Eq. (16))
4. calculating δ^{n+1} from Eq. (17)

3 The POD Method

The POD basis mode is a function such as $\mathbf{\Phi}$ that can express the structure of an ensemble of vector field, i.e.,

$$\varphi = \{\mathbf{U}^{(i)}: \quad 1 \le i \le N\} \tag{22}$$

where $\mathbf{U}$ is the vector field of the dependent variables (h and u in the 1D case and ξ, η, and δ in the 2D case), and the ith record (i=time level) is denoted by $\mathbf{U}^i(\mathbf{x})$ ($\mathbf{x}=(x,y)$) and N is the number of the snapshots. For example, in the time marching problems, i denotes the time level in which the snapshots are recorded. In order to obtain the basis function, the ensemble of the vector field is projected onto the function $\mathbf{\Phi}$. This can be implemented by defining the inner product as

$$(\mathbf{f}, \mathbf{g}) = \int_\Omega \mathbf{f}(\mathbf{x})\mathbf{g}(\mathbf{x})d\mathbf{x} \tag{23}$$

where Ω is the flow region and $\mathbf{f}$ and $\mathbf{g}$ are the arbitrary functions. Using the definition in Eq. (23) the projection of the vector field onto a basis function is shown as $(\mathbf{U}^{(i)}, \mathbf{\Phi})$. The basis function $\mathbf{\Phi}$ must be as nearly parallel to the ensemble of the vector field as possible. For this purpose, the defined inner product must be maximized, and it should be normalized to remove the amplitude of the inner product. This has been shown in detail in Ref. [7], and we have

$$R\mathbf{\Phi} = \lambda \mathbf{\Phi} \tag{24}$$

where

$$R\mathbf{\Phi} = \frac{1}{N}\sum_{i=1}^{N} \int_\Omega \mathbf{U}^{(i)}(\mathbf{x})\mathbf{U}^{(i)}(\mathbf{x}')\mathbf{\Phi}(\mathbf{x}')d\mathbf{x}' \tag{25}$$

and λ is the Lagrange multiplier in the optimization problem and it is an eigenvalue of the system.

In order to obtain the desired function $\mathbf{\Phi}$, we assume that it can be expressed in terms of the members of ensemble φ given in Eq. (22), i.e.,

$$\mathbf{\Phi} = \sum_{i=1}^{N} w_i \mathbf{U}^{(i)} \tag{26}$$

Since $\mathbf{U}^{(i)}$s are linearly independent, if Eqs. (25) and (26) are introduced into Eq. (24) and after bypassing some manipulations, we reach

$$\mathbf{CW} = \Lambda \mathbf{W} \tag{27}$$

where $\Lambda = \mathrm{diag}[\lambda_1, \lambda_2, \ldots, \lambda_N]$ and

$$C_{i,j} = \frac{1}{N}\int_\Omega \mathbf{U}^{(i)}(\mathbf{x})\mathbf{U}^{(j)}(\mathbf{x})d\mathbf{x} \quad \text{and} \quad \mathbf{W} = [\mathbf{w}_1, \mathbf{w}_2, \ldots, \mathbf{w}_N] \tag{28}$$

where i and j refer to the ith and jth records (snapshots). In Eq. (27), $\mathbf{C}$ is a non-negative Hermitian matrix, which is called the correlation matrix. The eigenvectors correspond to eigenvalues, $\lambda_1 \ge \lambda_2 \ge \cdots \ge \lambda_N \ge 0$, respectively. Now the basis functions can be written as

$$\mathbf{\Phi}_1 = \sum_{i=1}^{N} w_i^1 \mathbf{U}^{(i)}, \quad \mathbf{\Phi}_2 = \sum_{i=1}^{N} w_i^2 \mathbf{U}^{(i)}, \quad \ldots, \mathbf{\Phi}_N = \sum_{i=1}^{N} w_i^N \mathbf{U}^{(i)} \tag{29}$$

The eigenvector matrix $\mathbf{W}$ must be normalized in such a way that the basis function matrix $\mathbf{\Phi}$ satisfies the following relation:

$$(\mathbf{\Phi}_l, \mathbf{\Phi}_m) = \begin{cases} 1, & l = m \\ 0, & l \ne m \end{cases} \tag{30}$$

For Eq. (30) to be true, the eigenvector $\mathbf{w}_l$ must satisfy the following equation:

$$\langle \mathbf{w}_l, \mathbf{w}_l \rangle = \sum_{i=1}^{N} w_i^l w_i^l = \frac{1}{N\lambda_l} \tag{31}$$

where $\langle , \rangle$ denotes the inner product of eigenvectors and differs from that of Eq. (23), because the eigenvectors are not functions of $\mathbf{x}$.

4 Galerkin-Projection POD/ROM Method for the 1D Case

Numerical simulation of Eqs. (1) and (2), using the Beam & Warming method [25], provides numerical data (snapshots) in different time steps. The correlation matrix is then generated using the numerical data with equal time intervals as snapshots, e.g., $t_1, t_2, \ldots, t_N$, where N is the number of snapshots. In the first step, these data are decomposed into the mean value part (as a space dependent part) and the deviation part (as a function of time and space), i.e.,

$$\mathbf{U}(x,t) = \overline{\mathbf{U}}(x) + \hat{\mathbf{U}}(x,t), \quad \overline{\mathbf{U}}(x) = \frac{1}{N}\sum_{i=1}^{N} \mathbf{U}(x,t_i) \tag{32}$$

The correlation matrix, $\mathbf{C}$, is obtained using snapshots of $\hat{\mathbf{U}}$. Solving Eq. (27) results to eigenvalues and eigenvectors to compute the POD basis functions as follows:

$$\mathbf{\Phi}_k(x) = \sum_{i=1}^{N} w_i^k \hat{\mathbf{U}}^i(x), \quad k = 1,2,\ldots,N \tag{33}$$

To make a reduced-order model, the Galerkin-projection of the governing equations based on a number of the POD basis functions (R out of N) is performed. These basis functions represent the essential dynamics of the system or equivalently capture the significant percentage of energy. These R basis modes correspond to R largest eigenvalues, $\lambda_1, \lambda_2, \ldots, \lambda_R$. Using these basis functions, the dependent variables are presented by Eq. (32) and $\hat{\mathbf{U}}(x,t)$ is defined as

$$\hat{\mathbf{U}}(x,t) = \sum_{k=1}^{R} a_k(t)\mathbf{\Phi}_k(x), \quad R < N \tag{34}$$

As indicated in Eq. (34), $\hat{\mathbf{U}}(x,t)$ is decomposed into the time dependent part, $a_k(t)$, and the space dependent part, $\mathbf{\Phi}_k(x)$. To apply the Galerkin-projection, Eq. (3) is rearranged in the following form [9]:

$$\frac{\partial \mathbf{U}}{\partial t} = L(\mathbf{U}) + Q(\mathbf{U},\mathbf{U}) \tag{35}$$

where

$$L(\mathbf{U}) = -\begin{pmatrix} gh_x \\ 0 \end{pmatrix}, \quad Q(\mathbf{U}^i,\mathbf{U}^j) = -\begin{pmatrix} u^i u_x^j \\ u^i h_x^j + h^i u_x^j \end{pmatrix}$$

By this kind of grouping, the linear and nonlinear parts of the equations are separated into $L(\mathbf{U})$ and $Q(\mathbf{U},\mathbf{U})$, respectively. The Galerkin-projection, in fact, is the inner product of Eq. (35) and $\mathbf{\Phi}_k$s for $k=1,2,\ldots,R$, i.e.,

$$(\mathbf{U}_t,\mathbf{\Phi}_k) = (L(\mathbf{U}),\mathbf{\Phi}_k) + (Q(\mathbf{U},\mathbf{U}),\mathbf{\Phi}_k), \quad k = 1,2,\ldots,R \tag{36}$$

Substitution of Eq. (32) into Eq. (36) and simplifying the resulting equation using Eq. (30) yield

$$\frac{da_k}{dt} = b_k^1 + b_k^2 + \sum_{i=1}^{R} (L_{ik}^1 + L_{ik}^2)a_i + \sum_{i,j=1}^{R} Q_{ijk}a_i a_j, \quad k = 1,2\ldots,R \tag{37}$$

where

$$b_k^1 = (L(\overline{\mathbf{U}}),\mathbf{\Phi}_k), \quad b_k^2 = (Q(\overline{\mathbf{U}},\overline{\mathbf{U}}),\mathbf{\Phi}_k), \quad L_{ik}^1 = (L(\mathbf{\Phi}_i),\mathbf{\Phi}_k)$$

$$L_{ik}^2 = (Q(\overline{\mathbf{U}},\mathbf{\Phi}_i) + Q(\mathbf{\Phi}_i,\overline{\mathbf{U}}),\mathbf{\Phi}_k), \quad Q_{ijk} = (Q(\mathbf{\Phi}_i,\mathbf{\Phi}_j),\mathbf{\Phi}_k)$$

In Eq. (37) there are two kinds of interaction: quadratic interactions, i.e., b_k^1 and L_{ik}^1, and triadic interactions, i.e., b_k^2, L_{ik}^2, and Q_{ijk}. Equation (37) is R nonlinear evolution equations, which can be solved by a classical numerical method, e.g., Runge–Kutta method. It is now clear that the large degrees of freedom of the problem have been decreased, and the reduced-order model has been constructed.

4.1 Computational Results of the Galerkin-Projection POD/ROM for the 1D Case. In this section, we present the numerical results of the Galerkin-projection POD/ROM method. In order to investigate the results of the POD/ROM application to the SWEs, we assume a 1D free surface channel with 400 m length and three different initial conditions as follows:

$$h(x,0) = 1 + 0.01\sin(\pi x)$$

$$u(x,0) = 0 \tag{38}$$

$$h(x,0) = 1 + 0.01\sin(10\pi x)$$

$$u(x,0) = 0 \tag{39}$$

and

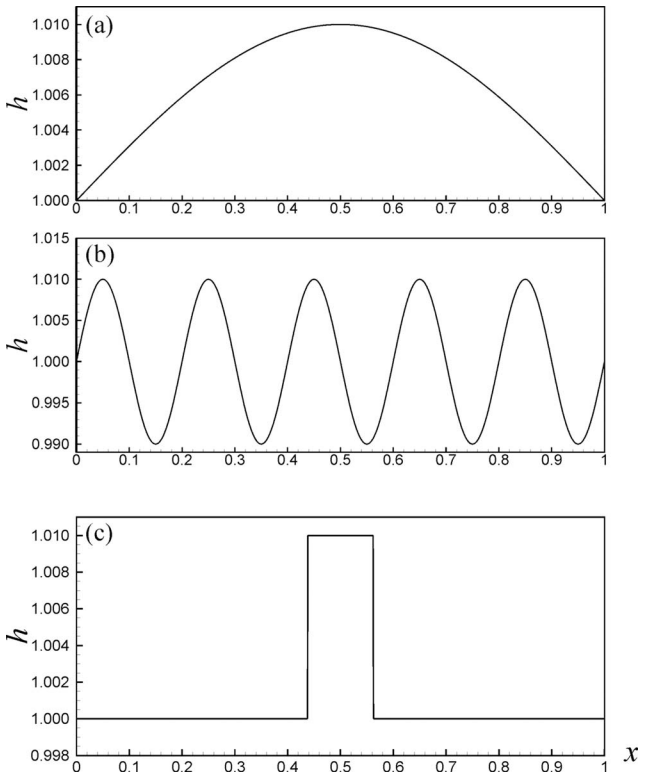

Fig. 1 Three different initial conditions for the POD/ROM of the 1D SWEs: (*a*) smooth initial condition, (*b*) high frequency initial condition, and (*c*) hydraulic jump initial condition

$$h(x,0) = \begin{cases} 1.01 & \text{if} \quad 0.4375 < x < 0.5625 \\ 1.0 & \text{if} \quad x < 0.4375, x > 0.5625 \end{cases}$$

$$u(x,0) = 0 \tag{40}$$

The above initial conditions are in a nondimensional form and are illustrated in Fig. 1. As shown in Fig. 1, Eqs. (38)–(40) provide three different initial conditions as smooth, high frequency, and hydraulic jump initial conditions, respectively. The physical boundary conditions are also assumed to be solid boundary for the velocity field in the following form:

$$u(0,t) = u(1,t) = 0.0 \tag{41}$$

Numerical simulation of Eq. (3) using the Beam & Warming scheme with the above initial and boundary conditions provides the snapshots to construct the POD basis functions. Grid analysis is performed for three types of given initial condition. The independent solutions of the grid size are obtained by 101, 1001, and 1001 grid points for the flow with smooth, high frequency, and hydraulic jump initial conditions, respectively. Also, the numerical boundary condition for h is determined using extrapolation of h values from interior grid points.

By recording of the snapshots at $t_1=0.0$, $t_2=0.5$, $t_3=1.0$, …, $t_{N=101}=50$(s), the ensemble of the dependent variables $\mathbf{U}^1, \mathbf{U}^2, \ldots, \mathbf{U}^{N=101}$ are obtained. Now the correlation matrix $\mathbf{C}$, which is a 101×101 matrix, can be computed by Eq. (28). Eigenvalues of matrix $\mathbf{C}$ for the three mentioned initial conditions are shown in Fig. 2 in a logarithmic scale. In the case of the flow with a smooth initial condition, the magnitude of eigenvalues except for the few first ones is very small, whereas the magnitudes of the eigenvalues for the flows with high frequency and hydraulic jump initial conditions have the small decreasing rate.

The number of the POD basis functions considered to perform the Galerkin-projection POD/ROM is determined by the amount of energy captured through the basis functions. Percentages of

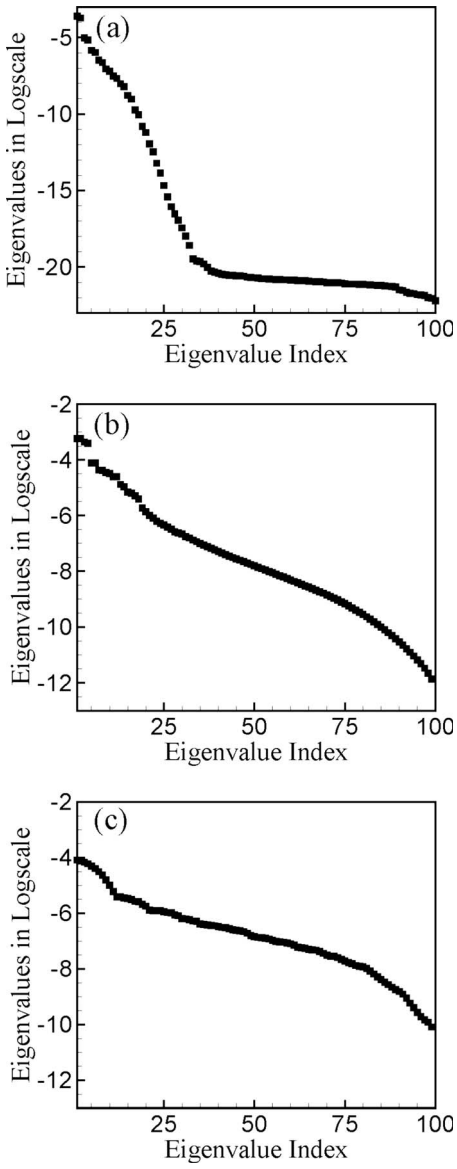

Fig. 2 Eigenvalues of the correlation matrix C with 0.5 s time interval for snapshots: (*a*) flow with a smooth initial condition, (*b*) flow with a high frequency initial condition, and (*c*) flow with a hydraulic jump initial condition

energy captured by the POD modes are given in Table 1. The numbers of modes, which capture the 99.99% of energy, are 10, 44, and 79 modes for flow with smooth, high frequency, and hydraulic jump initial conditions, respectively. Hereafter this criterion is used for the Galerkin-projection POD/ROM method.

Using the POD basis modes (capturing the 99.99% of energy) leads to the ODEs, which can be solved numerically. Numerical

Table 1 Percentage of captured energy by 5, 10, 20, 30, 50, 70, and 90 POD modes, using 100 snapshots for three kinds of initial condition

	No. of modes						
Flow prototype	5	10	20	30	50	70	90
Smooth	99.59	99.99	~100	100	100	100	100
High frequency	86.11	95.62	99.74	99.94	99.995	99.9996	~100
Hydraulic jump	66.11	89.74	96.22	98.30	99.64	99.95	99.999

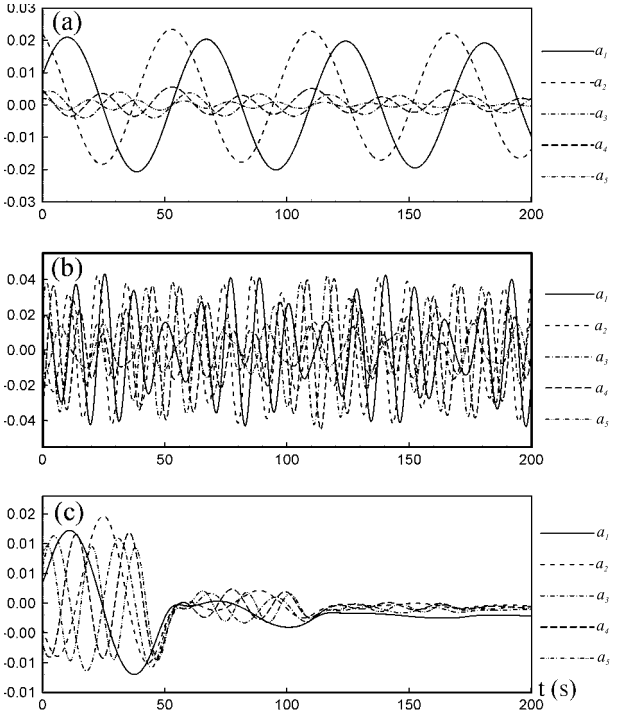

Fig. 3 Time evolutions of the first five a_ks: (*a*) Flow with a smooth initial condition, (*b*) flow with a high frequency initial condition, and (*c*) flow with a hydraulic jump initial condition

solution of these ODEs are obtained using the Runge–Kutta algorithm. It should be noted that the POD basis functions are computed using the data obtained by the first 50 s integration time, but the ODEs of the POD/ROM are integrated until 400 s. The time evolutions of a_ks are indicated in Fig. 3 for flows with three different initial conditions. In this figure, only the first five modes out of the mentioned number of modes are illustrated for each kind of flow. As shown in Fig. 3(*a*) the time evolution of a_ks for a smooth initial condition takes correct trends without damping after POD basis functions' construction time (50 s). Also as illustrated in Figs. 3(*b*) and 3(*c*), the flows with high frequency and hydraulic jump initial conditions involve the higher-order POD modes with larger corresponding a_ks.

The dependent variables, i.e., h and u, can be determined by substituting the values of a_ks into Eq. (34). The height and velocity fields in comparison with the results of the Beam & Warming method are shown in Figs. 4–7. In these cases, the computations are based on the POD modes, which their corresponding eigenvalues are shown in Fig. 2. In Figs. 4 and 5 the height fields are shown for 200 s and 400 s, respectively. The velocity fields for 200 s and 400 s are also illustrated in Figs. 6 and 7, respectively. It must be noted that in Figs. 4–7, the POD basis functions' construction time is 50 s. As shown in Figs. 4–7 (pattern (a) in these figures), the flow with a smooth initial condition can be predicted by the Galerkin-projection POD/ROM but not as accurate. Also these figures (patterns (b) and (c) in Figs. 4–7) show that the Galerkin-projection POD/ROM method cannot predict the SWEs with high frequency and hydraulic jump initial conditions.

The potential failure of the Galerkin-projection POD/ROM of the SWEs is divided into two parts.

- The component of the solution on the higher neglected POD modes is not zero.
- The future dynamics of the nonlinear system in nonperiodic problems in time cannot be captured by modes obtained using the data computed in the beginning of the integration

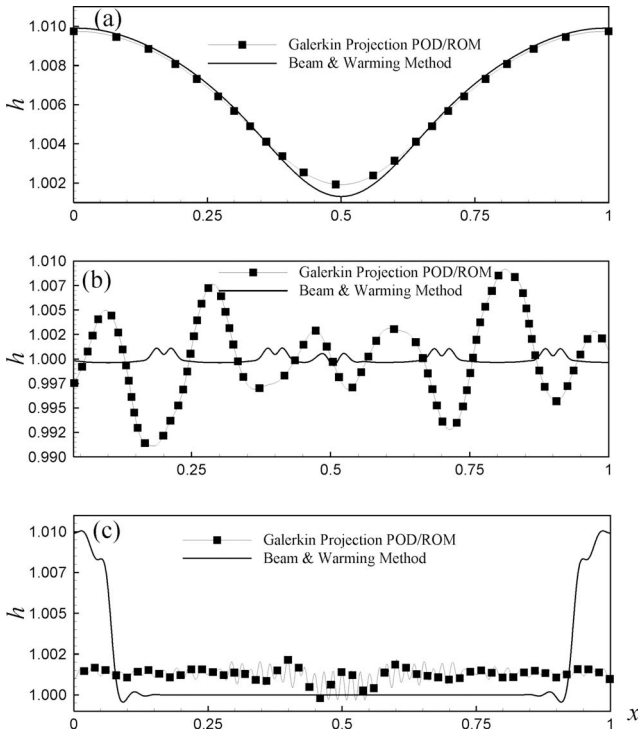

Fig. 4 A 200 s predicted height field by the Galerkin-projection POD/ROM method compared to the Beam & Warming method, the POD basis functions' construction time is 50 s and the numbers of modes are 10, 44, and 79 modes for (*a*), (*b*), and (*c*), respectively. (*a*) Flow with a smooth initial condition, (*b*) flow with a high frequency initial condition, and (*c*) flow with a hydraulic jump initial condition.

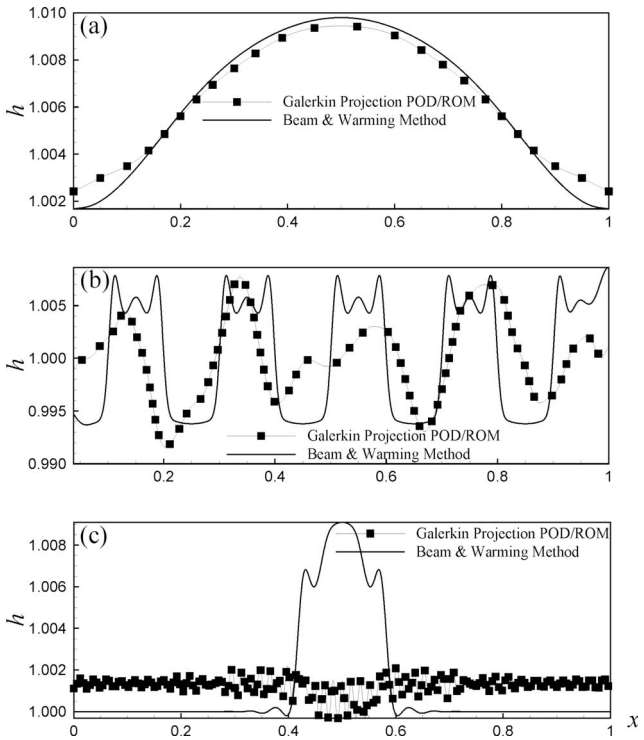

Fig. 5 A 400 s predicted height field by the Galerkin-projection POD/ROM method compared to the Beam & Warming method, the POD basis functions' construction time is 50 s, and the numbers of modes are 10, 44, and 79 modes for (*a*), (*b*), and (*c*), respectively. (*a*) Flow with a smooth initial condition, (*b*) flow with a high frequency initial condition, and (*c*) flow with a hydraulic jump initial condition.

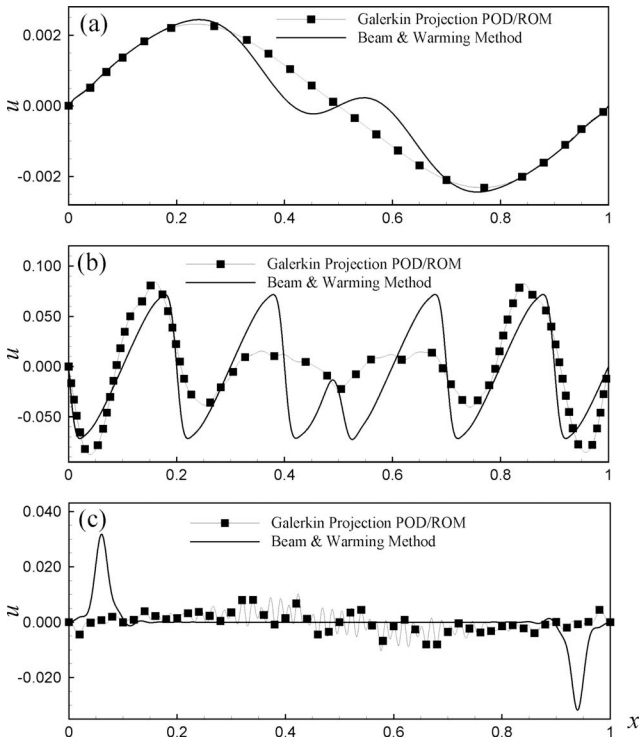

Fig. 6 A 200 s predicted velocity field by the Galerkin-projection POD/ROM method compared to the Beam & Warming method, the POD basis functions' construction time is 50 s, and the numbers of modes are 10, 44, and 79 modes for (*a*), (*b*), and (*c*), respectively. (*a*) Flow with a smooth initial condition, (*b*) flow with a high frequency initial condition, and (*c*) flow with a hydraulic jump initial condition.

time that is much smaller than the requested integration time.

In order to solve these problems in the traditional Galerkin-projection POD/ROM method the larger number of the POD basis functions must be considered and the construction time of these modes must be expanded to the whole integration time, but these approaches ruin the main purposes of the reduced-order modeling. Therefore, considering these results, the Galerkin-projection POD/ROM is not applied to the 2D case and an alternative method should be examined instead of the traditional Galerkin-projection.

5 Equation-Free/Galerkin-Free POD/ROM Method

As an alternative method, the equation-free/Galerkin-free method can be applied to the SWEs. The main idea here is that, using the few changing POD modes in time intervals can solve problems associated with Galerkin-projection POD/ROM. The few changing POD modes can be used to parametrize the low-dimensional attracting slow manifold and since they are changing with time, the effect of the higher-order neglected POD modes can be compensated using time integration of the fine-scale model. Assuming the separation of time scales between a few slow master POD modes and remaining fast slave ones, one can use larger time steps for slow master POD modes than the time step of the original fine-scale model. Applying this technique to the SWEs has the following main steps.

1. Starting at time level t^n and solving the fine-scale model (i.e., Beam & Warming and semi-implicit schemes for the 1D and 2D cases, respectively) for $n_f > 1$ steps with time step size δt and recording data to compute the POD modes in time interval $\Delta t_f = n_f \delta t$.
2. Computing the POD basis functions.

3. Expansion of the dependent variables in terms of the POD basis functions and computing the coefficients of the POD modes.
4. Projective integration of the POD modes' coefficients with time step size $\Delta t_c = n_c \delta t$. Although the traditional Galerkin-projection can be used as the closure equations for solving the POD basis coefficients, here we use the equation-free framework for integration without Galerkin-projection to save the computational time.
5. Switching from the projected POD coefficients to dependent variables of the fine-scale model at time $t^{n+1} = t^n + \Delta t_f + \Delta t_c$.
6. Repeating the first step until the required time is achieved.

The graphical illustration of the above procedure is shown in Fig. 8. The details of each step are given as follows.

1. *Numerical integration of the fine-scale model.* The fine-scale integration is integrated to time $t^n + \Delta t_f = t_n + n_f \delta t$ to provide data for the POD basis functions' construction. The detail of time steps and grid sizes will be discussed in Sec. 5.2.
2. *Computing of the POD basis functions and coefficients of expansion.* The POD basis functions can be obtained in a snapshot framework using Eqs. (27)–(29) given in Sec. 3. Here, the correlation matrix **C** is computed in time interval Δt_f using recorded fields. The recording time can be any time interval like $\delta t, 2\delta t, 3\delta t, \ldots, n_f \delta t$ or any other time intervals such as $2\delta t, 4\delta t, 6\delta t, \ldots, n_f \delta t$. Once the POD basis functions are determined, the dependent variables can be expanded in terms of the POD modes as follows:

$$\mathbf{U}(\mathbf{x},t) = \mathcal{P}\mathbf{a}(t) \equiv \sum_{k=1} a_k(t)\mathbf{\Phi}_k(\mathbf{x}) \tag{42}$$

where **a** is the vector of the a_ks and operator $\mathcal{P}$ is defined to convert the POD basis functions' coefficients to physical dependent variables. The inner production of Eq. (42) and $\mathbf{\Phi}_k$ results to the following relationship to determine $\mathbf{a}(t)$:

$$\mathbf{a}(t) = \mathcal{Q}\mathbf{U} \equiv \{(\mathbf{U}(\mathbf{x},t),\mathbf{\Phi}_k(\mathbf{x})),\ \forall\ k\} \tag{43}$$

in which the operator $\mathcal{Q}$ is defined as a convertor of physical dependent variables to the POD modes' coefficients. Since, both $\mathcal{P}$ and $\mathcal{Q}$ are linear operators hence $\mathcal{Q}\mathcal{P}\mathbf{a} = \mathbf{a}$ and $\mathcal{P}\mathcal{Q}\mathbf{U} = \mathbf{U}$. Also, the finite-term POD expansion can be defined as

$$\mathbf{U}_R(\mathbf{x},t) = \mathcal{P}_R\mathbf{a}(t) \equiv \sum_{i=k}^{R} a_k(t)\mathbf{\Phi}_k(\mathbf{x}) \tag{44}$$

and

$$\mathbf{a}(t) = \mathcal{Q}_R\mathbf{U} \equiv \{(\mathbf{U}(\mathbf{x},t),\mathbf{\Phi}_k(\mathbf{x})), k = 1,2,\ldots,R\} \tag{45}$$

where $\mathcal{P}_R$ and $\mathcal{Q}_R$ are called the truncated operators and we have $\mathcal{P}_R\mathcal{Q}_R\mathbf{U} = \mathbf{U}_R$. The convergence of the POD expansion is assumed to be

$$\|\mathbf{U} - \mathbf{U}_R\| \to R^{-\gamma} \quad \text{as} \quad R \to \infty \tag{46}$$

in which γ is a non-negative real number that quantifies the convergence rate. Theoretical obtaining of the convergence rate is difficult and it depends strongly on the correlation matrix **C** and the smoothness of the flow field, i.e., **U** [13]. Using Eq. (45) one can obtain the coefficients of the POD basis functions from the numerical simulation of the flow field. Subsequently, as described in the following paragraph, the projective integration of these coefficients is performed.
3. *Projective integration.* As discussed before, the right hand side (RHS) of the POD basis functions' coefficients can be determined using Galerkin-projection of the SWEs onto the POD basis functions. In addition to disadvantages of such a method explained before, this method suffers from spurious long-term dynamics [29,30]. In the equation-free/Galerkin-free framework, the RHS of coefficients of the POD modes can be obtained from backward discretization. Time integration of the fine-scale model until $t^n + \Delta t_f$ provides the numerical data and snapshots for construction of the POD basis functions and corresponding coefficients. Having the fine-scale simulation of the SWEs and as a result the POD basis functions, the projective integration procedure is as follows.

(a) Obtain the POD basis functions' coefficient $a_k(t) = (\mathbf{U}(\mathbf{x},t),\mathbf{\Phi}_k(\mathbf{x}))$ for $t^n \le t \le t^n + \Delta t_f$.

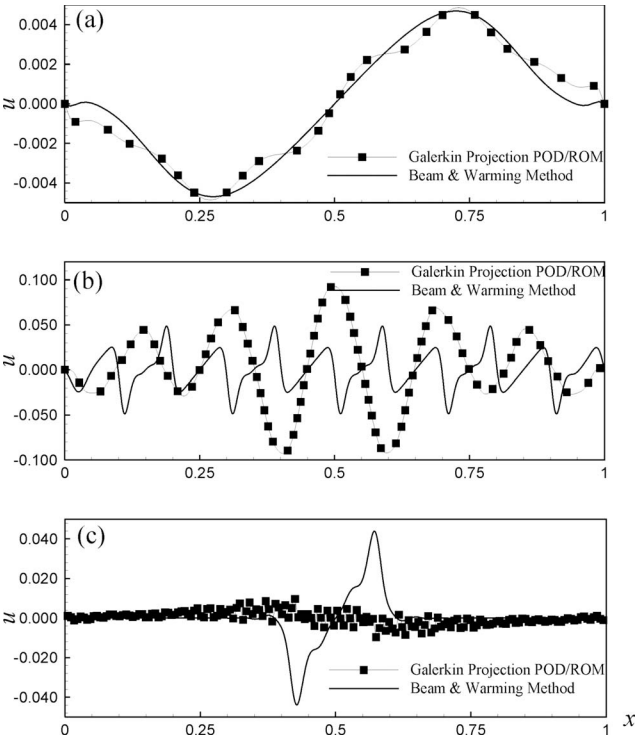

Fig. 7 A 400 s predicted velocity field by the Galerkin-projection POD/ROM method compared to the Beam & Warming method, the POD basis functions' construction time is 50 s, and the numbers of modes are 10, 44, and 79 modes for (*a*), (*b*), and (*c*), respectively. (*a*) Flow with a smooth initial condition, (*b*) flow with a high frequency initial condition, and (*c*) flow with a hydraulic jump initial condition.

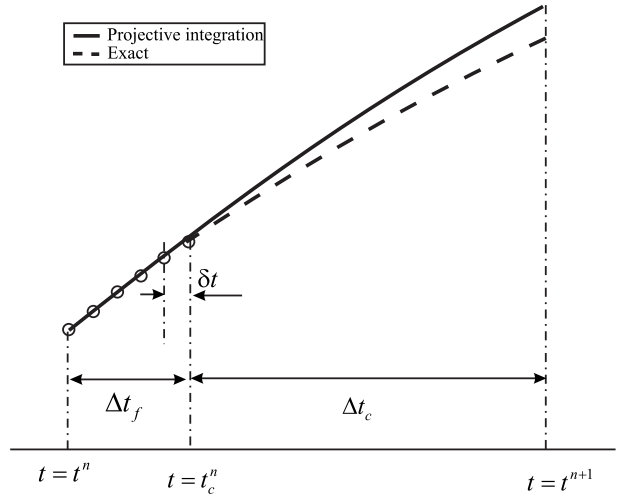

Fig. 8 Sketch of a projective integration over one global time step [13]

Table 2 The constant coefficients, β_js, for different orders of approximation

Order of approximation (J_f)	n_e	β_0	β_1	β_2	β_3	β_4
1	1	$\frac{1}{\delta t}$	$-\frac{1}{\delta t}$	–	–	–
2	2	$\frac{3}{2\delta t}$	$-\frac{4}{2\delta t}$	$\frac{1}{2\delta t}$	–	–
3	3	$\frac{11}{6\delta t}$	$-\frac{18}{6\delta t}$	$\frac{9}{6\delta t}$	$-\frac{2}{6\delta t}$	–
4	4	$-\frac{25}{12\delta t}$	$\frac{48}{12\delta t}$	$-\frac{36}{12\delta t}$	$\frac{16}{12\delta t}$	$-\frac{3}{12\delta t}$

(b) Approximate the RHS of $da_k(t)/dt$ at $t=t_c$ as

$$\frac{da_k(t)}{dt} + \mathrm{O}(\delta t^{J_f}) = \sum_{j=0}^{n_e} \beta_j a_k(t_j) = g_k(t_c^n) \tag{47}$$

where $1 \le n_e \le n_f$, $t_j = t_c^n - j\delta t$, and J_f denotes the order of backward approximation. The β_js are the constant coefficients and depend on the approximation order J_f. The values of n_e and β_js are given in Table 2 for different approximation orders.

(c) When the RHS of Eq. (47) is determined using numerical approximation, one can integrate Eq. (47) via standard ODE solvers. The single step forward Euler projective integration takes the form

$$a_k(t^{n+1}) = a_k(t_c^n) + \Delta t_c g_k(t_c^n) + \mathrm{O}(\Delta t_c^2) \tag{48}$$

Higher-order time integration schemes can be used to integrate Eq. (47), for instance, the following scheme can be used:

$$a_k(t^{n+1}) = a_k(t_c^n) + \sum_{k=1}^{J_c} \frac{(\Delta t_c)^k}{k!} \frac{\partial^{(k-1)}}{\partial^{(k-1)}_t} g_k(t_c^n) + \mathrm{O}(\Delta t_c^{J_c+1}) \tag{49}$$

where J_c is the order of approximation and higher-order derivatives of $g_k(t_c^n)$ are estimated similar to Eq. (47) using backward approximation.

4. *Switching.* Switching from the projected POD coefficients to dependent variables of the fine-scale model at time $t^{n+1} = t^n + \Delta t_f + \Delta t_c$ is performed using Eq. (42). The computed variables can be used in a numerical fine-scale model as initial conditions to generate data and snapshots for the next group of the POD basis functions.

5.1 Consistency and Accuracy. The detailed discussion of consistency and accuracy of equation-free/Galerkin-free POD/ROM is presented by Sirisup et al. [13]. Here only the results of the consistency and accuracy analysis are presented and one can refer to Ref. [13] for more details.

The equation-free/Galerkin-free is a consistent approach provided that the POD basis functions satisfy the convergency property defined by Eq. (46).

The truncation error of the equation-free/Galerkin-free approach takes the form

$$\epsilon \sim O\left(\text{fine-scale model truncation error}, \ \delta t^{J_f-1}, \Delta t_c^{J_c}, \frac{R^{-\gamma}}{\Delta t}\right) \tag{50}$$

In Eq. (50), $O(\delta t^{J_f-1}, \Delta t_c^{J_c})$ and $R^{-\gamma}/\Delta t$ denote the equation-free/Galerkin-free POD/ROM truncation error. Order of δt is usually small in comparison to Δt_c and Δt; therefore the dominant errors are Δt_c and Δt. The two latest terms in Eq. (50) compete in opposite ways, i.e., when the global time step decreases, it can reduce the term $\Delta t_c^{J_c}$ and amplify the term $R^{-\gamma}/\Delta t$. It is clear that in the problems with fast convergence rate of the POD modes the dominant error is $O(\Delta t_c^{J_c})$.

Table 3 Control parameters of the equation-free/Galerkin-free POD/ROM method for three flow prototypes

Flow prototype	I max	δt	Δt_f	Δt_c	N	R	J_f
Smooth	101	0.01	0.1	0.1	10	6	2
High frequency	1001	0.01	0.2	0.1	20	11	2
Hydraulic jump	1001	0.01	0.2	0.1	20	11	2

5.2 Numerical Results for Equation-Free/Galerkin-Free POD/ROM Method

5.2.1 The 1D Case. The equation-free/Galerkin-free POD/ROM method is applied to three prototype flows mentioned before. Here, the Beam & Warming method plays the fine-scale model role. To achieve the fine-scale resolution, some numerical experiments are performed and as a result the numbers of grids for the three types of flows are obtained as 101, 1001, and 1001 for flows with smooth, high frequency, and hydraulic jump initial conditions, respectively. In Table 3, the important control parameters of equation-free/Galerkin-free POD/ROM method including the number of grid points of the fine-scale model I max, time step size of the fine-scale model δt, recording time of the snapshots Δt_f, time step size of projective integration Δt_c, number of snapshots N, number of the POD modes for model reduction R, and the order of backward approximation J_f, are given for three prototype of flows. Since the dominant error of the method is measured by $\Delta t_c^{J_c}$, the projective integration errors for different values of J_c are obtained by applying the equation-free/Galerkin-free POD/ROM method to SWEs. The rms errors between the equation-free/Galerkin-free POD/ROM and the fine-scale model for different values of J_c, after 200 s time integration of the height and velocity fields, are given in Tables 4 and 5, respectively. As indicated in Tables 4 and 5, $J_c=2$ is enough to obtain a reliable solution for flow with a smooth initial condition and using higher-order projective integration for this prototype of flow only increases the computation cost. The proper value of J_c for flow with high frequency and hydraulic jump initial conditions is 3 because increasing J_c from 3 to 4 changes the rms error very slightly. Another important issue in Tables 4 and 5 is that the projective integration of high frequency flow and flow with hydraulic jump

Table 4 The rms error of the height field between the equation-free/Galerkin-free POD/ROM and the Beam & Warming method for different values of J_c

Flow prototype	$J_c=1$	$J_c=2$	$J_c=3$	$J_c=4$
Smooth	2.478×10^{-4}	2.125×10^{-5}	2.192×10^{-5}	2.264×10^{-5}
High frequency	Unstable	5.600×10^{-4}	6.537×10^{-5}	6.469×10^{-5}
Hydraulic jump	Unstable	2.982×10^{-4}	5.857×10^{-5}	5.813×10^{-5}

Table 5 The rms error of the velocity field between the equation-free/Galerkin-free POD/ROM and the Beam & Warming method for different values of J_c

Flow prototype	$J_c=1$	$J_c=2$	$J_c=3$	$J_c=4$
Smooth	1.758×10^{-1}	1.877×10^{-2}	2.783×10^{-2}	2.833×10^{-2}
High frequency	Unstable	1.814×10^{-2}	9.341×10^{-3}	9.157×10^{-3}
Hydraulic jump	Unstable	3.235×10^{-1}	4.153×10^{-2}	4.135×10^{-2}

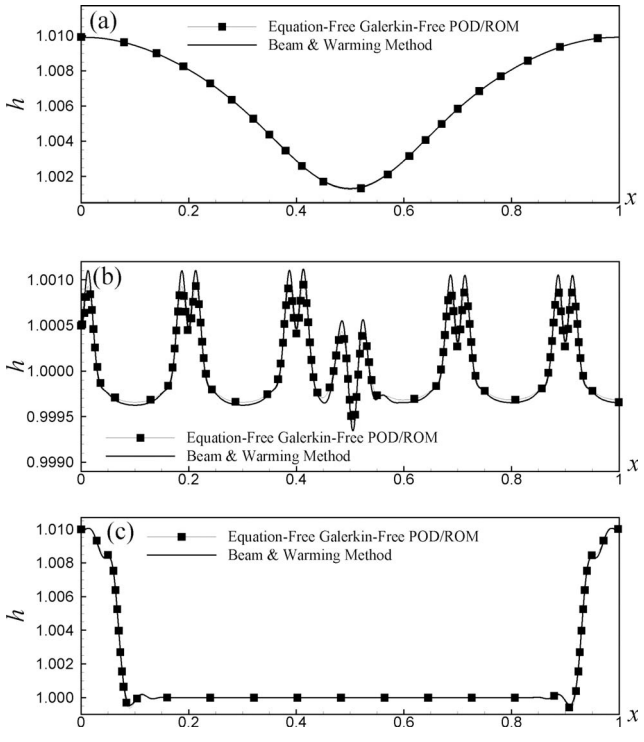

Fig. 9 A 200 s predicted height field by the equation-free/Galerkin-free POD/ROM method compared to the Beam & Warming method. (*a*) Flow with a smooth initial condition, (*b*) flow with a high frequency initial condition, and (*c*) flow with a hydraulic jump initial condition.

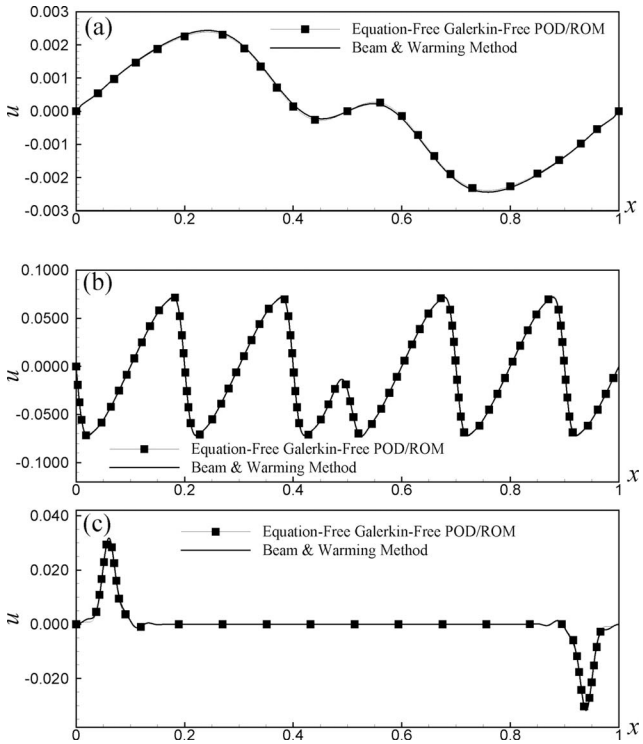

Fig. 11 A 200 s predicted velocity field by the equation-free/Galerkin-free POD/ROM method compared to the Beam & Warming method. (*a*) Flow with a smooth initial condition, (*b*) flow with a high frequency initial condition, and (*c*) flow with a hydraulic jump initial condition.

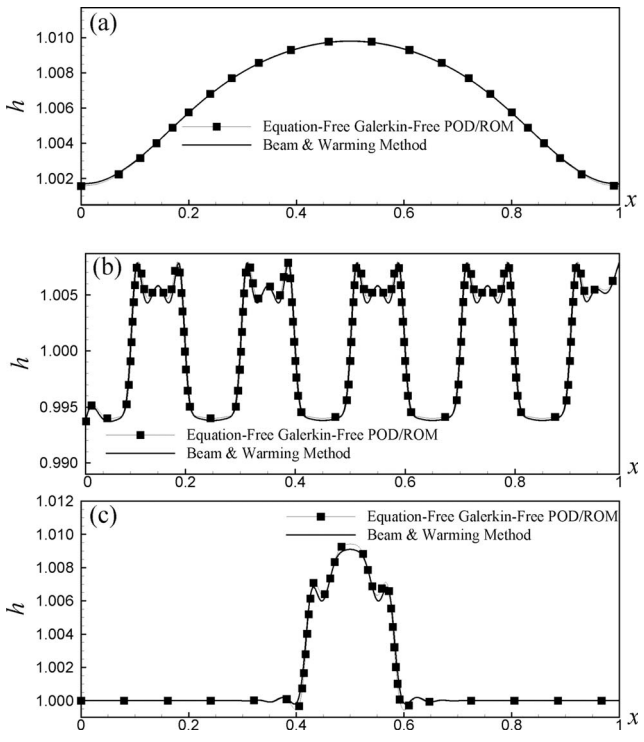

Fig. 10 A 400 s predicted height field by the equation-free/Galerkin-free POD/ROM method compared to the Beam & Warming method. (*a*) Flow with a smooth initial condition, (*b*) flow with a high frequency initial condition, and (*c*) flow with a hydraulic jump initial condition.

using the first order forward Euler method is unstable and applying the higher orders of projective integration makes the solutions stable. Similar conclusion has been found by Sirisup et al. [13] for Navier–Stokes equations.

The height and velocity fields in comparison with the results of the Beam & Warming method are shown in Figs. 9–12. In these cases, the control parameters of the equation-free/Galerkin-free POD/ROM are given in Table 3 and also $J_f=2$ and $J_c=3$. In Figs. 9 and 10 the height fields are shown in 200 s and 400 s, respectively. The velocity fields for 200 s and 400 s are also illustrated in Figs. 11 and 12, respectively. Figures 9–12 show good agreement between the equation-free/Galerkin-free POD/ROM and the fine-scale model while there was no agreement between the traditional Galerkin-projection POD/ROM method and the fine-scale model results (Figs. 4–7).

The CPU-times of the equation-free/Galerkin-free POD/ROM approach (including the fine-scale model integration time and the POD basis functions' construction time in Δt_f's intervals, and coarse-scale model integration time in Δt_c's intervals) for three prototypes of flows relative to the CPU-time of the Beam & Warming scheme are given in Table 6. As indicated in Table 6, the reduction in the CPU-time is about 13–22% depending on the type of the flow. The CPU-time reduction in equation-free Galerkin-free POD/ROM does not result into decrease in accuracy as much as a coarse grid with equal CPU-time. The comparison of fine grid (I max=1001), coarse grid (I max=881 and CPU-time equals to POD/ROM), and POD/ROM all with shock as an initial condition for velocity field is shown in Fig. 13. As shown in this figure the POD/ROM prediction is much better than the coarse grid with equal CPU-time.

5.2.2 The 2D Case. The numerical simulation domain is considered as $[0,2\pi]\times[0,2\pi]$ with periodic boundary conditions. Parameters c_0 and f_0 are chosen to be $4\pi^2$ and 2π, respectively, so

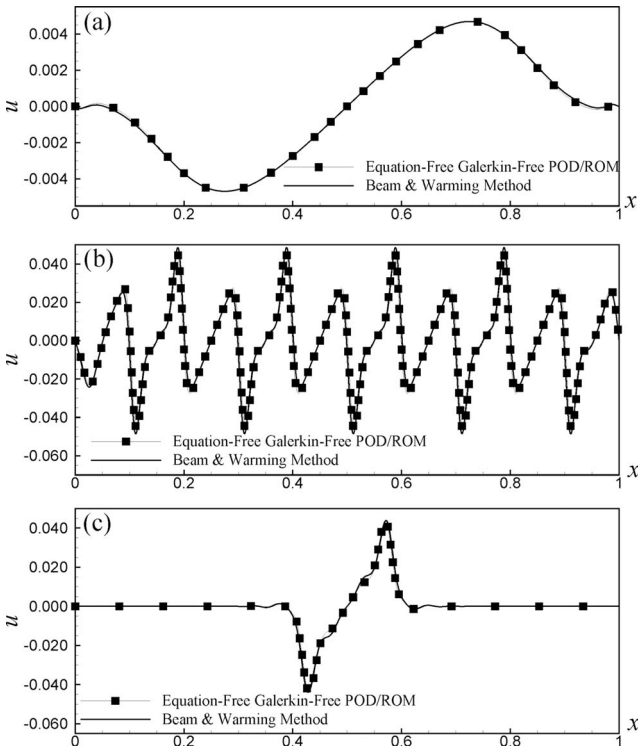

Fig. 12 A 400 s predicted velocity field by the equation-free/Galerkin-free POD/ROM method compared to the Beam & Warming method. (*a*) Flow with a smooth initial condition, (*b*) flow with a high frequency initial condition, and (*c*) flow with a hydraulic jump initial condition.

that time $T=1$ corresponds to one planar rotation (1 day). Using these values, the Rossby deformation radius becomes $L_R=\sqrt{c_0}/f_0=1$.

For numerical simulation the initial condition for layer depth [31] is defined by

$$h(\mathbf{x},0)=\frac{1}{1+\Delta q(\mathbf{x})}+\kappa \tag{51}$$

in which

$$\Delta q(\mathbf{x})=\frac{1}{\pi}(y-\pi)e^{-2(y-\pi)^2}\left(1+\frac{1}{10}\sin 2x\right) \tag{52}$$

and κ is chosen so that mean$(h)=1$; thus

$$\kappa=1-\frac{1}{4\pi^2}\int_0^{2\pi}\int_0^{2\pi}\frac{d\mathbf{x}}{1+\Delta q(\mathbf{x})} \tag{53}$$

The initial conditions for u and v are obtained using geostrophic approximation

Table 6 The CPU-time of the equation-free/Galerkin-free POD/ROM relative to the Beam & Warming method for three flow prototypes.

Flow prototype	CPU-time of equation-free Galerkin-free POD/ROM / CPU-time of Beam & Warming method
Smooth	0.78
High frequency	0.88
Hydraulic jump	0.87

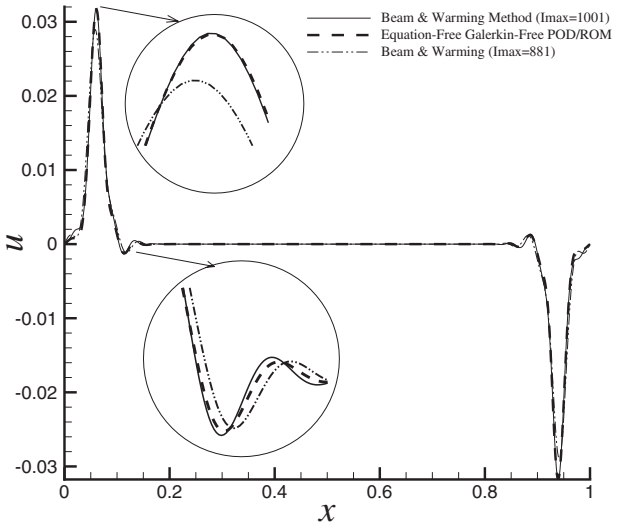

Fig. 13 A 200 s predicted velocity field by the equation-free/Galerkin-free POD/ROM method compared to Beam & Warming method in fine and coarser grids (the CPU-time of the coarser grid is equal to POD/ROM)

$$u(\mathbf{x},0)=-\frac{c_0}{f_0}\frac{\partial h(\mathbf{x},0)}{\partial y},\quad v(\mathbf{x},0)=\frac{c_0}{f_0}\frac{\partial h(\mathbf{x},0)}{\partial x} \tag{54}$$

Using the velocity and height fields, the vorticity, divergence, and potential vorticity are obtained. In Fig. 14 the initial condition for potential vorticity is shown.

The numerical modeling is performed in three different grids: 65×65, 129×129, and 257×257. The numerical results of potential vorticity for the mentioned grids after 4 days, 8 days, and 12 days of integration are illustrated in Fig. 15.

Since our purpose is the equation-free/Galerkin-free POD/ROM of SWEs, we chose 129×129 grid points (enough accuracy and reasonable computational cost) to investigate the efficiency of this approach. The control parameters of the equation-free/Galerkin-free POD/ROM including the number of grid points I max $\times J$ max, time step for the fine-scale model δt, time for snapshot recording Δt_f, time step for the coarse-scale model Δt_c, number of

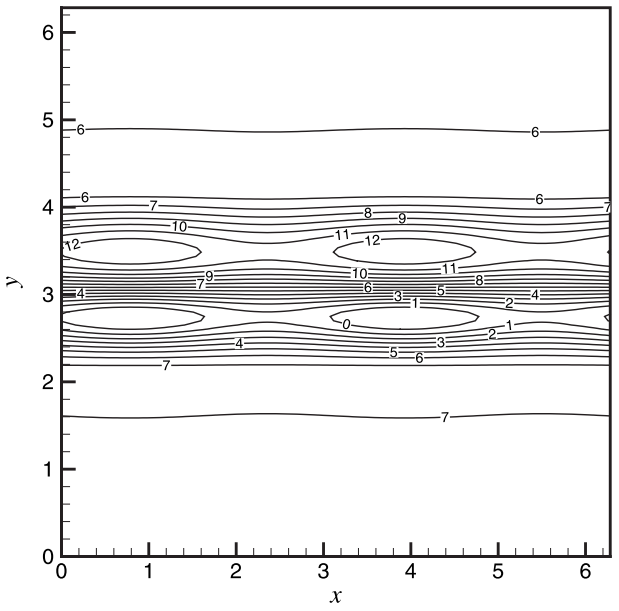

Fig. 14 Initial condition for potential vorticity

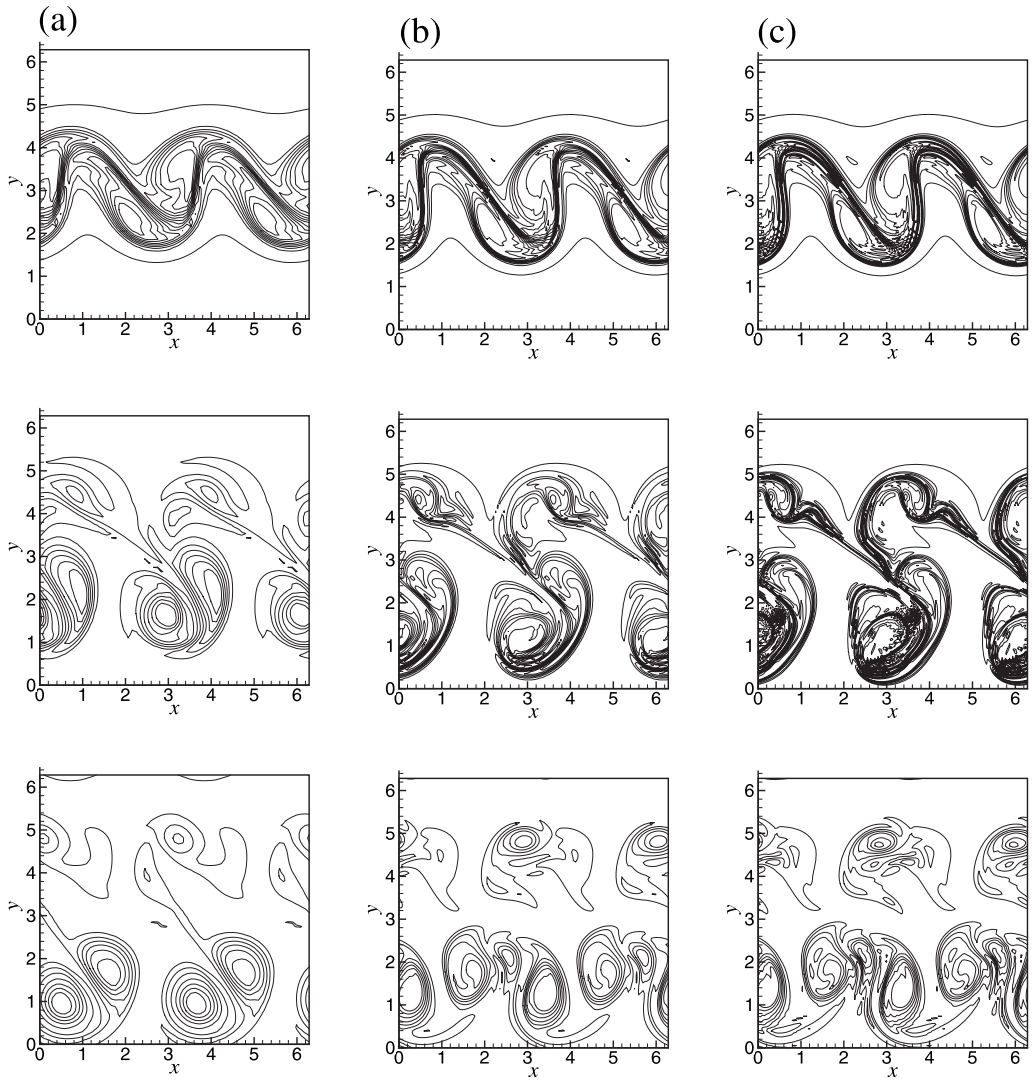

Fig. 15 Potential vorticity patterns after 4 days of integration (top), 8 days of integration (middle), and 12 days of integration (bottom). (*a*) 65×65 grid points, (*b*) 129×129 grid points, and (*c*) 257 ×257 grid points.

recorded snapshots at each Δt_f, and number of the POD modes, are given in Table 7. Also, the second order backward finite differencing ($J_f=2$), in the same order of the fine-scale model, is applied to obtain $g(t)$. As indicated in the 1D case and by Sirisup et al. [13], the third order integration is the optimum value for projective integration; thus $J_c=3$ is chosen for projective integration.

The contour plots of the potential vorticity after 4 days, 8 days, and 12 days of integration using the equation-free/Galerkin-free POD/ROM compared with the fine-scale model are displayed in Fig. 16. As shown in Fig. 16, the flow patterns using POD/ROM are similar to those obtained by the fine-scale modeling. Furthermore, the rms errors between POD/ROM and the fine-scale model are given in Table 8 after 4 days, 8 days, and 12 days of integration. Table 8 indicates that the rms error increases whit increase in integration time.

Table 7 Control parameters for the equation-free/Galerkin-free POD/ROM of SWEs

I max × J max	δt	Δt_f	Δt_c	N	R
129×129	0.002	0.05	0.02	25	13

The computation cost saving of the equation-free/Galerkin-free POD/ROM of the SWEs in comparison with the fine-scale model (semi-implicit time integration model) is about 30%.

6 Conclusion

In this paper, two categories of the POD/ROM including traditional Galerkin-projection and the equation-free/Galerkin-free POD/ROM were examined to the SWEs. First, applying the Galerkin-projection POD/ROM to the 1D SWEs showed that the method cannot capture the flow dynamics especially in complex cases. Then, as an alternative approach, the equation-free/Galerkin-free POD/ROM of the 1D and 2D SWEs was presented. The Beam & Warming and semi-implicit time integration schemes were applied to the 1D and 2D SWEs, respectively, as fine-scale models in order to provide numerical data to construct the POD basis functions. Also, complex initial conditions were considered for the SWEs to validate the accuracy and efficiency of the approach. The coarse-scale model was designed by the POD basis functions' coefficients using expansion of the dependent variables (the height and velocity fields in the 1D case and the vorticity, divergence, and height fields in the 2D case) in terms of the POD modes.

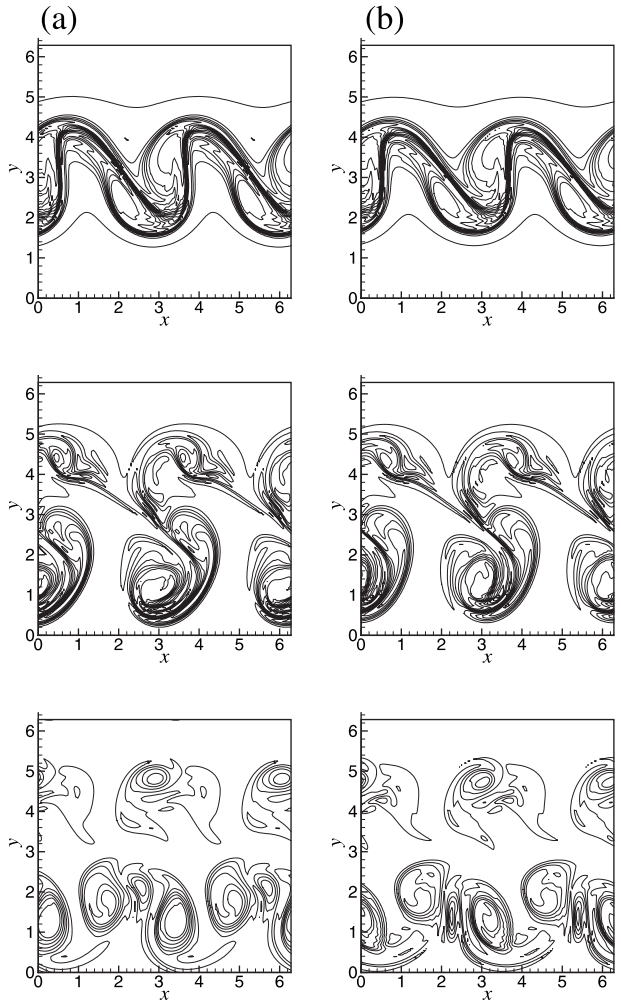

Fig. 16 Comparison of potential vorticity patterns between semi-implicit time integration (fine-scale model) and the equation-free/Galerkin-free POD/ROM of the SWEs after 4 days of integration (top), 8 days of integration (middle), and 12 days of integration (bottom). (*a*) Semi-implicit time integration and (*b*) equation-free/Galerkin-free POD/ROM.

It is shown that one can integrate the coarse-scale model with much greater time steps (about ten times) than the one used for the fine-scale model. As a result it is demonstrated that the dynamics of the SWEs can be captured with less computational cost (about 30% in the 2D case) compared to the original fine-scale model.

More studies are required to investigate the accuracy and efficiency of this approach in spherical and multilevel SWEs and also in operational numerical weather prediction models. The comparison of the CPU-time saving in the 1D and 2D cases shows more time saving in the 2D case. For this reason, hopefully in sophisticated cases with a large number of grid points, the decrease in the computational cost would be more significant; however, it should be examined in future works.

Table 8 The rms error between the equation-free/Galerkin-free POD/ROM of SWEs and the semi-implicit time integration of SWEs

Time (day)	rms error
4	0.0922074570
8	0.1522886907
12	0.1799198309

Acknowledgment

The authors would like to thank the University of Tehran and Atmospheric Science and Meteorological Research Center (ASMERC) of Iran for their financial support of this research.

References

[1] Lucia, D., Beran, P., and Silva, W., 2004, "Reduced-Order Modeling: New Approaches for Computational Physics," Prog. Aerosp. Sci., **40**(1–2), pp. 51–117.

[2] Karhunen, K., 1946, "Zur spektral theorie stochasticher prozesse," Ann. Acad. Sci. Fenn., Ser. A1: Math.-Phys., **34**, pp. 1–7.

[3] Loeve, M., 1946, "Sur le fonctions alatoire de second ordre," Rev. Sci., **84**, pp. 195–206.

[4] Lumley, J., 1967, "The Structure of Inhomogeneous Turbulent Flows," *Atmospheric Turbulence and Radio Wave Propagation*, A. M. Yaglow and V. I. Tatarski, eds., Nauka, Moscow, pp. 166–178.

[5] Sirovich, L., 1987, "Turbulence and the Dynamics of Coherent Structures: Parts I—III," Q. Appl. Math., **45**(3), pp. 561–590.

[6] Holmes, P., Lumley, J., and Berkooz, G., 1998, *Turbulence, Coherent Structures, Dynamical Systems and Symmetry*, Cambridge University Press, Cambridge.

[7] Ravindran, S., 2000, "A Reduced-Order Approach for Optimal Control of Fluids Using Proper Orthogonal Decomposition," Int. J. Numer. Methods Fluids, **34**(5), pp. 425–448.

[8] Couplet, M., Basdevant, C., and Sagaut, P., 2005, "Calibrated Reduced-Order POD Galerkin System for Fluid Flow Modeling," J. Comput. Phys., **207**(1), pp. 192–220.

[9] Rowley, C., Colonius, T., and Murray, R., 2004, "Model Reduction for Compressible Flows Using POD and Galerkin Projection," Physica D, **189**(1–2), pp. 115–129.

[10] Achatz, U., and Opsteegh, J., 2003, "Primitive-Equation-Based Low-Order Models With Seasonal Cycle. Part i: Model Construction," J. Atmos. Sci., **60**(3), pp. 465–477.

[11] Achatz, U., and Opsteegh, J., 2003, "Primitive-Equation-Based Low-Order Models With Seasonal Cycle. Part ii: Application to Complexity and Nonlinearity of Large-Scale Atmosphere," J. Atmos. Sci., **60**(3), pp. 478–490.

[12] Majda, A., Timofeyev, I., and Vanden-Eijnden, E., 2003, "Systematic Strategies for Stochastic Mode Reduction in Climate," J. Atmos. Sci., **60**(14), pp. 1705–1722.

[13] Sirisup, S., Karniadakis, G., Xiu, D., and Kevrekidis, I., 2005, "Equation-Free/Galerkin-Free POD-Assisted Computation of Incompressible Flows," J. Comput. Phys., **207**(2), pp. 568–587.

[14] Theodoropoulos, C., Qian, Y., and Kevrekidis, I., 2000, "Coarse Stability and Bifurcation Analysis Using Time-Steppers: A Reaction-Diffusion Example," Proc. Natl. Acad. Sci. U.S.A., **97**(18), pp. 9840–9843.

[15] Kevrekidis, I., Gear, C., Hyman, J., Kevrekidis, P., Runborg, O., and Theodoropoulos, C., 2003, "Equation-Free Coarse-Grained Multiscale Computation: Enabling Microscopic Simulators to Perform System-Level Analysis," Commun. Math. Sci., **1**(4), pp. 715–762.

[16] Kevrekidis, I., Gear, C., and Hummer, G., 2004, "Equation-Free: The Computer Assisted Analysis of Complex, Multiscale System," AIChE J., **50**(7), pp. 1346–1354.

[17] Gear, C., and Kevrekidis, I., 2003, "Projective Methods for Stiff Differential Equations: Problems With Gaps in Their Eigenvalues Spectrum," SIAM J. Sci. Comput. (USA), **24**(4), pp. 1091–1106.

[18] Gear, C., and Kevrekidis, I., 2003, "Telescopic Projective Methods for Parabolic Differential Equations," J. Comput. Phys., **187**(1), pp. 95–109.

[19] Rico-Martinez, R., Gear, C., and Kevrekidis, I., 2004, "Coarse Projective kMC Integration: Forward/Reverse Initial and Boundary Value Problems," J. Comput. Phys., **196**(2), pp. 474–489.

[20] Gear, C., Li, J., and Kevrekidis, I., 2003, "The Gap-Tooth Method in Particle Simulations," Phys. Lett. A, **316**(3–4), pp. 190–195.

[21] Li, J., Kevrekidis, P., Gear, C., and Kevrekidis, P., 2003, "Deciding the Nature of the Coarse Integration Through Microscopic Simulations: The Baby-Bathwater Scheme," SIAM J. Multiscale Model. Simulation, **1**(3), pp. 391–407.

[22] Makeev, A., Maroudas, D., and Kevrekidis, I., 2002, "Coarse Stability and Bifurcation Analysis Using Stochastic Simulators: Kinetic Monte Carlo Examples," J. Chem. Phys., **116**(23), pp. 10083–10091.

[23] Makeev, A., Maroudas, D., Panagiotopoulos, A., and Kevrekidis, I., 2002, "Coarse Bifurcation Analysis of Kinetic Monte Carlo Simulations: A Lattice-Gas Model With Lateral Interactions," J. Chem. Phys., **117**(18), pp. 8229–8240.

[24] Abbott, M., and Basco, D., 1989, *Computational Fluid Dynamics: An Introduction for Engineers*, Wiley, Harlow, England.

[25] Beam, R., and Warming, R., 1978, "An Implicit Factored Scheme for the Compressible Navier-Stokes Equations," AIAA J., **16**(4), pp. 393–402.

[26] Duran, D., 1999, *Numerical Methods for Wave Equations in Geophysical Fluid Dynamics*, Springer, New York.

[27] Heikes, R., and Randall, D., 1995, "Numerical Integration of the Shallow-Water Equations on a Twisted Icosahedral Grid. Part i: Basic Design and Results of Tests," Mon. Weather Rev., **123**(6), pp. 1862–1880.
[28] Dritschel, D., Polvani, L., and Mohebalhojeh, A., 1999, "The Contour-Advective Semilagrangian Algorithm for the Shallow Water Equations," Mon. Weather Rev., **127**(7), pp. 1551–1565.
[29] Foias, C., Jolly, M., Kevrekidis, I., and Titi, E., 1991, "Dissipativity of the Numerical Schemes," Nonlinearity, **4**, pp. 591–613.
[30] Sirisup, S., and Karniadakis, G., 2004, "A Spectral Viscosity Method for Correcting the Long-Term Behavior of POD Models," J. Comput. Phys., **194**(1), pp. 92–116.
[31] Frank, J., Gottwald, G., and Reich, S., 2002, "A Hamiltonian Particle-Mesh Method for the Rotating Shallow-Water Equations," *Lecture Notes in Computational Science and Engineering*, Vol. 26, Springer, Berlin, pp. 131–142.

Nonaxisymmetric Three-Dimensional Stagnation-Point Flow and Heat Transfer on a Flat Plate

Ali Shokrgozar Abbassi
Graduate Student

Asghar Baradaran Rahimi[1]
Professor
e-mail: rahimiab@yahoo.com

Faculty of Engineering,
Ferdowsi University of Mashhad,
P.O. Box No. 91775-1111,
Mashhad 1111, Iran

*The existing solutions of Navier–Stokes and energy equations in the literature regarding the three-dimensional problem of stagnation-point flow either on a flat plate or on a cylinder are only for the case of axisymmetric formulation. The only exception is the study of three-dimensional stagnation-point flow on a flat plate by Howarth (1951, "The Boundary Layer in Three-Dimensional Flow—Part II: The Flow Near Stagnation Point," Philos. Mag., **42**, pp. 1433–1440), which is based on boundary layer theory approximation and zero pressure assumption in direction of normal to the surface. In our study the nonaxisymmetric three-dimensional steady viscous stagnation-point flow and heat transfer in the vicinity of a flat plate are investigated based on potential flow theory, which is the most general solution. An external fluid, along z-direction, with strain rate a impinges on this flat plate and produces a two-dimensional flow with different components of velocity on the plate. This situation may happen if the flow pattern on the plate is bounded from both sides in one of the directions, for example x-axis, because of any physical limitation. A similarity solution of the Navier–Stokes equations and energy equation is presented in this problem. A reduction in these equations is obtained by the use of appropriate similarity transformations. Velocity profiles and surface stress-tensors and temperature profiles along with pressure profile are presented for different values of velocity ratios, and Prandtl number.*
[DOI: 10.1115/1.3153366]

Keywords: similarity solution, nonaxisymmetric three-dimensional, stagnation flow and heat transfer, steady, viscous fluid

1 Introduction

There are many three-dimensional axisymmetric solutions for Navier–Stokes and energy equations regarding the problem of stagnation-point flow and heat transfer in the vicinity of a flat plate or a cylinder. Fundamental three-dimensional axisymmetric studies in which the nonlinearity is removed by superposition of fundamental exact solutions that lead to nonlinear coupled ordinary differential equations by separation of coordinate variables are uniform shear flow over a flat plate in which the flow is induced by a plate oscillating in its own plane beneath a quiescent fluid by Stokes [1], two-dimensional stagnation-point flow by Hiemenz [2], and the flow induced by a disk rotating in its own plane by Von Karman [3]. The works in which nonlinearity is readily superposed but still axisymmetric are flow over a flat plate with uniform normal suction by Griffith and Meredith [4], three-dimensional stagnation-point flow by Homann [5]. The same kind of work but on a cylinder is the axisymmetric stagnation flow on a circular cylinder by Wang [6]. Further three-dimensional axisymmetric exact solutions to the Navier–Stokes equations are obtained by superposition of the uniform shear flow on a body oscillating or translating in its own plane, with or without suction. The examples are superposition of two-dimensional and three-dimensional stagnation-point flows by Howarth [7], Reshotko [8], and Libby [9]. The ones using superposition of stagnation flow are by Gersten [10] and Papenfuss [11]. Also, the three-dimensional axisymmetric solution for a fluid oscillating about a nonzero mean flow parallel to a flat plate with uniform suction was given by Stuart [12]. More three-dimensional axisymmetric solutions with superposition of stagnation-point flow on a flat plate oscillating in its own plate, and also consideration of the case where the plate is stationary and the stagnation stream is made to oscillate was done by Glauert [13], uniform shear flow aligned with out flowing two-dimensional stagnation-point flow has been presented by Stuart [14], and uniform flow along a flat plate with time-dependent suction and included periodic oscillations of the external stream was studied by Kelly [15]. In addition, Gorla [16] has studied unsteady laminar axisymmetric stagnation flow over a circular cylinder, nonsimilar axisymmetric stagnation flow on a moving cylinder [17], transient response behavior of an axisymmetric stagnation flow on a circular cylinder due to time-dependent free stream velocity [18], and unsteady viscous flow in the vicinity of an axisymmetric stagnation-point on a cylinder [19]. Additionally, suppression of turbulence in wall-bounded flows by high-frequency spanwise oscillations has been studied by Jung et al. [20], axisymmetric stagnation flow toward a moving plate by Wang [21], and axisymmetric stagnation-point flow impinging on a transversely oscillating plate with suction by Weidman and Mahalingam [22]. Studies under the same category as above but with a rotating body include superposition of uniform suction at the boundary of a rotating disk by Stuart [23], shear flow over a rotating plate by Wang [24], and radial stagnation flow on a rotating cylinder with uniform transpiration by Cunning et al. [25].

Three-dimensional axisymmetric studies considering exact solutions of the Navier–Stokes equations along with energy equation include the problems of heat transfer in an axisymmetric stagnation flow on a cylinder by Gorla [26], axisymmetric stagnation-point flow and heat transfer of a viscous fluid on a moving cylinder with time-dependent axial velocity and uniform transpiration by Saleh and Rahimi [27], and axisymmetric stagnation-point flow and heat transfer of a viscous fluid on a rotating cylinder with time-dependent angular velocity and uniform transpiration by Rahimi and Saleh [28], and similarity solution of nonaxisymmetric heat transfer in stagnation-point flow on a cylinder with simultaneous axial and rotational movements by Rahimi and Saleh [29].

In this study the nonaxisymmetric three-dimensional steady viscous stagnation-point flow and heat transfer in the vicinity of a flat plate are investigated. A similarity solution of the Navier–Stokes equations and energy equation is derived in this problem. A reduction in these equations is obtained by use of these appropriate similarity transformations [30]. The obtained coupled ordinary differential equations are solved using numerical techniques. Velocity profiles and surface stress-tensors and temperature profiles along with pressure profile are presented for different values of impinging fluid strain rate, different forms of jet arrangements, and Prandtl number.

2 Problem Formulation

Flow is considered in Cartesian coordinates (x,y,z) with corresponding velocity components (u,v,w), Fig. 1. This figure represents a three-dimensional surface which is the boundary of a po-

[1]Corresponding author.

Contributed by the Fluids Engineering Division of ASME for publication in the JOURNAL OF FLUIDS ENGINEERING. Manuscript received December 25, 2007; final manuscript received May 4, 2009; published online June 24, 2009. Assoc. Editor: Malcolm J. Andrews.

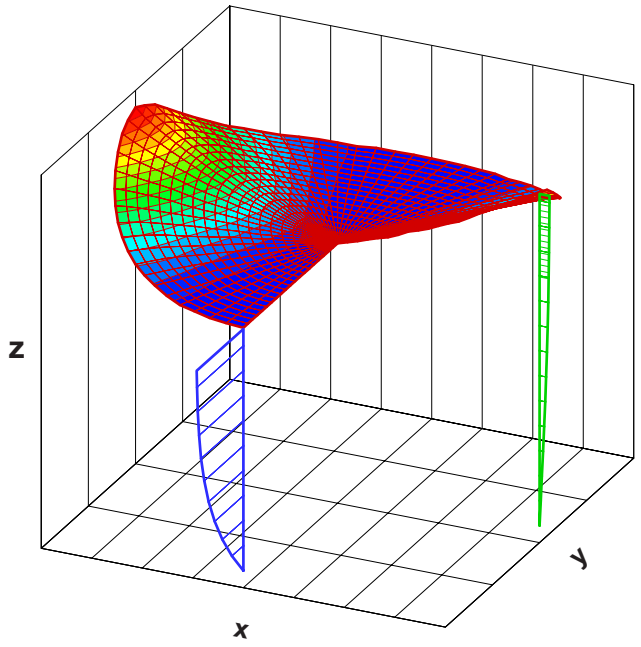

Fig. 1 Three-dimensional stream surface and velocity profiles

tential region, and with the region of rapid changes of velocity components for all $0<\lambda\leq 1$, in which λ is the coefficient that indicates the difference between the velocity components in x- and y-directions. The velocity components in these directions are the same if $\lambda=1$, the axisymmetric case. We consider the laminar steady incompressible flow and heat transfer of a viscous fluid in the neighborhood of the stagnation-point on a flat plate located in the plane $z=0$. An external fluid along the z-direction with strain rate a impinges on this flat plate and produces a two-dimensional flow with different components of velocity on the plate. This situation may be encountered if the flow pattern on the plate is bounded in one of the directions, for example on the x-axis, because of physical limitations. The three-dimensional, steady Navier–Stokes and energy equations in Cartesian coordinates are used in which p, ρ, ν, and α are the fluid pressure, density, kinematic viscosity, and thermal diffusivity.

3 Self-Similar Solution

3.1 Fluid Flow Solution. An inviscid solution of governing equations valid far above the plane is given by

$$U=a\lambda x, \quad 0<\lambda\leq 1 \tag{1}$$

$$V=ay \tag{2}$$

$$W=-a(\lambda+1)z \tag{3}$$

$$p=p_0-\tfrac{1}{2}\rho a^2[\lambda^2x^2+y^2+(\lambda+1)^2z^2] \tag{4}$$

p_0 is stagnation pressure.

A reduction in the Navier–Stokes equations is sought by the following coordinate separation in which the solution of the viscous problem inside the boundary layer is obtained by composing the inviscid and viscous parts of the velocity components as the following:

$$u=a\lambda x f'(\eta), \quad 0<\lambda\leq 1 \tag{5}$$

$$v=ay[f'(\eta)+g'(\eta)] \tag{6}$$

$$w=-\sqrt{a\nu}[(\lambda+1)f(\eta)+g(\eta)] \tag{7}$$

$$\eta=\sqrt{a/\nu}z \tag{8}$$

in which the terms involving $f(\eta)$ and $g(\eta)$ in Eqs. (5)–(7) comprise the Cartesian similarity form for steady stagnation-point flow, and prime denotes differentiation with respect to η. Note that the boundary layer is defined here as the edge of the points where its velocity is 99% of its corresponding potential velocity. Transformations (5)–(7) satisfy continuity automatically, and their insertion into momentum equations yields a coupled system of ordinary differential equations in terms of $f(\eta)$ and $g(\eta)$, and an expression for the pressure:

$$f'''+[(\lambda+1)f+g]f''+\lambda[1-(f')^2]=0 \tag{9}$$

$$g'''+[(\lambda+1)f+g]g''-[g'+2f']g'-(1-\lambda)[(f')^2-1]=0 \tag{10}$$

$$p=p_0-\tfrac{1}{2}\rho a^2(\lambda^2x^2+y^2)-\rho a\nu\left\{\tfrac{1}{2}[(\lambda+1)f+g]^2+\lambda f'+(f'+g')-(\lambda+1)-\gamma\eta(\lambda+1)\right\} \tag{11}$$

$\gamma=\lim_{\eta\to\infty} g(\eta)=$constant. This constant is obtained after solving Eqs. (9) and (10). The boundary conditions are

$$\eta=0: f=0, \quad f'=0, \quad g=0, \quad g'=0 \tag{12}$$

$$\eta\to\infty: f'=1, \quad g'=0 \tag{13}$$

Note that when $\lambda=1$, the case of axisymmetric three-dimensional results are obtained [5]. When $\lambda=0$, the results are the same as a two-dimensional problem.

3.2 Heat Transfer Solution. To transform the energy equation into a nondimensional form for the case of defined wall temperature, we introduce

$$\theta=\frac{T(\eta)-T_\infty}{T_w-T_\infty} \tag{14}$$

Making use of Eqs. (5)–(8), the energy equation may be written as

$$\theta''+\mathrm{Pr}[g+(1+\lambda)f]\theta'=0 \tag{15}$$

with the boundary conditions as

$$\eta=0: \theta=1 \tag{16}$$

$$\eta\to\infty: \theta=0 \tag{17}$$

where $\mathrm{Pr}=\nu/\alpha$ is the Prandtl number, and prime indicates differentiation with respect to η.

Note that for $\mathrm{Pr}=1$, the thickness of the fluid boundary layer and heat boundary layer become the same, and therefore this concept is proved by reaching Eq. (15) from Eq. (9) through substitution of $\theta=f'$.

Eqs. (9), (10), and (15) are solved numerically using a shooting method trial and error and based on the Runge–Kutta algorithm, and the results are presented for selected values of λ and Pr in Secs. 4 and 5. Since Eqs. (9) and (10) are coupled, we guess a value for $g(\eta)$ function first and solve Eq. (9) for $f(\eta)$. Then Eq. (10) is integrated and a new value of $g(\eta)$ is obtained, which is used to solve Eq. (9) again. This procedure is repeated until the differences between the results are less than 0.00001.

4 Shear-Stress

The shear-stress at the wall surface is calculated from:

$$\tau=\mu\left(\frac{\partial u}{\partial z}\boldsymbol{e}_x+\frac{\partial v}{\partial z}\boldsymbol{e}_y\right)_{z=0} \tag{18}$$

where μ is the fluid viscosity. Using the transformation equations (5)–(8), the shear-stress at the flat plate surface becomes

$$\tau=\rho\nu^{1/2}a^{3/2}(\lambda^2x^2f''^2+y^2(f''+g'')^2)^{1/2} \tag{19}$$

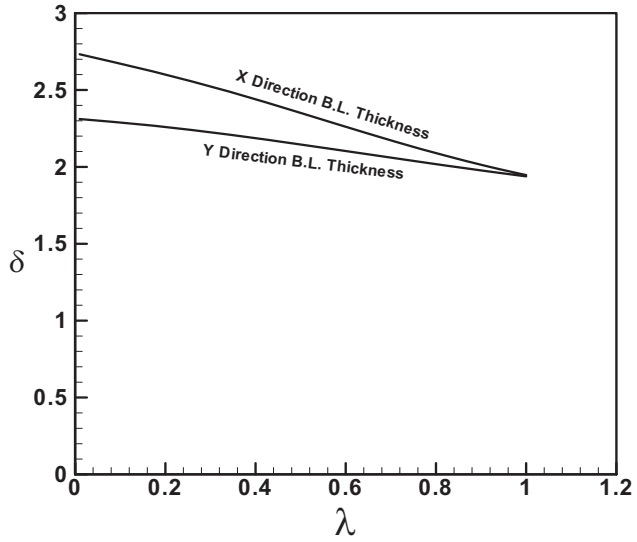

Fig. 2 Boundary layer thickness versus variation of velocity ratio

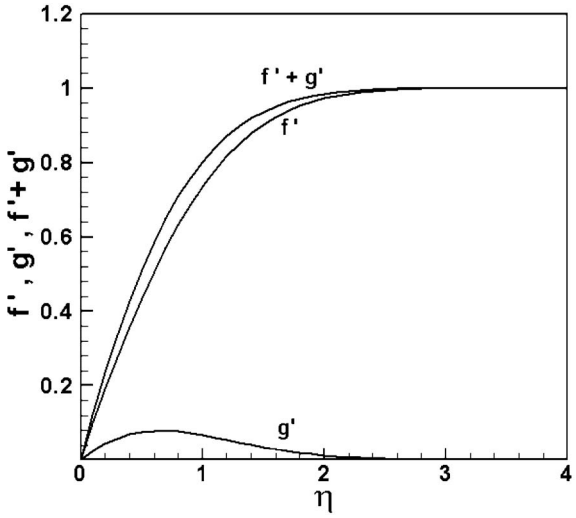

Fig. 4 Typical *u* and *v* velocity components for λ=0.5

The wall shear stress is presented for different values of λ in the Presentation of Results.

5 Presentation of Results

In this section, the solution of the self-similar equations (9), (10), and (15) along with the surface shear-stresses for different values of velocity ratios and Prandtl numbers are presented.

The boundary layer thickness in the two directions on the flat plate versus the velocity ratio is presented in Fig. 2. This thickness is larger in the *x*-direction compared with the *y*-direction, because of the difference of the velocity components in these directions. The difference of the boundary layer thickness in directions *x* and *y* decreases as λ increases until the value of unity where these two layers meet each other. From Fig. 2, the following relations can be obtained for the boundary layer thickness versus the ratio of the velocities in potential flow:

$$\delta_x = -0.75\lambda + 2.75$$
$$\delta_y = -0.35\lambda + 2.35 \tag{20}$$

Comparing these results with the ones in Howarth [7], the difference between the boundary layer thickness in *x*-direction is 2% and in *y*-direction is 18%, which is because of the inablity of his approximation solution method.

Figures 3 and 4 present the profiles of f', g', and $f'+g'$ for different values of velocity ratio λ. The smaller the λ, the bigger g' and therefore the difference between the velocity components is larger. For $\lambda \to 1$, then $g' \to 0$ and the two velocity components become the same.

Figures 5 and 6 depict the f and g profiles, and therefore *w*-component of velocity versus velocity ratio. The bigger the λ, the larger the absolute value of the *w*-component of the velocity, as expected. This component of velocity, which is the penetration of momentum into the boundary layer in the *z*-direction, changes abruptly as λ increases. This is because the boundary layer increases faster as λ gets larger, and therefore there is need for more penetration of the momentum and hence this component of velocity gets bigger.

The temperature profiles for different values of velocity ratio and selected values of Prandtl numbers are presented in Figs. 7 and 8. The increase in velocity ratio and increase in Prandtl number both cause the decrease in the temperature profile. It is also noted that for $\lambda \to 1$ and Pr=1, the temperature boundary layer is obtained the same as the velocity boundary layer.

Figure 9 presents the change in shear-stress on the flat plate surface in terms of velocity ratio λ. The following relations can be deduced from this plot

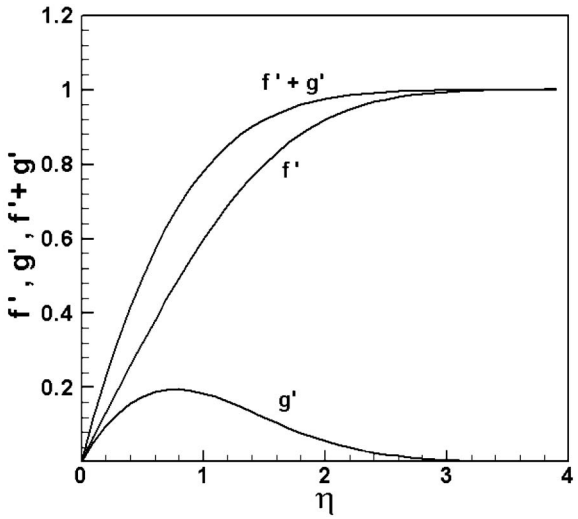

Fig. 3 Typical *u* and *v* velocity components for λ=0.1

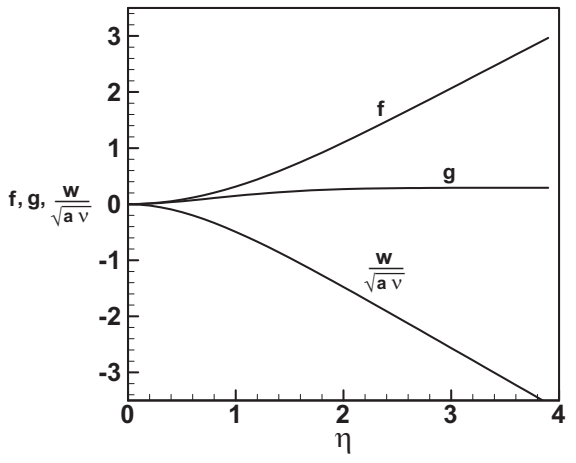

Fig. 5 Typical *w*-component of velocity for λ=0.1

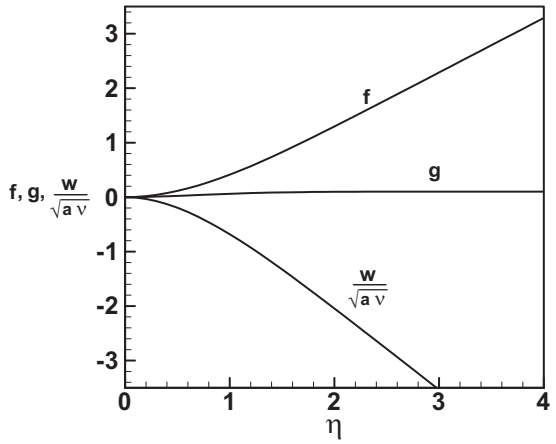

Fig. 6 Typical *w*-component of velocity for λ=0.50

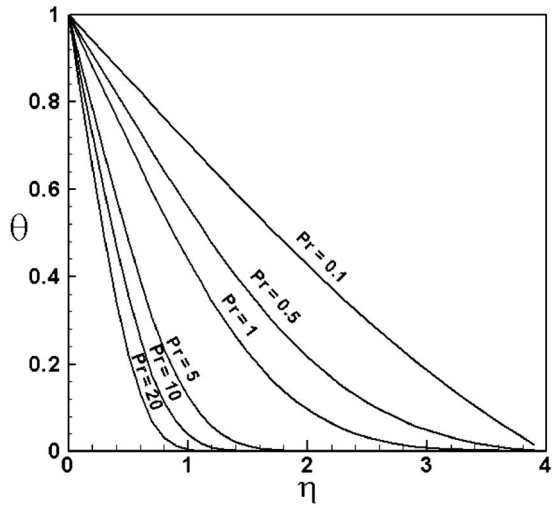

Fig. 7 Temperature profile for the case of λ=0.1 and different Pr values

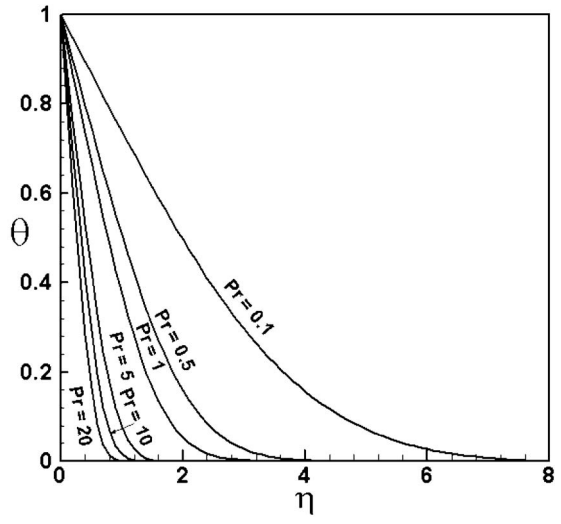

Fig. 8 Temperature profile for the case of λ=0.50 and different Pr values

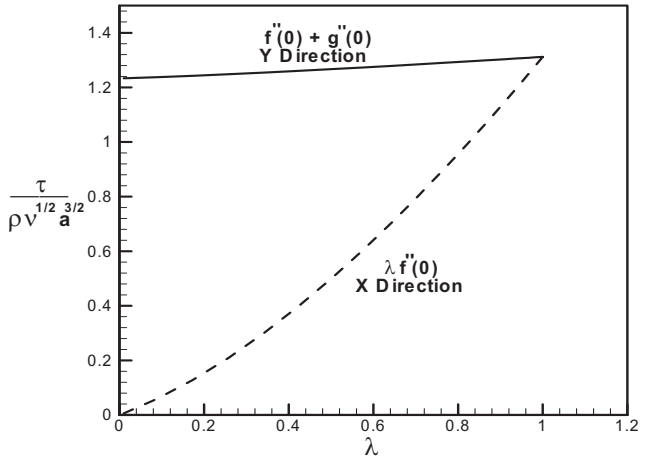

Fig. 9 Surface shear-stress components on the flat plate

$$\tau_x = \lambda^{1.55} + 0.3\lambda$$
$$\tau_y = 0.1\lambda^{1.1} - 0.03\lambda + 1.235 \quad (21)$$

As $\lambda \to 0$, the stress tensor in *x*-direction tends to zero but note that $\lambda = 0$ does not represent a physical situation. In Howarth's work [7], for the case of the velocity aspect ratio (in our study, λ) equal to zero, the shear-stress in *x*-direction is calculated to be an amount equal to 0.570, though it must be close to zero physically, as it has been shown by τ_x relation obtained above. This shows again the inability of his solution method and the error approximation it brings about.

Pressure profiles inside the boundary layer are shown in Fig. 10 for selected values of λ. From these profiles it can be seen that with an increase in velocity ratio in *x*- and *y*-directions and tending toward the symmetric situation, the variation in pressure inside the boundary layer increases because λ affects velocity directly, and the pressure changes with velocity in power form.

6 Conclusions

The most general solution of the Navier–Stokes equations and energy equation for nonaxisymmetric three-dimensional stagnation-point flow and heat transfer on a flat plate has been presented in this paper based on potential flow theory. This task

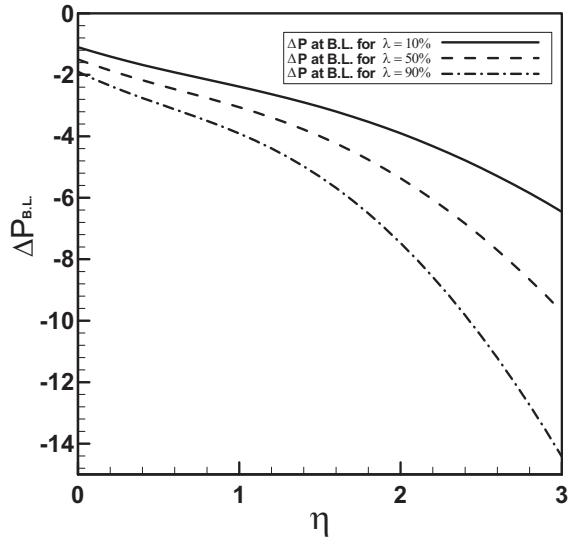

Fig. 10 Pressure profiles for selected values of λ

has been accomplished by choosing appropriate similarity transformations and reduction in these governing equations to a system of coupled ordinary differential equations and subsequent numerical integration. Velocity components, temperature profiles, pressure change, and surface stress tensor have been presented for selected values of velocity ratios and Prandtl numbers. This solution represents many physical situations, including the stagnation-point problem in which the flow pattern on the plate is bounded from both sides in one direction because of any physical limitation.

References

[1] Stokes, G. G., 1851, "On the Effect of the Internal Friction of Fluids on the Motion of Pendulum," Trans. Cambridge Philos. Soc., **9**, pp. 8–106.

[2] Hiemenz, K., 1911, "Boundary Layer for a Homogeneous Flow Around a Dropping Cylinder," Dinglers Polytechnic J., **326**, pp. 321–410.

[3] Von Karman, T., 1921, "Friction of Laminar Flow and Laminar Over a Surface," Z. Angew. Math. Mech., **1**, pp. 233–252.

[4] Griffith, A. A., and Meredith, F. W., 1936, "The Possible Improvement in Aircraft Performance Due to the Use of Boundary Layer Suction," Royal Aircraft Establishment Report No. E 3501, p. 12.

[5] Homann, F. Z., 1936, "Effect of High Speed Over Cylinder and Sphere," Z. Angew. Math. Mech., **16**, pp. 153–164.

[6] Wang, C. Y., 1974, "Axisymmetric Stagnation Flow on a Cylinder," Q. Appl. Math., **32**, pp. 207–213.

[7] Howarth, L., 1951, "The Boundary Layer in Three-Dimensional Flow—Part II: The Flow Near Stagnation Point," Philos. Mag., **42**, pp. 1433–1440.

[8] Roshetko, E., 1958, "Heat Transfer at a General Three-Dimensional Stagnation Point," Jet Propul., **28**, pp. 58–60.

[9] Libby, P. A., 1967, "Heat and Mass Transfer at a General Three-Dimensional Stagnation Point," AIAA J., **5**, pp. 507–517.

[10] Gersten, K., 1973, "Three-Dimensional Compressible Boundary Layer Along With Suction and Blowing From Its Surface," Warme-und Stoffubertrag., **6**, pp. 52–61.

[11] Papenfuss, H. D., 1975, "Effect of Three-Dimensional, Compressible Second-Degree Boundary Layer Along With Blowing From a Surface," Ph.D. thesis, Ruhr-Universitat Bochum, Germany.

[12] Stuart, J. T., 1955, "A Solution of the Navier–Stokes and Energy Equations Illustrating the Response of Skin Friction and Temperature of an Infinite Plate Thermometer to Fluctuations in the Stream Velocity," Proc. R. Soc. London, Ser. A, **231**, pp. 116–130.

[13] Glauert, M. B., 1956, "The Laminar Boundary Layer on Oscillating Plates and Cylinders," J. Fluid Mech., **1**, pp. 97–110.

[14] Stuart, J. T., 1959, "The Viscous Flow Near a Stagnation-Point When the External Flow has Uniform Vorticity," J. Aerosp. Sci., **26**, pp. 124–125.

[15] Kelly, R. E., 1965, "The Flow of a Viscous Fluid Past a Wall of Infinite Extent With Time-Dependent Suction," Q. J. Mech. Appl. Math., **18**, pp. 287–298.

[16] Gorla, R. S. R., 1977, "Unsteady Laminar Axisymmetric Stagnation Flow Over a Circular Cylinder," Development in Mechanics Journal, **9**, pp. 286–288.

[17] Gorla, R. S. R., 1978, "Nonsimilar Axisymmetric Stagnation Flow on a Moving Cylinder," Int. J. Eng. Sci., **16**, pp. 392–400.

[18] Gorla, R. S. R., 1978, "Transient Response Behavior of an Axisymmetric Stagnation Flow on a Circular Cylinder Due to Time-Dependent Free Stream Velocity," Lett. Appl. Eng. Sci., **16**, pp. 493–502.

[19] Gorla, R. S. R., 1979, "Unsteady Viscous Flow in the Vicinity of an Axisymmetric Stagnation-Point on a Cylinder," Int. Sci., **17**, pp. 87–93.

[20] Jung, W. L., Mangiavacchi, N., and Akhavan, R., 1992, "Suppression of Turbulence in Wall-Bounded Flows by High-Frequency Spanwise Oscillations," Phys. Fluids A, **4**, pp. 1605–1607.

[21] Wang, C. Y., 1973, "Axisymmetric Stagnation Flow Towards a Moving Plate," American Institute of Chemical Engineering Journal, **19**, pp. 961–970.

[22] Weidman, P. D., and Mahalingam, S., 1997, "Axisymmetric Stagnation-Point Flow Impinging on a Transversely Oscillating Plate With Suction," J. Eng. Math., **31**, pp. 305–318.

[23] Stuart, J. T., 1954, "On the Effects of Uniform Suction on the Steady Flow Due to a Rotating Disk," Q. J. Mech. Appl. Math., **7**, pp. 446–457.

[24] Wang, C. Y., 1989, "Shear Flow Over a Rotating Plate," Appl. Sci. Res., **46**, pp. 89–96.

[25] Cunning, G. M., Davis, A. M. J., and Weidman, P. D., 1998, "Radial Stagnation Flow on a Rotating Cylinder With Uniform Transpiration," J. Eng. Math., **33**, pp. 113–128.

[26] Gorla, R. S. R., 1976, "Heat Transfer in an Axisymmetric Stagnation Flow on a Cylinder," Appl. Sci. Res., **32**, pp. 541–553.

[27] Saleh, R., and Rahimi, A. B., 2004, "Axisymmetric Stagnation-Point Flow and Heat Transfer of a Viscous Fluid on a Moving Cylinder With Time-Dependent Axial Velocity and Uniform Transpiration," ASME J. Fluids Eng., **126**, pp. 997–1005.

[28] Rahimi, A. B., and Saleh, R., 2007, "Axisymmetric Stagnation-Point Flow and Heat Transfer of a Viscous Fluid on a Rotating Cylinder With Time-Dependent Angular Velocity and Uniform Transpiration," ASME J. Fluids Eng., **129**, pp. 106–115.

[29] Rahimi, A. B., and Saleh, R., 2008, "Similarity Solution of Unaxisymmetric Heat Transfer in Stagnation-Point Flow on a Cylinder With Simultaneous Axial and Rotational Movements," ASME J. Heat Transfer, **130**, p. 054502.

[30] Nayfeh, A. H., 1985, *Perturbation Techniques*, Wiley, New York.